Volume 68C
Number 4
Oct.–Dec. 1964

Engineering and Instrumentation

U.S. DEPARTMENT OF COMMERCE

SECTION C

JOURNAL OF RESEARCH

NATIONAL BUREAU OF STANDARDS

Journal of Research

of the

National Bureau of Standards

C. Engineering and Instrumentation

OCT.–DEC. • 1964

VOLUME • 68C

NUMBER • 4

Editor: Martin Greenspan

Associate Editors: G. F. Montgomery, Thomas N. Flynn

Publication dates:
Feb. 15, May 15, Aug. 15, Nov. 15, 1964

JOURNAL OF RESEARCH

The National Bureau of Standards Journal of Research reports research and development in the fields of activity shown at right. Also included from time to time are survey articles on topics closely related to the Bureau's scientific and technical program.

The Journal is published in four separate sections as follows:

A. Physics and Chemistry

Contains papers of interest primarily to scientists working in these fields. Issued six times a year. Annual subscription: domestic, $4.00; foreign, $4.75. Single copy, 70¢.

B. Mathematics and Mathematical Physics

Presents studies and compilations designed mainly for the mathematician and the theoretical physicist. Issued quarterly. Annual subscription: domestic, $2.25; foreign, $2.75. Single copy, 75¢.

C. Engineering and Instrumentation

Reports research and development results of interest chiefly to the engineer and the applied scientist. Issued quarterly. Annual subscription: domestic, $2.25; foreign, $2.75. Single copy, 75¢.

D. Radio Science (formerly Radio Propagation)

Published in cooperation with U.S. National Committee of URSI. Presents papers in radio propagation, communications, and radio science generally. Issued monthly. Annual subscription: domestic, $9.00; foreign, $11.50. Single copy, $1.00.

The National Bureau of Standards is a principal focal point in the Federal Government for assuring maximum application of the physical and engineering sciences to the advancement of technology in industry and commerce. Its responsibilities include development and maintenance of the national standards of measurement, and the provisions of means for making measurements consistent with those standards; determination of physical constants and properties of materials; development of methods for testing materials, mechanisms, and structures, and making such tests as may be necessary, particularly for government agencies; cooperation in the establishment of standard practices for incorporation in codes and specifications; advisory service to government agencies on scientific and technical problems; invention and development of devices to serve special needs of the Government; assistance to industry, business, and consumers in the development and acceptance of commercial standards and simplified trade practice recommendations; administration of programs in cooperation with United States business groups and standards organizations for the development of international standards of practice; and maintenance of a clearinghouse for the collection and dissemination of scientific, technical, and engineering information.

Institute for Basic Standards. Electricity. Metrology. Heat. Radiation Physics. Mechanics. Applied Mathematics. Atomic Physics. Physical Chemistry. Laboratory Astrophysics.* Radio Standards Laboratory: Radio Standards Physics; Radio Standards Engineering.** Office of Standard Reference Data.

Institute for Materials Research. Analytical Chemistry. Polymers. Metallurgy. Inorganic Materials. Reactor Radiations. Cryogenics.** Office of Standard Reference Materials.

Central Radio Propagation Laboratory.** Ionosphere Research and Propagation. Troposphere and Space Communications. Radio Systems. Upper Atmosphere and Space Physics.

Institute for Applied Technology. Textiles and Apparel Technology Center. Building Research. Industrial Equipment. Information Technology. Performance Test Development. Instrumentation. Transport Systems. Office of Technical Services. Office of Weights and Measures. Office of Engineering Standards. Office of Industrial Services.

*NBS Group, Joint Institute for Laboratory Astrophysics at the University of Colorado.
**Located at Boulder, Colo.

U.S. DEPARTMENT OF COMMERCE
Luther H. Hodges, Secretary
NATIONAL BUREAU OF STANDARDS
A. V. Astin, Director

Order all publications from the Superintendent of Documents
U.S. Government Printing Office, Washington, D.C., 20402.

Use of funds for printing this publication approved by the Director of the Bureau of the Budget (June 19, 1961).

JOURNAL OF RESEARCH of the National Bureau of Standards—C. Engineering and Instrumentation
Vol. 68C, No. 4, October–December 1964

Theory of Mirror Spectrographs
I. Astigmatic Illumination of Plane Gratings and Prisms

Klaus D. Mielenz

(July 15, 1964)

By application of an eikonal theory, the image forming properties of plane gratings and prisms are shown to be quite similar. With uncollimated illumination, the astigmatism of both vanishes for an in-plane mounting at the minimum of deviation. Both produce perfect images if illuminated with perfectly collimated (parallel) light. In mirror spectrographs, where this requirement cannot be fulfilled, aberrations are minimized if parallelism of rays is achieved in the cross section normal to the grating grooves, or prism edge.

1. Introduction

Neither plane gratings nor prisms cause image aberrations when used in perfectly collimated light. Parallel light between collimator and camera, therefore, is standard practice in designing spectrographs. Concave collimating mirrors, however, produce astigmatic pencils of light and, thus, cannot provide the desired perfect collimation. The resulting aberrations of the grating or prism will be examined in this paper. The conditions to minimize these aberrations will be derived.

An eikonal theory will be applied to both plane grating and prism. In principle, this method was already used in H. A. Rowland's [1] [1] and C. Runge's [2] work on plane and concave gratings. Its modern form is due to P. Zernicke [3] and has subsequently proved to be the most fruitful way to analyze concave gratings [4, 5].

The plane grating has been sparingly treated only. Usually, parallel illumination is assumed [1, 4]. M. V. Murty [6] has studied the plane grating in convergent and divergent light. Astigmatic illumination, however, has apparently never been considered.

An eikonal theory of the prism does not appear to exist at all. Yet, it will be shown here to provide a closed theory of image formation by the latter, also. It also leads to interesting analogies between gratings and prisms.

[1] Figures in brackets indicate the literature references at the end of this paper

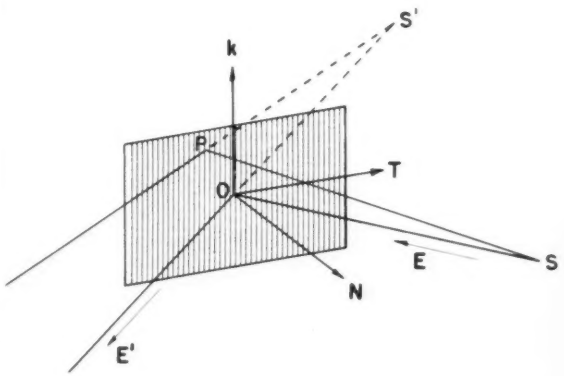

FIGURE 1. *Plane reflectance grating.*

2. Plane Grating

2.1. Characteristic Function

Consider a plane reflectance grating illuminated by a point source S, as in figure 1. The grating produces a virtual image, S', of the source, and S' is a perfect image of S if, for an arbitrary ray, the characteristic function (eikonal)

$$V=|SP|-|PS'|+p\mu\lambda/d \qquad (1)$$

is independent of the point, P, at which the ray intersects the grating (P. Zernicke [3]). Here, p is the coordinate of P in the direction perpendicular to

the grating grooves, μ the spectral order, λ the wavelength of the diffracted beam, and d the grating constant. As usual in geometrical optics, the virtual path, $|PS'|$, is counted as negative.

Introduce base vectors, **N**, **T**, and **k**, with the origin at the grating center O so that **N** is the grating normal, and **T** and **k** are the grating tangents perpendicular and parallel to the grooves. Let

$$\mathbf{S}=-s\mathbf{E}=-s(A, B, C), \tag{2}$$

$$\mathbf{S}'=-s'\mathbf{E}'=-s'(A', B', C') \tag{3}$$

be the point vectors $\overrightarrow{OS}$ and $\overrightarrow{OS'}$, **E** and **E**′ being unity vectors along the principal rays incident and diffracted at O, and let

$$\mathbf{P}=(O, p, q) \tag{4}$$

be the point vector, $\overrightarrow{OP}$, of P. Thus,

$$\overrightarrow{SP}=-\mathbf{S}+\mathbf{P},\ \overrightarrow{PS'}=\mathbf{S}'-\mathbf{P},$$

and, for the characteristic function (1),

$$\begin{aligned} V&=\sqrt{(\mathbf{S}-\mathbf{P})^2}-\sqrt{(\mathbf{S}'-\mathbf{P})^2}+p\mu\lambda/d \\ &=v-v'+p\mu\lambda/d. \end{aligned} \tag{5}$$

2.2. Series Expansion

From (2) and (4),

$$\begin{aligned} v&=s[1+2(Bp+Cq)/s+(p^2+q^2)/s^2]^{1/2} \\ &=s[1+(Bp+Cq)/s+\tfrac{1}{2}(p^2+q^2)/s^2 \\ &\quad -\tfrac{1}{2}(Bp+Cq)^2/s^2-\tfrac{1}{2}(p^2+q^2)(Bp+Cq)/s^3 \\ &\quad +\tfrac{1}{2}(Bp+Cq)^3/s^3], \end{aligned}$$

where fourth-order terms are neglected.

Hence, with the corresponding expression for v',

$$\begin{aligned} V&=(s-s')+(B-B'+\mu\lambda/d)p+(C-C')q \\ &\quad +\tfrac{1}{2}(p^2+q^2)(1/s-1/s') \\ &\quad -\tfrac{1}{2}[(Bp+Cq)^2/s-(B'p+C'q)^2/s'] \\ &\quad -\tfrac{1}{2}(p^2+q^2)[(Bp+Cq)/s^2-(B'p+C'q)/s'^2] \\ &\quad +\tfrac{1}{2}[(Bp+Cq)^3/s^2-(B'p+C'q)^3/s'^2]. \end{aligned} \tag{6}$$

2.3. Focus Condition

The first four terms of (6) vanish, and V is of second-order dependence upon p and q only, if

$$s=s', \tag{7}$$

$$B-B'+\mu\lambda/d=0, \tag{8}$$

$$C=C'. \tag{9}$$

These equations describe the location of the virtual image in space.

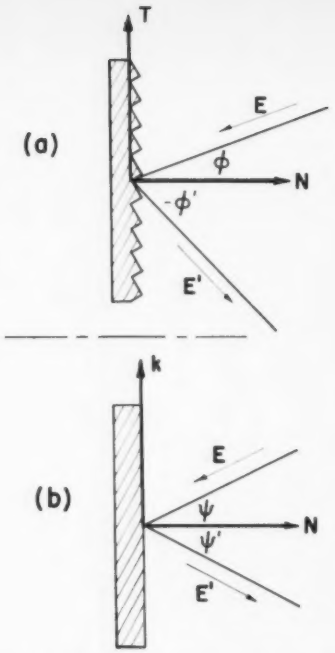

FIGURE 2. *The two principal cross sections of the grating.*

For the **N,T**-plane (fig. 2a), (8) is reduced to the familiar, two-dimensional grating equation,

$$\sin\phi+\sin\phi'=\mu\lambda/d, \tag{8a}$$

since we have, here, $C=C'=0$, and

$$B=\mathbf{E}\cdot\mathbf{T}=\cos(90°+\phi)=-\sin\phi, \tag{8b}$$

$$B'=\mathbf{E}'\cdot\mathbf{T}=\cos(90°-\phi')=\sin\phi', \tag{8c}$$

where ϕ and ϕ' are the angles which the projections of the principal ray enclose with the grating normal. In accordance with convention, ϕ is here always taken as positive, and ϕ' as positive or negative depending on whether incident and diffracted ray lie on the same or on different sides of the normal.

Equation (9) constitutes the reflection law,

$$\psi=\psi', \tag{9a}$$

for the **N,k**-plane (fig. 2b), where the grating simply acts as a mirror. For it is, with $B=B'=0$,

$$C=\mathbf{E}\cdot\mathbf{k}=\cos(90°+\psi)=-\sin\psi, \tag{9b}$$

$$C'=\mathbf{E}'\cdot\mathbf{k}=\cos(90°+\psi')=-\sin\psi', \tag{9c}$$

where ψ and ψ' (both positive) are the angles which the projections of the principal ray enclose with the normal.

V vanishes altogether if, furthermore,

$$s=\infty. \tag{10}$$

Used in perfectly collimated light, the grating produces no aberrations.

2.4. Second-Order Aberrations, Minimum of Deviation

With (7), (8), and (9), the second-order term of V becomes

$$-[\tfrac{1}{2}(B^2-B'^2)p+(B-B')Cq]p/s.$$

Except for $B=B'$ (zero-order reflection from the grating) and for $s=\infty$ (parallel illumination), it vanishes for

$$B'=-B,\ C=0, \tag{11}$$

which is the case of the grating used in autocollimation; i.e., of an in-plane mounting at the minimum of deviation. The astigmatism of the grating, therefore, vanishes for this mounting.

2.5. Higher-Order Aberrations, Astigmatic Illumination

Throughout the above discussion, illumination of the grating with a spherical or plane wave front was assumed by considering object and image as mathematical points so that the focal distances s and s' are the same in all cross sections of the grating. If the grating is however illuminated with an astigmatic pencil of rays; i.e., a cylindrical wave front, different focal distances must be assumed for different cross sections.

Equation (10) can then no longer be satisfied since an astigmatic pencil contains, at best, parallel rays in one cross section only. It must be determined, therefore, how this cross section has to be laid in order that the aberrations of the grating are at least minimized. The two principal cross sections of the grating will be considered separately for this purpose.

N, T-Plane: With $q=0$ and $s=s'=s_H$, the third-order term of (6) is

$$\tfrac{1}{2}[(B^3-B'^3)-(B-B')]p^3/s_H^2.$$

Except for $B_1'=B$ and $B_{2,3}'=-\tfrac{1}{2}(B\pm\sqrt{4-3B^2})$,[2] it vanishes for

$$s_H=\infty, \tag{12}$$

only, when V will be identically zero in the **N, T**-plane. Parallel illumination is therefore essential in this cross section.

N, k-Plane: With $p=0$, $C=C'$, and $s=s'=s_V$, the characteristic function V is identically zero for all choices of s_V. Parallel illumination, therefore, is not required in this cross section at all.

The aberrations of a grating in astigmatic illumination will thus be minimized if parallelism of rays is only accomplished in the **N, T**-plane.

[2] B_1' is again the trivial case of zero-order reflection from the grating. $B_{2,3}'$ yields imaginary values of ϕ'. The remaining solution B_3', though real, is not compatible with (11) and therefore of no significance since there is no point in removing third-order aberrations when second-order ones remain uncorrected.

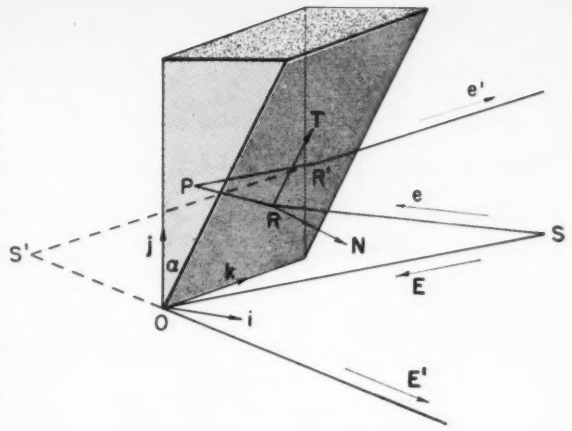

FIGURE 3. *Littrow prism.*

3. Prism

3.1. Characteristic Function

Consider a Littrow prism in air illuminated by a point source S, as in figure 3. The prism produces a virtual image, S', which is a perfect image if, for an arbitrary ray, the characteristic function

$$V=|SR|+n(|RP|+|PR'|)-|R'S'| \tag{13}$$

is independent of the point, P, at which the ray intersects the back face of the prism. Here, R and R' are the points at which the ray is refracted at the front face, and n is the refractive index of the prism material. The virtual path, $|R'S'|$, is counted as negative.

Introduce base vectors, **i**, **j**, and **k**, with the origin O on the prism edge, so that **i** is normal to the back face and **k** extends along the edge. Let α be the angle between the two prism faces, so that

$$\mathbf{N}=(\cos\alpha,\ -\sin\alpha,\ 0) \tag{14}$$

is the normal of the front face and

$$\mathbf{T}=(\sin\alpha,\ \cos\alpha,\ 0) \tag{15}$$

is the tangent perpendicular to the edge.

Let

$$\mathbf{S}=-s\mathbf{E}, \tag{16a}$$

$$\mathbf{R}=\mathbf{S}+|SR|\mathbf{e}, \tag{16b}$$

$$\mathbf{P}=(O,p,q)=\mathbf{R}+|RP|\mathbf{r}=\mathbf{R}'-|PR'|\mathbf{r}', \tag{16c}$$

$$\mathbf{R}'=\mathbf{S}'+|R'S'|\mathbf{e}', \tag{16d}$$

$$\mathbf{S}'=-s'\mathbf{E}' \tag{16e}$$

be the point vectors $\overrightarrow{OS}$, $\overrightarrow{OR}$, $\overrightarrow{OP}$, $\overrightarrow{OR'}$, and $\overrightarrow{OS'}$, where $\mathbf{E}$ and $\mathbf{E}'$ are the directions of the incident and emerging ray at O, $\mathbf{e}$ and $\mathbf{r}$ the directions of the incident and refracted ray at R, and $\mathbf{r}'$ and $\mathbf{e}'$ the directions of the incident and emerging ray at R'.

Thus, as R and R' lie on the front face,

$$\mathbf{R}\cdot\mathbf{N}=O=-s\mathbf{E}\cdot\mathbf{N}+|SR|\mathbf{e}\cdot\mathbf{N},$$
$$\mathbf{P}\cdot\mathbf{N}=-p\sin\alpha=|RP|\mathbf{r}\cdot\mathbf{N}=-|PR'|\mathbf{r}'\cdot\mathbf{N},$$
$$\mathbf{R}'\cdot\mathbf{N}=O=-s'\mathbf{E}'\cdot\mathbf{N}+|R'S'|\mathbf{e}'\cdot\mathbf{N},$$

and

$$|SR|=s\mathbf{E}\cdot\mathbf{N}/\mathbf{e}\cdot\mathbf{N}=sU, \tag{17a}$$

$$|RP|=-p\sin\alpha/\mathbf{r}\cdot\mathbf{N}, \tag{17b}$$

$$|PR'|=p\sin\alpha/\mathbf{r}'\cdot\mathbf{N}, \tag{17c}$$

$$|R'S'|=s'\mathbf{E}'\cdot\mathbf{N}/\mathbf{e}'\cdot\mathbf{N}=s'U'. \tag{17d}$$

The refraction law [7] requires

$$n(\mathbf{r}-\mathbf{r}\cdot\mathbf{NN})=\mathbf{e}-\mathbf{e}\cdot\mathbf{NN}, \tag{18}$$

or,

$$n\mathbf{r}\cdot\mathbf{N}=-\sqrt{n^2-1+(\mathbf{e}\cdot\mathbf{N})^2}=-W<0, \tag{19}$$

where the negative sign was taken as, in (17b), the length $|RP|$ must be positive.

Likewise,

$$n(\mathbf{r}'-\mathbf{r}'\cdot\mathbf{NN})=\mathbf{e}'-\mathbf{e}'\cdot\mathbf{NN}, \tag{18'}$$

$$n\mathbf{r}'\cdot\mathbf{N}=+\sqrt{n^2-1+(\mathbf{e}'\cdot\mathbf{N})^2}=+W'>0, \tag{19'}$$

and hence, for the characteristic function (13),

$$V=(sU+n^2p\sin\alpha/W)-(s'U'-n^2p\sin\alpha/W')$$
$$=v-v'. \tag{20}$$

3.2. Series Expansion

From (16) through (19),

$$\mathbf{S}=-sU\mathbf{e}-|RP|\mathbf{r}+\mathbf{P},$$
$$\mathbf{E}=(U+p\sin\alpha/sW)\mathbf{e}$$
$$-\sin\alpha(1+\mathbf{e}\cdot\mathbf{N}/W)\mathbf{N}p/s-(0,\,p/s,\,q/s). \tag{21}$$

Writing,

$$\mathbf{E}\cdot\mathbf{N}=A,\ \mathbf{E}\cdot\mathbf{T}=B,\ \mathbf{E}\cdot\mathbf{k}=C, \tag{22a}$$

$$\mathbf{e}\cdot\mathbf{N}=A/U,\ p/s=x,\ q/s=y, \tag{22b}$$

$$(\mathbf{e}\cdot\mathbf{T})^2+(\mathbf{e}\cdot\mathbf{k})^2=1-(\mathbf{e}\cdot\mathbf{N})^2=1-A^2/U^2, \tag{22c}$$

$$W=\sqrt{n^2-1+A^2/U^2}, \tag{22d}$$

we obtain, by scalar multiplication of (21) by $\mathbf{T}$ and $\mathbf{k}$, squaring, and adding,

$$(U+x\sin\alpha/W)^2(1-A^2/U^2)$$
$$-(B+x\cos\alpha)^2-(C+y)^2=0, \tag{23}$$

as an implicit representation of $U=U(x,y)$.

From here, the partial derivatives of U,

$$U_x=(\partial U/\partial x)_0$$
$$=B\cos\alpha-(1-A^2)\sin\alpha/W_0, \tag{24a}$$

$$U_{xx}=(\partial^2U/\partial x^2)_0$$
$$=1-U_x^2-n^2\sin^2\alpha/W_0^2, \tag{24b}$$

etc., taken at

$$x=y=0,\ U_0=1,\ W_0=+\sqrt{n^2-1+A^2}, \tag{24c}$$

can be obtained by repeated implicit differentiation. Then,

$$U=1+U_xx+U_yy+\ldots, \tag{24d}$$

whence, by substitution into (22d) and further expansion,

$$1/W=1/W_0+A^2(U_xx+U_yy)/W_0^3+\ldots, \tag{24e}$$

and, from (20),

$$v=s+(W_0\sin\alpha+B\cos\alpha)sx+Csy+\ldots. \tag{24f}$$

Similarly,

$$(U'-x'\sin\alpha/W')^2(1-A'^2/U'^2)$$
$$-(B'+x'\cos\alpha)^2-(C'+y')^2=0, \tag{23'}$$

with

$$\mathbf{E}'\cdot\mathbf{N}=A',\ \mathbf{E}'\cdot\mathbf{T}=B',\ \mathbf{E}'\cdot\mathbf{k}=C', \tag{22a'}$$

$$p/s'=x',\ q/s'=y'. \tag{22b'}$$

Hence,

$$U'_{x'}=B'\cos\alpha-(1-A'^2)\sin\alpha/W'_0, \tag{24a'}$$

$$U'_{x'x'}=1-U'^2_{x'}-n^2\sin^2\alpha/W'^2_0, \tag{24b'}$$

with

$$W'_0=+\sqrt{n^2-1+A'^2}, \tag{22d'}$$

and, eventually,

$$v'=s'-(W'_0\sin\alpha-B'\cos\alpha)s'x'+C's'y'+\ldots. \tag{24f'}$$

In the manner thus outlined one obtains by tedious but straightforward calculation, as a third-order approximation for V,

$$V=v-v'=V_0+V_1p+V_2q+V_3p^2+V_4pq+V_5q^2+V_6p^3+V_7p^2q+V_8pq^2+V_9q^3, \quad (25)$$

with

$$V_0=s-s', \quad (25a)$$

$$V_1=(W_0+W_0'')\sin\alpha+(B-B')\cos\alpha, \quad (25b)$$

$$V_2=C-C', \quad (25c)$$

$$V_3=\tfrac{1}{2}[(1-U_x^2)/s-(1-U_{x'}'^2)/s'] -\tfrac{1}{2}n^2\sin\alpha[(W_0\sin\alpha-2A^2U_x)/W_0^3s -(W_0''\sin\alpha+2A'^2U_{x'})/W_0''^3s'], \quad (25d)$$

$$V_4=-(U_xC/s-U_{x'}'C'/s') +n^2\sin\alpha(A^2C/W_0^3s+A'^2C'/W_0''^3s'), \quad (25e)$$

$$V_5=\tfrac{1}{2}[(1-C^2)/s-(1-C'^2)/s'], \quad (25f)$$

$$V_6=-\tfrac{1}{2}(U_xU_{xx}/s^2-U_{x'}'U_{x'x'}'/s'^2) +\tfrac{1}{2}n^2\sin\alpha[A^2(U_{xx}-3(n^2-1)U_x^2/W_0^2)/W_0^3s^2 +A'^2(U_{x'x'}'-3(n^2-1)U_{x'}'^2/W_0''^2)/W_0''^3s'^2], \quad (25g)$$

$$V_7=-\tfrac{1}{2}[(U_{xx}-2U_x^2)C/s^2-(U_{x'x'}'-2U_{x'}'^2)C'/s'^2] -n^2\sin\alpha[A^2U_x(1+3(n^2-1)/W_0^2)/W_0^3s^2 +A'^2U_{x'}'(1+3(n^2-1)/W_0^2)/W_0''^3s'^2], \quad (25h)$$

$$V_8=-\tfrac{1}{2}[U_x(1-3C^2)/s^2-U_{x'}'(1-3C'^2)/s'^2] +\tfrac{1}{2}n^2\sin\alpha[A^2(1-C^2-3(n^2-1)C^2/W_0^2)/W_0^3s^2 +A'^2(1-C'^2-3(n^2-1)C'^2/W_0''^2)/W_0''^3s'^2], \quad (25i)$$

$$V_9=-\tfrac{1}{2}[(1-C^2)C/s^2-(1-C'^2)C'/s'^2]. \quad (25j)$$

3.3. Focus Condition

The first three terms in (25) vanish, and V is of second-order dependence upon p and q, only if

$$s=s', \quad (26)$$

$$(W_0+W_0'')\sin\alpha+(B-B')\cos\alpha=0 \quad (27)$$

$$C=C'. \quad (28)$$

These equations describe the location of the virtual image.

For the **N**, **T**-plane (fig. 4a), we have $C=C'=0$ and, therefore,

$$A=\mathbf{E}\cdot\mathbf{N}=\cos(180°-\phi)=-\cos\phi, \quad (27a)$$

$$A'=\mathbf{E}'\cdot\mathbf{N}=\cos\phi', \quad (27b)$$

$$B=\mathbf{E}\cdot\mathbf{T}=\cos(90°-\phi)=-\sin\phi, \quad (27c)$$

$$B'=\mathbf{E}'\cdot\mathbf{T}=\cos(90°-\phi')=\sin\phi', \quad (27d)$$

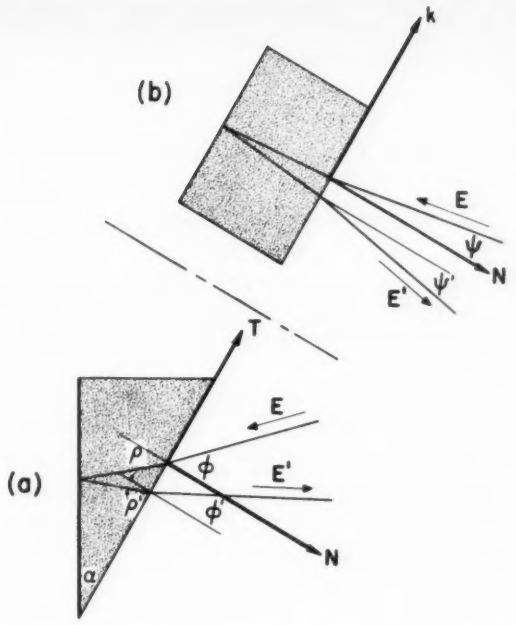

FIGURE 4. *The two principal cross sections of the prism.*

(The ray shown is parallel to the ray through O in fig. 3.)

where ϕ and ϕ' (both positive) are the angles of incidence and emergence in this plane. Thus, from (24c, c') and (27),

$$\sin\alpha(\sqrt{n^2-\sin^2\phi}+\sqrt{n^2-\sin^2\phi})-\cos\alpha(\sin\phi+\sin\phi')=0.$$

With

$$\sin\phi=n\sin\rho,\ \sin\phi'=n\sin\rho', \quad (27e)$$

where ρ and ρ' are the angles of refraction pertaining to ϕ and ϕ', this may be written as

$$n[\sin(\alpha-\rho)+\sin(\alpha-\rho')]=0,$$

which is satisfied if

$$\rho+\rho'=2\alpha. \quad (27f)$$

Equations (27f and g) are the familiar relations that describe the passage of a ray through this cross section of the prism.

Equation (28) constitutes the reflection law,

$$\psi=\psi', \quad (28a)$$

for the N, k-plane (fig. 4b), where the prism simply acts as a mirror. For it is, with $B=B'=0$,

$$C=\mathbf{E}\cdot\mathbf{k}=\cos(90°+\psi)=-\sin\psi, \quad (28b)$$

$$C'=\mathbf{E}'\cdot\mathbf{k}=\cos(90°+\psi')=-\sin\psi', \quad (28c)$$

where ψ and ψ' (both positive) are the angles of incidence and emergence in this cross section.

V vanishes altogether if

$$s=\infty, \tag{29}$$

Illuminated with perfectly collimated light, the prism causes no aberrations.

3.4. Second-Order Aberrations, Minimum of Deviation

When the prism is used in autocollimation; i.e., in an in-plane mounting at the minimum of deviation, its astigmatism becomes zero. For one has, in this case,

$$A'=-A,\ B'=-B,\ C'=C=0, \tag{30}$$

and, with (24a, a′, c, and c′),

$$U_{x'}=-U_x,\ W_0'=W_0,$$

so that, from (25d, e, f) and (26),

$$V_3=V_4=V_5=0,$$

for arbitrary values of s.

3.5. Higher-Order Aberrations, Astigmatic Illumination

With astigmatic illumination, eq (29) can be satisfied in one cross section of the prism, only, and the two principal cross sections of the prism must therefore be considered separately.

N, T-Plane: With $q=0$ and $s=s'=s_H$, the characteristic function (25) is seen to vanish for

$$s_H=\infty, \tag{31}$$

only. To eliminate higher-order aberrations in this cross section of the prism, parallel illumination must be used.

N, k-Plane: With $p=0$, $C=C'$, and $s=s'=s_V$, the characteristic function (25) is identically zero for all choices of s_V. Parallel illumination is therefore not required in this cross section of the prism.

Hence, the aberrations of the prism will be minimized if parallel illumination is at least provided for the **N, T**-plane.

4. Conclusions

The above treatment of plane reflectance gratings and Littrow prisms in a like fashion shows that the two dispersive elements act alike in the following respects:

(a) Dispersion takes place in the cross section normal to the grating grooves, or prism edge, only. In the cross section containing the grooves, or edge, the grating and the prism act as plane mirrors.

(b) In an in-plane mounting at the minimum of deviation; i.e., in autocollimation, the astigmatism of the grating, or prism, is zero regardless of illumination.

(c) In perfectly collimated light, the grating and the prism form perfect images.

(d) Illumination with astigmatic light requires parallel rays in the cross section normal to the grating grooves, or prism edge, in order that aberrations are minimized. In the cross section containing the grooves, or edge, deviations from parallelism are permissible.

As reflection from a plane mirror does not at all cause aberrations, the same, or corresponding, results will be obtained by a comparison of transmission gratings and prisms.

While similarities between plane gratings and prisms have been pointed out before [8], it is believed that the above ones are of a less artificial and more intrinsic nature, for they allow the design of grating and prism spectrographs from common principles.

It will be shown in a succeeding paper that the above results have an important influence on the focal surfaces of mirror spectrographs with either a grating or a prism as the dispersive element.

5. References

[1] H. A. Rowland, Phil. Mag. (5) **35,** 397 (1893); Astron. and Astrophys. **12,** 129 (1893).

[2] See H. Kayser, Handbuch der Spectroscopie, p. 452 (S. Hirzel, Leipzig 1900).

[3] P. Zernicke in Pieter Zeeman, p. 325 (M. Nijhoff, The Hague, 1935).

[4] H. Beutler, J. Opt. Soc. Am. **35,** 311 (1945).

[5] T. Namioka, J. Opt. Soc. Am. **49,** 446 (1959).

[6] M. V. R. K. Murty, J. Opt. Soc. Am. **52,** 768 (1962).

[7] M. Herzberger, in Handbook of Physics, p. 6–22 (McGraw-Hill Book Co., New York, N.Y., 1958).

[8] V. von Keussler, Z. Astrophys. **24,** 247 (1948).

(Paper 68C4–163)

JOURNAL OF RESEARCH of the National Bureau of Standards—C. Engineering and Instrumentation
Vol. 68C, No. 4, October–December 1964

Theory of Mirror Spectrographs
II. General Theory of Focal Surfaces and Slit Curvatures

Klaus D. Mielenz

(July 28, 1964)

The focus conditions for Czerny-Turner type, two-mirror spectrographs with spatial beam path are derived. It is shown that, in general, the focal surface of the spectrograph is intermediate between the tangential and sagittal focus. A method is developed to calculate the three-dimensional focal surface, as well as to find the curvature of long monochromator slits.

1. Introduction

The first to build a mirror spectroscope with antisymmetrical beam path was H. Ebert in 1889 [1].[1] He had also suggested substitution of a photographic plate for the eyepiece, but H. Kayser [2] thought this was "entirely impractical," and the design was not carried out as a spectrograph at the time.

In 1930, M. Czerny and A. F. Turner [3] discovered the aberration corrective properties of antisymmetrical two-mirror spectrographs. Their work was realized in the subsequent construction of many two-mirror monochromators but had little impact on spectrograph design. Spectrographs, at that time, were mainly prism ones, which are usually better built with lens rather than mirror optics [4].

In 1952, W. G. Fastie [5] reinvented Ebert's one-mirror system as a simplified version of the Czerny-Turner monochromator. As the trend went to larger and, thus, grating spectrographs, Fastie also suggested the Ebert system for a large plane-grating spectrograph. In this "Ebert-Fastie spectrograph," which was first built in 1955 by R. F. Jarrell [6], Ebert's original in-plane (side-by-side) arrangement of slit, grating, and spectrum was replaced by an off-plane (vertical) arrangement so that a longer spectrum could be obtained.

In 1956, W. Leo [7] further improved the corrective properties of the two-mirror system by using different focal lengths for collimator and camera.

The Czerny-Turner system is still of great practical interest; the one-mirror mounting for its simplicity, and the two-mirror one because of a still better definition of the spectrum.

Yet, theory is still incomplete. Usually, a two-dimensional analysis is made, where an horizontal cross section is substituted for the spectrograph itself, and the corresponding focal curve for its actual focal surface. H. Kaiser, F. Rosendahl, and this author [8], and later S. A. Khrshanovskii [9] and O. Vierle [10], have treated Ebert and Ebert-Fastie systems in this manner. Eikonal theories that included two-mirror systems were worked out by K. Kudo [11] and this author [12] but, again, any appreciable deviation from a plane system was not accounted for.

In a two-dimensional analysis, no distinction can be made between in-plane and off-plane systems. It may easily be seen, however, that a significant distinction does exist.

In the in-plane Ebert spectrograph of figure 1a, for instance, slit and spectrum lines extend perpendicular to a tangential plane of the system. The optimal focus of the spectrograph is therefore simply the tangential focus of the mirror.

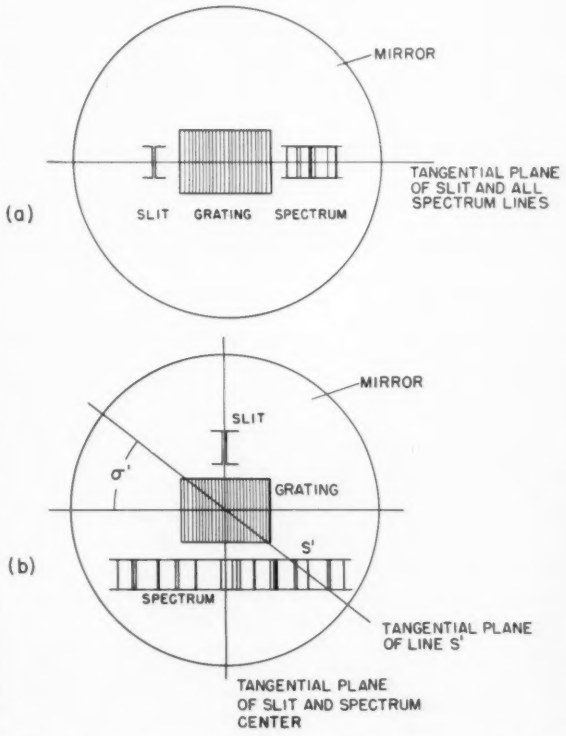

FIGURE 1. *End-on views of (a) Ebert spectrograph and (b) Ebert-Fastie spectrograph.*

[1] Figures in brackets indicate the literature references at the end of this paper.

In the off-plane Ebert-Fastie spectrograph of figure 1b, however, a common tangential plane exists only for the slit and the central line of the spectrum. Both lie in this plane and, so, must be at the sagittal foci of the mirror. All other spectrum lines form an angle σ' with the respective tangential planes of the spectrograph and must therefore be at an intermediate position between the two astigmatic foci, depending upon the value of σ'. For the extreme ends of the spectrum, σ' approaches zero so that these must be at, or near, the tangential focus of the mirror. Existing theory surmises the focus to be tangential throughout the spectrum.

A two-dimensional analysis will also fail to determine the curvature of monochromator slits, even for in-plane systems. Fastie [5, 13] has considered an additional vertical cross section through the spectrograph to solve the problem, but a three-dimensional analysis may be expected to give still more insight.

Thus, a theory is presented in this paper that takes into account the actual solid geometry of the spectrograph. Based upon the most general case of a three-dimensional two-mirror system, it comprises all known types of antisymmetrical mirror spectrographs, with either one or two mirrors, in-plane or off-plane, and with either plane reflectance gratings or Littrow prisms as dispersive elements (though gratings, only, will be explicitly treated in the following). The theory permits calculation of focal surfaces as well as slit curvatures.

An outline of the theory, only, is given. Applications to specific types of spectrographs will be published subsequently.

2. Basic Geometry of the Spectrograph

Figure 2 shows the beam path in the spectrograph, where S is a point of the slit and S' its image. The principal ray from S to S' intersects the grating center O and strikes the spherical collimator and camera mirrors at P and P', respectively. M and M' are the centers of curvature of the two mirrors, r and r' their radii.

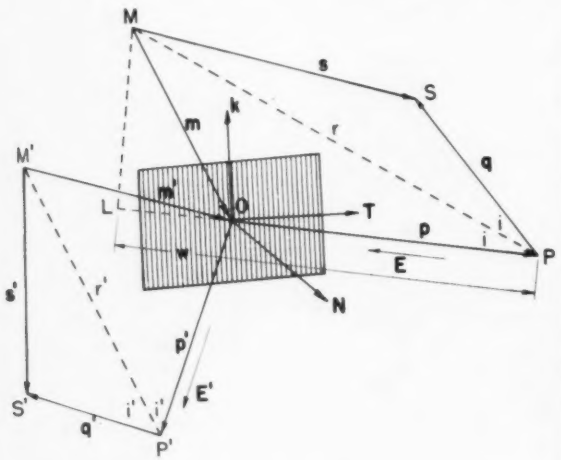

FIGURE 2. *Two-mirror spectrograph.*

Let, on the slit side, $\mathbf{s}$, $\mathbf{m}$, $\mathbf{p}$, and $\mathbf{q}$ be the vectors $\overrightarrow{MS}$, $\overrightarrow{MO}$, $\overrightarrow{OP}$, and $\overrightarrow{PS}$; s, m, p, and q their absolute values. Write

$$\mathbf{p}=-p\mathbf{E}, \tag{1}$$

where $\mathbf{E}$ is the unity vector in the direction of the principal ray incident upon the grating.

If, then, w is the distance LP, where L is the foot of the perpendicular from M on to OP, we have

$$w=r\cos i=\mathbf{E}\cdot(p\mathbf{E}-\mathbf{m})=p-\mathbf{m}\cdot\mathbf{E}, \tag{2}$$

$$ML^2=r^2\sin^2 i=[\mathbf{E}\times(p\mathbf{E}-\mathbf{m})]^2=(\mathbf{m}\times\mathbf{E})^2, \tag{3}$$

where $i=\angle SPM=\angle MPO$ is the angle of incidence and reflection at P. Hence,

$$w^2=r^2-ML^2=r^2-(\mathbf{m}\times\mathbf{E})^2, \tag{4}$$

$$p=w+\mathbf{m}\cdot\mathbf{E}. \tag{5}$$

The directions of incidence and reflection, $-\mathbf{E}$ and $\mathbf{q}/q$, and the normal at P, $(p\mathbf{E}-\mathbf{m})/r$, obey the law of reflection [14]; i.e.,

$$\mathbf{q}/q=-\mathbf{E}+2[\mathbf{E}\cdot(p\mathbf{E}-\mathbf{m})/r](p\mathbf{E}-\mathbf{m})/r,$$

or, with (2),

$$\mathbf{q}/q=-\mathbf{E}+2(w/r^2)(p\mathbf{E}-\mathbf{m}). \tag{6}$$

Hence, from figure 2,

$$\begin{aligned}\mathbf{s}&=\mathbf{m}-p\mathbf{E}+\mathbf{q}\\&=-q\mathbf{E}-(1-2qw/r^2)(p\mathbf{E}-\mathbf{m}).\end{aligned} \tag{7}$$

The corresponding primed expression,

$$\mathbf{s}'=q'\mathbf{E}'+(1-2q'w'/r'^2)(p'\mathbf{E}'+\mathbf{m}'), \tag{8}$$

with

$$w'^2=r'^2-(\mathbf{m}'\times\mathbf{E}')^2, \tag{9}$$

$$p'=w'-\mathbf{m}'\cdot\mathbf{E}', \tag{10}$$

is obtained for the point vector, $\mathbf{s}'=\overrightarrow{M'S'}$, of the image point S'. Here, p' and q' are the distances OP' and $P'S'$, $\mathbf{E}'$ is the unity vector in the direction of the diffracted principal ray, and $\mathbf{m}'$ is the vector $\overrightarrow{M'O}$.

Let, finally, $\mathbf{N}$, $\mathbf{T}$, and $\mathbf{k}$ be mutually orthogonal unity vectors attached to the grating center O so that $\mathbf{N}$ is the grating normal and $\mathbf{T}$ and $\mathbf{k}$ are the tangents perpendicular and parallel to the grooves. $\mathbf{E}$ and $\mathbf{E}'$ are then related to each other by the grating equations [15],

$$\mathbf{T}\cdot(\mathbf{E}-\mathbf{E}')+\mu\lambda/d=0, \tag{11}$$

$$\mathbf{k}\cdot(\mathbf{E}-\mathbf{E}')=0, \tag{12}$$

where μ is the spectral order, λ the wavelength of the diffracted beam, and d the grating constant.

3. Focal Distances of Slit and Slit Images

The focal distances of S and S', q and q', are still undetermined in eqs (7) and (8). They may be obtained as follows.

The usual design goal, perfectly collimated light between collimator and camera so that the grating or prism [2] does not cause aberrations, cannot be accomplished in the mirror spectrograph. The collimating mirror produces an astigmatic pencil of rays which, at best, contains parallel rays in one cross section only. While the aberrations of the grating can no longer be completely eliminated under these circumstances, they will be minimized if parallelism of rays is at least accomplished in the horizontal cross section of the grating [15].

In the mirror spectrograph, this requirement, too, can be met only approximately. The collimating mirror can produce perfectly parallel rays only in a tangential cross section if the slit is arranged at the focal distance

$$q_t=\tfrac{1}{2}r\cos i=\tfrac{1}{2}w, \tag{13}$$

or in a sagittal cross section if the focal distance is

$$q_s=r/(2\cos i)=r^2/(2w); \tag{14}$$

cf. reference [16] and eq (2), and neither of these will in general coincide with the horizontal cross section of the grating.

There is no intermediate focal distance at which perfectly parallel light is produced in an intermediate cross section. Rays will however be as nearly parallel as possible in a cross section that encloses an angle σ with the tangential plane if the focal distance is

$$\begin{aligned} q&=q_t+(q_s-q_t)\sin^2\sigma \\ &=\tfrac{1}{2}w+(\mathbf{m}\times\mathbf{E})^2\ (\sin^2\sigma)/(2w); \end{aligned} \tag{15}$$

cf. reference [17] and eq (4). In the spectrograph, the angle σ between the tangential plane of the collimating mirror (*MOP*-plane) and the horizontal cross section of the grating (**N, T**-plane) is given by

$$\sin^2\sigma=[\mathbf{k}\times(\mathbf{m}\times\mathbf{E})]^2/(\mathbf{m}\times\mathbf{E})^2, \tag{16}$$

since $(\mathbf{m}\times\mathbf{E})$ and $\mathbf{k}$ are normal to the two planes.

The focal distance, q, at which the slit must be located in order that the aberrations of the grating are minimized is then obtained from (15) and (16) as

$$q=\tfrac{1}{2}w+[\mathbf{k}\times(\mathbf{m}\times\mathbf{E})]^2/(2w). \tag{17}$$

[2] Anywhere in this chapter, "prism" may be substituted for "grating" [15].

The corresponding primed expression,

$$q'=\tfrac{1}{2}w'+[\mathbf{k}\times(\mathbf{m}'\times\mathbf{E}')]^2/(2w'), \tag{18}$$

holds for the focal distance, q', of S'.

4. Focal Surfaces

Upon introduction of (17) and (18) into (7) and (8), the focal surfaces of the spectrograph are fully determined. Equations (7) and (8) constitute mutually independent formulas that express the point vectors, $\mathbf{s}$ and $\mathbf{s}'$, of a slit point S and its images S' as functions of the directions, $\mathbf{E}$ and $\mathbf{E}'$, of the principal rays incident upon and diffracted by the grating. Any point on the focal surface, $\mathbf{s}$, of the collimator can therefore be imaged into any point on the focal surface, $\mathbf{s}'$, of the camera provided that the grating establishes the necessary relationship between $\mathbf{E}$ and $\mathbf{E}'$.

5. Focal Curves of Spectrographs

For spectrographs, where long slits are rarely used, it usually suffices to consider a point-by-point imaging of slit centers into line centers.

Thus, let a given point vector $\mathbf{s}_0$, i.e., a given principal ray $\mathbf{E}_0$ represent the slit center S_0 on the focal surface of the collimator mirror. The grating equations, (11) and (12), will then provide the directions, $\mathbf{E}_0'$, of the diffracted rays and, thus, fully determine the location of the line centers, S_0', as a curve $\mathbf{s}_0'$ on the focal surface of the camera mirror.

The full focal surfaces of a spectrograph have to be calculated to such an extent, only, as to establish how slit and photographic plate have to be arranged as tangents to these surfaces so that best possible line definition will be obtained.

6. Monochromator Slit Curves

For monochromators with long slits, the above theory is yet incomplete. It is still necessary to find the curves on the two focal surfaces along which entrance and exit slit must extend in order to remain images of each other when the grating is rotated about its vertical axis (direction of $\mathbf{k}$) to scan the desired wavelength range.

Let the position of the grating for which the two slits are mirror (zero-order) images of each other be given by

$$\mathbf{N}=\mathbf{i},\ \mathbf{T}=\mathbf{j}, \tag{19}$$

so that $\mathbf{i}$, $\mathbf{j}$, and $\mathbf{k}$ are base vectors that do not rotate with the grating. Then, let a curve $\mathbf{s}(\mathbf{E})$ on the focal surface of the collimator mirror represent the entrance slit. The exit slit, as the white-light image, is then given as a curve $\mathbf{s}'(\mathbf{E}')$ on the focal surface of the camera mirror for which the reflection law [14] postulates

$$\mathbf{E}-\mathbf{E}'=2(\mathbf{E}\cdot\mathbf{i})\mathbf{i}. \tag{20}$$

If, now, the grating is rotated by an arbitrary angle, so that eqs (19) no longer hold, the same curve $\mathbf{s}'$ must become a spectral image of the curve $\mathbf{s}$. The grating equation (11), which because of (20) is now reduced to

$$2(\mathbf{E}\cdot\mathbf{i})(\mathbf{T}\cdot\mathbf{i})+\mu\lambda/d=0,$$

must then apply to all slit points and therefore to the slit center as well;

$$2(\mathbf{E}_0\cdot\mathbf{i})(\mathbf{T}\cdot\mathbf{i})+\mu\lambda/d=0.$$

Hence, as the direction of $\mathbf{T}$ is arbitrary,

$$\mathbf{E}\cdot\mathbf{i}=\mathbf{E}_0\cdot\mathbf{i}. \tag{21}$$

With

$$\mathbf{E}\cdot\mathbf{k}=\mathbf{E}_0\cdot\mathbf{k}+\delta, \tag{22}$$

the third direction cosine of $\mathbf{E}$,

$$\mathbf{E}\cdot\mathbf{j}=\sqrt{1-(\mathbf{E}\cdot\mathbf{i})^2-(\mathbf{E}\cdot\mathbf{k})^2}, \tag{23}$$

is also expressed as a function of $\mathbf{E}_0$ and δ.

Upon introduction of (21), (22), and (23) into (7) the point vector, $\mathbf{s}$, of an arbitrary point of the entrance slit is obtained as

$$\mathbf{s}=\mathbf{s}_0+\Delta\mathbf{s}, \tag{24}$$

where $\mathbf{s}_0$, as before, denotes the slit center and $\Delta\mathbf{s}$ is a function of the coordinates of $\mathbf{s}_0$ and the running parameter δ. The shape of the entrance slit is thus fully determined.

From (20) and (21),

$$\mathbf{E}'\cdot\mathbf{i}=-\mathbf{E}_0\cdot\mathbf{i}, \tag{25}$$

and from (12) and (22),

$$\mathbf{E}'\cdot\mathbf{k}=\mathbf{E}_0\cdot\mathbf{k}+\delta, \tag{26}$$

whence we may determine the exit slit in a like manner.

The author is indebted to O. N. Stavroudis, NBS, for suggesting the vector notation used throughout this paper, which has resulted in a considerable simplification of all formulas.

7. References

[1] H. Ebert, Wiedem. Ann. **38,** 489 (1889).
[2] H. Kayser, Handbuch der Spectroscopie, p. 626 (S. Hirzel, Leipzig 1900).
[3] M. Czerny and A. F. Turner, Z. Phys. **61,** 792 (1930).
[4] K. D. Mielenz, Optik **16,** 500 (1959).
[5] W. G. Fastie, J. Opt. Soc. Am. **42,** 641 (1952).
[6] R. F. Jarrell, J. Opt. Soc. Am. **45,** 259 (1955).
[7] W. Leo, Z. angew. Phys. **8,** 196 (1956).
[8] H. Kaiser, K. D. Mielenz, and F. Rosendahl, Z. Instr. kde. **67,** 269 (1959).
[9] S. A. Khrshanovskii, Optics and Spectroscopy **9,** 207 (1960).
[10] O. Vierle, Dissertation TH Munich, 1962.
[11] K. Kudo, Sci. of Light **9,** 1 (1960).
[12] K. D. Mielenz, Optik **19,** 510 (1962).
[13] W. G. Fastie, J. Opt. Soc. Am. **42,** 647 (1952).
[14] M. Herzberger, in Handbook of Physics, p. 6–22 (McGraw-Hill Book Co., New York, N.Y., 1958).
[15] K. D. Mielenz, J. Res. NBS **68C** (Eng. and Instr.) No. 4, Pt. I, 195 (1964).
[16] W. Merte, in Handbuch der Physik, Vol. **18,** 81 (J. Springer, Berlin 1927).
[17] C. E. Weatherburn, Differential Geometry of Three Dimensions, Vol. **1,** 191 (The University Press, Cambridge 1955).

(Paper 68C4–164)

JOURNAL OF RESEARCH of the National Bureau of Standards—C. Engineering and Instrumentation
Vol. 68C, No. 4, October–December 1964

Theory of Mirror Spectographs

III. Focal Surfaces and Slit Curvature of Ebert and Ebert-Fastie Spectographs

Klaus D. Mielenz

(July 28, 1964)

A spatial theory of the focal surfaces and slit curves of Ebert and Ebert-Fastie monochromators and spectrographs is presented.

In a second-order approximation, it yields closed expressions for the focal surface, from which a "stop-shift" theory is developed to study the influence of the position of the grating in the spectrograph upon the curvature of the spectrum. The condition for an extended flat spectrum is derived, and the Ebert-Fastie system is shown to be the preferable one for spectrograph design.

The curvature of long monochromator slits is also derived as a closed, second-order expression. The Ebert system, only, can be equipped with long slits, so that it, in turn, constitutes the superior monochromator mounting.

A fourth-order approximation is also included for still more accurate computations.

1. Introduction

In two previous papers [1, 2],[1] a general theory was developed for calculating the focal surfaces and slit curves of Czerny-Turner type mirror spectrographs and monochromators. This theory will now be applied to Ebert and Ebert-Fastie systems with either plane reflectance gratings or Littrow prisms as dispersive elements (though gratings, only, will be explicitly treated in the following).

2. Exact Theory

2.1. Basic Expressions

In Ebert and Ebert-Fastie monochromators and spectrographs ([3, 4]; figs. 1 and 2), a single concave mirror is used to fulfill the tasks of both collimator and camera. Let r be the radius of curvature of the mirror, which we assume to be spherical.

A coordinate system (fig. 3), with its origin at the center of curvature, M, of the mirror, is chosen so that the x-axis intersects the grating center O, the y-axis encloses an angle θ with the grating tangent vector

$$\mathbf{T}=(\sin\theta,\ \cos\theta,\ 0), \tag{1}$$

and the z-axis is parallel to the grating grooves.

Then, let

$$\mathbf{m}=m\mathbf{i}, \tag{2}$$

[1] Figures in brackets indicate the literature references at the end of this paper.

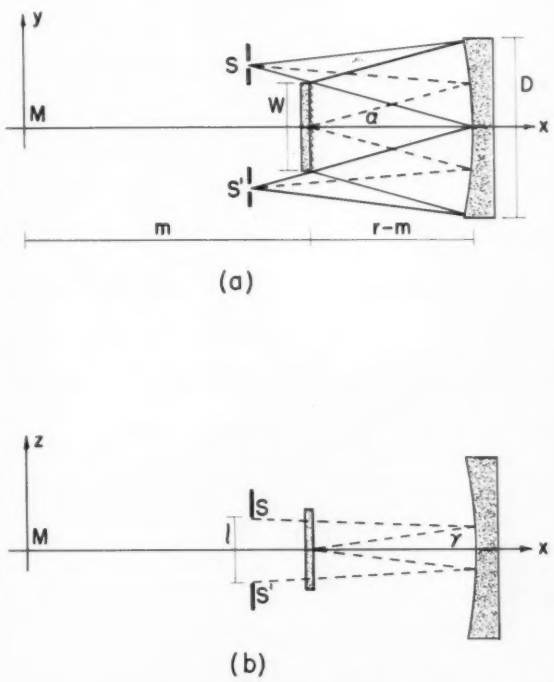

FIGURE 1. *Ebert monochromator.*

(a) Horizontal cross section with grating in zero-order position. (b) Vertical cross section; principal ray from upper end of entrance slit, S, to lower end of exit slit, S', is shown.

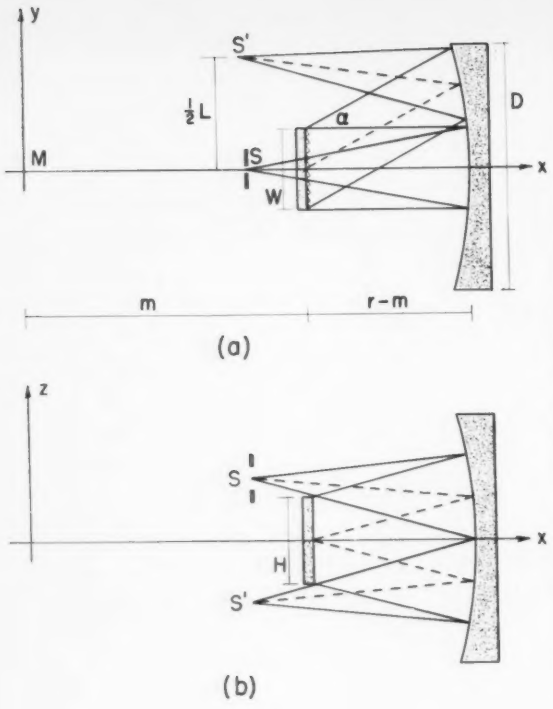

FIGURE 2. *Ebert-Fastie spectrograph.*

(a) Horizontal cross section with grating in symmetrical position; S' is outermost line of spectrum. (b) Vertical cross section.

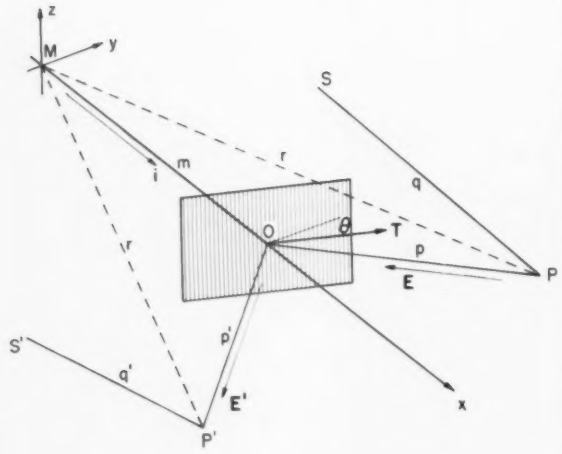

FIGURE 3. *One-mirror spectrograph.*

Beam path and coordinate system.

with $\mathbf{i}=(1, 0, 0)$, be the point vector $\overrightarrow{OM}$, and let

$$\mathbf{E}=(A, B, C), \tag{3}$$

$$\mathbf{E}'=(A', B', C'), \tag{3'}$$

represent the unity vectors of the principal rays incident upon and diffracted by the grating at O.

From eqs (2.7, 2.5, 2.17, and 2.4),[2] the point vector, $\mathbf{s}$, of a slit point S is then obtained as

$$\mathbf{s}=\overrightarrow{MS}=(x, y, z)=-(p+q-2pqw/r^2)\mathbf{E} + (1-2qw/r^2)m\mathbf{i}, \tag{4}$$

with

$$p=w+mA, \tag{5}$$

$$q=\tfrac{1}{2}w+m^2C^2/(2w), \tag{6}$$

$$w=+\sqrt{r^2-m^2(1-A^2)}. \tag{7}$$

With (2.6), the direction of the principal ray leaving S is given by the unity vector

$$-\mathbf{q}/q=-\overrightarrow{PS}/|PS|=(1-2pw/r^2)\mathbf{E}+(2mw/r^2)\mathbf{i}, \tag{8}$$

where P is the point of reflection on the collimator portion of the mirror.

Likewise, one obtains from [2], for the image point S',

$$\mathbf{s}'=\overrightarrow{MS'}=(x',\ y',\ z')=(p'+q'-2p'q'w'/r^2)\mathbf{E}' + (1-2q'w'/r^2)m\mathbf{i}, \tag{4'}$$

$$p'=w'-mA', \tag{5'}$$

$$q'=\tfrac{1}{2}w'+m^2C'^2/(2w'), \tag{6'}$$

$$w'=+\sqrt{r^2-m^2(1-A'^2)}, \tag{7'}$$

$$\mathbf{q}'/q'=\overrightarrow{P'S'}/|P'S'|=(1-2p'w'/r^2)\mathbf{E}' - (2mw'/r^2)\mathbf{i}. \tag{8'}$$

We see that the equations for S' are the same as those for S, with $-\mathbf{E}'$ substituted for $\mathbf{E}$. Hence, S and S' lie on a common focal surface, and it suffices to consider S, only, to determine this surface.

Separate expressions for S and S' are then merely needed to find the location of conjugate points on the focal surface. S' is a spectral image of S when the grating equations,

$$\mathbf{T}\cdot(\mathbf{E}-\mathbf{E}')+\mu\lambda/d=0, \tag{9}$$

$$C-C'=0, \tag{10}$$

are satisfied (μ=spectral order, λ=wavelength, d=grating constant; see reference [1]).

[2] Equations (7), (5), etc., of reference [2].

2.2. Focal Surface

From (4) through (8), one derives

$$\mathbf{s}=-a\mathbf{E}+b\mathbf{i}, \tag{11}$$

with

$$a=(w^2+m^2C^2)/(2w)+m^2B^2(w+mA)/r^2, \tag{12a}$$

$$b=m^3B^2/r^2, \tag{12b}$$

as a vector representation of the focal surface. Hence, for the coordinates of S,

$$x=-aA+b,\ y=-aB,\ z=-aC. \tag{13}$$

From here, a closed expression is obtained in two limiting cases, only:

For $m=0$ (grating at center of curvature of mirror), the above equations yield

$$\mathbf{s}^2=x^2+y^2+z^2=(\tfrac{1}{2}r)^2, \tag{14}$$

which describes a sphere of radius $\frac{1}{2}r$ about M.

For $m=r$ (grating at vertex of mirror), one obtains

$$(x-\tfrac{3}{4}r)^2+y^2+z^2(x-\tfrac{1}{2}r)/(x-r)=(\tfrac{1}{4}r)^2. \tag{15}$$

At the paraxial focus, where $z^2(x-\frac{1}{2}r)$ is negligibly small, this describes a cylinder of radius $\frac{1}{4}r$ about the axis $x=\frac{3}{4}r$, $y=0$.

Yet, no workable closed expression for the focal surface can be derived for arbitrary values of m. The following parameter representation may be used instead.

Write, as a general expression for $\mathbf{E}$,

$$A=-\cos\alpha, \tag{16a}$$

$$B=\mp\sqrt{\sin^2\alpha-\sin^2\gamma}, \tag{16b}$$

$$C=-\sin\gamma, \tag{16c}$$

where the choice of signs is due to the negative direction of $\mathbf{E}$ in figure 3. Hence, from (13),

$$x=a\cos\alpha+b, \tag{17a}$$

$$y=\pm a\sqrt{\sin^2\alpha-\sin^2\gamma}, \tag{17b}$$

$$z=a\sin\gamma, \tag{17c}$$

where

$$a=(r^2/2w)$$
$$-[(1/2w)-(w-m\cos\alpha)/r^2]m^2(\sin^2\alpha-\sin^2\gamma), \tag{17d}$$

$$b=(m^3/r^2)(\sin^2\alpha-\sin^2\gamma), \tag{17e}$$

and

$$w=+\sqrt{r^2-m^2\sin^2\alpha} \tag{17f}$$

are functions of m, α, and γ.

2.3. Slit Curve

The curvature of long monochromator slits, as derived in [2] from the grating equations, is now obtained as follows:

Let the above eqs (17a, b, . . .) represent an arbitrary point, $S=(x, y, z)$, of the entrance slit. Then, let the slit center, $S_0=(x_0, y_0, z_0)$, be given by

$$x_0=a_0\cos\alpha_0+b_0, \tag{18a}$$

$$y_0=\pm a_0\sqrt{\sin^2\alpha_0-\sin^2\gamma_0}, \tag{18b}$$

$$z_0=a_0\sin\gamma_0, \tag{18c}$$

with

$$a_0=(r^2/2w_0)$$
$$-[(1/2w_0)-(w_0-m\cos\alpha_0)/r^2]m^2(\sin^2\alpha_0-\sin^2\gamma_0), \tag{18d}$$

$$b_0=(m^3/r^2)(\sin^2\alpha_0-\sin^2\gamma_0), \tag{18e}$$

$$w_0=+\sqrt{r^2-m^2\sin^2\alpha_0}. \tag{18f}$$

It was shown in [2], eq (2.21), that, as a consequence of the grating equations, the first direction cosine of $\mathbf{E}$ is the same for all slit points. Thus we may write in eqs (17a, b, . . .),

$$\alpha_0=\alpha_0,\ w=w_0, \tag{19a}$$

so that

$$a=a_0+m^2[(1/2w_0)-(w_0-m\cos\alpha_0)/r^2](\sin^2\gamma-\sin^2\gamma_0), \tag{19b}$$

$$b=b_0-(m^3/r^2)(\sin^2\gamma-\sin^2\gamma_0). \tag{19c}$$

Hence,

$$x=x_0+(a-a_0)\cos\alpha_0+(b-b_0), \tag{20a}$$

$$y=y_0\pm a\sqrt{\sin^2\alpha_0-\sin^2\gamma}\mp a_0\sqrt{\sin^2\alpha_0-\sin^2\gamma_0}, \tag{20b}$$

$$z=z_0+a\sin\gamma-a_0\sin\gamma_0, \tag{20c}$$

which, upon introduction of an additional parameter δ,

$$\gamma=\gamma_0+\delta, \tag{20d}$$

is the parametric representation of a curve on the focal surface along which the entrance slit must extend.

It is then seen from eqs (2.25 and 26) that, on the image portion of the focal surface, the exit slit must lie on the same curve.

2.4. Discussion

It was shown in 2.2 that different values of m may yield entirely different focal surfaces. Proper positioning of the grating is therefore an important consideration in designing the spectrograph.

For a given m, the above parameter representations permit a straightforward point-by-point calculation

of the focal surface and the slit curve. Hence, an electronic computer may conceivably perform an analysis of the influence of m upon the system.

Closed expressions for arbitrary values of m, however, would provide a still better insight. Such expressions will be derived in the following chapter as a second-order approximation for the paraxial portion of the focal surface, which alone is of interest.

3. Second-Order Approximation

3.1. Focal Surface—Choice of Grating Position

Upon neglecting third-order terms in α and γ, eqs (16) and (12) may be written as

$$A=-1\pm\tfrac{1}{2}\alpha^2, \tag{21a}$$

$$B=\mp\sqrt{\alpha^2-\gamma^2}, \tag{21b}$$

$$C=-\gamma, \tag{21c}$$

$$a/r=\tfrac{1}{2}+\tfrac{1}{4}[3(m/r)^2-4(m/r)^3]\alpha^2-\tfrac{1}{2}[(m/r)^2-2(m/r)^3]\gamma^2, \tag{21d}$$

$$b/r=(m/r)^3(\alpha^2-\gamma^2). \tag{21e}$$

Hence, as a second-order approximation of (13) for the paraxial region,

$$x/r=\tfrac{1}{2}-\tfrac{1}{4}[1-3(m/r)^2]\alpha^2-\tfrac{1}{2}(m/r)^2\gamma^2, \tag{22a}$$

$$y/r=\pm\tfrac{1}{2}\sqrt{\alpha^2-\gamma^2}, \tag{22b}$$

$$z/r=\tfrac{1}{2}\gamma, \tag{22c}$$

which is easily seen to satisfy the relation

$$f(x,y,z)=(x/r)+[1-3(m/r)^2](y/r)^2+[1-(m/r)^2](z/r)^2-\tfrac{1}{2}=0. \tag{23}$$

The usual discussion [5] shows that this equation represents

$$\text{an elliptical paraboloid for } 0<m<r/\sqrt{3}, \tag{24a}$$

$$\text{a parabolic cylinder for } m=r/\sqrt{3}, \tag{24b}$$

$$\text{a hyperbolic paraboloid for } r/\sqrt{3}<m<r. \tag{24c}$$

At a point $S=(x,y,z)$, the vector

$$\mathbf{n}=-(\partial f/\partial x,\ \partial f/\partial y,\ \partial f/\partial z)$$

or, from (23),

$$\mathbf{n}=-(1/r,\ 2[1-3(m/r)^2]y/r^2,\ 2[1-(m/r)^2]z/r^2) \tag{25}$$

is normal to the focal surface [6]. The equation of the tangential plane of the focal surface at S, then, is

$$(\xi-x,\ \eta-y,\ \zeta-z)\cdot\mathbf{n}=0$$

or, with (25)

$$(\xi-x)+2[1-3(m/r)^2](y/r)(\eta-y)+2[1-(m/r)^2](z/r)(\zeta-z)=0, \tag{26}$$

where ξ, η, and ζ are the coordinates of a point in the plane [6]. These equations will be needed in the following discussion.

The horizontal cross sections of the paraxial focal surface (23), along which the spectrum extends, are

$$(x/r)+[1-3(m/r)^2](y/r)^2=\tfrac{1}{2},\qquad z=0. \tag{27}$$

As shown in figure 4a for different values of m, they are parabolas whose curvature vanishes for

$$m=r/\sqrt{3} \tag{28}$$

and assumes opposite signs for greater and smaller values of m.

H. Ebert [3] had originally placed the grating at the paraxial focus of the mirror, where $m=\frac{1}{2}r$. O. Vierle [7] claims that perpendicular light incidence upon the focal surface is the advantage of this mounting. It is true that the direction of the principal ray, which from (8) can be shown to be

$$-\mathbf{q}/q=-(1-\tfrac{1}{2}[1+2(m/r)^2]\alpha^2,\ [1-2(m/r)]\sqrt{\alpha^2-\gamma^2},\ [1-2(m/r)]\gamma) \tag{29}$$

is perpendicular to the yz-plane for $m=\frac{1}{2}r$. The focal surface, however, is curved away from that plane, and the angle of incidence, τ, is therefore given by

$$\cos\tau=(\mathbf{n}\cdot\mathbf{q})/(nq),$$

with $n=|\mathbf{n}|$. From (25) and (29),

$$\cos\tau=1-\tfrac{1}{2}(m/r)^2[4-12(m/r)+9(m/r)^2]\alpha^2-4(m/r)^3[1-(m/r)]\gamma^2. \tag{30}$$

Except for the border case $m=0$, normal incidence occurs for no value of m, and $m=\frac{1}{2}r$ does not appear to be distinguished from other values. The numerical example in figure 5 shows, moreover, that τ is a very small angle, so that the whole matter is of little practical importance.

R. F. Jarrell [4] chose $m=\frac{3}{4}r$, with the grating midway between paraxial focus and mirror, so that the mirror size could be reduced. According to figure 1a, the mirror diameter must be at least

$$D=W+2(r-m)\alpha, \tag{31}$$

in the horizontal cross section of an Ebert monochromator, where W is the grating width and α the maximum angle. The same formula holds for the Ebert-Fastie spectrograph also; see figure 2a. Hence, an increase of m will indeed considerably reduce the mirror size.

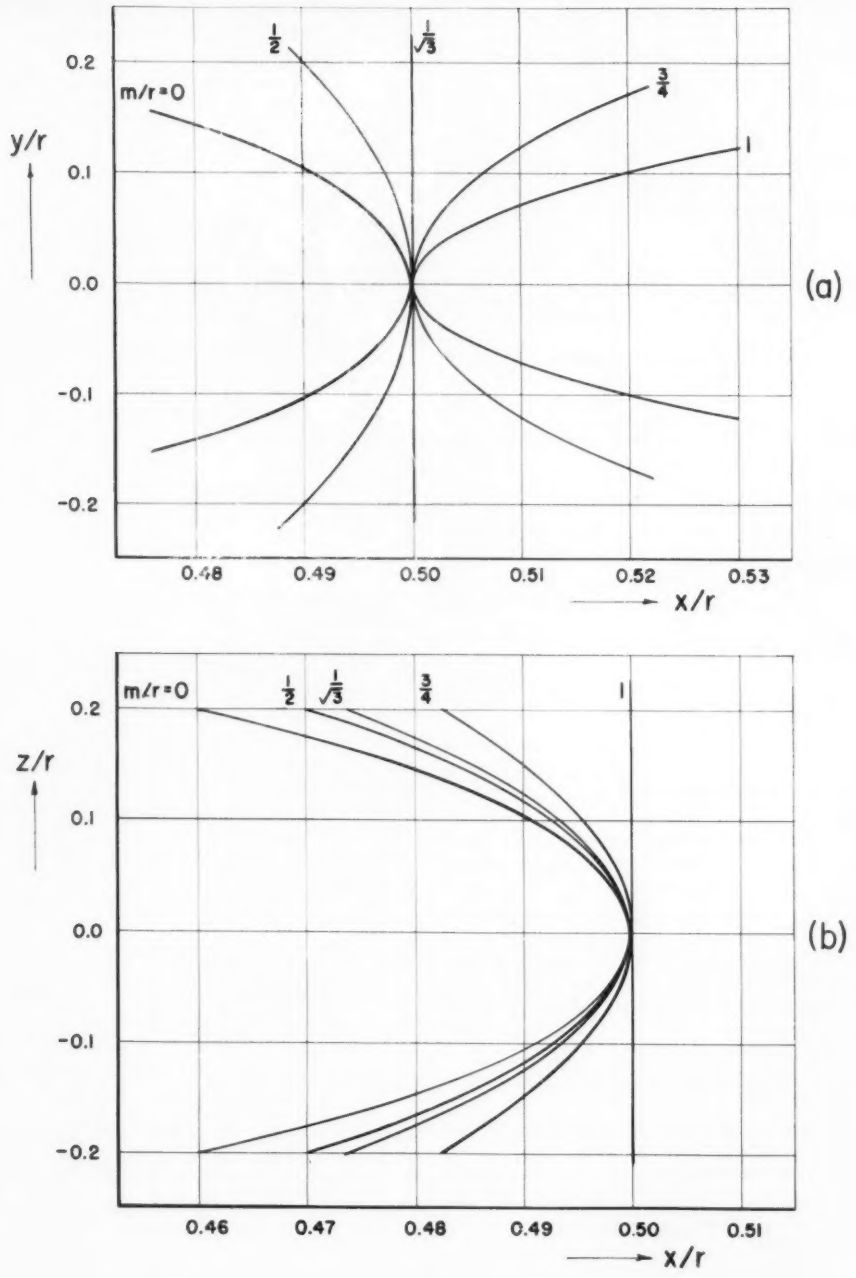

FIGURE 4. (a) *Horizontal and* (b) *vertical cross sections of paraxial focal surface for different grating positions* m.

Scale of abscissa is 10 times enlarged.

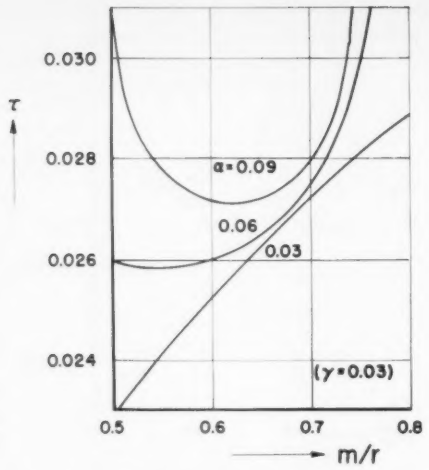

FIGURE 5. *Angle of incidence on focal surface, τ, versus grating position,* m.

Yet, a curved focal surface is obtained unless the "$\sqrt{3}$-condition" (28) is observed. This condition, which was first published by S. A. Khrshanovskii [8], holds as a second-order approximation and is now seen to apply to horizontal cross sections of the focal surface, only.

The vertical cross sections,

$$(x/r)+[1-(m/r)^2](z/r)^2=\tfrac{1}{2}, \qquad y=0, \qquad (32)$$

as shown in figure 4b, all curve away from the mirror. Their curvature decreases as the grating moves toward the mirror, and vanishes in the limiting case $m=r$, only.

A truly flat spectrum, in the sense of the focal surface being a plane, can therefore not be produced at all. Yet, the $\sqrt{3}$-condition defines the only position of the grating for which a plane photographic plate can be made tangent to the focal surface along a whole straight line, instead of at a single point, only, as for all other choices of m. It is seen from (26) that the photographic plate must then be arranged in the plane

$$(\xi-x_0)/r+\tfrac{4}{3}(z_0/r)(\zeta-z_0)/r=0, \qquad (33)$$

where x_0, $y_0=0$, and z_0 are the coordinates of the center point of the central line.

In a spectrograph, the spectrum lines are usually short, so that the above described removal of the horizontal curvature of field, only, is fully sufficient to yield a flat spectrum.

3.2. Slit Curve—In-Plane and Off-Plane Monochromators

It is seen from eqs (22) that, upon retention of second-order terms in α and γ, only,

$$(x-\tfrac{1}{2}r)^2+y^2+z^2=\tfrac{1}{4}r^2\sin^2\alpha.$$

If, in this equation, x, y, and z are assumed to represent an arbitrary point of the entrance slit of a monochromator, the right-hand side of the equation is seen, from (19a), to be a constant;

$$\tfrac{1}{4}r^2\sin^2\alpha=\tfrac{1}{4}r^2\sin^2\alpha_0=\rho_0^2, \qquad (34a)$$

where α_0 pertains to the slit center. Thus,

$$(x-\tfrac{1}{2}r)^2+y^2+z^2=\rho_0^2. \qquad (34b)$$

This is the equation of a sphere of radius ρ_0 about the paraxial focus $(\frac{1}{2}r, 0, 0)$. As set forth in [2], the exit slit, too, must obey this equation.

The slits must of course lie on the focal surface of the monochromator as well. They must therefore extend along the curve which is obtained as the section of the focal surface (23) with the sphere (34b).

In the vertical cross section

$$x=\tfrac{1}{2}r, \qquad (35a)$$

the slit curve is a circle about the paraxial focus $(y=z=0)$;

$$y^2+z^2=\rho_0^2, \qquad (35b)$$

see figure 6. W. G. Fastie has, indeed, greatly improved the image quality of an Ebert monochromator by curving the two slits along this circle [9, 10]. A further improvement might be accomplished by fitting the slits to the true spatial slit curve, as derived above.

In an Ebert-Fastie system, the slit curve intersects the slit center, S_{EF} in figure 6, in a direction perpendicular to the grating grooves; i.e., perpendicular to the natural direction of the spectrum lines. It must be concluded, therefore, that the Ebert-Fastie mounting cannot possibly be equipped with long slits.

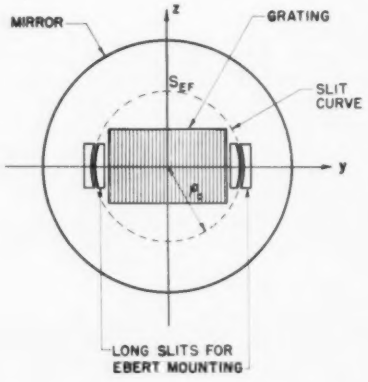

FIGURE 6. *End-on view of one-mirror monochromator and slit curve.*

3.3. Validity of Approximation

The angles α and γ that occur in practical spectrograph design may be determined as follows.

The angle α at which entrance and exit slits are arranged in a properly designed Ebert monochromator (where α is minimized) is obtained from figure 1a as

$$\alpha \sim \tan\alpha = \tfrac{1}{2}W/(r-m), \tag{36a}$$

where W is the grating width. The other angle, γ, is determined by the slit length, l. From figure 1b and eq (22c),

$$z = \tfrac{1}{2}l \sim \tfrac{1}{2}r\gamma,\ \gamma \sim l/r, \tag{36b}$$

for the slit ends.

A high-speed Ebert monochromator with a long slit ($W=16''$, $l=4.5''$, $r=180''$, $m=\frac{1}{2}r$) was constructed by W. G. Fastie [10], and a further enhancement of speed or slit length appears to be unlikely in the present state of the art. The corresponding angles are $\alpha=0.09$, $\gamma=0.025$.

In an Ebert-Fastie spectrograph, γ is given in the same manner as α is in an Ebert monochromator, but with the grating height, H, substituted for W; see figure 2b. Thus,

$$\gamma \sim \tfrac{1}{2}H/(r-m). \tag{37a}$$

For α, the spectrum length, L, is the determining factor. From figure 2a and eq (22b), for the spectrum ends,

$$y = \tfrac{1}{2}L \sim \tfrac{1}{2}r\sqrt{\alpha^2-\gamma^2},\ \alpha \sim \sqrt{(L/r)^2+\gamma^2}, \tag{37b}$$

with γ from (37a).

For two published designs of Ebert-Fastie spectrographs (R. F. Jarrell [4]: $r=22'$, $H=2\frac{1}{2}''$, $m=\frac{3}{4}r$; P. Kroeplin [11]: $r=4$ m, $H=5$ cm, m (estimated) $=\frac{1}{2}r$), we obtain $\gamma=0.02$ and 0.01, respectively. Jarrell chose $L=20''$, or $L/r=0.076$, and image quality at the spectrum ends seems to indicate that this constitutes an upper limit [12]. Kroeplin uses $L=30$ cm and, thus, $L/r=0.075$. From here and with the above values of γ, $\alpha=0.076$ and 0.078, respectively.

We may thus accept

$$\alpha=0.1,\ \gamma=0.03 \tag{38a}$$

as maximum values for both Ebert monochromators and Ebert-Fastie spectrographs. A computation of the focal surface, from both the exact formulas (17) and the second-order approximation (22), then shows that the latter involves a maximum error of approximately

$$\Delta S = \sqrt{(\Delta x)^2+(\Delta y)^2+(\Delta z)^2} = 5\cdot 10^{-5} r \tag{38b}$$

at these maximum angles and for various values of m between $\frac{1}{2}r$ and $\frac{3}{4}r$. Here ΔS is the distance of the approximate focal point from the true one.

For the usual mirror radii of a few meters this error is of the order of 0.1 mm, and it may therefore be concluded that the second-order approximation is sufficiently exact for most practical applications of the theory.

4. Fourth-Order Approximation, Flat Spectra

Where still more accuracy is needed, a fourth-order approximation of the focal surface may be used. If, in (21a, b, and c), the next higher terms in α and γ are also retained one finds, instead of (22a, b, and c),

$$x/r = \frac{1}{2}\left[1-(m/r)^2\gamma^2+\frac{1}{3}(m/r)^2\gamma^4\right] - \frac{1}{4}\{[1-3(m/r)^2]-[(m/r)^2-4(m/r)^3+3(m/r)^4]\gamma^2\}\alpha^2 + \frac{1}{48}[1-30(m/r)^2+48(m/r)^3-27(m/r)^4]\alpha^4, \tag{39a}$$

$$y/r = \pm\frac{1}{2}\sqrt{\alpha^2-\gamma^2}\left\{1-\frac{1}{6}[1+6(m/r)^2-12(m/r)^3]\gamma^2 - \frac{1}{6}[1-9(m/r)^2+12(m/r)^3]\alpha^2\right\}, \tag{39b}$$

$$z/r = \frac{1}{2}\gamma\left\{1-\frac{1}{6}[1+6(m/r)^2-12(m/r)^3]\gamma^2 + \frac{1}{2}[3(m/r)^2-4(m/r)^3]\alpha^2\right\}. \tag{39c}$$

These equations permit a point-by-point computation of the focal surface and, upon use of (19a), of the slit curve as well. The deviation from the true focal surface is

$$\Delta S \sim 2\cdot 10^{-7} r, \tag{39d}$$

for $\alpha=0.1$, $\gamma=0.03$, and $\frac{1}{2}r<m<\frac{3}{4}r$, as in 3.3. This is equivalent to about 1μ, only, for a mirror radius of a few meters, so that the fourth-order approximation will certainly suffice for any application of the theory.

Equation (39a) shows that, for $m=r/\sqrt{3}$, the x-coordinates of spectrum center and ends ($\alpha=\gamma$ and $\pm\alpha_{max}$, respectively) differ by fourth-order terms. With the grating in the $\sqrt{3}$-position, the horizontal cross sections of the focal surface are therefore still slightly curved.

The flatness of the spectrum may now be further improved by slightly correcting the grating position by an amount ϵ for which, in the fourth-order approximation of (39a), the spectrum center and the spectrum ends lie on a straight line. Thus, introduce

$$m = r/\sqrt{3}+\epsilon \tag{40}$$

into (39a), calculate $x=x(\epsilon)$ for $\alpha=\gamma$ and $\alpha=\pm\alpha_{max}$, and equate the two x-values so obtained in order to find ϵ.

The procedure, which has previously been published by this author [13] for in-plane mountings and is now extended to off-plane ones also, is best explained by a numerical example:

Consider an Ebert-Fastie spectrograph of $r=2$ m mirror radius, $H=80$ mm grating height, and $L=360$ mm spectrum length. Thus, with (37a, b),

$$\gamma=0.05,\ \alpha_{\max}=\pm 0.2, \tag{41a}$$

and, with (39a) and (40),

$$x=[(999.167+2.884\epsilon/r)-(0.129-1\ 731.381\epsilon/r)\alpha^2 -(115.100+309.401\epsilon/r)\alpha^4]\ \text{mm}, \tag{41b}$$

where linear terms in ϵ/r are retained, only. Hence, for the spectrum center ($\alpha=\gamma=0.05$),

$$x_0=(999.166+1.442\epsilon/r)\ \text{mm}, \tag{41c}$$

and, for the spectrum ends ($\alpha=\alpha_{\max}=\pm 0.2$),

$$x_{\max}=(998.978+65.862\epsilon/r)\ \text{mm}, \tag{41d}$$

so that

$$\epsilon/r=0.002\ 918,\ \epsilon=5.836\ \text{mm}, \tag{41e}$$

if one demands that x_0 and $x_{\max}$ be equal.

The focal curves obtained from (39 a and b) for the uncorrected and the corrected $\sqrt{3}$-position of the grating ($m=1154.700$ mm, and 1160.536 mm, respectively) are shown in figure 7. For the latter, the position of the photographic plate may be chosen as indicated by the broken line. In our example, a displacement of the grating of about 6 mm has thus resulted in a residual curvature of the spectrum of only $\triangle x=0.02$ mm.

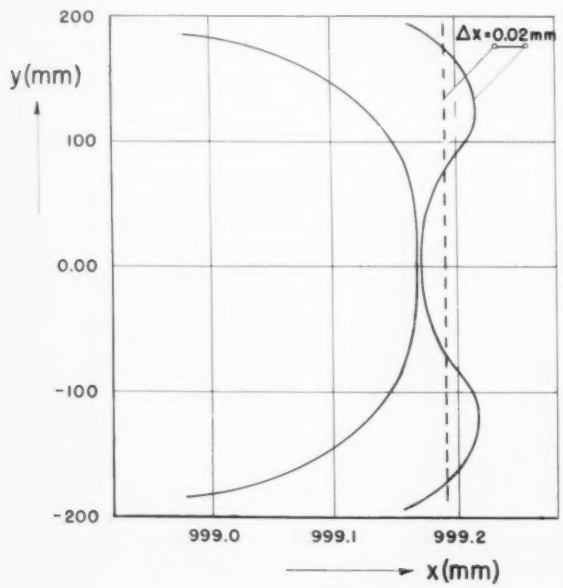

FIGURE 7. *Horizontal cross sections of focal surfaces of Ebert-Fastie spectograph.*

Left: uncorrected, right: corrected $\sqrt{3}$-position of grating. Scale of abscissa 1000 times enlarged.

For the uncorrected $\sqrt{3}$-position, the residual curvature is of the order of 0.1 mm and so is on the verge of being acceptable without further improvement [13]. Also, the above example involves a rather extreme relative spectrum length, where image quality at the ends of the spectrum, rather than deviation from flatness, is likely to be the chief consideration.

It may therefore again be concluded that the fourth-order approximation of the focal surface will be needed only rarely.

5. Conclusions

The chief results of the above theory of Ebert and Ebert-Fastie systems, and their consequences, may be summarized as follows.

(1) Closed expressions for the focal surfaces and slit curves can be derived in a second-order approximation only, but the accuracy obtained with it is sufficient in most practical cases.

(2) The curvature of the focal surface is strongly dependent upon the position of the grating in the spectrograph. An extended flat spectrum is obtained when the grating is arranged at the $\sqrt{3}$-position (28), which may be slightly corrected for still better flatness.

(3) The off-plane Ebert-Fastie system is the preferred mounting for spectrographs as it yields, other parameters equal, a spectrum twice as long as the in-plane Ebert system.

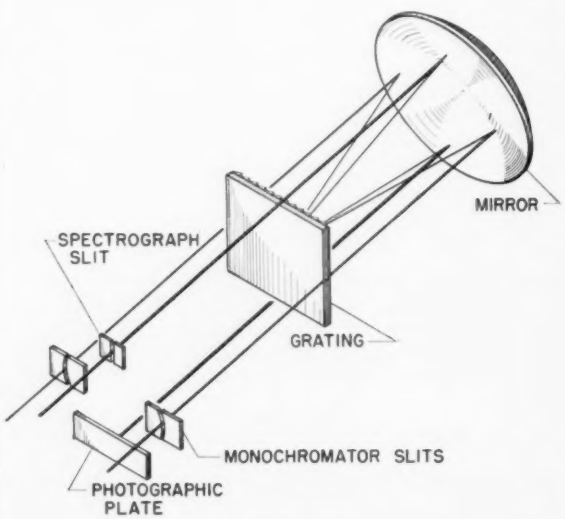

FIGURE 8. *Ebert-Fastie spectrograph combined with Ebert monochromator.*

(4) Long slits, as required to maximize the energy throughput of monochromators, must be curved but can be used in an in-plane arrangement only. The Ebert system is therefore the preferred mounting for monochromators.

(5) These relative merits of the two mountings immediately suggest the combined spectrograph-monochromator system of figure 8, where the mere addition of two curved monochromator slits to an Ebert-Fastie spectrograph converts the instrument into an Ebert monochromator as well. A versatile double-purpose system is obtained in this manner at little extra cost and effort. G. W. King [14] has actually built such an instrument.

The programming of numerical computations needed for this paper was done by J. J. Spijkerman, of NBS.

(Paper 68C4–165)

6. References

[1] K. D. Mielenz, Theory of mirror spectrographs I. Astigmatic illumination of plane gratings and prisms, J. Res. NBS **68C** (Eng. and Instr.), No. 4, 195 (Oct.–Dec. 1964).
[2] K. D. Mielenz, Theory of mirror spectrographs II. General theory of focal surfaces and slit curvatures, **68C** (Eng. and Instr.), No. 4, 201 (Oct.–Dec. 1964).
[3] H. Ebert, Wiedem. Ann. **38,** 489 (1889).
[4] R. F. Jarrell, J. Opt. Soc. Am. **45,** 259 (1955).
[5] K. Rottmann, Math. Formelsamml., p. 60 ff. (Bibliogr. Inst., Mannheim, 1961).
[6] I. S. Sokolnikoff and R. M. Redheffer, Math. of Physics and Mod. Engineering, p. 309 (McGraw-Hill Book Co., New York, N.Y., 1958).
[7] O. Vierle, Dissertation TH Munich, 1962.
[8] S. A. Khrshanovskii, Opt. Spectr. **9,** 207 (1960).
[9] W. G. Fastie, J. Opt. Soc. Am. **42,** 641 (1952).
[10] W. G. Fastie, J. Opt. Soc. Am. **42,** 647 (1952).
[11] P. Kroeplin, Optik aller Wellenlaengen, p. 123 (Akademie-Verlag, Berlin 1959).
[12] H. Kaiser, K. D. Mielenz, and F. Rosendahl, Z. Instr. kde. **67,** 269 (1959).
[13] K. D. Mielenz, Optik **20,** 28 (1963).
[14] G. W. King, J. Sci. Instr. **35,** 11 (1958).

JOURNAL OF RESEARCH of the National Bureau of Standards—C. Engineering and Instrumentation
Vol. 68C, No. 4, October–December 1964

Heat Flow in a Right Circular Cylinder With Arbitrary Temperature Boundary Conditions—Applications to the Determination of Thermal Conductivity

D. R. Flynn

(August 5, 1964)

Expressions are developed which permit calculation of the temperature-dependent thermal conductivity of a cylindrical specimen from the experimentally determined temperature distributions on its surfaces and from the heat flow through a central circular area at one end of the cylinder. Numerical factors are tabulated which permit rapid hand computation of thermal conductivity values from experimental data for the case of axially symmetric parabolic boundary conditions on the flat surfaces and a linear longitudinal temperature distribution on the convex surface. Applications to several published methods of thermal conductivity determinations are shown and examples are given.

1. Introduction

In a recent paper by Glaser et al. [1],[1] a method of measuring the thermal conductivity of solids was described in which the principal heat flow was parallel to the axis of a small circular disk-shaped specimen, but in which significant radial heat flows also occurred. Assuming axial symmetry, the authors used a least-mean-squares parabola to represent the measured radial temperature profile on each face of the specimen and assumed a linear longitudinal temperature distribution along the cylindrical surface of the specimen. Utilizing these boundary conditions, longitudinal temperature gradients at the cooler face of the specimen were determined by numerical solution of a finite difference equation using a digital computer. The thermal conductivity of the specimen was calculated from the average computed temperature gradient at the cooler surface and the measured heat flow leaving this surface.

A somewhat similar heat flow analysis is being used in the Heat Transfer Section of the National Bureau of Standards in conjunction with thermal conductivity measurements employing a guarded steam calorimeter for the measurement of heat flow through the central 3-in.-diam area of a 6-in.-diam disk-shaped specimen [2]. The method is one of chiefly longitudinal heat flow, but corrections are occasionally necessary to account for radial heat flows. In order to effect such corrections, an exact analytical solution was obtained to the boundary value problem in which parabolic temperature distributions having axial symmetry are assumed on the two plane end surfaces, and a linear longitudinal temperature distribution is assumed on the convex surface, of a right circular cylinder.

Subsequent to the development of this analysis at NBS, a paper was published by Hoch et al. [3], in which a somewhat similar, although less general, analytical solution was derived. In the latter paper, the heat conduction equation was solved for the case of a finite cylinder with the convex surface at a uniform temperature and the same axially symmetric parabolic temperature distribution on the two faces of the cylinder. The thermal conductivity of the specimen was calculated from the computed values of the temperature gradient at the center of the faces of the cylinder and of the heat flux radiated from these surfaces at the center, as determined by their temperature and emissivity.

In view of the general interest in this heat flow problem, it was decided to present, prior to formal publication of the paper [2] describing the NBS steam calorimeter apparatus, the mathematical analysis developed for it. The analysis given first treats the case of a right circular cylinder with arbitrary temperature boundary conditions, and then develops solutions for specific boundary conditions applicable to the determination of thermal conductivity.

2. Mathematical Development

Consider a homogeneous, isotropic, opaque, solid right cylinder of radius, b, and thickness, l. In general, the thermal conductivity of the cylinder material may vary with temperature. If so, the steady-state heat flow equation in cylindrical coordinates, assuming axial symmetry, is

$$\vec{\nabla}\cdot(k\vec{\nabla}v)=\frac{1}{r}\frac{\partial}{\partial r}\left(k(v)r\frac{\partial v}{\partial r}\right)+\frac{\partial}{\partial z}\left(k(v)\frac{\partial v}{\partial z}\right)=0, \quad (1)$$

where temperature above an arbitrary datum is denoted by the symbol v, the temperature-dependent thermal conductivity by $k(v)$, and the radial and longitudinal coordinates by r and z, respectively. Equation (1) can be reduced to a simpler form by introduction of a new variable, y, defined by the relation

$$y=\frac{1}{k^*}\int_0^v k(v')dv', \quad (2)$$

[1] Figures in brackets indicate the literature references at the end of this paper.

where k^* is the value of $k(v)$ at $v=0$.[2] Utilizing (2), (1) reduces to [4, 5]

$$\nabla^2 y=\frac{\partial^2 y}{\partial r^2}+\frac{1}{r}\frac{\partial y}{\partial r}+\frac{\partial^2 y}{\partial z^2}=0. \tag{3}$$

The variable, y, is essentially a potential whose gradient is proportional to the heat flux [6].

2.1. General Boundary Conditions

Assume the following boundary conditions:

$$z=0 \qquad 0\leq r\leq b \qquad y=f(r), \tag{4a}$$

$$z=l \qquad 0\leq r\leq b \qquad y=g(r), \tag{4b}$$

$$0<z<l \qquad r=b \qquad y=f(b)+[g(b)-f(b)]\frac{z}{l}+h(z), \tag{4c}$$

where $f(r)$ and $g(r)$ are arbitrary potential distributions on the flat surfaces of the disk, and where, in order to insure continuity, we shall require that the function $h(z)$ vanishes at the flat surfaces of the disk, so that $h(0)=h(l)=0$. The solution is [7]:[3]

$$y=f(b)+[g(b)-f(b)]\frac{z}{l}+\sum_{n=1}^{\infty}J_0\left(\alpha_n\frac{r}{b}\right)\times\left\{A_n\sinh\left(\alpha_n\frac{z}{b}\right)+B_n\sinh\left(\alpha_n\frac{l-z}{b}\right)\right\}+\sum_{k=1}^{\infty}C_kI_0\left(\frac{k\pi r}{l}\right)\sin\left(\frac{k\pi z}{l}\right), \tag{5}$$

where J_0 and I_0 are, respectively, the ordinary and the modified Bessel functions of the first kind; the α_n's are the positive roots of $J_0(\alpha_n)=0$. In order to satisfy the boundary conditions, the coefficients must be:

$$A_n=\frac{2}{b^2J_1^2(\alpha_n)\sinh(\alpha_nl/b)}\int_0^b\{g(r)-g(b)\}rJ_0(\alpha_nr/b)dr, \tag{6}$$

$$B_n=\frac{2}{b^2J_1^2(\alpha_n)\sinh(\alpha_nl/b)}\int_0^b\{f(r)-f(b)\}rJ_0(\alpha_nr/b)dr, \tag{7}$$

and

$$C_k=\frac{2}{lI_0\left(\frac{k\pi b}{l}\right)}\int_0^l h(z)\sin\left(\frac{k\pi z}{l}\right)dz. \tag{8}$$

Equation (5) can be used to calculate the steady-state potential distribution in a finite cylinder corresponding to arbitrary potential boundary conditions, $g(r)$, $f(r)$, and $h(z)$. If the indicated integrations of (6), (7), and (8) cannot be obtained analytically, values can be determined by numerical integration.

2.2. Parabolic Boundary Conditions

The boundary conditions used by Glaser et al. [1], Robinson et al. [2], and Hoch et al. [3] are all of the form

$$f(r)=Y_0+E_0\frac{r^2}{b^2},$$

$$g(r)=Y_1+E_1\frac{r^2}{b^2}, \tag{9}$$

and

$$h(z)=0,$$

where Y_0 and Y_1 are the potentials (corresponding to y) at the centers of the faces of the disk, and E_0 and E_1 are the potential differences between the edge and the center of the disk at $z=0$ and $z=l$, respectively. With these boundary conditions, (5) becomes

$$y=(Y_0+E_0)+(Y_1-Y_0+E_1-E_0)\frac{z}{l}-8\sum_{n=1}^{\infty}\frac{J_0(\alpha_nr/b)}{\alpha_n^2J_1(\alpha_n)\sinh(\alpha_nl/b)}\times\left\{E_1\sinh\left(\alpha_n\frac{z}{b}\right)+E_0\sinh\left(\alpha_n\frac{l-z}{b}\right)\right\}. \tag{10}$$

3. Calculation of Thermal Conductivity

The thermal conductivity of the disk is to be determined from the measured heat flow leaving a central portion of the disk of radius, $r=a$, and from the observed potential distributions on the surfaces of the disk. A mathematical expression giving the appropriate relationship between these quantities is derived by determining the total heat flow through a circle of radius a, at $z=0$:

$$Q=2\pi\int_0^a rk(v)\left(\frac{\partial v}{\partial z}\right)_{z=0}dr=2\pi k^*\int_0^a r\left(\frac{\partial y}{\partial z}\right)_{z=0}dr. \tag{11}$$

Performing the indicated differentiation and integration on (5),

$$Q=\pi a^2k^*\left[\frac{g(b)-f(b)}{l}+\frac{2}{a}\sum_{n=1}^{\infty}J_1\left(\alpha_n\frac{a}{b}\right)\times\left\{A_n-B_n\cosh\left(\alpha_n\frac{l}{b}\right)\right\}+\frac{2}{a}\sum_{k=1}^{\infty}C_kI_1\left(\frac{k\pi a}{l}\right)\right]. \tag{12}$$

Equation (12) can be rewritten in terms of the parabolic boundary conditions (9) discussed in section 2.2. If this is done, the heat flow through a circle of radius, a, becomes

[2] This is a special case of the more general relation $dy=Ck(v)dv$, where C is an arbitrary constant.

[3] This specific problem is not handled by Carslaw and Jaeger; the form of solution and the necessary integrals are given in the chapter cited.

$$Q=\pi a^2 \frac{k^*}{l}[Y_1-Y_0+E_1\Psi_1-E_0\Psi_0] \quad (13)$$

in which

$$\Psi_1=1-16\sum_{n=1}^{\infty}\frac{J_1(\alpha_n a/b)}{(a/b)\alpha_n^3 J_1(\alpha_n)}\times\frac{(l/b)}{\sinh(\alpha_n l/b)} \quad (14)$$

and

$$\Psi_0=1-16\sum_{n=1}^{\infty}\frac{J_1(\alpha_n a/b)}{(a/b)\alpha_n^3 J_1(\alpha_n)}\times\frac{(l/b)}{\tanh(\alpha_n l/b)} \quad (15)$$

are factors which depend only on the geometry of the disk and on the fraction of the disk from which the heat flow is measured. If all of the other quantities are known, eq (13) can be used to compute the thermal conductivity, k^*. In order to compute the values of the potential, y, for use in eq (13), some assumption must be made regarding the temperature-dependence of the thermal conductivity of the disk (see eq (2)). This is discussed in section 4.

In the special case, $l/b=0$, (14) and (15) reduce to

$$\Psi_1=\Psi_0=1-16\sum_{n=1}^{\infty}\frac{J_1(\alpha_n a/b)}{(a/b)\alpha_n^4 J_1(\alpha_n)}=\frac{1}{2}\left(\frac{a}{b}\right)^2. \quad (16)$$

In the special case, $a/b=0$, used by Hoch et al. [3],

TABLE 1. *The coefficient Ψ_1 as a function of l/b and a/b for parabolic boundary conditions*

l/b \ a/b	0.00	0.10	0.20	0.30	0.40	0.50	0.60	0.70	0.80	0.90	1.00	a/b \ l/b
0.0	0.00000	0.00500	0.02000	0.04500	0.08000	0.12500	0.18000	0.24500	0.32000	0.40500	0.50000	0.0
0.1	.00667	.01167	.02667	.05167	.08667	.13167	.18667	.25167	.32667	.41164	.50621	0.1
0.2	.02667	.03167	.04667	.07167	.10667	.15166	.20665	.27161	.34643	.43072	.52307	0.2
0.3	.05998	.06498	.07997	.10495	.13991	.18481	.23958	.30404	.37778	.45980	.54809	0.3
0.4	.10632	.11129	.12620	.15102	.18567	.23005	.28392	.34686	.41806	.49616	.57896	0.4
0.5	.16434	.16923	.18385	.20815	.24197	.28505	.33699	.39712	.46439	.53726	.61362	0.5
0.6	.23135	.23605	.25011	.27341	.30571	.34664	.39561	.45181	.51408	.58086	.65024	0.6
0.7	.30380	.30822	.32145	.34330	.37347	.41149	.45670	.50820	.56481	.62507	.68726	0.7
0.8	.37813	.38221	.39438	.41444	.44204	.47667	.51764	.56402	.61470	.66833	.72344	0.8
0.9	.45129	.45497	.46596	.48404	.50885	.53986	.57638	.61755	.66232	.70951	.75783	0.9
1.0	.52097	.52424	.53401	.55004	.57200	.59937	.63149	.66758	.70670	.74781	.78979	1.0
1.2	.64440	.64690	.65431	.66646	.68305	.70365	.72773	.75466	.78372	.81414	.84512	1.2
1.4	.74323	.74505	.75047	.75935	.77144	.78643	.80390	.82340	.84439	.86632	.88861	1.4
1.6	.81842	.81971	.82357	.82989	.83849	.84913	.86152	.87533	.89017	.90567	.92140	1.6
1.8	.87364	.87454	.87724	.88165	.88765	.89507	.90370	.91332	.92365	.93443	.94537	1.8
2.0	.91317	.91379	.91565	.91869	.92281	.92792	.93386	.94047	.94757	.95497	.96248	2.0
2.2	.94094	.94137	.94263	.94470	.94751	.95098	.95502	.95952	.96435	.96938	.97449	2.2
2.4	.96017	.96045	.96131	.96270	.96460	.96694	.96967	.97270	.97596	.97935	.98280	2.4
2.6	.97332	.97351	.97409	.97502	.97629	.97786	.97969	.98172	.98390	.98617	.98848	2.6
2.8	.98224	.98237	.98275	.98337	.98422	.98526	.98648	.98783	.98928	.99080	.99233	2.8
3.0	.98824	.98832	.98857	.98898	.98954	.99024	.99104	.99194	.99290	.99390	.99492	3.0
3.5	.99588	.99591	.99599	.99614	.99633	.99658	.99686	.99717	.99751	.99786	.99822	3.5
4.0	.99858	.99859	.99862	.99867	.99874	.99882	.99892	.99903	.99915	.99927	.99939	4.0
4.5	.99952	.99952	.99954	.99955	.99957	.99960	.99964	.99967	.99971	.99975	.99979	4.5
5.0	.99984	.99984	.99984	.99985	.99986	.99987	.99988	.99989	.99990	.99992	.99993	5.0
	0.00	0.10	0.20	0.30	0.40	0.50	0.60	0.70	0.80	0.90	1.00	

TABLE 2. *The coefficient Ψ_0 as a function of l/b and a/b for parabolic boundary conditions*

l/b \ a/b	0.00	0.10	0.20	0.30	0.40	0.50	0.60	0.70	0.80	0.90	1.00	a/b \ l/b
0.0	0.00000	0.00500	0.02000	0.04500	0.08000	0.12500	0.18000	0.24500	0.32000	0.40500	0.50000	0.0
0.1	−.01332	−.00832	.00667	.03167	.06667	.11167	.16667	.23167	.30667	.39170	.48728	0.1
0.2	−.05332	−.04832	−.03332	−.00832	.02667	.07168	.12669	.19173	.26691	.35267	.45149	0.2
0.3	−.11997	−.11497	−.09996	−.07494	−.03989	.00520	.06043	.12597	.20230	.29070	.39601	0.3
0.4	−.21297	−.20794	−.19285	−.16767	−.13232	−.08670	−.03054	.03661	.11577	.20918	.32401	0.4
0.5	−.33099	−.32587	−.31050	−.28479	−.24859	−.20163	−.14343	−.07317	.01071	.11143	.23839	0.5
0.6	−.47129	−.46600	−.45004	−.42330	−.38552	−.33624	−.27476	−.19987	−.10948	.00054	.14178	0.6
0.7	−.63026	−.62467	−.60783	−.57954	−.53942	−.48688	−.42095	−.34009	−.24168	−.12072	.03652	0.7
0.8	−.80408	−.79811	−.78009	−.74979	−.70670	−.65008	−.57874	−.49081	−.38317	−.24998	−.07542	0.8
0.9	−.98928	−.98285	−.96344	−.93074	−.88417	−.82283	−.74531	−.64945	−.53165	−.38525	−.19237	0.9
1.0	−1.18294	−1.17599	−1.15500	−1.11962	−1.06917	−1.00262	−.91837	−.81394	−.68528	−.52496	−.31301	1.0
1.2	−1.58699	−1.57889	−1.55439	−1.51307	−1.45408	−1.37613	−1.27724	−1.15440	−1.00267	−.81307	−.56155	1.2
1.4	−2.00374	−1.99439	−1.96613	−1.91842	−1.85029	−1.76019	−1.64581	−1.50358	−1.32776	−1.10776	−.81558	1.4
1.6	−2.42657	−2.41593	−2.38376	−2.32946	−2.25189	−2.14929	−2.01900	−1.85694	−1.65651	−1.40562	−1.07223	1.6
1.8	−2.85220	−2.84025	−2.80412	−2.74312	−2.65598	−2.54072	−2.39433	−2.21221	−1.98694	−1.70493	−1.33010	1.8
2.0	−3.27905	−3.26578	−3.22566	−3.15793	−3.06116	−2.93319	−2.77061	−2.56834	−2.31814	−2.00488	−1.58850	2.0
2.2	−3.70648	−3.69189	−3.64776	−3.57328	−3.46686	−3.32608	−3.14727	−2.92485	−2.64967	−2.30512	−1.84715	2.2
2.4	−4.13414	−4.11823	−4.07010	−3.98885	−3.87276	−3.71920	−3.52415	−3.28149	−2.98133	−2.60549	−2.10589	2.4
2.6	−4.56191	−4.54467	−4.49253	−4.40451	−4.27876	−4.11240	−3.90111	−3.63823	−3.31304	−2.90590	−2.36468	2.6
2.8	−4.98972	−4.97115	−4.91500	−4.82021	−4.68479	−4.50564	−4.27809	−3.99500	−3.64479	−3.20632	−2.62349	2.8
3.0	−5.41754	−5.39766	−5.33749	−5.23593	−5.09084	−4.89889	−4.65509	−4.35178	−3.97656	−3.50676	−2.88230	3.0
3.5	−6.48713	−6.46393	−6.39374	−6.27526	−6.10598	−5.88204	−5.59761	−5.24374	−4.80599	−4.25790	−3.52934	3.5
4.0	−7.55668	−7.53016	−7.44994	−7.31453	−7.12107	−6.86520	−6.54013	−6.13572	−5.63542	−5.00903	−4.17639	4.0
4.5	−8.62628	−8.59644	−8.50620	−8.35386	−8.13622	−7.84830	−7.48260	−7.02763	−6.46486	−5.76017	−4.82345	4.5
5.0	−9.69588	−9.66273	−9.56245	−9.39319	−9.15136	−8.83146	−8.42512	−7.91960	−7.29424	−6.51130	−5.47050	5.0
	0.00	0.10	0.30	0.30	0.40	0.50	0.60	0.70	0.80	0.90	1.00	

$$\Psi_1=1-8\sum_{n=1}^{\infty}\frac{1}{\alpha_n^2 J_1(\alpha_n)}\times\frac{(l/b)}{\sinh(\alpha_n l/b)} \tag{17}$$

and

$$\Psi_0=1-8\sum_{n=1}^{\infty}\frac{1}{\alpha_n^2 J_1(\alpha_n)}\times\frac{(l/b)}{\tanh(\alpha_n l/b)}. \tag{18}$$

For large values of l/b,

$$\Psi_1\to 1 \tag{19}$$

and

$$\Psi_0\to 1-(l/b)\Phi, \tag{20}$$

where

$$\Phi=16\sum_{n=1}^{\infty}\frac{J_1(\alpha_n a/b)}{(a/b)\alpha_n^3 J_1(\alpha_n)} \tag{21}$$

is a function of a/b only.

Using a high-speed digital computer, numerical values for Ψ_1 and Ψ_0 have been calculated for a range of values of a/b and l/b and are given in tables 1 and 2. Representative values are plotted in figure 1. The series for Ψ_1 is rapidly convergent, due to the quantity, $\sinh(\alpha_n l/b)$, which appears in the denominator. The series for Ψ_0, however, converges rather slowly and it was necessary to sum at least the first one thousand terms of this series in order to obtain the number of significant figures given in table 2.

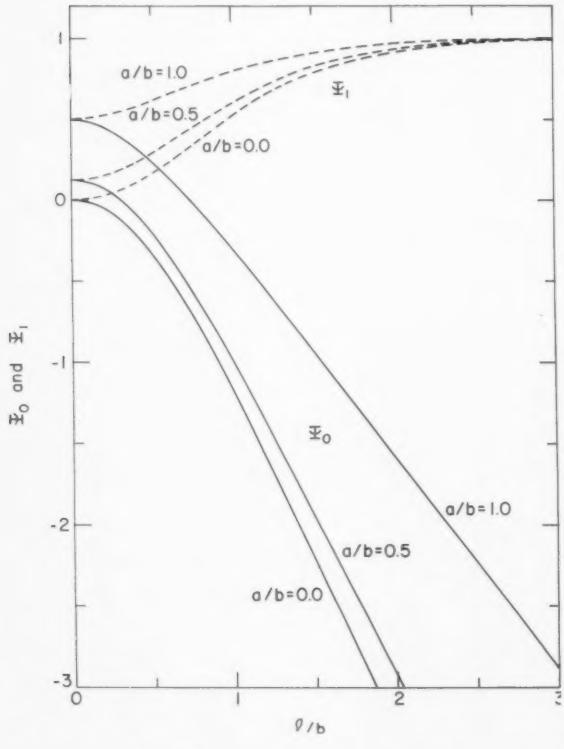

FIGURE 1. *The coefficients Ψ_0 and Ψ_1 for the case of parabolic boundary conditions; solid lines, Ψ_0; dashed lines, Ψ_1.*

For values of l/b larger than those given in tables 1 and 2, Ψ_1 is substantially unity and Ψ_0 may be computed using (20) and the values of Φ given in table 3.

TABLE 3. *The function Φ which is used for computing values of Ψ_0 corresponding to large l/b*

a/b	Φ
0.0	2.13918
0.1	2.13255
0.2	2.11249
0.3	2.07864
0.4	2.03028
0.5	1.99630
0.6	1.88502
0.7	1.78393
0.8	1.65885
0.9	1.50226
1.0	1.29410

4. Effective Mean Temperature

The thermal conductivity of the disk at $v=0$ can be computed from (12) for the general case or from (13) for the case of parabolic boundary conditions. The variable, v, is the temperature measured from an arbitrary reference temperature, say T^*. Thus the conductivity obtained, k^*, corresponds to the reference temperature T^*. The variable, y, as mentioned previously, depends on the temperature-dependence of the thermal conductivity of the disk. Two particular cases of interest are discussed here.

4.1. Thermal Conductivity Having Linear Temperature-Dependence

For many materials the thermal conductivity can be assumed to vary linearly with temperature over a moderate temperature range, such that

$$k(v)=k^*[1+\beta v]; \tag{22}$$

then, from (2),

$$y=v+\frac{\beta}{2}v^2. \tag{23}$$

The boundary conditions must be written in terms of y and then substituted into the appropriate equations.

For the case of parabolic boundary conditions, the following relations hold:

$$Y_0=V_0+\frac{\beta}{2}V_0^2 \qquad Y_1=V_1+\frac{\beta}{2}V_1^2 \tag{24}$$

$$E_0=D_0+\frac{\beta}{2}(D_0^2+2D_0V_0) \qquad E_1=D_1+\frac{\beta}{2}(D_1^2+2D_1V_1), \tag{25}$$

where $V_0=T_0-T^*$ and $V_1=T_1-T^*$, T_0 and T_1 being the temperatures at the center of the disk at $z=0$ and $z=l$, respectively, and D_0 and D_1 are the temperature differences between the edge and the center of the disk at $z=0$ and $z=l$, respectively.

In order to compute the thermal conductivity of the disk, eqs (24) and (25) must be substituted into (13). The resultant expression, however, involves β, the temperature coefficient of the thermal conductivity, a quantity which may not be known. This dependence can be eliminated by proper choice of the reference temperature, T^*. If T^* is defined as

$$T^*=\frac{T_1+T_0}{2}+\frac{D_1\Psi_1(T_1-T_0+D_1)+D_0\Psi_0(T_1-T_0-D_0)}{2[T_1-T_0+D_1\Psi_1-D_0\Psi_0]}, \tag{26}$$

then eq (13) reduces to

$$Q=\pi a^2\frac{k^*}{l}[T_1-T_0+D_1\Psi_1-D_0\Psi_0], \tag{27}$$

which is the expression that would be obtained for the case of a specimen having constant thermal conductivity, k^*. For the special case in which there is no radial heat flow, $D_1=D_0=0$, and (26) reduces to $T^*=(T_1+T_0)/2$ [8].

4.2. Thermal Resistivity Having Linear Temperature-Dependence

For many crystalline dielectric solids, the thermal resistivity, i.e., the reciprocal of thermal conductivity, varies substantially linearly with temperature over a considerable temperature range. In this case, the thermal conductivity can be written as

$$k(v)=\frac{k^*}{1+\gamma v}; \tag{28}$$

then, from (2),

$$y=\frac{1}{\gamma}\ln(1+\gamma v). \tag{29}$$

The relation between y and v can be better seen by expanding (29) in series form,

$$y=v\left(1-\frac{\gamma v}{2}+\frac{(\gamma v)^2}{3}-\ldots\right), \tag{30}$$

provided $|\gamma v|<1$.

In the present case the coefficient γ is not so amenable to elimination by choice of a particular reference temperature as was the coefficient β in section 4.1. In computing thermal conductivity values for a material whose thermal conductivity is expected to have a temperature dependence such as that in (28), one may first assume that $|\gamma v|$ is sufficiently small to permit terminating eq (30) after the second term of the series; i.e., $y=v-\gamma v^2/2$. Comparison of this expression with (23) shows that the assumption that $|\gamma v|$ is small is equivalent to assuming a linear temperature dependence for the thermal conductivity. Thus one may use (26) and (27) to compute a mean temperature and the approximate thermal conductivity at that temperature. The first approximations to the thermal conductivity thus obtained for several tests at different mean temperatures can be used to compute values of the coefficient γ which then can be used in (29) or (30) to obtain values of y, which can in turn be used in (13) to obtain more refined values for thermal conductivity. The resultant value of k^* can be used to obtain better values of γ, etc. The convergence is quite rapid in most practical cases, so that only one or two iterations will normally be required.

5. Examples

In order to illustrate the use of the mathematical developments presented in this paper, we now shall cite specific examples in which the factors Ψ_1 and Ψ_0 given in section 3 for parabolic boundary conditions are utilized to compute thermal conductivity values from measured temperatures and a measured heat flow. One example will be given for each of the three methods mentioned in section 1 [1, 2, 3].

5.1. Method of Glaser et al.

In the method described by Glaser et al. [1], the entire heat flow leaving the colder flat surface of the disk-shaped specimen is determined, i.e., in the nomenclature of the present paper, $a/b=1.0$. We postulate the following data as having been acquired experimentally: [4]

$$a=b=0.476\text{ cm} \qquad l=0.160\text{ cm}$$
$$Q=9.60\text{ W}$$
$$T_0=1319\text{ °C} \qquad D_0=-218\text{ deg}$$
$$T_1=1536\text{ °C} \qquad D_1=-338\text{ deg}$$

Interpolation of table 1 and 2 for the case $a/b=1.0$ and $l/b=0.336$ yields,

$$\Psi_1=0.559 \qquad \Psi_0=0.372.$$

Assuming linear temperature dependence, the thermal conductivity is computed using (27). Substituting the values given above for the various parameters and solving for thermal conductivity,

$$k^*=0.0198\text{ W/cm deg.}$$

The mean temperature is computed from (26) as:

$$T^*=1370\text{ °C.}$$

It should be remembered that, for a given specimen size and shape, the factors Ψ_1 and Ψ_0 remain constant. The only further information needed to compute thermal conductivity values for a given specimen is the heat flow and four temperatures (in effect). Thus the procedure described by Glaser et al. [1], in which each thermal conductivity value was obtained by numerical solution of a finite difference equation on a high-speed digital computer, can now be replaced by a fairly simple hand calculation using the values of Ψ_1 and Ψ_0 tabulated in this paper.

[4] This is an actual set of data which was made available through the courtesy of P. E. Glaser of Arthur D. Little, Inc.

5.2. Method of Robinson et al.

In the NBS steam calorimeter method [2], the total heat flow through only a central section of the specimen is measured. Let us assume that the thermal resistivity, rather than the thermal conductivity, of the specimen exhibits a linear temperature dependence; i.e., the thermal conductivity is of the form given in (28). We postulate the following data as having been acquired experimentally:

$$a=3.81 \text{ cm} \qquad b=7.62 \text{ cm} \qquad l=2.29 \text{ cm}$$
$$Q=542 \text{ W}$$
$$T_0=540 \text{ °C} \qquad D_0=-20 \text{ deg}$$
$$T_1=980 \text{ °C} \qquad D_1=-40 \text{ deg}$$

For the case $a/b=0.5$ and $l/b=0.3$, table 1 and 2 yield

$$\Psi_1=0.18481 \qquad \Psi_0=0.00520.$$

Substitution into (26) and (27) yields

$$k^*=0.0629 \text{ W/cm deg at } T^*=756.5 \text{ °C}$$

as a first approximation to the thermal conductivity at this temperature. If similar sets of data at other temperature levels are analyzed in this manner, the resultant thermal conductivity values can be used to compute values for γ, the thermal resistivity temperature coefficient. Let us assume that this has been done and that a value of $\gamma=9.0\times10^{-4}$ deg^{-1} at 757 °C was obtained. Using $T^*=757$ °C as a reference temperature,

$$V_0=-217 \text{ deg} \qquad V_1=223 \text{ deg}.$$

Substitution of these values for V_0 and V_1 and the above-mentioned values for D_0, D_1, and γ into (29) yields

$$Y_0=-241.4 \text{ deg} \qquad E_0=-25.1 \text{ deg}$$
$$Y_1=203.2 \text{ deg} \qquad E_1=-33.8 \text{ deg}$$

Substitution of these values of Y_0, Y_1, E_0, and E_1 into (13) yields

$$k^*=0.0621 \text{ W/cm deg at } T^*=757 \text{ °C}$$

as the improved value for the thermal conductivity. If thought necessary, the improved values for the thermal conductivity can be used to compute an improved value for γ for further refinement of the final thermal conductivity values.

5.3. Method of Hoch et al.

In the method described by Hoch et al. [3], the heat flux from the center of the flat surfaces of the disk is calculated from the temperature at that point and the total hemispherical emittance of the specimen, using the Stefan-Boltzmann radiation law. Since Hoch et al. derived an analytical solution for their case which is quite similar to that developed in the present paper for more general conditions, it is of interest to compare these solutions. Hoch et al. define a characteristic constant, K_0, which is given by [5]

$$K_0=2\sum_{n=1}^{\infty}\frac{\tanh\,(\alpha_n l/2b)}{\alpha_n^2 J_1(\alpha_n)}, \tag{31}$$

where the notation has been changed to conform with that of the present paper.

With the simplified boundary conditions assumed by Hoch et al. ($Y_1=Y_0$, $E_1=E_0$), the heat flux at the center of the surface of the disk is given by

$$k^*\left(\frac{\partial y}{\partial z}\right)_{\substack{r=0\\z=0}}=\frac{k^*}{l}E_0[\Psi_1-\Psi_0]. \tag{32}$$

This expression is analogous to (13), except that it refers to the heat flux at a point rather than to the total heat flow through a circular area. For the case $a/b=0$, with parabolic boundary conditions, the factors Ψ_1 and Ψ_0 are given by (17) and (18); the quantity $[\Psi_1-\Psi_0]$ becomes

$$[\Psi_1-\Psi_0]=8\sum_{n=1}^{\infty}\frac{l/b}{\alpha_n^2 J_1(\alpha_n)}\left[\frac{1}{\tanh\,(\alpha_n l/b)}-\frac{1}{\sinh\,(\alpha_n l/b)}\right], \tag{33}$$

which reduces to

$$[\Psi_1-\Psi_0]=8(l/b)\sum_{n=1}^{\infty}\frac{\tanh\,(\alpha_n l/2b)}{\alpha_n^2 J_1(\alpha_n)}. \tag{34}$$

Comparison of (31) and (34) yields

$$K_0=\frac{b}{4l}[\Psi_1-\Psi_0]. \tag{35}$$

Since Hoch et al. included a numerical example in their paper, it is needless to present one here. Values for K_0 can be computed using eq (35) and the appropriate values of Ψ_1 and Ψ_0 from the first column in tables 1 and 2. Hoch and Nitti [9] more recently have published an expanded version of their previous paper [3] in which they tabulate values of K_0 for several specimen shapes.

6. Discussion

For the case of parabolic radial potential distributions on the flat surfaces of the disk and a linear longitudinal potential distribution on the convex surface, the equations and tabulated coefficients given in this paper permit rapid hand computation of thermal conductivity values from experimental data. If boundary conditions other than those of eq (9) are required or indicated, thermal conductivity values should be computed from (12), rather than (13), with the appropriate coefficients being given

[5] Cf. equation (12), page 514, reference [3]; in the present paper this equation has been reduced, by means of recurrence relations, to a simpler form than that given originally by Hoch et al.

by (6), (7), and (8). Equation (12) is completely rigorous for the axially-symmetric boundary conditions (4a), (4b), and (4c). Proof of adequate compliance with these boundary conditions would appear to be indicated for any given test method. Hoch et al., [3, 9] have discussed the influence of one particular type of boundary condition, other than linear, on the convex surface of the disk. Other boundary conditions can be handled by evaluation of the appropriate integrals given in this paper.

The author thanks B. A. Peavy for checking the mathematical analysis given in this paper.

7. References

[1] P. E. Glaser, S. Merra, W. K. Sepetoski, D. F. Comstock, and A. G. Emslie, Radiation imaging technique for thermal conductivity measurement above 1000 °C, Rev. Sci. Instr. **33,** 57 (1962).

[2] H. E. Robinson, D. R. Flynn, and D. A. Didion, A steam calorimeter apparatus for measuring the thermal conductivity of refractories (to be published).

[3] M. Hoch, D. A. Nitti, C. F. Gottschlich, and P. E. Blackburn, New method for the determination of thermal conductivities between 1000° and 3000 °C, in Progress in International Research on Thermodynamic and Transport Properties, p. 512 (ASME, Academic Press, New York, 1962).

[4] M. S. Van Dusen, Note on the theory of heat conduction, NBS J. Res. **4,** 753 (1930) RP178.

[5] H. S. Carslaw and J. C. Jaeger, The Conduction of Heat in Solids, 2d Edition, pp. 10-11 (Oxford Univ. Press, 1959).

[6] P. Vernotte, Formes diverses de l'equation de la chaleur. Equation intrinseque, Comp. Rend. Acad. Sci. **218,** 39 (1944).

[7] Carslaw and Jaeger, op. cit., pp. 214-229.

[8] H. E. Robinson, Note on: Radiation imaging technique for thermal conductivity measurement above 1000 °C, Rev. Sci. Instr. **33,** 392 (1962).

[9] M. Hoch and D. A. Nitti, New Method for the determination of thermal conductivities between 1000° and 3000 °C, Aeronautical Systems Division Technical Report No. ASD TR 61-528 (June 1962).

(Paper 68C4–166)

JOURNAL OF RESEARCH of the National Bureau of Standards—C. Engineering and Instrumentation
Vol. 68C, No. 4, October–December 1964

Digitized Phasemeter

William S. Epstein

(July 23, 1964)

A device for measuring the phase of periodic signals in the audio or low ultrasonic frequency range is described. The error in the measurement is independent of signal amplitude within limits, and for signals usually met in practice is less than 0.1°. The device is easy to operate. The only adjustment required is the setting of the sensitivity of an electronic counter. Results of phase measurements are read on the counter. A way in which the measurement can be made independent of even order harmonics in the test signal is also discussed.

The purpose of the device being described is to measure phase of periodic electrical signals in the audio or low ultrasonic frequency range. The error in the measurement is independent of the amplitude of the signal within limits. For signals usually met in practice, the error is less than 0.1°.

The methods of phase detection generally employed are of two kinds: null detection [1] [1] and zero crossover detection [2]. In the first method, the difference in phase between the test signal and a standard is reduced to zero by the use of a calibrated phase shifter. This method has the disadvantage of requiring careful adjustment of the nulling circuits.

In the method of zero crossover detection, two signals are clipped and compared in a mixing circuit. The pulse width of the resultant rectangular wave is a linear measure of the phase difference between the original signals. This method is used frequently because of its relative simplicity; fewer adjustments are required. The accuracy depends upon the ability to clip inputs of various amplitudes close to their zero crossings. Such close clipping produces rectangular waves approximately in phase with their related input signals.

The device described here is an improvement over other phasemeters using zero crossover detection because of the use of stable circuits which accurately clip input signals at their zero crossings. The transistor circuitry is simple and requires no bias or other circuitry adjustments. The accuracy of the clipping action is preserved through the mixing and metering operations. Phase measurements are read on an electronic counter. Any counter capable of handling 1 MHz repetition rate pulses may be used. Over a 20 Hz to 20 kHz frequency range, a phase error of less than 0.1° is obtained for input signals of 0.1 to 20 V. Signals of a considerably wider frequency range and lower amplitude may be employed with some loss in accuracy.

The best null detection instruments presently have greater ultimate accuracy but require frequent complex adjustments or have restricted ranges of phase.

A block diagram of the overall phasemeter is shown in figure 1. There are two identical input channels. The input signals must be periodic with uniformly spaced zero crossings. The number of zero crossings per period must be the same for both input signals. The input channels each shape an input signal into a rectangular wave. The rectangular waves are combined in a mixer, and the resultant is applied to a gate. A series of 1 MHz pulses fed to a counter is interrupted when the gate is closed. The average number of pulses counted during a gating cycle is proportional to the phase difference between the input signals. The gated series of pulses usually includes a fraction of a pulse appearing at the beginning and end of each sequence. This fraction is determined by the width of the gating signal. The count of the fractional pulse is averaged over many gating periods so that the phase is sufficiently resolved at the 1 MHz rate. Adequate resolution is obtained even when the number of pulses to be counted is small, as occurs during a gating period of short duration.

When the phase detector and counter are used together for the first time, the counter sensitivity control should be adjusted so that the fractional pulse is averaged properly. This control may be adjusted in the following way: A signal of high frequency ω_1 is fed into one input of the phase detector and a signal of lower frequency ω_2 is fed into the other input. A gating signal results which causes the gate to transmit one quarter of the 1 MHz pulses to the counter. During each cycle of gating the signal from the mixer consists of a half cycle rectangular pulse derived from the lower frequency input added to a series of shorter half cycle rectangular pulses derived from the high frequency input. The number of pulses in the series depends upon the arbitrarily chosen ratio of ω_1 to ω_2. Unless ω_1 and ω_2 are integrally related, the time interval between the pulse recurring at the low frequency rate and the high frequency series of pulses varies in a continuous and periodic way. On the average, the gate is closed during half a gating cycle due to the lower frequency pulse and half of the remaining half of the gating cycle due to the high frequency pulses. With those inputs the sensitivity control is adjusted to give a 0.25 MHz reading on the counter. It is desirable to use input signals at the high end of the frequency range when making this

[1] Figures in brackets indicate the literature references at the end of this paper.

adjustment because the effect of fractional megahertz pulses is greatest when the gate is open for short times. Thus, an adequate adjustment with high frequency input signals will be correct for lower frequencies. In the method of adjustment described the presence of some noise in the input signal is unimportant since the count is averaged over many gating cycles.

The circuit used to convert an input wave to an accurately inphase rectangular wave is shown in figure 2. The basic elements consist of amplifier Q_3 of large gain, and feedback diodes CR_3 and CR_4. These work in the following way: An input signal applied to the base of Q_3 is greatly amplified until the collector output voltage breaks down the forward resistance of either diode CR_3 or CR_4. Above this breakdown voltage, any increase in the collector voltage is fed back to the base input of Q_3. The large negative feedback sharply reduces the gain of the amplifier. The action of Q_3 and Q_4, which results in a clipped wave, is symmetrical for positive and negative input signals. Since the gain of Q_3 is large, the breakdown occurs abruptly soon after the input voltage departs from zero. Consequently, the diode

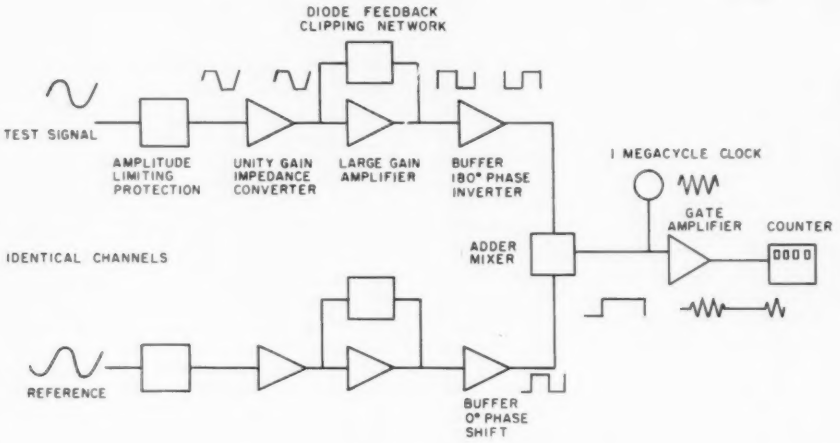

FIGURE 1. *Block diagram of phasemeter.*

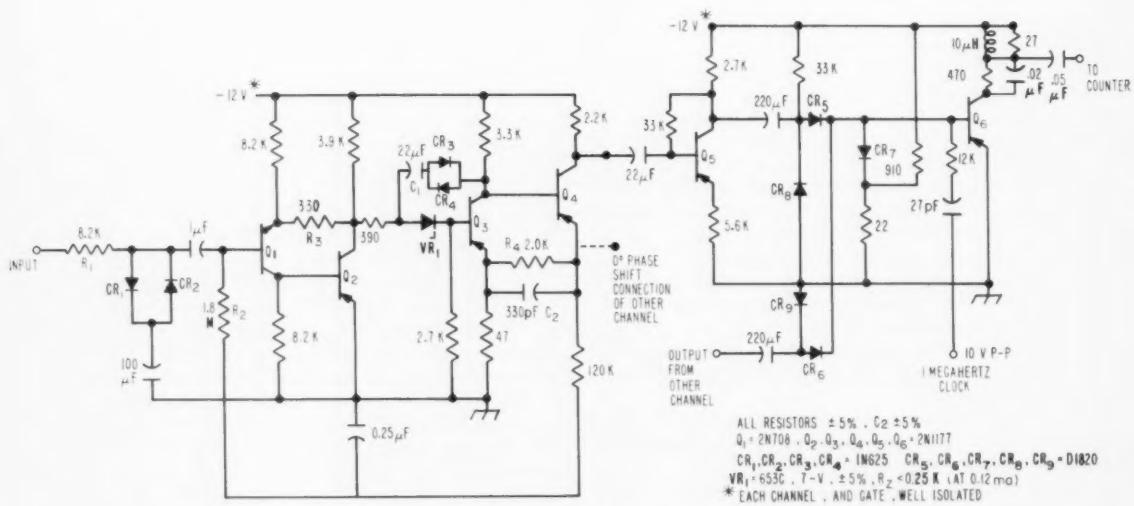

FIGURE 2. *Schematic pf phasemeter (one shaper channel shown).*

characteristics may differ somewhat without delaying the clipping action. The large negative feedback during breakdown prevents Q_3 from saturating or cutting off, avoiding transistor storage and delay problems. (The use of nonlinear devices as feedback elements in an operational amplifier is illustrated by Greenwood, I.A., et al. [3].)

The rest of the circuitry performs as follows: A portion of the signal from the output of Q_3 is returned to the input of Q_3, through Q_4, resistor R_4 and capacitor C_2. The feedback is positive and controlled so that the gain of Q_3 is large yet stable. C_2 opposes the "Miller effect" capacitance shunting the input of Q_3. The resulting speedup in the vertical rise of the clipped wave at high frequencies sharpens the gating action. A reduction of high frequency phase shift also occurs. The low source resistance coupling Q_2 to Q_3 minimizes this phase shift. The negative feedback through R_3, which lowers the source of resistance of Q_2, also raises the input resistance of Q_1 to several megohms shunted by R_2. The input capacitance of the unity gain amplifier Q_1–Q_2 is less than 10 pF.

The phase shift introduced by each channel is negligible in the midfrequency range, but increases at the extreme of the range for which the metering circuit is designed. This error may amount to a fraction of a degree at 20 Hz and at 20 kHz. However, as both channels are nominally identical in components, the relative phase error between the channels is much smaller.

The positive portions of the rectangular waves obtained from each channel are combined at the diode mixer CR_7. Diodes CR_5 and CR_6 are slightly forward biased so that small positive signals are readily transmitted to the mixer. The negative portions of the clipped wave from either channel are not transmitted. This prevents a negative signal from interfering by cancellation with the gating action of a positive signal. Thus, slowly rising high frequency pulses cause gating at their start with little delay. The positive rectangular pulses developed across CR_7 drive gating amplifier Q_6 to cutoff. The gated series of 1 MHz pulses is subsequently taken from the collector junction of Q_6 when the gate is open.

Each channel is protected from overload by diodes CR_1 and CR_2. Series resistor R_1 limits the amount of current through these diodes and tends to isolate the input signal source. R_1 is sufficiently small so that the attenuation and phase shift associated with it are unimportant. When diodes CR_1 and CR_2 break down, they may have a loading effect on the source. Greater isolation of the source from this loading effect may be desired. This would be desirable, for instance, when making simultaneous phase and voltage measurements of the source. A cathode follower or Darlington amplifier inserted ahead of R_1 provides sufficient isolation.

Phase measurements become independent of even order harmonics if minor changes are made in the circuitry of figure 2. Diodes CR_3 and CR_4 may be connected directly rather than through C_1 to the collector output of Q_3. This makes the pulse width of the clipped wave a function of the d-c voltage at the collector. R_2 is adjusted so that the diodes break down symmetrically. Without compensation, even harmonics may cause unsymmetrical clipping. Figure 3 indicates a composite input wave with unequally spaced zero crossings resulting from the presence of an even order harmonic. The corresponding clipped wave has unequal positive and negative portions. The d-c error component caused by this inequality is returned to the input of Q_1 through R_2 as negative feedback. This gives rise to a corrective voltage drop developed across CR_3 and CR_4. This voltage drop shifts the triggering level so that the clipping is symmetrical. Consequently, the phase shift due to the even order harmonic is corrected.

If odd harmonics are present, no correction occurs. In this case (fig. 4) the zero crossings of the composite wave are shifted uniformly in the same direction, so that the positive and negative portions of the wave are equal. As a result, there is no d-c component to restore the phase.

Occasional readjustment of R_2 is required with C_1 removed, because of the tendency of the diode voltage to drift. This tendency can be controlled, if the d-c error component resulting from drift is amplified before returning as feedback to Q_1.

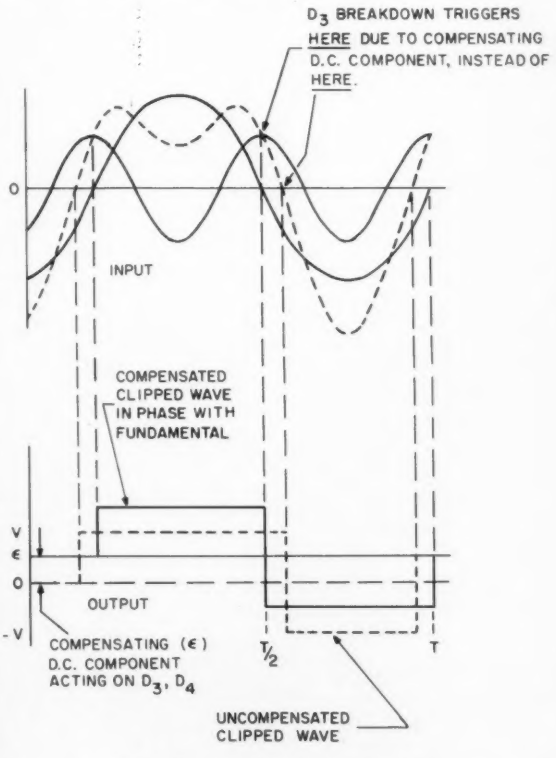

FIGURE 3. *Zero phase of clipped wave with compensation of phase shift due to 2d harmonic.*

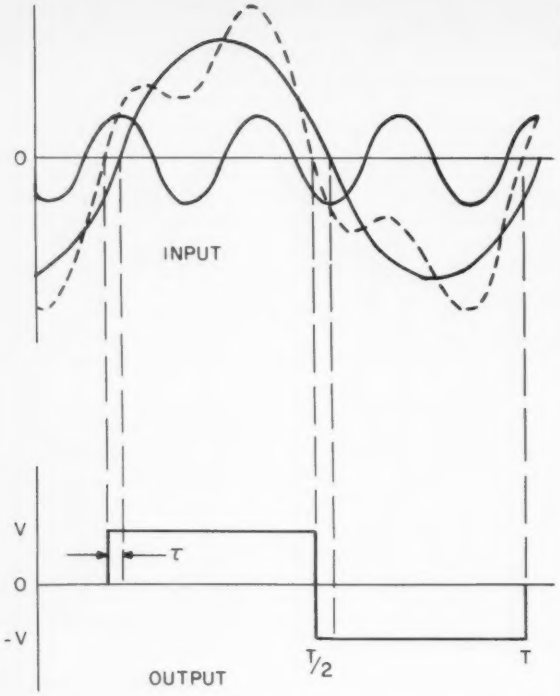

FIGURE 4. *Phase shift* (τ) *of clipped wave due to 3d harmonic.*

Although good accuracy is obtained with non-critical general purpose components, improvement can be made by the use of faster-acting diodes and transistors. Their faster rise times should produce sharper gating with less delay.

References

[1] V. O. Arutynov, Circuit of a compensation instrument for measuring the phase difference between two voltages, Izmeritel'naya Tekhnika **11,** 27 (Nov. 1963).

[2] Y. P. Yu, Coincident slicer measures phase directly, Electronics, P. 99 (Sept. 12, 1958).

[3] I. A. Greenwood et al., Electronic Instruments Radiation Laboratory series **21,** ch. 5 (McGraw-Hill Book Co., Inc., New York, N.Y., 1948).

(Paper 68C4–167)

JOURNAL OF RESEARCH of the National Bureau of Standards—C. Engineering and Instrumentation
Vol. 68C, No. 4, October–December 1964

Active and Passive Direct-Reading Ratio Sets for the Comparison of Audio-Frequency Admittances

Robert D. Cutkosky

(July 17, 1964)

Design considerations and constructional details for two audio-frequency direct-reading ratio sets are presented. These devices allow the comparison of admittances with accuracies up to one part in 10^7. The first direct-reading ratio set (DRRS) is based upon operational amplifier circuitry, and utilizes a two-stage amplifier system. With this technique, only a moderate voltage amplification per stage is required, and the circuitry is therefore not difficult to stabilize to prevent oscillation. The second DRRS is purely passive and makes use of two-stage voltage transformers to reduce the detrimental effects of transformer excitation current upon the linearity and ratio stability of the device. Equivalent circuits representing the behavior of critical parts of the two direct-reading ratio sets are presented and analyzed. A convenient procedure for calibrating a DRRS is treated mathematically.

1. Introduction

For many years direct-reading ratio sets have been used extensively for the most precise comparisons of d-c resistances. The extension of the direct-reading ratio set (DRRS) principle to audio-frequency bridges is a logical step, but one which is, unfortunately, somewhat difficult to achieve. The principle complication results from the necessity of providing the a-c ratio with both in-phase and quadrature adjustments.

Two types of a-c DRRS constructed at NBS are described here. The first type (sec. 2 of this paper) is based upon operational amplifier circuitry. The use of active networks in bridges is not new, and has been seen in various forms in both special purpose and commercial bridges [1, 2].[1] Our application called for considerably higher accuracy than was attained in the above cited references, and required the development of special circuitry with high effective loop gains.

Experience with the active DRRS indicated that the bridge circuit was more dependent upon oscillator waveform than had been anticipated. It was found that limiting the active circuit input voltage was necessary to secure satisfactory operation. A completely passive DRRS is described in sec. 3 of this paper. The passive device is much more linear and reliable than the active circuit and was constructed to meet our anticipated need for routine admittance comparisons at a fixed frequency, with precisions up to one part in 10^9 for admittances between 10^{-8} and 10^{-5} mhos.

The actual mathematics of a-c direct-reading ratio sets is merely a complex version of the mathematics associated with their d-c prototypes [3]. An analysis of some calibration problems is included in sec. 4 of this paper.

2. Active Circuit

The active networks to be described in this section are all modifications and extensions of the operational amplifier circuit of figure 1. An analysis of this circuit yields the equation

$$e_0=-e_s\frac{Y_1}{Y_2}\times\frac{1}{1+\dfrac{(1+Y_2R+Y_s'R)(Y_d+Y_1+Y_2)}{(A-Y_2R)Y_2}}. \tag{1}$$

If the amplification A is very high, eq (1) reduces to

$$e_0\approx-e_s\frac{Y_1}{Y_2}. \tag{2}$$

[1] Figures in brackets indicate the literature references at the end of this paper.

741-635—64——3

The desirable features of this network are the following:

(1) The device generates a voltage e_0 which is proportional to an input e_s and depends only slightly upon the active circuit parameters.

(2) The proportionality constant is essentially the ratio of two three-terminal admittances, may be real or complex, and may be made to exhibit a high order of stability.

(3) The circuit input admittance is approximately equal to Y_1+Y_s. If it is made small enough, the source e_s will not be strongly loaded.

(4) The circuit output impedance is usually quite low; a calculation yields $Z_{out} \approx \frac{R(Y_1+Y_2+Y_d)}{AY_2}$. Reasonable loads may therefore be driven by the device, with no appreciable change in e_0.

The circuit of figure 1 may be modified as in figure 2 to accommodate two inputs. The usual superposition arguments may be used to relate the behavior of this circuit to eqs (1) and (2). The case in which

$$Y_2=Y_1=-jY_1' \tag{3}$$

is of particular interest. Then, given sufficiently high amplification,

$$e_0=-e_s-je_s'. \tag{4}$$

A bridge for comparing two admittances Y_3 and Y_4 is shown in figure 3. The bridge features a phase splitting transformer, T_1, and two decade transformers to allow operation in all four electrical quadrants. If K_1 and K_2 are the decade transformer readings when the bridge is balanced, we find in the limit as $A\to\infty$

$$Y_4=2Y_3[(K_1-0.5)+j(K_2-0.5)]. \tag{5}$$

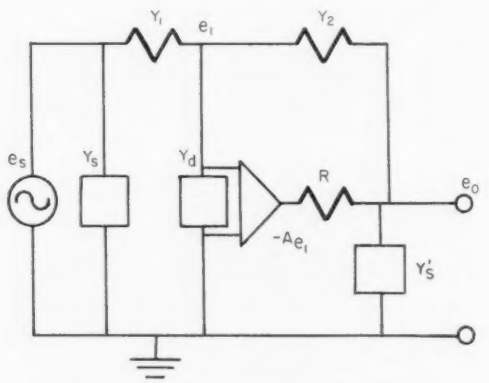

FIGURE 1. *Basic operational amplifier circuit.*

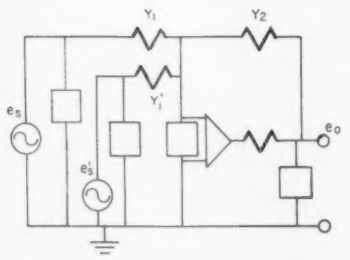

FIGURE 2. *Double-input operational amplifier circuit.*

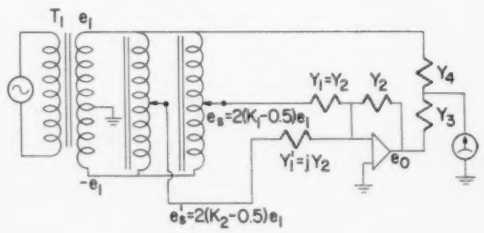

FIGURE 3. *Generalized admittance bridge.*

A DRRS may be produced from the circuit of figure 3 by adding a small fraction of the operational amplifier output voltage, e_0, to the voltage of a three winding bridge transformer by means of a step-down transformer as in figure 4. The resultant system behaves like a bridge transformer whose ratio may be varied over a small range by varying K_1 and K_2. The stepdown transformer may be a simple two winding transformer, but in this case the voltage ratio will differ from the turns ratio due to primary winding resistance and excitation current. The voltage ratio will then be slightly voltage dependent and unreliable. A better system uses a three winding transformer with the amplifier feedback admittance driven by one of the secondary windings. The other secondary winding then provides a highly accurate voltage which is added to the voltage of the bridge transformer.

Amplifier stability is one of the most difficult problems likely to be encountered in the construction of active systems such as figure 4. In order to make the amplifier output accurate to about one part in 10^5, the amplifier must have a loop voltage amplification of about 10^5, or a power gain of 100 dB. Although this could probably be done with a single amplifier, a two-stage amplifier system, illustrated with a single input in figure 5, was found to be easier to stabilize. A calculation indicates that with the two-stage circuit, the first amplifier of amplification A_1 produces an output e_1 with a proportional error in the order of $\left(1+\frac{1}{A_1}\right)$. This is corrected by the second amplifier of amplification A_2 to yield an output with a proportional error in the order of $\left(1+\frac{1}{A_1A_2}\right)$. Roughly, then, one may make use of two amplifiers with voltage amplification of 300 to replace one amplifier with a voltage amplification of 100,000.

The final version of the circuit in use at NBS is drawn in figure 6. Photographs of the completed unit appear in figures 7 and 8. Some difficulty was experienced in stabilizing the circuit for all seven tuned frequencies, but these problems were solved using conventional techniques. The circuit is in no sense to be considered an optimum design, but merely as one way of making the system work. The critical admittances are maintained in a constant temperature enclosure and are individually adjusted with suitable shunt, series, or "T" networks using the criteria of section 4. These networks may take the form of figure 9.

The circuit of figure 6 has been in use for about two years, principally at 1592 hertz. It has been found to be remarkably stable, and has required no maintenance other than replacement of tubes. It has proved reliable to a part in 10^5 provided that the input voltage does not exceed 0.2 V rms. If higher voltages are applied to the amplifier input, the bridge balance may depend upon oscillator harmonic content, the active device filtering action, and detector or active network nonlinearity. These limitations greatly restrict the usefulness of the device, but could possibly be reduced by redesigning the amplifiers. The existing circuit has proved to be highly useful for development work requiring a wide range but only low accuracy; and when used in the DRRS circuit, has been proved reliable to an accuracy of 1 part in 10^9.

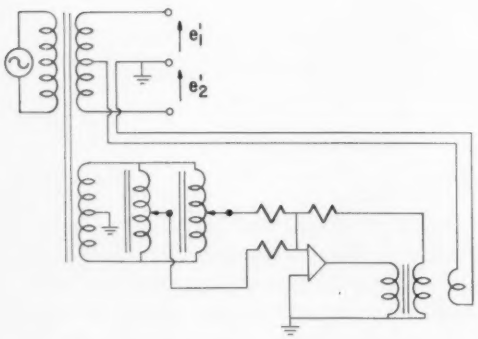

FIGURE 4. *Active direct reading ratio set.*

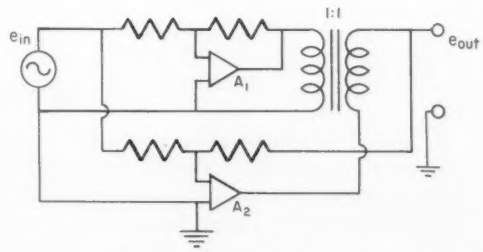

FIGURE 5. *Double operational amplifier circuit.*

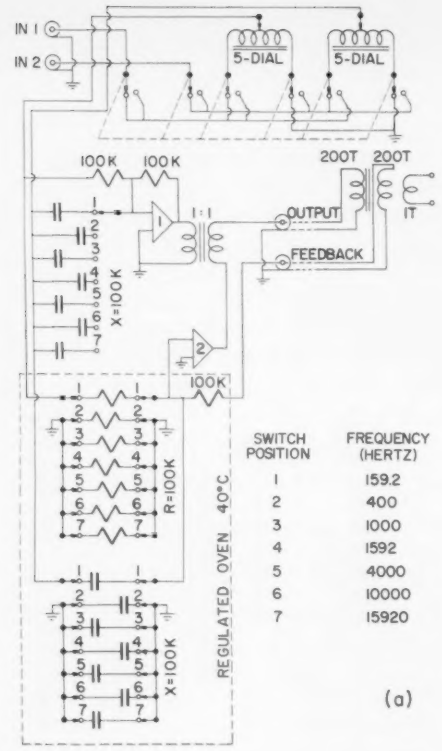

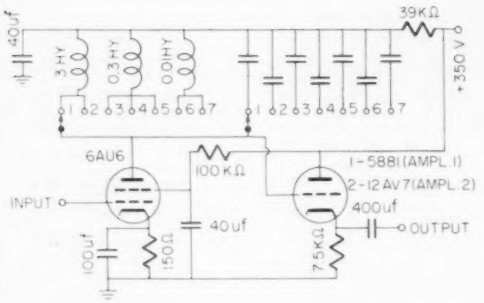

FIGURE 6. *Practical two-stage, double-input, operational amplifier circuit.*

(a) General arrangement and switching.
(b) Electronic circuits.

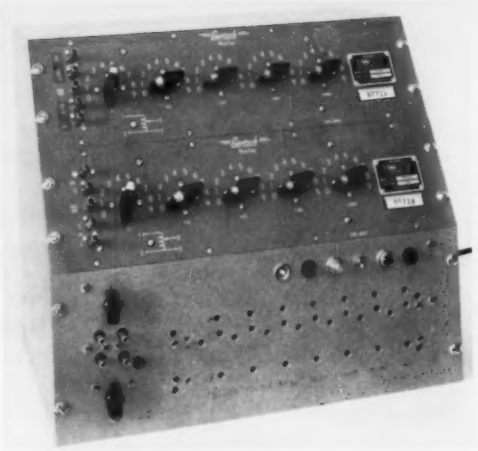

FIGURE 7. *Front view of operational amplifier.*

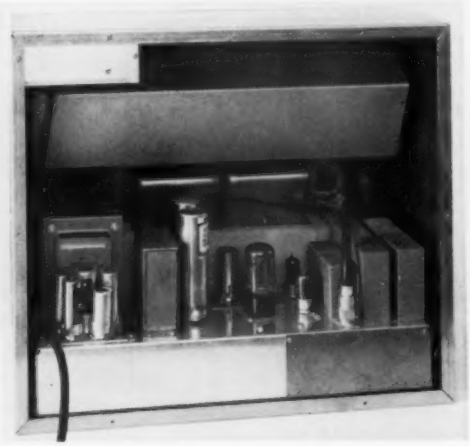

FIGURE 8. *Rear view of operational amplifier.*

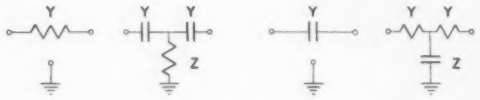

FIGURE 9. *Typical admittance trimmer circuits.*

From left to right: positive real, negative real, positive imaginary, and negative imaginary. Valid for $|YZ| \ll 1$ where applicable.

3. Passive Circuit

All of the functions performed by operational amplifiers in the previous section could have been performed manually by the use of a null detector in place of the amplifier input, and with an adjustable voltage source phase locked with the bridge oscillator in place of the amplifier output. A bridge based on such a system would be awkward to use, since it would require that simultaneous balances be obtained on two null detectors. The situation would be operationally similar to balancing a Schering bridge with a Wagner circuit.

Bridges with multiple balances are at times extremely useful, and can provide accuracies greater than can be obtained in any other way; but if they can be avoided, a great saving in time results. Since one of the prime advantages of direct-reading ratio sets is speed and ease of operation, a doubly balanced system defeats the whole purpose of the instrument.

Although operational amplifiers can provide a convenient alternative to doubly balanced bridges, most of the workers in precision electrical measurements cultivate a healthy disrespect for all active devices, including even null detectors. The drawbacks of active circuits are many and fairly obvious. They include limited dynamic range without distortion, susceptibility to failure with or without a visible sign of having failed, the inconvenience of having to supply power to the system, and the constructional difficulties of stabilizing a high gain feedback loop.

All of these reasons suggested that a passive DRRS requiring no auxiliary balances would be a most desirable instrument provided that it could be made stable and accurate. A preliminary investigation disclosed that, although a sufficiently accurate in-phase voltage ratio adjustment could be built, some trouble was to be expected with the phase angle adjustment.

One of the passive circuits investigated and eventually discarded is illustrated in figure 10. It was found that a combination of factors involving power dissipation in the resistors, nonlinearities in the various transformers, and the dependence of the decade transformer input and output impedances upon dial setting would have restricted the quadrature adjustment accuracy to about one part in 10^3 using readily available components. Since an overall least count of one part in 10^9 was required, the total phase angle adjustment could not have been greater than one part in 10^6, which was judged to be insufficient.

A technique involving a double circuit, one to provide a rough voltage and the other to correct it, was found to be capable of providing the desired range and accuracy. Prominent in the design is a device which may be called a two-stage voltage transformer by virtue of its similarity with the two-stage current transformer [4]. An understanding of two stage voltage transformers is necessary for the understanding of the complete DRRS, and will be dealt with first.

A generalized two stage transformer is represented in figure 11, based on ideal transformers and the usual transformer equivalent circuits [5].

A calculation yields

$$Ne_3=\frac{e_2\left(1+\frac{z_1}{Z}+\frac{z_1}{Z'}+\frac{z_2+z_2'}{Z'}\right)-\frac{z_2+z_2'}{Z'}(e_2-e_1)}{1+\frac{z_1}{Z}+\frac{z_1}{Z'}+\frac{z_2+z_2'}{Z'}+\frac{z_1(z_2+z_2')}{ZZ'}}. \tag{6}$$

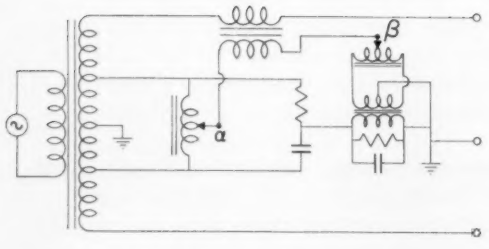

FIGURE 10. *Simple passive direct reading ratio set: α= in-phase adjustment, β= quadrature adjustment.*

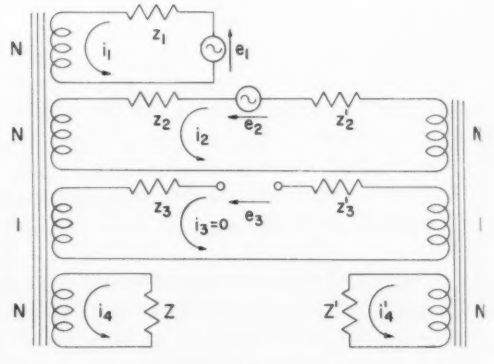

FIGURE 11. *Two stage voltage transformer equivalent circuit.*

If we let $e_2 - e_1 = \Delta e$, and neglect terms in the order of $\left(\frac{z}{Z}\right)^3$, $\Delta e \left(\frac{z}{Z}\right)^2$, and higher, we have

$$Ne_3 \approx e_2 \left[1 - \frac{z_1(z_2+z_2')}{ZZ'}\right] - \frac{z_2+z_2'}{Z'} \Delta e. \tag{7}$$

It follows that if one uses a common generator, so that $\Delta e = 0$, the device acts like a two winding transformer with a highly accurate primary to secondary ratio. Since the ratio of an ordinary transformer varies as $\left(1 - \frac{z}{Z}\right)$, quite large improvements can be expected.

Equation 7 also indicates that provided Δe is sufficiently small, e_3 is determined principally by e_2. A detailed analysis shows in addition that under no-load conditions, appreciably more current flows from generator e_1 than from generator e_2, leading to the conclusion that e_1 may be treated as a "rough" generator to supply excitation current to the two-stage transformer and to obtain approximately the desired output voltage. Generator e_2 then corrects this approximate voltage, and is itself only slightly loaded in the process. The two-stage transformer of figure 11 can be conveniently constructed as a composite unit, as indicated in figure 12a. This circuit will be represented in what follows by figure 12b.

The complete passive DRRS, figure 13, is a double version of the circuit of figure 10.

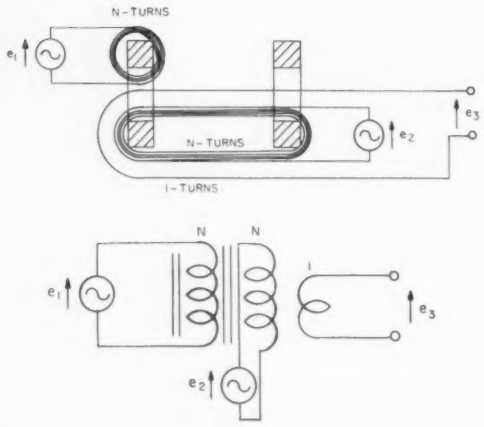

FIGURE 12. *Two stage voltage transformer.*
(a) Pictorial representative.
(b) Circuit symbol.

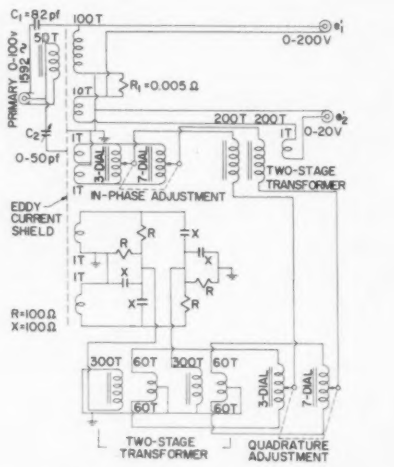

FIGURE 13. *Practical passive direct reading ratio set.*

The operation of this final version follows from the preceding discussion. The circuit was designed to yield an in-phase voltage ratio variation of ± 500 ppm and a phase angle variation of ± 50 μ radians. The overall voltage ratio accuracy, after the application of small corrections, was desired to be at least one part in 10^9.

The double system is applied in figure 13 to a nominally 10:1 transformer at a single fixed frequency, 1592 Hz ($\omega = 10^4$). Two views of the completed instrument appear in figures 14 and 15.

Each of the double decade inductive dividers appearing in figure 13 is a commercial 7-dial inductive divider modified by the addition of a 3-dial divider ganged to the first three switches. The added 3-dial divider is constructed with one small toroidal Supermalloy core, and need be no more accurate than 0.1 percent.

The resistors and capacitors of the "rough" and "good" quadrature sources are maintained

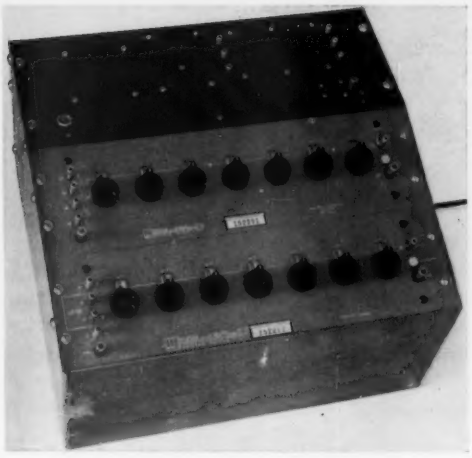

FIGURE 14. *Top view of passive direct reading ratio set.*

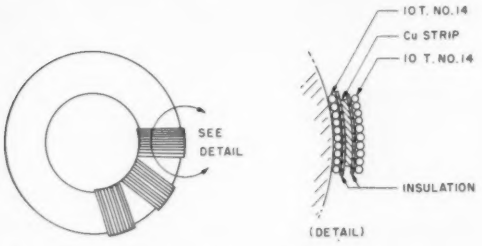

FIGURE 16. *Passive direct reading ratio set main transformer.*

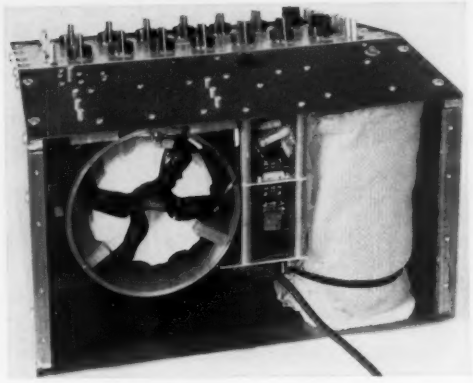

FIGURE 15. *Rear view of passive direct reading ratio set with cover removed.*

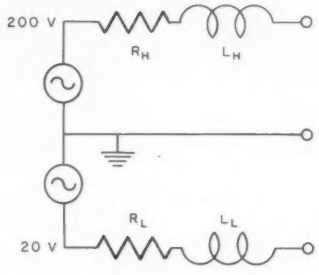

FIGURE 17. *Direct reading ratio set equivalent series impedances.*

in a constant temperature enclosure and are of a quality sufficient to ensure that the quadrature part of e_3 is stable to better than one part in 10^5. The magnitude and phase angle of e_3 are adjusted by trimming the appropriate resistors and capacitors of the networks with parallel combinations of small capacitors and large resistors.

The main transformer in figure 13 is constructed on a toroidal Supermalloy core of dimensions 4.5 in. o.d. x 3.25 in. i.d. x 1.5 in. high. A copper eddy current shield two skin depths (⅛ in.) thick between the primary and secondary windings reduces the magnetic fields in the region of the secondary windings caused by excitation current in the primary winding, and hence improves the accuracy of the secondary ratio.

The 100 turn secondary winding is constructed by first winding 100 turns of #14 wire as indicated in figure 16. A strip of copper is then wound directly over this to provide the 10 turn secondary winding. Following this, another 100 turns of #14 wire are wound, and connected in parallel with the first.

A measurement of equivalent series impedances for this transformer yields the circuit of figure 17 and the associated table 1. The relatively high resistance R_H is reduced by use of the resistor R_1 in figure 13. Although R_H could be easily made equal to zero or even negative by increasing R_1, this would be at the expense of increasing R_L. The choice of 0.005 ohm for R_1 represents a compromise based on the intended use for the DRRS.

TABLE 1. *The dependence of the DRRS output impedances upon* R_1 (*see fig. 17*)

$R_1=0$	$R_1=0.005$ ohm
R_H 0.085	0.035 ohm
L_H -2×10^{-6}	-2×10^{-6} H
R_L 0.005	0.010 ohm
L_L $+2\times10^{-7}$	$+2\times10^{-7}$ H

A final feature of the DRRS worthy of comment is the use of capacitors C_1 and C_2 to balance out the capacitance from the primary winding to the shield. The capacitive current that would otherwise flow through this capacitance could lead to the net flow of current from the oscillator to the bridge, and to ground through other paths. Such noncoaxial current paths are usually avoided by using two shields between primary and secondary transformer windings.

4. Calibration Procedures

The direct-reading ratio sets described above may be functionally represented by figure 18. Figure 18a may be called "common lead insertion," since the variable voltage e_3 appears in series with the main generators e_1 and e_2. This system was used with the active DRRS. Figure 18b may be called "single lead insertion," and was used with the passive DRRS. We have from the figure the relationships

$$\frac{e_1'}{e_2'}=\frac{e_1+e_3}{e_2-e_3} \text{ for common lead insertion,} \tag{8}$$

and

$$\frac{e_1'}{e_2'}=\frac{e_1}{e_2+e_3} \text{ for single lead insertion.} \tag{9}$$

If the instruments behaved ideally, we could write in both cases

$$e_3=e_2[M_1(K_1-0.5)+jM_2(K_2-0.5)] \tag{10}$$

where K_1 and K_2 are the readings of the "real" and "imaginary" inductive dividers, and M_1 and M_2 are the appropriate scale factors. The terms $(K_1-0.5)$ and $(K_2-0.5)$ occur because the circuit wiring makes $e_3=0$ when the inductive dividers are in the middle of their ranges, or read 0.5. Inserting eq (10) into eqs (8) and (9), we have

$$\frac{e_1'}{e_2'}=\frac{e_1}{e_2}\times\frac{1+\frac{e_2}{e_1}[M_1(K_1-0.5)+jM_2(K_2-0.5)]}{1-[M_1(K_1-0.5)+jM_2(K_2-0.5)]} \tag{11}$$

for common lead insertion and

$$\frac{e_1'}{e_2'}=\frac{e_1}{e_2}\times\frac{1}{1+M_1(K_1-0.5)+jM_2(K_2-0.5)} \tag{12}$$

for single lead insertion.

The first form is rather peculiar because of the second order dependence of $\frac{e_1'}{e_2'}$ upon the K's. The principal advantage of the common lead insertion method seems to be in the construction of multiple bridges involving more than two equivalent generators, and in 1:1 bridges ($e_1\approx e_2$) for which the resulting symmetrical form of equation 1 may be desirable. The discussion to follow will center around the single lead insertion technique because of its simplicity and its similarity to d-c direct-reading ratio sets. Most of the results may be readily adapted to the common lead insertion technique.

A great many possible deviations from the ideal eq (12) are possible. A strict and unambiguous calibration would require that e_2'/e_1' be measured for every possible combina-

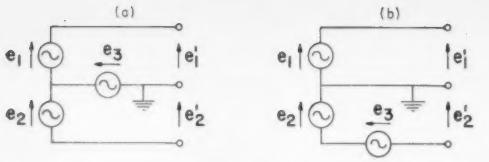

FIGURE 18. *Direct reading ratio set functional representation.*

(a) Common lead insertion.
(b) Single lead insertion.

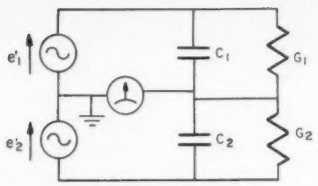

FIGURE 19. *Bridge circuit.*

tion of dial settings. A less time-consuming approach is to assume initially that eq (12) is "almost" true, and then to hunt for small discrepancies as K_1 and K_2 are systematically varied. Certain errors may conceivably remain undetected under these conditions, but if care is taken to investigate many combinations of dial settings the likelihood will be quite small.

Consider the bridge circuit of figure 19, for which the balance condition is

$$\frac{e'_2}{e'_1}=\frac{j\omega C_1+G_1}{j\omega C_2+G_2}\equiv\frac{Y_1}{Y_2}. \tag{13}$$

Inserting eq (9) we obtain $\frac{Y_1}{Y_2}=\frac{e_2+e_3}{e_1}$. If Y_1 is changed by ΔY_1, then $\frac{\Delta Y_1}{Y_2}=\frac{\Delta e_3}{e_1}$. By increasing ΔY_1 in known increments we may determine whether or not e_3 is a linear function of K_1 and K_2. In practice it may be convenient to insert first a group of equal capacitances in parallel with C_1, and then to insert a group of equal conductances.

If e_3 is indeed a linear function of K_1 and K_2, then eq (12) follows immediately; but M_1 and M_2 may be complex. If e_3 is nonlinear, then special techniques must be developed to account for the nonlinearity. The nonlinearity may be of simple form; for example, it may have a second power dependence upon K_1 and K_2, or the nonlinearity may be describable with an additive correction to the first dials of the inductive dividers.

Let us assume that the instrument has passed the linearity test, so that eq (12) holds. Then if $M_1=m_{11}+jm_{12}$ and $M_2=m_{22}+jm_{21}$ where the lower case m's are real, N equal to the nominal ratio, and finally, if K_1° and K_2° are the values of K_1 and K_2 for which $\frac{e'_2}{e'_1}=N$, we may expand eq (12) to yield

$$\left.\begin{aligned}
&\frac{e'_2}{e'_1}=N\,\frac{1+M_1(K_1-0.5)+jM_2(K_2-0.5)}{1+M_1(K_1^\circ-0.5)+jM_2(K_1^\circ-0.5)}\\
&\frac{e'_2}{e'_1}\approx N[1+M_1(K_1-K_1^\circ)+jM_2(K_2-K_2^\circ)]\\
&\frac{e'_2}{e'_1}\approx N[1+(m_{11}+jm_{12})(K_1-K_1^\circ)+j(m_{22}+jm_{21})(K_2-K)_2^\circ]
\end{aligned}\right\} \tag{14}$$

The terms K_1° and K_2° are the components of the complex "zero" reading so familiar to users of d-c direct-reading ratio sets. They need not be known if the instrument is used only for direct substitution measurements, but must be measured, for example, if the DRRS is used to step up from small to large admittances. Methods for measuring K_1° and K_2° directly may be obtained by slightly modifying the results of a previous paper [6].

The determination of m_{11}, m_{12}, m_{21}, m_{22} may be performed with the aid of eqs (13) and (14). Balancing the bridge initially as in figure 19, we write

$$\frac{j\omega C_1+G_1}{j\omega C_2+G_2}=N[1+(m_{11}+jm_{12})(K_1-K_1^\circ)+j(m_{22}+jm_{21})(K_2-K_2^\circ)]. \tag{15}$$

Adding in succession two admittances, first $j\omega\Delta C_1'+\Delta G_1'$ and then $j\omega\Delta C_1''+\Delta G_1''$, we have, upon subtracting eq (15),

$$\left.\begin{aligned}\frac{j\omega\Delta C_1'+\Delta G_1'}{j\omega C_2+G_2}&=N[(m_{11}+jm_{12})(K_1'-K_1)+j(m_{22}+jm_{21})(K_2'-K_2)]\\ \text{and}\\ \frac{j\omega\Delta C_1''+\Delta G_1''}{j\omega C_2+G_2}&=N[(m_{11}+jm_{12})(K_1''-K_1)+j(m_{22}+jm_{21})(K_2''-K_2)]\end{aligned}\right\}, \tag{16}$$

from which, if $\dfrac{j\omega\Delta C_1'+\Delta G_1'}{j\omega\Delta C_1''+\Delta G_1''}$ is not real, the m's may be determined.

It is expected that normally $G_2<<\omega C_2$, $\Delta G_1'<<\omega\Delta C_1'$, $\Delta G_1''>>\omega\Delta C_1''$, $m_{12}<<m_{11}$ and $m_{21}<<m_{22}$, so that

$$m_{11}\approx\frac{\Delta C_1'}{NC_2}\times\frac{1}{K_1'-K_1},$$

$$m_{12}\approx\frac{\Delta G_1''(K_2'-K_2)}{N\omega C_2(K_1'-K_1)(K_2''-K_2)}-\frac{\Delta G_1'}{N\omega C_2(K_1'-K_1)},$$

$$m_{22}\approx\frac{-\Delta G_1''}{N\omega C_2}\times\frac{1}{K_2''-K_2}$$

and

$$m_{21}\approx\frac{\Delta C_1'(K_1''-K_1)}{NC_2(K_1'-K_1)(K_2''-K_2)}-\frac{\Delta C_1''}{NC_2(K_2''-K_2)}.$$

The problem is thus reduced to determining the complex ratios of admittances, where only a very modest accuracy is required.

5. References

[1] N. L. Kusters and O. Petersons, A Transformer-ratio-arm bridge for high-voltage capacitance measurements, IEEE Trans. on Communications and Electronics, No. 63–168, **69,** 606 (1963).

[2] H. P. Hall and R. G. Fulks, The use of active devices in precision bridges, Electrical Engineering **81,** 367 (1962).

[3] Paul P. B. Brooks, Calibration procedures for direct-current resistance apparatus, NBS Mono. 39 (1962).

[4] H. B. Brooks and F. C. Holtz, The two-stage current transformer, AIEE Trans. **41,** 383 (1922).

[5] A. M. Thompson, The precise measurement of small capacitances, IRE Trans. on Inst. **I–7,** Nos. 3 and 4, 245 (1958).

[6] R. D. Cutkosky and J. Q. Shields, The precision measurement of transformer ratios, IRE Trans. on Inst. **I–9,** No. 2, 243 (1960).

(Paper 68C4–168)

JOURNAL OF RESEARCH of the National Bureau of Standards—C. Engineering and Instrumentation
Vol. 68C, No. 4, October–December 1964

Review of Methods for the Excitation of Atomic and Ionic Spectra by Means of High-Frequency Discharges and Sliding Sparks

Lennart Minnhagen [1]

(May 26, 1964)

Two groups of excitation techniques useful for the production of ionic spectra are reviewed, namely high-frequency excitation and the sliding spark. The development of the arrangements is described and their characteristics given as regards power generation, electrodes, and spectroscopic features. The ionization stages obtained by each method of excitation are considered.

1. Introduction

The development of appropriate sources for the excitation of atomic and ionic spectra is a fundamental task in atomic spectroscopy. The demands on the sources are, generally speaking, that they should produce the actual spectra with a high degree of completeness, with the best possible line quality, and, as far as possible, free from impurities. Further, the sources should make it possible to decide from which ionization stage the spectrum lines originate. The required sharpness of the lines depends on the character of the investigation. Obviously the greatest possible reduction of the line width—caused by Doppler effect, collisions, Stark effect etc.—is necessary for the determination of highly accurate wavelengths and for the investigation of hyperfine structure by means of high-resolution spectroscopy, while the demands for sharpness are much less in some kinds of straightforward analytical work. It is sometimes an advantage to have excitation conditions which give observable Stark-effect broadenings, since the broadenings depend on the quantum properties and energies of the levels involved and thus facilitate the analysis. Analogously, light sources giving rise to strong self-reversal are inappropriate in some investigations, whereas they may be advantageous in the analysis of a spectrum.

In the present review two groups of sources useful for the production of spectra of low and medium ionization stages will be treated, namely high-frequency excitation and the sliding spark.

2. High-Frequency Excitation

The method of exciting spectra by means of a high-frequency discharge is quite old. Up to about 1930, spark-generated high-frequency oscillations, which are strongly damped, were used almost exclusively for exciting spectra; more recently the enormous progress in the field of transmitter technique has made possible the excitation of spectra by means of continuous oscillations, even in the form of pulsed oscillations, over a very wide frequency range.

As regards the transfer of high-frequency power to the contents of the discharge tube, four experimental arrangements are utilized:

1. Internal electrodes
2. External electrodes
3. Coil surrounding the discharge tube
4. Discharge tube in a cavity resonator.

Some examples of typical experimental arrangements and their excitation properties are given below.

2.1. Spark-Generated Oscillations

a. Internal Electrodes

The original method for generating high-frequency oscillations is to use a circuit consisting of a condenser, a coil, and a spark gap, and feeding it by a-c or d-c high voltage. Along these lines de Bruin [1, 2][2] and Humphreys [3], among others, have worked with much success on the spark spectra of the inert gases. In a typical coupling de Bruin used a 0.02-μF oil condenser in the HF circuit fed from a 25-kV transformer which in turn was connected to the a-c mains via a variable transformer. The discharge tube was of the Geissler type with a quartz capillary 10 cm long and with a $\frac{3}{4}$ mm inner diameter. The hollow aluminum electrodes were connected to the coil. In one of his papers on the spark spectra of neon, de Bruin [1] reports that the highest intensity was obtained in the capillary at a rather high pressure, namely 2 cm Hg. The following ionization stages have been attained: Ne VI [4], Ar IV [5], Kr IV [6], Xe IV [7]. The association of the various lines of a spectrum with the different ionization stages may be done by variation of the charging voltage and the inductance. There seem, however, to be some difficulties in distinguishing the higher ionization stages.

[1] On leave of absence from Lund Institute of Technology, Lund 7, Sweden.

[2] Figures in brackets indicate the literature references at the end of this paper.

Drawbacks of this excitation method are that the electrodes can give impurity lines; further, the inner walls of the narrow capillary are attacked, particularly at high excitations and, under certain circumstances, a quartz capillary can give an impurity spectrum which is dominating and which masks the lines of the element under investigation, over extended wavelength ranges.

b. Electrodeless Discharge

One of the first to investigate the spark-generated electrodeless high-frequency discharge was J. J. Thomson [8]. This type of discharge was later used for the excitation of spectra. The high-frequency oscillations may be generated as described in the previous section. A large number of spectroscopic investigations have been carried out by this method, the pioneer work being to a great extent due to E. and L. Bloch and their co-workers. In a typical experiment [9] they used a quartz or Pyrex discharge tube having a length of 20 cm and a diameter of 30 mm—in other cases they have used shorter tubes. The tube is surrounded by a coil containing 10 to 12 turns of 1.5-mm copper wire. The coil, a condenser, and a spark gap form a high-frequency circuit which is fed from a high-voltage transformer working at 42 c/s. A high-frequency of about 400 kc/s was used in investigating the spark spectra of mercury; in obtaining the spark spectra of Ar, Kr, and Xe, gas pressures of 0.6, 0.3, and 0.9 torr (mm Hg), respectively, were used [10]. The so-called electrodeless ring discharge obtained in this way has the important property of permitting the separation of spectra from different ionization stages with some certainty, since the ionization stage excited is a function of the coordinates of the ions. If the common axis of the discharge tube and the coil coincides with the axis of a spectrograph (end on observation), then the spectrum appears as follows when a stigmatic spectrograph is used: At a certain breakdown voltage, depending on the dimension of the spark gap, certain lines have an intensity which does not vary much along the line or which is strongest at the center; they emanate from neutral atoms. Other lines indicate low intensity at the axis of the discharge tube and increasing intensity towards the walls of the tube; they are emitted by ionized atoms. The separation of different ionization stages is based mostly on a study of the intensity distribution along the lines. An increased spark gap, which means an increased breakdown voltage, results in a decreased intensity at the ends of the arc lines, the intensities of which are more and more concentrated at the center of the lines, whereas the spark lines get stronger towards the ends of the lines. At sufficiently strong excitations, new "short" lines appear, apparently emitted by higher ionized atoms near the walls of the discharge tube. The authors report that they have been able to a great extent to separate Hg II–IV, Ne II–III, Ar II–IV, Kr II–IV, Xe II–IV, etc. Impurity lines often show characteristic features by means of which they can be recognized.

Boyce's [11–14] well-known investigations of the spark spectra of the inert gases in the vacuum ultraviolet were performed by means of electrodeless high-frequency excitation; he has attained the following ionization stages: Ne IV, Ar V, Kr IV, Xe IV. It should be noticed, however, that the lines observed for the highest ionization stages are those most easily excited, namely the combinations of the lowest excited levels with the ground term. Since the measurements are confined to the vacuum ultraviolet the observations tell little about the excitation of levels of high angular momentum.

A similar excitation method was used by Eriksson [15] in investigating N II. The quartz discharge tube, 18 cm long and with a central cylindrical part having 15 mm inner diameter, was surrounded by a coil made of silvered copper wire. With a 0.007 μF capacitor the frequency was about 700 kc/s. In some experiments a 0.014 μF capacitor was used. The optimum conditions for developing the N II spectrum were obtained at a nitrogen pressure of 0.05 to 0.07 torr—which was found to be rather critical—and a spark voltage of 24 to 36 kV. The admission of helium to the discharge tube was found to bring about an increased excitation along the axis of the tube, particularly in its central part. The discharge in the nitrogen-helium mixture gives N II lines which have nearly the same intensity along the lines, whereas the N I lines are weak at the center and the N III lines have strong central parts. Thus the appearance of lines belonging to different ionization stages is reversed in relation to the one observed by L. and E. Bloch, but it is in accordance with that observed by Esclangon. From a spectroscopic point of view the important feature certainly is that lines from different ionization stages have different characteristics.

The absence of electrodes contributes to the purity of the spectrum. Further, since high intensities can be obtained even in a wide discharge tube, the walls are much less attacked than those of Geissler tubes with inner electrodes.

A particular form of excitation is the theta-pinch discharge. A light source, recently described by Beckasten, Hallin, Johansson, and Tsui [16], consists of a Pyrex tube 50 cm long, 6 cm in diameter, surrounded by a single turn loop through which a 6.6 μF condenser bank is discharged. The voltage can be chosen between 7 and 25 kV, and gas pressures between 0.006 and 0.025 torr have been used. A characteristic of the design is a low inductance, which means that fairly high ionization stages can be obtained; investigations of the O III–VI and the N III–VI spectra are in progress.[3]

2.2. Continuous Radiofrequency Oscillations and High-Frequency Pulses

By means of modern transmitter technique it is possible to generate high-frequency oscillations over a very large frequency and power range. Continuous oscillations as well as high-frequency pulses are useful for the excitation of spectra.

[3] Spectroscopic features of the large installations for the production of magnetically compressed plasma are not within the scope of the present review.

Among early investigations with continuous wave oscillators, the work of Esclangon [17] should be mentioned. With a 6-kV anode voltage on the final tube, 3 kW could be generated at frequencies between 2 and 6 Mc/s. The commercial therapeutical apparatus used by Gatterer and Frodl [18] has 600 W power at frequencies between 40 and 100 Mc/s. At frequencies of the above magnitude, the high-frequency power can be transferred to the contents of the discharge tube either by outer electrodes in contact with the outer walls of the discharge tube or by a coil surrounding it. In the former case a displacement current appears in the tube. The current density is, however, low at radio frequencies, if the cross section of the tube is large. For ordinary spectroscopic purposes the transfer by means of a coil is suitable. Although the discharge process is complicated, it may be presumed that the dominating excitation is due to impact with electrons, which are accelerated in the high-frequency magnetic field generated in the coil. The electrons should, therefore, have a strong tendency to move in curved paths which are perpendicular to the axis of the surrounding coil. A careful investigation of the discharge process is needed from a spectroscopic point of view, since a better theoretical basis is required for the development of the high-frequency excitation sources.

The discharge can be maintained at low gas pressures in the tube, which contributes to the emission of sharp lines; in fact, the line quality can be good enough to allow interferometer measurements. The low pressure is also an advantage for work in the vacuum ultraviolet, in the wavelength ranges where no transparent windows exist; the leakage of gas through the slit is necessarily lower when the pressure in the discharge tube is low. Low pressures in the source and spectrograph are particularly required in investigating resonance lines of neutral atoms in order to limit self-reversal. The absence of electrodes contributes to a spectrum free from impurity lines. Continuous high-frequency oscillations give only low ionization stages; usually, the first spectrum, and—more or less complete—the second spectrum are excited. The excitation degree depends, of course, on the power transferred to the discharge and also on the nature of the atoms excited. Molecular spectra are easily excited, which means that the discharge tube and the circulating system must be clean and contain good cooling traps in order to reduce the appearance of impurity bands. Experience seems to indicate that in itself the frequency of the oscillations has no marked influence on the excitation. It might, however, have a secondary influence since its magnitude determines the dimensions of circuits, coils, etc., which, in turn, partly determine the transfer of power to the discharge tube. Since very large high-frequency powers can be generated in a modern continuous wave transmitter, very brilliant light sources can be obtained. The transfer of high-frequency power is limited by the effectiveness of the method of cooling the discharge tube. This cooling is usually done by forced air because of the difficulties of arranging liquid cooling in the high-frequency field. Water cooling is inappropriate since the high-frequency losses are large.

The increase of the excitation of the second spectrum relative to the first spectrum, and the excitation of higher ionization stages, requires higher instantaneous powers at a mean power which is limited by the cooling conditions. This may be done by running an oscillator intermittently. By means of pulsing, it is possible to increase the plate voltage of the transmitting tubes well above the normal values. The anode voltage is limited by the high voltage insulation and the anode dissipation. As a rule the insulation permits a plate voltage much higher than that recommended for continuous operation. If the mean power does not exceed the power at continuous operation, then the average plate dissipation will not exceed allowed values, in spite of the high instantaneous power. Provided that the anode voltage is not raised so much that the anode current attains its saturation value, the instantaneous high-frequency power will be proportional to the square of the anode voltage. The pulsing procedure was introduced into experimental spectroscopy fairly late. Self-oscillating devices were used by Goudet, Herreng, and Nief [19], as well as by Roig and Buret [20]. In the first case the 150-Mc/s oscillator was pulsed by anode voltage peaks and in the latter case the 20 Mc/s oscillator was grid-modulated at 500 c/s.

In a more elaborate arrangement described by Minnhagen and Stigmark [21], the oscillator is controlled by a pulse generator, which starts the oscillator at the beginning of a pulse and stops it at the end of the pulse. The oscillator frequency is multiplied and then fed into a driver which gives sufficient power for the final tube. Via a coupling link, the high-frequency power is transferred to a tuned circuit composed of a variable condenser and a coil surrounding the discharge tube. Various tube dimensions have been used; in some of the inert gas investigations the total length of the quartz tube was 19 cm with a central cylindrical part having 20 mm outer diameter. The pulse duration and the pulse frequency are adjustable within certain limits and the oscillator frequency between 7.8 and 9.6 Mc/s. With no pulse generator, the oscillator runs continuously. When the final tube runs continuously the anode voltage is 3 kV and the anode dissipation 450 W. For pulsed operation it is possible to increase the anode voltage to 9 kV at a pulse frequency of about 500 pulses per sec and a pulse duration of 400 μsec. The average power is about 550 W under these circumstances and the estimated instantaneous power 3 kW. Appropriate gas pressures for the excitation of the spark spectra of the inert gases were found to be 0.02 to 0.10 torr. The correct tuning of the electrical circuit associated with the discharge tube is important in order to get optimal loading, which means the transfer of large high-frequency powers to the contents of the discharge tube. In the case of argon the apparatus is able to excite Ar I, Ar II, and, partly, Ar III. By variation of the pulse power it is possible to separate,

with a high degree of certainty, Ar II—which is developed in a very complete way—from Ar I and Ar III. There is no perceptible variation of the intensity and the degree of ionization along a diameter of the discharge tube. When the oscillator is run continuously, Ar I and parts of the Ar II spectrum appear. During pulsed operation, the Ar I intensity decreases when the pulse power is increased, whereas the Ar II spectrum develops and gets stronger. Further, Ar III gets more complete and gains intensity in relation to Ar II. If a line is weak even at the highest pulse powers attainable with the oscillator, it may be difficult to decide whether it belongs to Ar II or to Ar III. This decision would require still higher pulse powers, which have been generated by means of 25-kW transmitting tubes [22, 23] run at 20-kV anode voltage (12 kV is recommended when they are run continuously). Because of the high d-c and rf voltages, special variable tubular condensers are required. One installation, containing a single final tube, has a high frequency which is adjustable around 9 Mc/s, a pulse frequency adjustable between 40 and 900 pulses per sec, and a pulse duration that can be chosen between 80 and 1000 μsec. It is a great problem to transfer the large pulse powers into the discharge tube; the best arrangement found is described in reference [22]. The high-frequency power is taken from the tank circuit of the power amplifier by means of a coupling coil and, via a coaxial conductor, fed to a separate tuning circuit containing a coil which surrounds the discharge tube. High quality insulations and large flashover distances are needed.

Another installation containing two final tubes in "push-push" coupling has an 18 Mc/s frequency but the doubled frequency has no marked influence on the excitation. Typical values of pulse duration and pulse frequency are 80 μsec and 40 pulses per sec.

The high pulse power oscillators have been used to excite spark spectra of the inert gases. The argon investigation is, as yet, the most advanced one and part of it was performed by means of the single tube installation. When Ar II, Ar III, and Ar IV are excited, the variation of the line intensity with the pulse power permits a decisive separation of the ionization stages. The Ar IV lines appear only at the highest pulse powers. The situation is similar for xenon. The excitation of the spark spectra of neon, on the other hand, is much more difficult. This may be due to several causes. One probably is that the Ne I, II, and III ionization potentials are larger than those for the heavier inert gases.

Lines due to impurities can usually be recognized since they show a variation in intensity with the pulse power which differs from that of the element under investigation. Sometimes it is useful to employ pulsed operation even to produce spectra of neutral atoms, namely in spectral ranges which contain impurity bands, since an increased high-frequency power means a decreased intensity of the band lines.

A new construction of a self-excited oscillator (Stigmark [24]) has been tested for the excitation of spectra. The oscillator contains an industrial tube with such characteristics that the tube will withstand very large variation in loading conditions without being damaged. The tube has been used in a tuned plate, tuned grid circuit in which the anode tank consists of a cavity tuned to 27.12 Mc/s. Because of the rather high Q value of the cavity, even under heavy loading conditions, the frequency shift of this type of oscillator is very small and can easily be kept within narrow frequency limits ($\pm 0.6\%$). The power is transferred from the cavity to an outer, tuned discharge-tube circuit by means of link coupling. The power is about 15 kW at the normal anode voltage of 6 kV, the anode efficiency being 60 percent. By means of pulse techniques and a raised anode voltage, the output pulse power may be increased considerably.

2.3. Electrodeless Microwave Excitation

The electrodeless excitation of spectra by radio frequencies above 100 Mc/s and by microwaves, often in the 2000 to 3000 Mc/s range, has been very successful. Under proper conditions, very sharp and unperturbed lines are produced, useful even for high-precision interferometric work. However, for very accurate wavelength determinations the sources should be used with some caution since there are indications that they may give shifts of higher excited levels [25, 26].

Since continuous microwave oscillations do not produce higher ionization stages they will not be discussed in the present review but reference given to some useful articles (Meggers and Westfall [27], Jacobsen and Harrison [28], Zelikoff et al. [29], Corliss, Bozman, and Westfall [30], Tomkins and Fred [31], Worden, Gutmacher, and Conway [32]).

3. Excitation by Means of Sliding Sparks

The excitation of higher spark spectra has to a great extent been performed by means of vacuum sparks, which can give very high ionization stages. Because of the large voltages and current densities necessary, the lines may be broadened and shifted through Stark effect and this is particularly true for levels with large azimuthal quantum numbers. In this respect the sliding spark, suggested by Vodar and Astoin [33], is superior, since it can be operated at lower voltage than the vacuum spark. In the original arrangement of Vodar and Astoin a spark is produced which slides along the surface of a carbon rod provided with two ring electrodes connected to a condenser charged to a 30-kV voltage. (For further developments by Vodar et al., see for example ref. [34].)

This idea was further developed by Bockasten [35, 36] for his investigation of C III and C IV. His arrangement, which is described in detail in reference [35], is essentially as follows. The source consists basically of two cylindrical graphite electrodes which are separated by a porcelain disk. The latter has a small bore along its axis through which the dis-

charge takes place. This confinement of the discharge brings about a large gain in intensity. The discharge is viewed through a radial channel in the porcelain disk. In order to get proper working conditions it is important that the end surfaces of the electrodes fit very well to the surfaces of the disk. The light source works well at 10^{-3} torr and at lower pressures. To control the working conditions it is necessary to have an external spark gap. The separation of different ionization stages is done by variation of the inductance in the spark circuit. The sliding spark works well even with a large inductance, which is not the case with the vacuum spark. Typical conditions for the excitation of C III and C IV are: external spark gap 1.5 to 4.5 mm with corresponding spark voltages 6 to 15 kV, spark frequency at 15 kV 6 to 8 sparks per second with a 0.3 μF capacitance. The sliding spark spectra contain lines from the electrodes as well as from the insulating disk between them. In his first paper Bockasten reports tests with various metal electrodes: Be, Al, Fe, Cu, and W and disks of quartz and various kinds of porcelain. Strong Si II-IV and O II-VI lines are produced by means of a quartz disk with appropriate metal electrodes.

The same arrangement was used by Toresson [37, 38], who produced Si III and Si IV by means of a quartz disk between silicon electrodes. Since silicon is a poor conductor at ordinary temperatures, the spark frequency is kept high enough to reach a temperature where the material becomes conducting. Boron also is a very poor conductor at temperatures below some hundreds of degrees centigrade. In order to produce the B III spectrum, Gunnvald [39] uses conducting electrodes prepared in the following way. A mixture of boron and aluminum powder is pressed in a mold and heated to a temperature above the melting point of aluminum. In combination with a quartz disk of Bockasten's design, these electrodes produced new B II and B III lines. The excitation of B III requires a high condenser voltage and a small inductance and this results in diffuse lines.

The sliding spark arrangement used by Sugar [40] to excite spectra of ionized rare earths, works at much lower voltage. The spark chamber contains helium at a pressure of 30 torr, and disks of the metal to be investigated serve as electrodes separated about 3 mm by a lavite spacer. The spark gap is in series with a 10 μF capacitor, a damping resistor, a rotating spark gap, and an inductor. With a 1000 V charging voltage and a 500 μH inductance a fully developed Pr III spectrum was obtained. With no inductor, the same charging voltage, and a suitable damping resistance, the Pr IV spectrum was enhanced. Critical damping was found to suppress Pr II better than an oscillatory discharge.

In order to separate Ce II from Ce III, Sugar [41] has used larger inductances—about 1000 μH—and lower voltages (down to 300 V), thus producing the Ce II spectrum and suppressing Ce III. The arrangements allow a very good separation of ionization stages.

Low-inductance sliding spark sources have been designed recently for the excitation of higher ionization stages [42], Bogen and Conrads [43] (containing further references) having obtained strong C V and C VI spectra. In these experiments the inductance is in the 5 to 20 nH range.

The use of the sliding spark is not limited to solid materials. It is also possible to excite gases by letting them in through a bore in one of the electrodes, in accordance with the arrangement used for vacuum sparks by Phillips and Parker [44]. This has been done by Toresson [45] and by Bockasten, Hallin, and Hughes [46]. The former has obtained spectra of S I–S VI and O I–O VI, and the most easily excited Kr VIII lines in the vacuum ultraviolet; the latter authors report the observation of a strong Ne IV and a weak Ne V spectrum.

4. Comparison Between High-Frequency Excitation and Excitation by Sliding Sparks

The high-frequency method can be used for the excitation of gases as well as of vapors from liquids and solids provided that the vapor pressure is sufficiently high at the working temperature of the discharge tube. The sliding spark method was originally developed for the excitation of solid materials but was later found to be suitable for gases and vapors as well. As regards high-frequency excitation, we will confine ourselves to the electrodeless discharge. High-frequency pulses from existing tube oscillators can produce the fourth spectra of argon, krypton, and xenon. Since the analysis is not finished it is not possible at the moment to tell to what completeness these spectra are developed. Boyce reports still higher ionization stages obtained by spark-generated oscillations, namely Ar V; as already pointed out, the observed Ar V lines are transitions to the ground term from the lowest excited states and so are those most easily excited. The excitation by means of sliding sparks gives still higher ionization stages—the eighth spectrum is reported in one case.

As regards line quality, a just comparison between the electrodeless high-frequency and the sliding spark methods would require the observation of the same lines by means of both methods and, preferably, with the same kind of high-dispersion spectrographs. In the absence of such careful observations, the comparison must be approximate. Experience from the investigation of ionized inert gases shows that high frequency pulses give very good lines; even the *nf–ng* lines are sharp. In that respect the high-frequency excitation is believed to be superior to the sliding spark, which produces Stark-effect shifts of sensitive levels. It should be easier to avoid impurity lines at high-frequency excitation. Although the separation of lines belonging to different ionization stages can be done in both cases, the high-frequency excitation method is probably superior.

In fact, the two methods complement each other. Roughly speaking, the excitation by means of high-frequency pulses is recommended for gaseous

elements or compounds and vapors up to about the third ionization stage. The sliding spark should be used for the excitation of solid elements and, also, for gases in order to reach still higher ionization stages.

The present review was originally prepared for internal use at the National Bureau of Standards. It is published in the hope that it may have a somewhat wider interest in spite of its limited scope.

5. References

[1] de Bruin, T. L., Zeit. Phys. **46,** 856 (1928).
[2] de Bruin, T. L., Zeeman Verhandlingen p. 413 (1935).
[3] Humphreys, C. J., Phys. Rev. **47,** 712 (1935).
[4] Paul, F. W., and Polster, H. D., Phys. Rev. **59,** 424 (1941).
[5] de Bruin, T. L., Physica **3,** 809 (1936).
[6] Rao, A. B., and Krishnamurty, S. G., Proc. Phys. Soc. **51,** 772 (1939).
[7] Humphreys, C. J., unpublished (1953).
[8] Thomson, J. J., Phil. Mag. **32,** 321 (1891).
[9] Bloch, L., and Bloch, E., J. Phys. Radium **4,** 333 (1923).
[10] Bloch, L., Bloch, E., and Déjardin, G., Ann. Phys. (Paris) **1–2,** 461 (1924).
[11] Boyce, J. C., Phys. Rev. **46,** 378 (1934).
[12] Boyce, J. C., Phys. Rev. **47,** 718 (1935).
[13] Boyce, J. C., Phys. Rev. **48,** 396 (1935).
[14] Boyce, J. C., Phys. Rev. **49,** 730 (1936); also unpublished (1936).
[15] Eriksson, K. B., Ark. Fys. **13,** 303 (1958).
[16] Bockasten, K., Hallin, R., Johansson, K. B., and Tsui, P., Physics Letters **8,** 181 (1964).
[17] Esclangon, F., Ann. Phys. (Paris) **1,** 267 (1934).
[18] Gatterer, A., and Frodl, V., Ricerche Spettroscopiche **1,** 201 (1946).
[19] Goudet, G., Herreng, P., and Nief, G., Compt. Rend. **214,** 62 (1942).
[20] Roig, J., and Buret, A., Compt. Rend., **230,** 1394 (1950).
[21] Minnhagen, L., and Stigmark, L., Ark. Fys. **8,** 471 (1954).
[22] Minnhagen, L., and Stigmark, L., Ark. Fys. **13,** 27 (1957).
[23] Minnhagen, L., Stigmark, L., and Petersson, B., Ark. Fys. **16,** 541 (1960).
[24] Stigmark, L., to be published.
[25] Kaufman, V., and Andrew, K. L., J. Opt. Soc. Am. **52,** 1223 (1962).
[26] Minnhagen, L., J. Opt. Soc. Am. **54,** 320 (1964).
[27] Meggers, W. F., and Westfall, F. O., J. Res. NBS **44,** 447 (1950).
[28] Jacobsen, E., and Harrison, G. R., J. Opt. Soc. Am. **39,** 1054 (1949).
[29] Zelikoff et al., J. Opt. Soc. Am. **42,** 818 (1952).
[30] Corliss, C. H., Bozman, W. R., and Westfall, F. O., J. Opt. Soc. Am. **43,** 398 (1953).
[31] Tomkins, F. S., and Fred, M., J. Opt. Soc. Am. **47,** 1087 (1957).
[32] Worden, E. F., Gutmacher, R. G., and Conway, J. G., Appl. Optics **2,** 707 (1963).
[33] Vodar, B., and Astoin, N., Nature **166,** 1029 (1950).
[34] Roman, J., and Vodar, V., Spectrochim. Acta **8,** 229 (1956).
[35] Bockasten, K., Ark. Fys. **9,** 457 (1955).
[36] Bockasten, K., Ark. Fys. **10,** 567 (1956).
[37] Toresson, Y., Ark. Fys. **18,** 389 (1961).
[38] Toresson, Y., Ark. Fys. **17,** 179 (1960).
[39] Gunnvald, P., unpublished.
[40] Sugar, J., J. Opt. Soc. Am. **53,** 831 (1963).
[41] Sugar, J., J. Opt. Soc. Am. (in press) (1964).
[42] Conrads, H., Diplomarbeit (Aachen 1961).
[43] Bogen P., and Conrads, H., Compt. Rend. de la VI^e Conférence Internationale sur les Phenomènes d'Ionisation dans les Gaz, III, 337 (Paris 1963).
[44] Phillips L. W., and Parker, W. L., Phys. Rev. **60,** 301 (1941).
[45] Toresson, Y., Thesis, Lund (1960).
[46] Bockasten, K., Hallin, R., and Hughes, T. P., Proc. Phys. Soc. **81,** 522 (1963).

(Paper 68C4–169)

JOURNAL OF RESEARCH of the National Bureau of Standards—C. Engineering and Instrumentation
Vol. 68C, No. 4, October–December 1964

Standards for the Calibration of Q-Meters 50 kHz to 45 MHz

R. N. Jones*

(May 27, 1964)

The National Bureau of Standards is now equipped to provide improved calibration services for Q-standards in the frequency range extending from 50 kHz to 45 MHz. As a result of recent development work, calibration uncertainties have been reduced to magnitudes which are comparable to the resolution of Q-meters in both resonating capacitance and Q. The uncertainties in the values of the NBS standards are consistent with the best two-terminal impedance measurements currently obtainable, but beyond this the values of the NBS standards have been statistically adjusted to provide a higher degree of standardization. Included in the paper is a discussion of the differences between the Q-meter indicated values for a standard and the effective values of the standard as given by NBS. These differences are largely due to residual immittances in the Q-meter circuit and methods for evaluating these residuals are presented.

1. Introduction

For grounded, two-terminal immittance measurements at radio frequencies, rf bridges are probably the most commonly used type of instrumentation. However, in the measurement of high Q devices, bridge techniques become impractical because of insufficient resolution for the resistive or conductive component. For such measurements, instrumentation based upon resonance principles is frequently used, with the most notable example being the Q-meter. As a result of this wide application of Q-meters, many laboratories have been required to show calibration traceability to NBS.

Most Q-meters covering the 50 kHz to 50 MHz frequency range are a combination of five more basic instruments including an oscillator, an insertion impedance, a thermoelement, an adjustable capacitor, and a vacuum tube voltmeter. A complete calibration of the Q-meter would require that each of these instruments be calibrated individually. This is impractical because they are not readily accessible, and also because of the large requirements in time and equipment.

The most satisfactory alternative is to employ transfer standards which may be used as spot checks for various points over a selected range of impedance and frequency. It is this method which is being employed, and the following discussion will be devoted to the NBS standards: What they are, how their values were derived, how to use them to best advantage, and the accuracies involved.

2. Q Defined

The mathematical definition for the Q of a circuit is 2Π times the ratio of the maximum instantaneous energy stored to the energy dissipated over a unit of time corresponding to one cycle. In equation form it may be written as:

$$Q=2\Pi \frac{\text{energy stored}}{\text{energy dissipated per cycle}}.$$

At the instant when maximum energy is stored in the inductance of a resonant circuit, the amount of energy stored may be expressed as $\frac{1}{2}L(I_{\max})^2$, where I denotes current and L is the inductance. The amount of energy dissipated per cycle in the circuit resistance is the product of the resistance and the square of the rms current times the period, t, of one cycle, or

$$R\left(\frac{I_{\max}}{\sqrt{2}}\right)^2\Big/_f \text{ since } t=1/f.$$

Using these values the expression for Q becomes:

$$Q=2\Pi \frac{\frac{1}{2}L(I_{\max})^2}{R\left(\frac{I_{\max}}{\sqrt{2}}\right)^2\Big/_f}=\frac{\omega L}{R},$$

and thus we have Q in terms of impedance.

3. Problems Associated With the Standardization of Q

Standards of measurement are ordinarily very fundamental, so that their values are directly related to basic physical dimensions or some invariant natural constant. This practice has been followed in the development of rf impedance standards [1, 2],[1] and prototype standards have been constructed which have uncertainties of the order of 0.1 percent relative to the true values. Actually Q-standards are only a special type of impedance

*Radio Standards Engineering Laboratories, NBS Boulder Laboratories, Boulder, Colo.

[1] Figures in brackets indicate the literature references on page 247.

standard because their values are derived from impedance measurements and, therefore, the same accuracy limitations apply. The complications arise in attempting to qualify the percentage uncertainty of Q. Any practical alternating current circuit contains both reactance and resistance, and at the present state of the art of impedance measurement there is no way to evaluate either component so that its value is free of errors contributed by the other. This is true, regardless of the method of measurement employed, be it bridge, slotted line, or a resonance technique. All of these methods merely compare impedances rather than measuring resistance and reactance individually, regardless of the readout of the instrument. This places serious limitations on the absolute accuracy to which Q can be determined. As large values of Q are encountered, the magnitude of the reactive component approaches the magnitude of the complex impedance, and it becomes increasingly difficult to achieve accurate resolution of the resistance. Q, then, is limited in accuracy by the accuracy of the impedance measurement from which it is derived. Figure 1 is a plot of the percentage uncertainty of Q as a function of Q for impedance uncertainties of 0.1 and 1.0 percent. The uncertainties shown are pessimistic because they are based upon the assumption that all of the error in the impedance is attributable to the resistance and none to the reactive component. A second modification is necessary for the upper percentage limit, because by definition Q cannot be negative in a passive network. Therefore the maximum limits of uncertainty in any value for Q would be plus infinity and minus 100 percent. In individual circumstances these limits might be reduced by

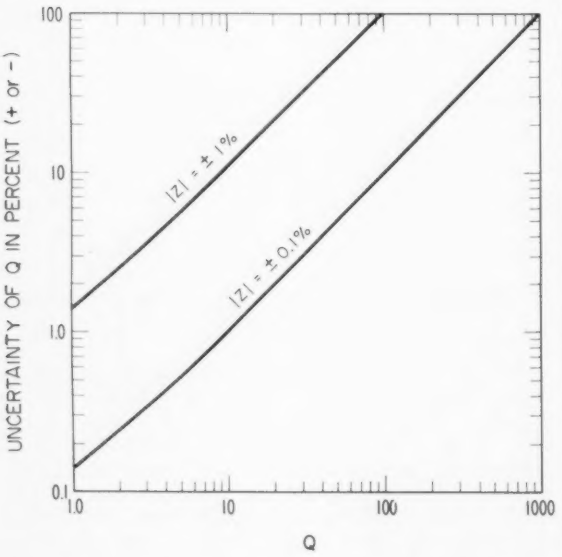

FIGURE 1. *Uncertainty of* Q *as a function of* Q *for an impedance uncertainty of 0.1 and 1.0 percent.*

the weight of experimental evidence, but it would be difficult to impose other limits categorically.

A second area of difficulty associated with the establishment of Q-standards, and one common to all types of immittance measurement, is associated with connectors. Precision coaxial connectors with well-defined reference planes are a distinct advantage in immittance measurement because they establish measurement conditions which are conducive to higher accuracy and better repeatability. Such conditions are important at all frequencies, but become increasingly so at the higher frequencies where wavelengths become short, or where measured immittances approach connector error immittances. Ideally, standards for immittance measurement of any type should utilize such laboratory precision connectors to permit the most direct evaluation in terms of national standards.

4. NBS Q-Standards

The complications arising from connector uncertainties, and the inability to make absolute determinations of Q to high percentage accuracies, have made it necessary to compromise ideal conditions in order to provide a practical system of reference standards and calibration services.

Experience gained from a large number of calibration requests over a period of several years has provided a clear indication of the type of Q-standards required. Most Q-meters provide a readout in terms of resonating capacitance and Q, and the NBS standards provide an arbitrary reference for these quantities. The established group of reference standards provides for calibrations at fifteen frequencies in the interval from 50 kHz to 45 MHz. The standards are wire-wound, air-core inductors, hermetically sealed, and equipped with banana plug connectors at a spacing of 1 in. on centers. At each frequency there are three standards, all having nearly the same value of resonating capacitance and Q. This permits periodic intercomparison to insure that no instabilities exist, and also permits three essentially independent determinations to be made on any standard received for calibration.

At this point it is important to make a distinction between indicated and effective values of a Q-standard. The indicated values of resonating capacitance and Q are those values obtained from measuring the standard on a Q-meter and may vary from one Q-meter to another. The effective values, on the other hand, are intended to be the values of the Q-standard when it is dissociated from any other circuitry or surrounding object and are, therefore, independent of the Q-meter. The effective values of the NBS standards have been assigned after extensive evaluation procedures involving both bridge and resonance techniques.

In the calibration procedure, the Q-standard to be calibrated is compared with each of the three NBS standards by observing the difference between the indicated values of resonating capacitance and Q on a Q-meter. These differences are then applied to

the effective values of the NBS standards to obtain the effective values of the unknown, and the averages obtained from the three determinations provide the values given in the Report of Calibration. Thus it is desirable that the unknown and the standards be as nearly alike in value as possible to avoid the errors which can accrue from assuming that the differences in indicated value are equal to the differences in effective value.

5. Effective Versus Indicated Values

It is not unusual for the NBS effective values of the unknown to differ appreciably from the indicated values obtained from the Q-meter. These differences become increasingly pronounced at the higher frequencies and are attributable to three major causes. In order of significance these include the residual immittances of the Q-meter circuitry, the inaccuracy of the NBS effective values, and the nonrepeatability of the connectors. For purposes of checking the calibration of a Q-meter, it is most convenient to attribute the entire discrepancy to the residual Q-meter immittances and include the contribution of the latter two causes in the accuracy statement.

The following numerical example is included to assist the user in rationalizing the indicated values obtained from his Q-meter with the effective values as given by NBS for a particular Q-standard. This method may be used to evaluate the Q-meter circuit residuals at any frequency within its range, thereby achieving a definite traceability to NBS standards. The values used in the example were taken from actual measurement results to provide a general quantitative idea of the magnitude of the residuals in the Q-meter circuit, and their relative importance in any particular measurement situation.

For a particular Q-standard, the indicated values given by a Q-meter were 191 for Q and 429 pF for resonating capacitance at 15 MHz. The corresponding NBS effective values for the same Q-standard were 360 for Q and 461 pF for resonating capacitance.

Consider the approximate equivalent circuit of figure 2, which we will use to represent the measuring circuit of the Q-meter. Here C is the resonating capacitor in the Q-meter, and L_r is its residual series inductance. L_c and R_c are the inductance and resistance of the coil to be measured, and R_i is the insertion resistance. G_c and G_v are the respective conductances of the resonating capacitor and the Q-voltmeter.

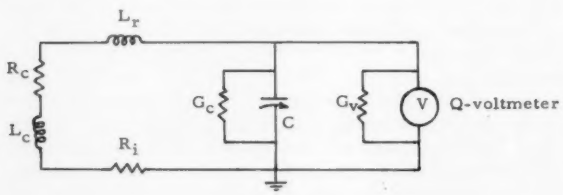

FIGURE 2

The residual inductance, L_r, may be computed from the following relationship:

$$L_r=\frac{C_e-C_i}{\omega^2 C_e C_i}, \tag{1}$$

where:

L_r=residual inductance in henries,
C_e=effective resonating capacitance in farads,
C_i=indicated resonating capacitance in farads,
ω=angular frequency in radians per second.

Here it is assumed that the Q-meter capacitor has been calibrated at low frequency and appropriate corrections applied. The expression (1) results from equating the reactance of C_e to the reactance of an equivalent circuit for the Q-meter capacitor composed of the inductance, L_r, in series with the capacitance, C_i, at the angular frequency ω. At 15 MHz this yields a value of 0.018 μH for the residual inductance, L_r. Having the value for L_r, the expression (1) may be rearranged to compute C_e, if C_i is known, or C_i, if C_e is known.

Having evaluated the reactive residual in the Q-meter measuring circuit, we can proceed to an analysis of the resistive residuals. Taking the Q-meter indicated values for resonating capacitance and Q, we arrive at a value of 0.129 ohm for the resistance of the entire circuit of figure 2. From the NBS effective values for the Q-standard, its resistance, R_c, is 0.064 ohm. Thus the residual resistance in the Q-meter circuit is the difference between these two values or 0.065 ohm. In this particular instance the d-c resistance of the insertion resistor, R_i, was given by the manufacturer as 0.020 ohm. Assuming this d-c value to be valid up to a frequency of 1 MHz and taking into account the rise in resistance of R_i due to skin effect, we achieve a value of 0.020 $\sqrt{15}$=0.077 ohm at 15 MHz.[2] This represents a disagreement of $\frac{0.077-0.065}{23.0}\times 100=0.05\%$ in $|Z|$.

This, of course, would be degraded somewhat if the conductances G_c and G_v had been taken into account, but the losses contributed by them are small and the agreement is well within expected tolerance limits for measurements of this type.

6. Statistical Adjustment of NBS Effective Values

Having assigned arbitrary values for effective resonating capacitance and effective Q based upon the best impedance measurements obtainable, further improvement in the absolute accuracy is extremely difficult to realize. For the purpose of establishing a set of reference standards, it is important that the values of the individual standards for each frequency be consistent with respect to one another.

[2] Above one megahertz, the resistance is assumed to be proportional to the square root of the frequency in megahertz.

A statistical analysis of all the data obtained from previous calibrations was undertaken to accomplish a threefold objective: (1) Determine whether or not the values assigned to the standards were consistent with one another, (2) to determine the corrections necessary to eliminate any inconsistencies found to exist, and (3) to utilize past experience to derive expected tolerance limits for future calibrations. The data used in the analysis were taken from calibrations performed over a period of approximately 5 years. The number of unknowns calibrated at each frequency varied from 74 to 106, thus providing an ample amount of data for statistical treatment.

As described in section 3, each unknown received for calibration is compared with each of the three NBS standards at a particular frequency. Because the statistical procedure is identical for analyzing and adjusting the values for both effective resonating capacitance and effective Q, the discussion will be confined to the Q-values for the sake of brevity. The data resulting from intercomparing the unknowns with the NBS standards at any one frequency may be arranged as follows:

$$\begin{array}{ccc} Q_{11} & Q_{12} & Q_{13} \\ Q_{21} & Q_{22} & Q_{23} \\ Q_{31} & Q_{32} & Q_{33} \\ \cdot & \cdot & \cdot \\ \cdot & \cdot & \cdot \\ \cdot & \cdot & \cdot \\ Q_{n1} & Q_{n2} & Q_{n3} \end{array}$$

The first subscript denotes a particular unknown, and the second subscript denotes the NBS standard with which it was compared. Thus Q_{ij} is the effective Q of unknown number i resulting from comparing it with standard number j. From this arrangement, three arithmetic averages were computed:

$$\overline{Q}_{\cdot 1}=\frac{\sum_{i=1}^{n} Q_{i1}}{n},\ \overline{Q}_{\cdot 2}=\frac{\sum_{i=1}^{n} Q_{i2}}{n},\ \text{and}\ \overline{Q}_{\cdot 3}=\frac{\sum_{i=1}^{n} Q_{i3}}{n},$$

where n is the total number of unknowns calibrated at a particular frequency. Comparison of these averages $\overline{Q}_{\cdot 1}$, $\overline{Q}_{\cdot 2}$, and $\overline{Q}_{\cdot 3}$ provided an indication of the inconsistency of the values originally assigned to the standards. Following this, the arithmetic mean of the values $\overline{Q}_{\cdot 1}$, $\overline{Q}_{\cdot 2}$, and $\overline{Q}_{\cdot 3}$, which we will call $\overline{A}$, was used as a criterion for adjusting the original values to bring about better agreement. Standard number 1 was adjusted by an amount $\overline{D}_1=\overline{A}-\overline{Q}_{\cdot 1}$. Standard number 2 was adjusted by $\overline{D}_2=\overline{A}-\overline{Q}_{\cdot 2}$, and standard number 3 by $\overline{D}_3=\overline{A}-\overline{Q}_{\cdot 3}$. By this procedure the first two objectives were accomplished.

To derive expected tolerance limits for future calibrations, using the new values for the NBS standards, the previous data were compensated to take into account the adjustments made on the values for the standards. The variance,

$$s_i^2=\frac{1}{3-1}\sum_{j=1}^{3}(Q'_{ij}-\overline{Q}'_{i\cdot})^2,$$

was computed for each unknown where $Q'_{ij}=Q_{ij}+\overline{D}_j$ is the compensated value obtained from comparing the ith unknown with the adjusted jth standard and $\overline{Q}'_{i\cdot}=\overline{Q}_{i\cdot}$ is the average of the three values of the unknown resulting from comparing it with each of the three adjusted standards. A best estimate of the common true variance, s^2, was then derived from the individual variances by means of a weighted average. This was done by the relationship:

$$s^2=\frac{\sum_{i=1}^{n}(3-1)s_i^2}{(n-1)(3-1)}=\frac{\sum_{i=1}^{n}s_i^2}{n-1}.$$

The fact that the denominator is $(n-1)(3-1)$ follows from the application of a general method, two-way analysis of variance. The square root of this estimate of the common true variance was then used as the standard deviation upon which the tolerance limits for future calibrations should be based. However, such tolerance limits are valid only if the data from which they were derived conform to a normal or gaussian distribution. In an attempt to verify normality of the data, histograms were plotted and the chi-square coefficient computed and compared with tabulated theoretical values. At this point some difficulty was encountered because the measurements displayed a very high degree of repeatability with respect to the resolution of the Q-meter. This resulted in many measurements deviating from the mean by the same amount and tended to distort the shape of the histogram by concentrating too many values near the center. Consequently, the chi-square coefficient failed to establish normality in a number of instances for both resonating capacitance and Q.

Under the criteria of normality, the significance of a factor, K, times the standard deviation is that the probability is γ that at least a proportion, P, of the distribution will be included between $\bar{x}\pm Ks$, where $\bar{x}$ and s are estimates of the mean and the standard deviation computed from a sample size of n [3]. In these instances, the sample size was taken as 150 because there were approximately 75 unknowns compared against each of three standards, giving two degrees of freedom per unknown. Choosing a value of 0.99 for both the probability, γ, and the proportion, P, gives a value for K of approximately 3 for a sample size of 150. Examination of the data indicated that the number of measurements falling outside the $3s$ limits conformed very well to that expected of a normal distribution, and it was therefore deemed appropriate that these limits be imposed as the tolerance for use in connection with the calibration of Q-standards. Table 1 shows the frequen-

TABLE 1. *Approximate effective values of NBS Q-standards and estimated calibration tolerances based upon previous calibration data.*

Frequency	Effective resonating capacitance	Effective Q
50 kHz	[a] 400 pF (±0.6)	[a] 100 (±2)
100 kHz	90 pF (±0.1)	150 (±2)
150 kHz	34 pF (±0.1)	150 (±2)
150 kHz	430 pF (±0.6)	180 (±2)
300 kHz	100 pF (±0.3)	200 (±2)
450 kHz	40 pF (±0.1)	160 (±2)
0.5 MHz	400 pF (±0.6)	190 (±2)
1.0 MHz	90 pF (±0.2)	240 (±2)
1.5 MHz	37 pF (±0.2)	210 (±2)
1.5 MHz	430 pF (±0.7)	180 (±2)
3.0 MHz	100 pF (±0.2)	240 (±2)
4.5 MHz	40 pF (±0.1)	250 (±2)
5 MHz	390 pF (±0.7)	220 (±2)
10 MHz	90 pF (±0.1)	270 (±3)
15 MHz	36 pF (±0.1)	240 (±2)
15 MHz	440 pF (±1.0)	350 (±8)
30 MHz	100 pF (±0.3)	500 (±9)
45 MHz	40 pF (±0.1)	620 (±7)

[a] Numbers in parentheses indicate 3s calibration tolerances.

cies and approximate effective values of the NBS standards together with the tolerance limits for calibrations.

7. Conclusion

The system of standards described has been developed to meet a specialized need for standardization and traceability for high Q impedance measurements. So far as possible their accuracies are consistent with the best impedance measurements obtainable. Beyond this, the values have been statistically adjusted to provide a still higher degree of precision so that it is practical to provide calibration data which utilize nearly all of the significant figures that the Q-meter can resolve.

The tolerance limits established by the statistical analysis serve a twofold purpose. The first is to provide reliability limits within which the data may be expected to repeat. Secondly, but of equal importance, such limits enable calibration personnel to evaluate measurement results. This further reduces the probability of large excursions due to human error or erratic performance of the instrumentation.

The major possibility for improvement in the standards is in the absolute accuracy. Should means become available to improve this accuracy through better impedance measurement, the assigned values of the standards may be altered, but the same tolerance limits for calibration repeatability would still be applicable.

The data used in the development of these standards were accumulated over a period of several years and involved the cooperation of many NBS personnel. The author would like to thank all those who participated. Particular mention is due three individuals who were especially helpful. These include R. C. Powell for his helpful technical suggestions, Carl Love for his assistance with computer programming and data analysis, and E. L. Crow for his advice in statistical procedures.

8. References

[1] R. C. Powell, R. M. Jickling, and A. E. Hess, High frequency impedance measurements at the National Bureau of Standards, IRE Transactions on Instrumentation, Vol. I-7, numbers 3 and 4, December, 1958.

[2] R. N. Jones and R. E. Nelson, The role of capacitance in the National Reference Standards of high frequency impedance, Proceedings of the 17th Annual I.S.A. Conference and Exhibit, 1962, Paper No. 18.1.62.

[3] M. G. Natrella, Experimental statistics, NBS Handbook 91, pp. T-10 to T-12.

9. Appendix

In dealing with resonant circuits it is often convenient to utilize the expression:

$$\frac{1}{Q_{ckt}}=\frac{1}{Q_L}+\frac{1}{Q_C},$$

which expresses the relationship between the Q of the entire circuit and the Q of its individual reactive components. The derivation of this relationship is not commonly found in the literature and it is included here because of its usefulness in measurement applications involving the Q-meter.

Consider the following circuit:

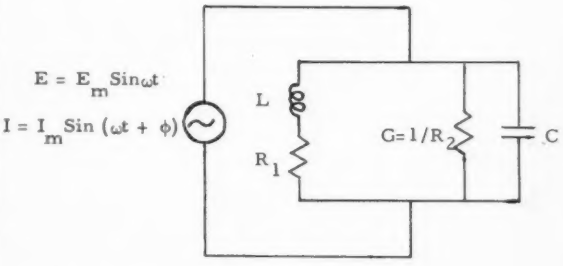

By definition

$$Q=\frac{\omega_0\ (\text{energy stored in circuit})}{\text{average power lost}}.$$

At the instant when all of the energy is stored in the magnetic field of the inductor, the energy stored is:

$$U=1/2LI_m^2.$$

At the instant when all of the energy is in the electrostatic field of the capacitor, the energy stored is:

$$U=1/2CE_m^2.$$

The average power lost per cycle in the resistance, R_1, and the conductance, G, are $1/2R_1I_m^2$, and $1/2GE_m^2$,

respectively. From the above definition, the circuit Q may be expressed as:

$$Q_{ckt}=\frac{\omega_0\frac{LI_m^2}{2}}{1/2R_1I_m^2+1/2GE_m^2},$$

or

$$Q_{ckt}=\frac{\omega_0\frac{CE_m^2}{2}}{1/2R_1I_m^2+1/2GE_m^2};$$

$$\frac{1}{Q_{ckt}}=\frac{R_1I_m^2+GE_m^2}{\omega_0LI_m^2}.$$

But $E_m=\frac{I_m}{G}$, and using this substitution the expression becomes:

$$\frac{1}{Q_{ckt}}=\frac{R_1}{\omega_0L}+\frac{1}{\omega_0LG}.$$

Since $\omega_0L=\frac{1}{\omega_0C}$, we have $\frac{1}{Q_{ckt}}=\frac{1}{Q_L}+\frac{1}{Q_C}$ where $Q_c=\frac{\omega_0C}{G}$.

Q.E.D.

(Paper 68C4–170)

JOURNAL OF RESEARCH of the National Bureau of Standards—C. Engineering and Instrumentation
Vol. 68C, No. 4, October–November 1964

X-Ray Measurement of Residual Strains in Individual Grains of Polycrystalline Aluminum

Clarence J. Newton

(April 24, 1964)

Shifts in peak position of {333} and {511} diffractions of cobalt $K\alpha_1$ x rays from individual grains of coarse-grained polycrystalline aluminum observed in the annealed condition and after 10 percent plastic extension revealed residual strains in each crystallite. These strains, however, did not conform to the strain quadric with a principal axis parallel to the axis of deformation, as is the case of observations from fine-grained metallic specimens that have been plastically deformed; nor was any consistency or meaningful average trend observed in the strains of the various grains. Irregularities of loading constraints by one grain upon its neighbors and the resulting great nonuniformity of deformation may account for the absence of systematic results.

1. Introduction

The angle of x-ray diffraction θ is related to the spacing d_{hkl} between layers of atoms in a crystalline solid through Bragg's law,

$$\lambda = 2d_{hkl} \sin \theta, \tag{1}$$

where λ is the x-ray wavelength. The use of the shift of the diffraction angle as an indication of strain in the lattice structure of the solid is more than 30 years old. One of the first observations of this type was made by Lester and Aborn [1][1] in 1925 on the change of spacing of crystalline planes in steel subjected to stress. A comprehensive review article concerned with x-ray strain measurement as well as other aspects of quantitative x-ray diffraction observations on strained metal aggregates was published by G. Greenough [2] in 1952. Perhaps the most interesting aspect of these strains in the crystal lattice structure is the residual elastic strain observed in a metal specimen that has been plastically deformed and then unloaded. Recently the various theories attempting to explain these residual strains and stresses measured by x-ray diffraction have been evaluated by Vasil'ev and Smirnov [3] in 1961 in a review article discussing a variety of x-ray diffraction methods of investigating cold-worked metals.

It is generally accepted that the residual stresses arise on account of differences of "hardness" or resistance to plastic flow in various regions of the material. After the release of a uniform uniaxial deforming stress of a given sign, the weaker regions A will be constrained into a state of stress of the opposite sign by the greater amount of elastic strain recovery in the stronger regions B. Although the microscopic nature of these two regions has not been clearly determined, the model that seems to be most widely accepted today is based upon ideas first advanced by Smith and Wood [4]. They suggested that the soft regions A and the hard regions B are regions of low and high lattice structure distortion, respectively. This hypothesis has been supported by the observations of many recent workers [5, 6, 7], although there is some evidence that more than one mechanism may be contributing to the observed strains and stresses under certain circumstances [8]. The original idea that the distorted harder regions B were at the grain boundaries has gradually been generalized to include all regions of high dislocation density, such as slip planes, subgrain boundaries, and the dislocation tangles that constitute cell walls observed in some deformed metals [9]. Since the x-ray diffraction peak position is determined principally by the more perfect A material, the peak shift represents the elastic strain and the related stress in that material only.

Related to the question of the source of the residual elastic strains and stresses in the polycrystalline metal is the paradox of their observed quasi-isotropic behavior. The strains measured on a given surface are observed to satisfy the equation of a strain quadric, with one of the principal strains parallel to the axis of plastic deformation. This feature is implicit in most of the reports of this type of measurement and has occasionally been explicitly verified [10]. Most workers agree, moreover, that in practice it is permissible to use the gross average values of Young's modulus and Poisson's ratio as obtained from mechanical tests on polycrystalline specimens free of preferred crystallite orientation [11, 12] to relate the strains to a system of stresses using isotropic elastic theory; and there seems to be no question that the net observed behavior in the x-ray "powder" diffraction effects from the aggregate of individual anisotropic crystallites is itself isotropic.

There are at least two possible explanations for this isotropic behavior on the part of the diffracting regions A of the grains. First, these regions may be so constrained by their randomly oriented neighboring grains and by the hard, quasi-amorphous B material at grain or subgrain boundaries that the

[1] Figures in brackets indicate the literature references at the end of this paper.

strains are forced into an isotropic pattern relating to the applied deformation. Alternately, although the distribution of strain in any one crystallite might be itself quite anisotropic and unrelated to the geometry of the preceding deformation of the gross specimen, the strain indicated by the shift in the diffraction line, coming typically from hundreds of crystallites, might represent a nonzero average that exhibits the isotropic behavior.

The principal line of attack in the present investigation was to measure the shift in the Bragg angle of diffraction from individual crystallites in a coarse-grained polycrystalline specimen that had been plastically deformed in tension. The purpose of the study was to see if there was an impressed residual stress-strain system, if it was isotropic with principal axes determined by the external deformation, as is the case with ordinary fine-grained material, and what the magnitude of the residual strain might be. It was hoped that such an investigation might throw some light on the alternate hypotheses of pseudo-isotropic behavior of the strains and possibly lead to further studies that might reveal some grain-size effects.

2. Experimental Procedures

The specimen was of 99.99 percent pure aluminum with threaded ends and a reduced section about 1¼ in. long with a square cross section ½ in. on a side. The specimen was supplied in a fully annealed, stress-free condition, surface etched, with grains ranging in mean diameter from about 1/16 in. to ¼ in., grown by the strain-anneal method. Prior to examination the specimen was further annealed for 24 hr at 150 °C and furnace cooled. The specimen in its initial condition may be seen in figure 1, a and b.

The x-ray diffraction measurements were obtained by a combination of film and counter methods on a commercial x-ray diffraction apparatus, employing auxilliary equipment designed and built at the National Bureau of Standards. The first step of the procedure was the determination of the crystallographic orientation by means of back-reflection Læue diffraction patterns of all the grains in the central ½ in. of each of the four faces of the reduced section of the specimen. The number of grains so oriented, countings duplicates around specimen edges twice, was 51. All of the {111} and {511} plane normals were located on the stereographic projection of the pattern from each grain, and the angular coordinates, azimuth α and co-altitude ψ, for all such poles within approximately 65° of the normal to the surface being studied were measured on a Wulff net and recorded.

After the determination of orientation of each grain, the specimen in its special holder, which may be seen in figure 2, was transferred to the diffractometer. By means of a collimator sighting adjustment, the surface of the specimen was placed in coincidence with the common vertical axis of the diffractometer and the holder; and while the specimen was observed with a low-powered microscope, a desired grain was translated into the incident collimated x-ray beam about 1 mm in diameter. The proportional counter was set at the expected 2θ diffraction angle, which was 162.50° for both the {511} and {333} planes, for copper $K\alpha_1$ radiation. The alpha doublet was well resolved in all cases. The two angular adjustments on the specimen holder were then set, corresponding to α and ψ, in order to

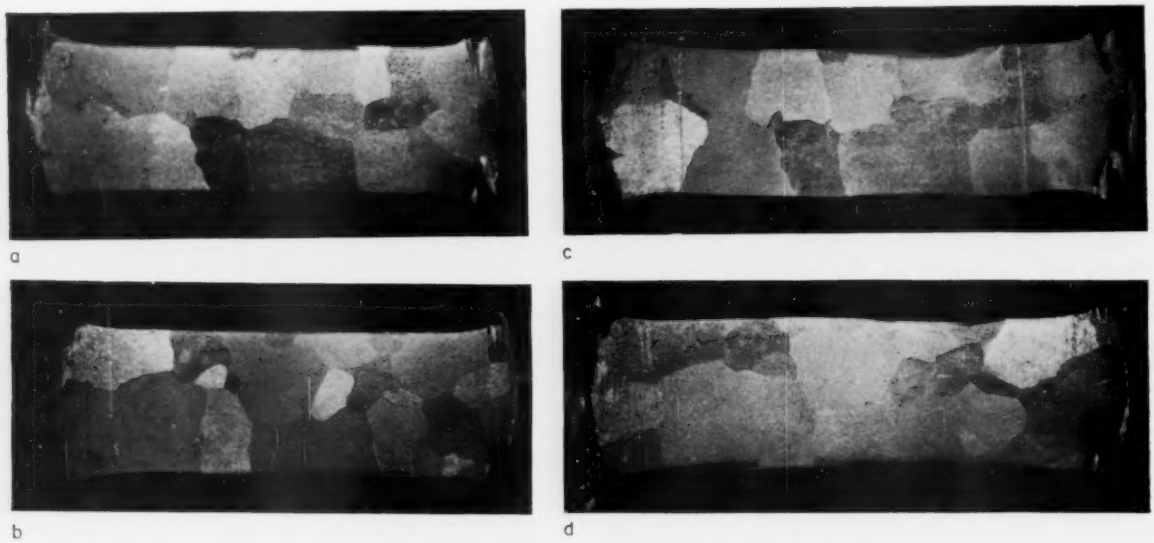

FIGURE 1. *Aluminum Specimen, Magnification 2 ×.*

a. Face A annealed condition.

b. Face B, annealed condition (at right angle to Face A).

c. Face A, after 10 percent plastic extension

d. Face B, after 10 percent plastic extension.

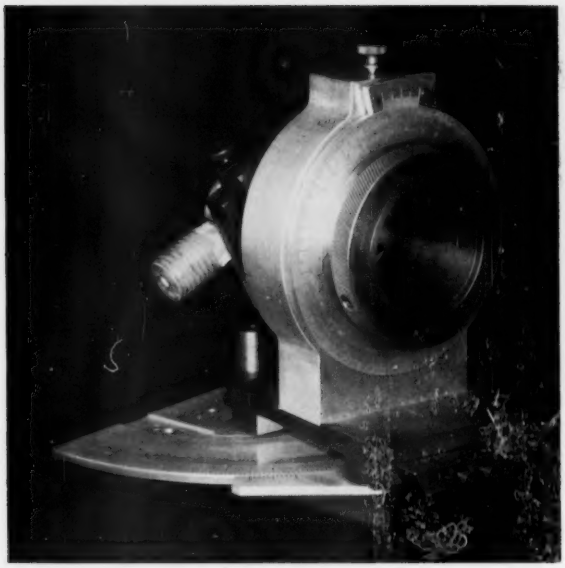

FIGURE 2. *Goniometer specimen holder for use on the x-ray diffractometer.*

place the desired pole of a diffracting plane in the horizontal plane of the diffractometer and in the position of bisector of the angle between the incident and diffracted rays. In order to minimize defocusing effects, the surface normal was always tilted away from the detector. All three angular adjustments were then "fine tuned" to give a maximum signal in the counter. The counter was then backed up a few hundredths of a degree and then "step-scanned" across the top of the diffraction peak. The steps were 0.01 of a degree apart and were held for a fixed time interval; the intensity in total counts was printed out at the end of each interval.

After the reference peak values of 2θ had been determined for all poles of interest in the specimen in the annealed condition, the specimen was strained in uniaxial tension at 23 °C to a final true strain of 10 percent. The cross-head speed for most of the deformation, including the latter part, was held at 0.001 in. per minute. The flow stress at the 10 percent plastic true strain was found to be approximately 4080 psi. At this strain, this coarse-grained specimen showed, as may be seen in figure 1 c and d, considerable inhomogeneity of strain, more than is usually the case with fine-grained material, but less than is typical with deformed single crystals.

After the prescribed plastic strain, the specimen was realined in the diffractometer and the peak 2θ values were redetermined for all of the {511} and {333} planes in the region of interest on two of the four faces. Since the diffraction peaks were somewhat broadened and considerably reduced in height after the deformation, the steps in the scanning were now spaced 0.02° apart and the time intervals of counting considerably lengthened. The peak position was determined analytically by a three-point parabola-fitting equation, with a precision estimated to be $\pm 0.01°$ or better. The θ-dependent corrections of the intensity often used in this type of peak determination were examined for a few cases in this study, but were not used, being negligible because the distance between first and last step positions of 2θ on each side of the apex of a peak was only 0.04° in these single crystal diffractions, as compared to the several tenths or even whole degrees involved in the case of polycrystalline diffraction. Before the changes in 2θ going from the annealed to the strained state were calculated, however, the individual values were corrected for the effects of thermal expansion from the temperature of measurement to a standard 25 °C. The handbook value of the coefficient used was 23.8×10^{-6} per degree C for the lattice constant. This resulted in a temperature correction in the Bragg angle, in degrees, at 2θ equal 162.50°, of

$$\delta(2\theta°)=(-0.0177)\delta T, \tag{2}$$

where δT is the difference in temperature in degrees C from the reference temperature.

If the measured strain is small, as it was in these cases, it is not necessary to calculate values of d_{hkl}, the lattice plane spacing, from the observed Bragg angles; it is more convenient simply to use $\Delta(2\theta)$, the change in Bragg angle, since it is directly proportional to the strain through the following equation:

$$\epsilon=\frac{\Delta d}{d}=-\frac{\cot\theta}{2}\Delta(2\theta)=(-1.343\times10^{-3})\Delta(2\theta°). \tag{3}$$

The angle θ is approximately 81.25° in the case we are examining. Since only changes in Bragg angle need be observed, the question of absolute calibration of the diffractometer is avoided. For the sake of simplicity and directness, $\Delta(2\theta°)$ values rather than actual strains are used throughout this paper.

If the uncertainty in a given 2θ reading is $\pm0.01°$, as estimated, the uncertainty in $\Delta(2\theta)$ should be about $\pm0.014°$; hence the uncertainty in a strain calculated by equation (3) would be $\pm1.5\times10^{-5}$.

3. Results

On the two faces of the specimen, shown in figure 1, for which complete post-strain data were taken, changes in 2θ were measured for an average of about nine planes on each of 25 grains. The data for two typical grains on Face A are tabulated in table 1. The $\Delta(2\theta)$ values, and hence the strains, are very small, but in most cases they are several times the estimated uncertainty in the measurement.

As stated in the introduction, residual strains measured by x rays on conventional polycrystalline material that has been plastically strained uniaxially satisfy the strain quadric equation

$$\epsilon=a_1^2\epsilon_1+a_2^2\epsilon_2+a_3^2\epsilon_3, \tag{4}$$

TABLE 1. *X-ray strain data (i.e., diffraction peak shift) from two typical grains*

Grain	*hkl*	Annealed					Extended					$\Delta(2\theta^\circ)$
		α	ψ	T(°C)	$2\theta_T$	$2\theta_{23^\circ}$	α	ψ	T(°C)	$2\theta_T$	$2\theta_{23^\circ}$	
1	333	169.8	22.2	24.1	162.43	162.41	168.9	21.6	24.0	162.52	162.50	+0.09
	333	323.9	49.9	24.1	162.44	162.42	324.1	50.2	23.6	162.51	162.49	.07
	15$\bar{1}$	271.7	48.3	24.3	162.44	162.43	271.3	46.5	24.1	162.52	162.50	.07
	151	241.8	40.7	24.2	162.45	162.44	241.8	40.0	24.5	162.53	162.52	.08
	511	64.3	47.1	24.4	162.46	162.45	64.3	47.7	27.7	162.48	162.53	.08
	511	58.3	25.2	24.5	162.45	162.44	58.5	25.8	26.0	162.49	162.51	.07
	51$\bar{1}$	37.1	54.1	24.5	162.45	162.44	38.2	54.9	26.1	162.44	162.46	.02
	51$\bar{1}$	18.8	35.8	24.6	162.46	162.45	19.1	36.3	26.4	162.45	162.47	.02
	115	154.9	60.2	24.8	162.43	162.43	154.4	60.0	26.4	162.49	162.51	.08
2	333	64.1	47.8	23.2	162.52	162.49	66.4	47.8	22.5	162.54	162.50	.01
	333	154.7	59.4	23.4	162.50	162.47	156.4	60.0	23.0	162.50	162.46	−.01
	333	237.4	62.8	23.6	162.51	162.49	242.2	64.7	23.6	162.65	162.63	.14
	333	324.5	50.4	23.8	162.52	162.50	324.0	48.6	23.8	162.43	162.41	−.09
	511	88.0	9.7	24.5	162.49	162.48	81.0	4.3	24.3	162.48	162.47	−.01
	511	169.2	21.3	25.0	162.49	162.49	182.8	20.9	24.6	162.51	162.50	.01
	511	229.4	23.1	25.1	162.50	162.50	229.2	25.4	25.1	162.58	162.58	.08
	511	299.5	13.1	25.4	162.47	162.48	293.6	20.1	25.1	162.52	162.52	.04

where ϵ is the strain measured in some direction whose direction cosines are:

$$a_1=\sin\psi\cos\varphi$$

$$a_2=\sin\psi\sin\varphi$$

$$a_3=\cos\psi$$

and ϵ_1, ϵ_2, and ϵ_3 are the principal strains, in the orthogonal directions identified in figure 3 with respect to the geometry of the specimen and its deformation. The instrumental azimuth angle α in this study was related to the usual coordinate φ by

$$\varphi=270^\circ-\alpha$$

also illustrated in this figure. The direction cosines in terms of ψ and α were

$$a_1=-\sin\psi\sin\alpha$$

$$a_2=-\sin\psi\cos\alpha$$

$$a_3=\cos\psi.$$

The direction cosines were calculated for all the directions in which the strains were measured in the two grains referred to in table 1, and selected sets of three simultaneous equations were set up from which sets of three principal strains were computed for a particular form of planes within each grain. In no case, however, was even an approximately consistent set of principal strains with this preassigned orientation found.

In the isotropic analysis of strains in fine-grained material, a plot of strain versus $\sin^2\psi$ is found to be linear when the directions of measured strain are confined to a plane normal to the surface of the specimen [7]. In an attempt to find analogous "cooperative" behavior from the coarse-grained material, two plots of $\Delta(2\theta)$ versus $\sin^2\psi$ were prepared for each of the two faces A and B. By restricting α to $90^\circ\pm10^\circ$ and $270^\circ\pm10^\circ$, values of strain from very many grains were measured for various ψ values close to a longitudinal plane (x_1x_3) normal to the surface and parallel to the axis of deformation. By restricting α to $0^\circ\pm10^\circ$ and $180^\circ\pm10^\circ$, similar data were obtained near a transverse plane (x_2x_3). These four plots of $\Delta(2\theta)$ versus $\sin^2\psi$ are shown in figure 4. There does not appear to be any relationship of the strain to $\sin^2\psi$ in any of the four cases examined. Indeed, no self-consistency or general trend or "average" behavior among the grains was anywhere in evidence among the 229 strain determinations on the two faces of this specimen.

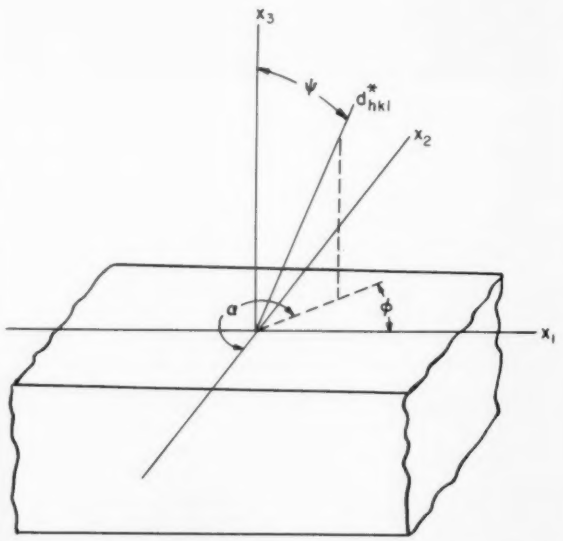

FIGURE 3. *Diagram illustrating directions of axes and defining angles with respect to the geometry of the specimen and its deformation.*

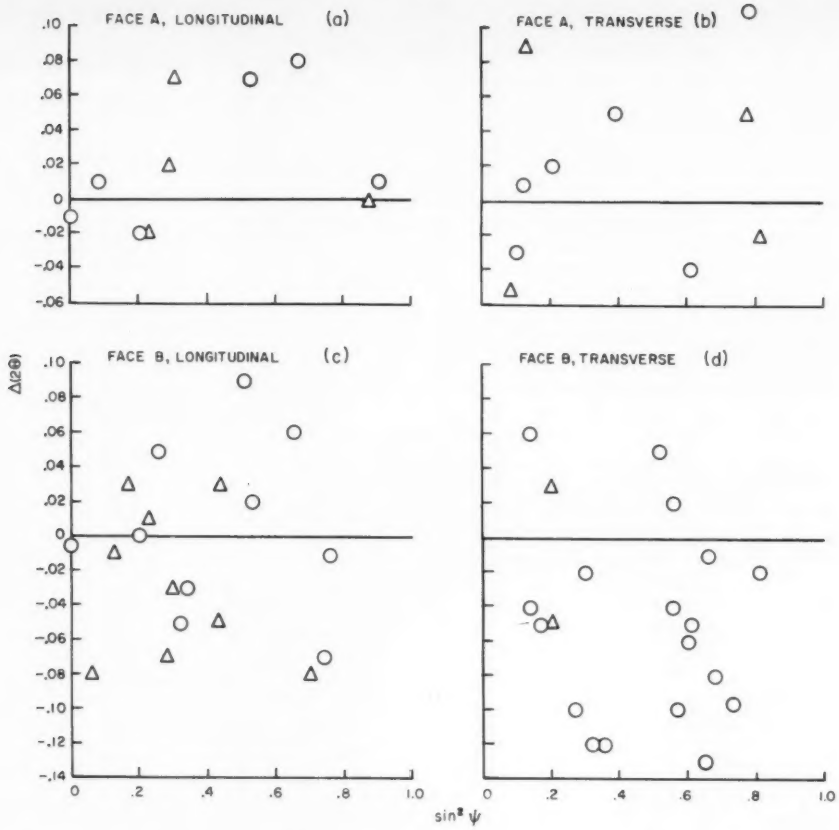

FIGURE 4. *Plots of Strain in Terms of* $\Delta(2\theta)$ *versus* $\sin^2\Psi$.

a. Longitudinal Plane Normal to Face A.
b. Transverse Plane Normal to Face A.
c. Longitudinal Plane Normal to Face B.
d. Transverse Plane Normal to Face B.
Circles—{511} diffraction data.
Triangles—{333} diffraction data.

4. Discussion

The results of this investigation show that it is possible to detect directed residual strains by the peak shift of x-ray diffractions in single crystals within a coarse-grained polycrystalline aggregate that has been plastically deformed in tension. Even when the material, however, is aluminum, a metal which is not so strongly anisotropic as many others, these individual crystallite strain values do not conform to the type of isotropic elastic behavior observed with ordinary fine-grained polycrystalline material after plastic deformation; at least such was the case for the specimen studied here.

It may be assumed that the strain data from any one of the grains in this study could be subjected to a rigorous anisotropic elastic analysis, such as that of Imura, Weissman, and Slade [13] in their work with divergent beam diffraction from single crystals. It is doubtful, however, that the information return in this case of highly irregular loading constraints would justify the involved computations. Perhaps such an analysis of residual strains measured by x rays in plastically deformed specimens that were true single crystals would yield meaningful information. The author is not aware that results of this type have as yet been published.

It is interesting to consider whether the anisotropic result obtained with the coarse-grained material in this study is more consistent with the "constraint" hypothesis or the "averaging" hypothesis of the isotropic behavior of the fine-grained material. The change in grain size involved is from that of a few millimeters in the present case to a few hundredths of a millimeter or less in the typical fine-grained case. This change of scale is relevant to the consideration of either hypothesis. It will change drastically the ratio of the volume of soft A-type regions, discussed in the Introduction, to the volume of hard B-type regions, if the regions near grain

boundaries are of paramount importance to the latter. This consideration, along with the change of average distances over which forces would act, should account for marked changes in behavior with size if the "constraint" hypothesis is valid. On the other hand, it must be admitted that the "averaging" of strain behavior is also improved in the statistical sense when the grain size is reduced by two orders of magnitude. However, one might have expected, in this case, that even a relatively small sampling of 16 grains, as on Face B of our specimen, might have revealed some trace of a consistent trend, and this was not the case. It is believed, therefore, that, while neither hypothesis is clearly tested by the results of this investigation, the picture of the effect of constraints upon the diffracting material when the grain size is small is the more favored one.

The author wishes to acknowledge the assistance of colleagues at the National Bureau of Standards, H. C. Vacher, who designed the special specimen holder-goniometer, and A. N. Graef, who built it.

5. References

[1] H. Lester and R. Aborn, Army Ordnance **6,** 120, 200, 283, 384 (1925).
[2] G. Greenough, Progr. Metal Phys. **3,** 176 (1952).
[3] D. M. Vasil'ev and B. I. Smirnov, Usp. Fiz. Nauk **73,** 505–558 (March, 1961). English Transl: Sov. Phys. Usp. **4,** No. 2, 226–259 (Sept.–Oct. 1961).
[4] S. Smith and W. Wood, Proc. Roy. Soc. **A182,** 404 (1944).
[5] C. J. Newton and H. C. Vacher, J. Inst. Met. **7,** 1193 (1955).
[6] D. M. Vasil'ev, Fiz. Tverd. Tela **1,** No. 11, 1736–1746 (Nov. 1959). English Transl: Sov. Phys.—Solid State **1,** No. 11, 1586–1595 (May 1960).
[7] M. J. Donachie, Jr., and J. T. Norton, Trans. Met. Soc. AIME **221,** 962 (1961).
[8] R. I. Garrod and G. A. Hawkes, Brit. J. Appl. Phys. **14,** 422–428 (July 1963).
[9] B. D. Cullity, Trans. Met. Soc. AIME **227,** 356–358 (April 1963).
[10] C. J. Newton, J. Res. NBS **67C** (Eng. and Instr.) No. 2, 101–109 (April–June 1963).
[11] C. S. Barrett, Structure of Metals, p. 328 (McGraw-Hill Book Co., Inc., New York, N.Y., 1952).
[12] H. C. Vacher, R. Liss, and R. W. Mebs, Acta Metallurgica **4,** 532–540 (Sept. 1956).
[13] T. Imura, S. Weissmann, and J. J. Slade, Jr., Acta. Cryst. **15,** 786 (1962).

(Paper 68C4–171)

JOURNAL OF RESEARCH of the National Bureau of Standards—C. Engineering and Instrumentation
Vol. 68C, No. 4, October-December 1964

Ferrimagnetic Resonance Measurements Using IF Substitution Techniques

W. E. Case,* R. D. Harrington, and L. B. Schmidt

(April 24, 1964)

Advantages of using an IF substitution method with a waveguide below cutoff attenuator for obtaining ferrimagnetic resonance line width of polycrystalline materials are discussed. An improvement in the IF system involving phase locking the local oscillator to the signal generator is described. Measurements were obtained which indicate that the above IF attenuator method compares favorably with accurate frequency measuring techniques for plotting entire resonance curves.

1. Introduction

The American Society for Testing and Materials has recently established a standard test method for determining the ferrimagnetic resonance line width and gyromagnetic ratio of nonmetallic magnetic materials [1].[1] The method essentially utilizes a precision RF attenuator located on the input side of the transmission cavity for determining the half-power points on the resonance curve of the sample. We have recently published tables which facilitate the calculation of the half-power points using the ASTM techniques [2]. At the same time, some of the advantages and disadvantages of using an IF substitution technique with a 30 Mc/s piston attenuator for obtaining these measurements were pointed out.

A typical advantage of IF detection may be found in greater sensitivity which increases the range of sample size and loss which can be measured. Another advantage is related to the increased accuracy inherent in the use of an IF substitution method using a waveguide below cutoff attenuator [3]. Furthermore, since the IF frequency is constant in such a setup, the same attenuator and detection system may be used in equipment designed for measurements at different microwave frequencies.

The primary disadvantage associated with the IF substitution method lies in the inconvenience and additional time required for manually tracking the local IF oscillator with the signal oscillator. This introduces delay in the time needed for the measurement of the maximum and 3 dB points on the resonant curve of the sample since the signal generator must be retuned at these points to maintain the cavity at resonance. The IF method of course requires somewhat more equipment than the RF substitution technique; however, with the exception of a precision waveguide below cutoff attenuator, the extra equipment is usually available in a typical laboratory. Furthermore, at the present time, complete IF attenuation measuring systems are becoming commercially available.

Our previous experience using the method adopted by the ASTM with an IF substitution arrangement had indicated that the advantages in many cases outweighed the disadvantages. For this reason, we have recently carried out further studies in an effort to gain a greater appreciation of the applicability of IF substitution methods in ferrimagnetic resonance setups in general as well as to develop a system for avoiding the disadvantage associated with local oscillator tuning. The purpose of this paper is to describe in somewhat more detail the results of these studies. This discussion will be divided into essentially two areas. First of all, the development of a ferrimagnetic resonance measurement system using a phase lock arrangment for automatically tracking the local oscillator with the signal oscillator will be described. Secondly, a comparison of the use of the attenuation method using a waveguide below cutoff attenuator with a method using an accurate frequency measuring technique for determining entire resonance loss curves will be discussed.

2. Experimental Setup

A typical experimental setup utilizing an IF substitution technique designed for measuring line width by means of the ASTM method has a waveguide below cutoff attenuator preceding the IF detector. Changes in the RF attenuation of the cavity due to the sample properties are measured by the corresponding changes in the IF attenuator which maintain a constant level signal to the IF detector. In a typical measurement of line width, the signal frequency is first adjusted to give cavity resonance for the empty cavity and the IF attenuator is set to a value, A_0, to give a convenient output reference level on the galvanometer. The sample is then inserted, the d-c magnetic field adjusted for maximum absorption in the sample, the frequency adjusted for cavity resonance, and the IF attenuator set to a new value which we designate as A_r in order to obtain the

*Radio Standards Physics Division, NBS Boulder Laboratories, Boulder, Colo.

[1] Figures in brackets indicate the literature references at the end of this paper.

same output reference level. Knowing A_0–A_r, it is possible to calculate the IF attenuator reading corresponding to the half-power points on the resonance curve of the sample. The attenuator is then set at this calculated value, and the line width is determined from the two d-c field settings necessary to alter the sample properties until the fixed output reference signal is obtained. Once again, the signal frequency must be adjusted to maintain cavity resonance corresponding to these new sample conditions. It is readily apparent from the above discussion that the magnetic d-c field and signal oscillator frequency settings are interdependent and require considerable trail and error adjustment for obtaining optimum conditions. The added complication of tuning a local oscillator to maintain a fixed IF frequency is obvious.

The availability of commercial phase lock systems offers a solution to the above problem. Such systems are usually used to lock the frequency of a klystron oscillator to some multiple of a low frequency crystal oscillator to produce stable microwave frequencies. The same equipment should be applicable for phase locking the klystron local oscillator to the signal oscillator in an IF system. An arrangement using a frequency discriminator to vary the local oscillator frequency to automatically track the frequency variation of the RF source has already been described in the literature [4].

We have recently developed a ferrimagnetic resonance measurement setup using a commercially available phase lock system in a 30 Mc/s IF substitution arrangement. In this system, the local oscillator is phase locked to a frequency 30 Mc/s below the signal frequency. A block diagram of this setup designed for a signal frequency, f_0, is shown in figure 1. Basically, the phase lock system compares the difference of the signal frequency f_0 and the IF local oscillator frequency f_0—30 Mc/s with a 30 Mc/s reference signal which is contained in the phase-lock unit. A d-c correction signal is applied to the local oscillator, a klystron, such that it tracks the signal oscillator. This local oscillator signal at a frequency of f_0—30 Mc/s is, of course, mixed with the cavity output signal at the frequency f_0 to produce

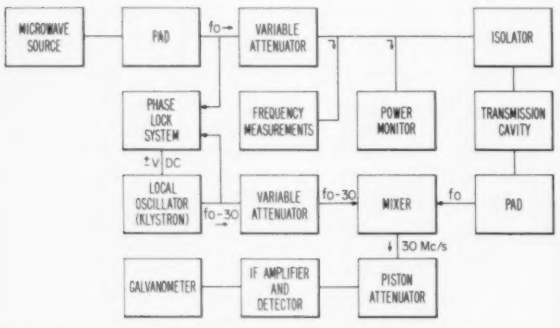

FIGURE 1. *Schematic diagram of equipment used for ferrimagnetic resonance work using a phase-locked IF substitution system.*

the IF frequency of 30 Mc/s. All attenuation measurements are made using the 30 Mc/s piston attenuator which controls the level of this IF signal. The remaining components in the system are used for level setting, power monitoring, and frequency measurements which are all common to setups of this type. These measurements also require d-c field measuring equipment such as a nuclear resonance gaussmeter, which is not shown in the diagram.

It should be recognized that attenuation measurements such as above require that the power levels in the overall system remain stable during a measurement. This is, of course, true for both the RF and IF substitution methods. A good temperature independent power monitoring setup is thus necessary in order that corrections can be made for any small variations in the power level of the system which may occur during a measurement. The crystal used in the power monitoring unit shown in figure 1 was mounted in a temperature controlled oven.

It is also apparent that the accuracy of measurements of this type is dependent upon the type of precision attenuator used. The piston attenuator used in the setup in figure 1 can detect attenuation changes of 0.01 dB. This type of performance is considerably better than can be obtained from most RF attenuators. Furthermore, accurate RF attenuators are in general available only over limited microwave frequency ranges. This frequency restriction is not applicable to the piston attenuator operating at the fixed IF frequency. Impedance matching is much less of a problem in piston attenuators than is the case for RF attenuators. While it is recognized that the insertion loss of a piston attenuator is rather high, this is not a serious disadvantage due to the high sensitivity in the IF detection system and the fact that the range of attenuation of concern in an ordinary measurement is not great.

An experimental evaluation of the above setup has given very satisfactory results. The local oscillator accurately tracks the signal oscillator during a typical measurement. As a result, the ease of operation of the IF method with this phase lock system compares favorably with the RF substitution method ordinarily used in the ASTM method.

3. Resonance Curve Plotting

The discussion thus far in the paper has referred primarily to the measurement of the 3 dB points on the resonance curve of a sample. However, many situations arise in which a knowledge of the shape of the complete loss curve is desirable. This is usually expressed as the imaginary susceptibility χ'' as a function of the applied field. Many techniques for plotting curves of this type are based on VSWR measurements using reflection type cavities [5]. Some of the earlier work in obtaining these measurements with transmission type cavities was based on the RF substitution method [6]. A more

recent description of the use of RF attenuators in such work has also been given by Silber [7]. However, with the development of transfer oscillators in conjunction with frequency counters, it has become possible to more accurately measure resonance curves in terms of changes in the Q when transmission cavities are used. On the other hand, a study of the working equations for plotting resonance curves suggests that the use of an accurate piston attenuator such as described above should allow such curves to be obtained from IF attenuation measurements with accuracies comparable to those obtained from frequency measurements. The advantages of the IF substitution method have also been recognized in the measurements of other types of materials such as high loss liquids [8]. It was thus the purpose of the present work to make a direct comparison of ferrimagnetic resonance curves obtained using a frequency counter and transfer oscillator with those obtained using a piston attenuator. In both cases, the IF system shown in figure 1 was used for obtaining the data.

It may be shown using an analysis such as described in reference 5 or 6 that the effective imaginary susceptibility of a small sample in a transmission cavity is given by

$$\chi'' = \frac{1}{2}\left(\frac{1}{Q_s} - \frac{1}{Q_0}\right) C \frac{V_c}{V_s}, \tag{1}$$

where

Q_s=loaded Q of the cavity with the sample;
Q_0=loaded Q of the empty cavity;
C=a constant dependent on the cavity and its mode;
V_c, V_s=volume of cavity and sample respectively.

When using the frequency method, the Q's in this equation are evaluated from $f/\Delta f$, where f is the resonant frequency and Δf is the frequency difference between the three dB points on the resonance curve. It might be mentioned that even for this frequency method, the accuracy of the piston attenuator is useful in calibrating these half-power points on the cavity resonance curve.

When using the attenuation method with a transmission cavity, it may be shown that eq (1) [see appendix] becomes

$$\chi'' = \frac{1}{2Q_0}\left(10^{\frac{A_0 - A_s}{20}} - 1\right) C \frac{V_c}{V_s}, \tag{2}$$

where

A_0=piston attenuator reading corresponding to empty cavity at resonance;
A_s=piston attenuator reading corresponding to any point on resonance curve of sample with cavity at resonance.

Measurements were taken on several different materials which directly compared the use of the frequency counter and eq (1) with the use of the piston attenuator and eq (2). Typical data taken at 110 Mc/s on one of these ferrite materials is shown in figure 2. It was found that excellent agreement was obtained between the two methods for several different materials provided care was taken to avoid or compensate for drift in the gain of the IF detection system in the attenuation measurement. As was pointed out for the RF substitution measurements described in the literature [6, 7], this drift may readily be corrected by using a high field reference level corresponding to the empty cavity.

It is felt that one of the more serious errors in either the frequency or attenuation method would be due to the dependence of the transmission loss of various components in the system on frequency. Both methods of course require small frequency changes to maintain the cavity at resonance during a measurement. Such effects are difficult to evaluate for both methods; however, errors due to the frequency sensitivity of transmission loss, impedance mismatches, etc., should be slight if only small frequency variations are encountered. Data obtained on disks such as shown in figure 2 indicated that the frequency and attenuation method in general agreed to better than 1 to 2 percent in the vicinity of the half-power points on the curves where the greatest frequency changes were necessary to maintain resonance in the cavity. This agreement suggests that transmission errors such as described above are in general quite small. Somewhat larger variations between the two methods are experienced in the wings of the resonance curve; however, the losses

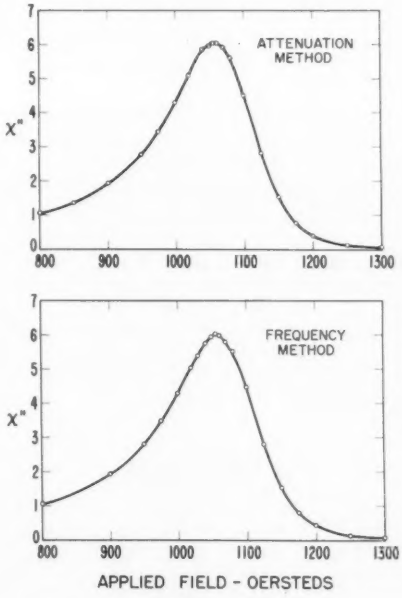

FIGURE 2. *Typical ferrimagnetic resonance loss curve of a thin disk sample at 1100 Mc/s obtained from frequency and attenuation measurements.*

are becoming so low in these areas that accurate measurements by either method becomes difficult.

The curves shown in figure 2 give the imaginary susceptibility of the material in the vicinity of ferrimagnetic resonance as a function of d-c field. In order to obtain the attenuation curve in terms of susceptibility, it was necessary to obtain a measurement of the loaded Q of the empty cavity as can be seen in eq (2). This would in general be obtained with the frequency method. However, this Q is assumed constant during the measurement and thus eq (2) can be written

$$\chi''=K\left(10^{\frac{A_0-A_n}{20}}-1\right), \tag{3}$$

where

$$K=\frac{1}{2Q_0}C\frac{V_c}{V_s}.$$

If $A_n=A_r$ and $\chi''=\chi''$ at the maximum point on the resonance curve, then

$$\chi_0''=K\left(10^{\frac{A_0-A_r}{20}}-1\right)$$

and

$$\frac{\chi''}{\chi_0''}=\frac{10^{\frac{A_0-A_n}{20}}-1}{10^{\frac{A_0-A_r}{20}}-1}, \tag{4}$$

which essentially means that the shape of the resonance curve normalized to its maximum value may be obtained by attenuation measurements alone. This may be convenient in various research programs.

4. Summary

It is concluded that the IF substitution technique may be applied to the ASTM method of line width measurement. It has particular advantages when measuring high loss samples or when data is desired at microwave frequencies where good RF attenuators are difficult to obtain. The convenience of the IF substitution method is considerably improved by phase locking the local IF oscillator to the signal oscillator. It has been demonstrated that this system can be used to plot entire resonance curves in terms of attenuation measurements with an accuracy comparable to that obtained with a frequency counter.

5. Appendix

Starting with eq (1),

$$\chi''=\frac{1}{2}\left(\frac{1}{Q_n}-\frac{1}{Q_0}\right)C\frac{V_c}{V_s}, \tag{1}$$

it can be shown from eq (9), p. 291, of reference [9] that

$$\frac{P_0}{P_i}=\frac{4Q_0^2}{Q_1Q_2}$$

for the empty cavity and

$$\frac{P_n}{P_i}=\frac{4Q_n^2}{Q_1Q_2}$$

for the cavity with sample where:

P_0 is the power output from the empty cavity;

P_i is the power input to the cavity;

P_n is the power output from the cavity with sample;

Q_0 is loaded Q of empty cavity;

Q_n is loaded Q of cavity with sample;

Q_1 and Q_2 are the coupling Q's of the input and output ports and are assumed constant during the measurements.

If P_i is held constant as is the case for the IF system,

$$\frac{P_0}{P_n}=\left(\frac{Q_0}{Q_n}\right)^2,$$

and substituting in equation (1)

$$\chi''=\frac{1}{2Q_0}\left(\sqrt{\frac{P_0}{P_n}}-1\right)C\frac{V_c}{V_s}.$$

This same equation is also given in references [6] and [7] except the power ratio is expressed in terms of equivalent voltage ratios.

Let the power input to the piston attenuator be BP_0 for the empty cavity and BP_n for the cavity with the sample where B is a proportionality constant. If P is the constant output power level of the piston attenuator, then the corresponding attenuator readings in decibels are given by

$$A_0=10\log_{10}\frac{BP_0}{P}$$

and

$$A_n=10\log_{10}\frac{BP_n}{P},$$

$$A_0-A_n=10\log_{10}\frac{P_0}{P_n}=20\log_{10}\frac{\sqrt{P_0}}{\sqrt{P_n}},$$

$$\frac{\sqrt{P_0}}{\sqrt{P_n}}=10^{\frac{A_0-A_n}{20}};$$

therefore,

$$\chi''=\frac{1}{2Q_0}\left(10^{\frac{A_0-A_n}{20}}-1\right)C\frac{V_c}{V_s},$$

which is eq (2) in the text.

6. References

[1] ASTM Test Method C524–63T. This method is under the jurisdiction of the ASTM Committee C–25 on Ceramics for Electronics.

[2] C. C. Preston and W. E. Case, Tables to facilitate the determination of the ferrimagnetic resonance line width of nonmetallic magnetic materials, NBS Tech. Note No. 173 (April 1963).

[3] R. E. Grantham and J. J. Freeman, A standard of attenuation for microwave measurements, AIEE Trans. **67,** 329–335 (1948).

[4] B. O. Weinschel, An accurate attenuation measuring system with great dynamic range, Microwave Jour. pp. 77–83 (September 1961).

[5] J. O. Artman and P. E. Tannenwald, Measurement of susceptibility in ferrites, J. Appl. Phys. **26,** No. 9, 1124–1132 (1955).

[6] E. G. Spencer, R. C. LeCraw, and F. Reggia, Measurement of microwave dielectric constants and tensor permeabilities of ferrite spheres, Proc. IRE **44,** 790–800 (1956).

[7] Handbook of microwave measurements, edited by M. Sucher and J. Fox, Polytechnic Institute of Brooklyn, Microwave Research Institute, Brooklyn, New York pp. 777–803 (1963).

[8] J. A. Lane and J. A. Saxton, Dielectric dispersion in pure polar liquids at very high radio-frequencies, Royal Soc. of London Proc. Ser. A, **213,** p. 400 (1952).

[9] C. G. Montgomery (ed.), Techniques of microwave measurements, pp. 289–291 (McGraw-Hill Book Co., Inc., New York, N.Y., 1947).

(Paper 68C4–172

741-635—64——5

JOURNAL OF RESEARCH of the National Bureau of Standards—C. Engineering and Instrumentation
Vol. 68C, No. 4, October-December 1964

A Pienkowsky-Type Calibration Scheme for 5211Σ1 Weight Series Using Two Knife-Edge Direct-Reading Balances

H. S. Peiser

(July 15, 1964)

To supplement information given in an earlier paper (J. Res. NBS **66C** (Eng. and Instr.) No. 1, 33 (1962)) a Pienkowsky-type series is presented for the calibration of a set of weights having a combined mass of 10 units and individual masses of 5, 2, 1, 1, and Σ1 where Σ1 may represent a group of weights the sum of whose masses is one. The scheme includes the usual observational and computational checks, especially those against standard weights included in the series. Effects of linear balance drift are eliminated from the calibration of the unknown weights.

1. Introduction

Weight calibration schemes were discussed generally by Almer et al.[1] After giving examples of Pienkowsky-type schemes the authors stated that such weighing series can be designed by a user to fit any combination of weights. In practice it has not been adequately easy for readers to design satisfactory Pienkowsky-type series. Fortunately the examples given in the earlier paper directly apply to most weight sets. The only important exception concerns weight sets made by German manufacturers with 5211Σ1 weight combinations. A suggested weighing sequence for 5211Σ1 series is therefore now published using the nomenclature and definitions given by Almer et al.

[1] H. E. Almer, L. B. Macurdy, H. S. Peiser, and E. A. Weck, Weight calibration schemes for two knife-edge direct-reading balances, J. Res. NBS **66C**, (Eng. and Instr.) No. 1, 33 (1962).

2. Weighing Scheme

In addition to the (5), (2), $(1)_1$, and $(1)_2$, and Σ(1) weights, standard $\_\_5$, and $\_\_2$ weights are included as well as any 3 weight of good constancy. This 3 weight is not evaluated in the series and is here designated C3. The weighing sequence is given in table 1. $\Sigma(10)=(5)+(2)+(1)_1+(1)_2+\Sigma(1)$ is assumed to have been previously evaluated; Its correction is a constraint as previously discussed. The range in sums $(c+l)$, $(d+h)$, $(e+i)$, $(f+j)$, $(g+k)$, and $(l+m)$ provide a precision check; ideally all the sums should be identical. $(b+m)-(c+n)$ is another precision check; ideally this difference should be zero. The check on balance sensitivity is provided by the comparison of the difference $(n'-n)$ with the accepted mass of the sensitivity weight.

The mass corrections of the weights to be determined are now given by the suggested solutions

TABLE 1

Scale reading			a	b	c	d	e	f	g	h	i	j	k	l	m	n	n′
Pan Load (indicated by cross).		Standard_5	x														
		(5)		x												x	x
		C3								x	x	x	x	x			
		Standard_2				x	x	x	x					x			
	Σ(5)	(2)			x		x	x	x	x					x		
		$(1)_1$			x	x		x			x		x		x		
		$(1)_2$			x	x			x		x	x			x		
		Σ(1)			x	x	x					x	x		x		
	Sensitivity weight																x
Total nominal load			5	5	5	5	5	5	5	5	5	5	5	5	5	5	
Linear balance drift error			$-\epsilon$	0	ϵ	2ϵ	3ϵ	4ϵ	5ϵ	6ϵ	7ϵ	8ϵ	9ϵ	10ϵ	11ϵ	12ϵ	

TABLE 2. K=$Cr\Sigma(10)$

Scale reading		a	b	c	d	e	f	g	h	i	j	k	l	m	n	K	Linear balance drift error	Variance	Variance of least squares solutions
Cr..5	$=\frac{1}{4}($	$4a$	$-3b$	$-c$										$-m$	$+n$	$+2K)$	-1ϵ	1.75	1.22
Cr (5)	$=\frac{1}{4}($		b	$-c$										$-m$	$+n$	$+2K)$	0	0.25	0.22
Cr..2	$=\frac{1}{10}($		$-b$	$-2c$	$+3d$	$+e$	$+f$	$+g$	$-h$	$-i$	$-j$	$-k$	$+4l$	$-2m$	$-n$	$+2K)$	-0.8ϵ	.42	.39
Cr (2)	$=\frac{1}{10}($		$-b$	$+c$	$-3d$	$+e$	$+f$	$+g$	$+3h$	$-i$	$-j$	$-k$		$+m$	$-n$	$+2K)$	0	.28	.28
Cr $(1)_1$	$=\frac{1}{20}($		$-b$	$+c$	$+2d$	$-4e$	$+6f$	$-4g$	$-2h$	$+4i$	$-6j$	$+4k$		$+m$	$-n$	$+2K)$	0	.37	.37
Cr $(1)_2$	$=\frac{1}{20}($		$-b$	$+c$	$+2d$	$-4e$	$-4f$	$+6g$	$-2h$	$+4i$	$+4j$	$-6k$		$+m$	$-n$	$+2K)$	0	.37	.37
$Cr\Sigma$ (1)	$=\frac{1}{20}($		$-b$	$+c$	$+2d$	$+6e$	$-4f$	$-4g$	$-2h$	$-6i$	$+4j$	$+4k$		$+m$	$-n$	$+2K)$	0	.37	.37
Linear balance drift error		$-\epsilon$	0	ϵ	2ϵ	3ϵ	4ϵ	5ϵ	6ϵ	7ϵ	8ϵ	9ϵ	10ϵ	11ϵ	12ϵ				

The sum of the coefficients for a through n must vanish for each line.

given in table 2. The solutions have conveniently small coefficients yet are very close to least squares solutions.

Optimum trend elimination for linear balance drift is given for all unknown weights but not for the standard weights, so that the values obtained for the standard weights are more likely to be affected by drift.

The correction values for the standards are compared with the accepted values.

Convenient computational checks are:

$$\mathrm{Cr}(1)_1-\mathrm{Cr}(1)_2=\tfrac{1}{2}(f-g-j+k)$$

$$\mathrm{Cr}\Sigma(1)-\mathrm{Cr}(1)_2=\tfrac{1}{2}(e-g-i+k)$$

$$\mathrm{Cr}(2)-\mathrm{Cr}..2=\tfrac{1}{2}(c-d+h-l)$$

$$\mathrm{Cr}(1)+\mathrm{Cr}\Sigma(1)-\mathrm{Cr}..2=\tfrac{1}{2}(c-g+k-l)$$

$$\mathrm{Cr}(1)_1+\mathrm{Cr}(1)_2-\mathrm{Cr}(2)=\tfrac{1}{2}(d-e-h+i)$$

The series has six degrees of freedom calculated as described in the previous paper.

It should be noticed that during the series all weights other than the standard ..5 and C3 are put on the balance more than once which reduces the likelihood of false weight placings remaining undetected. Consistent with that requirement the series is designed to reduce interchanges of weights for successive observations.

Although the responsibility for this weighing scheme rests solely with the author, he is deeply conscious of having drawn freely on the superior knowledge and experience of other past and present members of the National Bureau of Standards: especially A. T. Pienkowsky, L. B. Macurdy, J. M. Cameron, and Mrs. M. E. Jones.

(Paper 68C4–173)

JOURNAL OF RESEARCH of the National Bureau of Standards—C. Engineering and Instrumentation
Vol. 68C, No. 4, October–December 1964

Reference Tables for the Platinel II Thermocouple

L. O. Olsen and P. D. Freeze

(May 28, 1964)

A new thermocouple, Platinel II, was developed by Engelhard Industries, Inc., for sustained operation in oxidizing gases at temperatures higher than those possible with Type K thermocouples, yet having a temperature thermal emf relation comparable to them. The need of reference tables for this thermocouple was made evident by the growing acceptance and increased usage of it.

Twenty-seven thermocouples made of 20-, 30-, and 40-mil diameter elements drawn from three separate melts of the positive and negative alloys were calibrated. Three equations for three temperature ranges were found to fit the averaged data of all thermocouples with a maximum deviation of only 9 microvolts. The reference tables presented were computed from these three equations. They give emfs for each degree Celsius from −100 to 1371 °C and for each degree Fahrenheit from −150 to 2500 °F. Usually these tables, when used in conjunction with any typical undamaged Platinel II thermocouple, will provide temperatures which are not in error by more than 3, 5, and 10 °F at 500, 1000, and 2500 °F, respectively. Other tables are of temperatures in both degrees C and degrees F with emf in millivolts as the argument.

Tables of temperature versus emf of the two elements of Platinel II versus Pt 27 and of copper versus the two elements are also presented. A comparison of the thermal emf of Platinel II with that of Chromel-Alumel is shown. The two thermocouples develop identical emfs at 32, 1300, and 2225 °F. Between 1000 and 2500 °F the maximum indicated difference is only 18 °F when the Chromel-Alumel reference table is used.

1. Introduction

Along with the advances in the technologies of combustion and metallurgy have come substantial increases in the temperature of gaseous products emanating from heat engines. The continuing effort to increase thrust and efficiencies of propulsion engines presages even higher temperatures of exhaust gas in the future. As a result of these higher temperatures a need has arisen for thermocouples capable of sustained operation in hot oxidizing gases. In the past and for most applications at present the base-metal type K thermocouples are adequate for the measurement and control of temperatures of gaseous mixtures. However, as temperatures increase, the thermoelectric stability and life expectancy of such thermocouples will not be satisfactory. For instance, they will not last for the usual 1000 hours between jet engine overhauls. Replacement of thermocouples in jet engines is a very costly procedure not only because of thermocouple expense but also because of the very large labor cost. Therefore, any thermocouple system which needs neither repairs nor replacement during the period between major overhauls will result in substantial savings. The same advantages will accrue to other industrial equipment and processes that involve temperatures that are too high for long-time continued use of the conventional thermocouples.

For these reasons Accinno and Schneider [1] [1] and [2] developed Platinel.[2] Two different combinations have been produced and are named Platinel I and Platinel II. The negative element in each of the thermocouples consists of 65 percent gold and 35 percent palladium (Platinel 1503). The positive element in Platinel I is an alloy containing 83 percent palladium, 14 percent platinum and 3 percent gold (Platinel 1786) and that used in Platinel II contains 55 percent palladium, 31 percent platinum and 14 percent gold (Platinel 1813). Zysk [3] reports that because of its superior mechanical fatigue properties Platinel II is the preferred type.

Following the development of the Platinel thermocouple, a considerable amount of work of evaluating its properties was performed at both Engelhard Industries, Inc. [4] and the National Bureau of Standards [5]. The results of these works indicated the Platinel II thermocouple to be considerably more resistant to oxidation than the type K thermocouples over the entire usable range of temperatures. In addition, the thermoelectric stability was found to be quite good. The changes in thermal emf remained within a ±3/4 percent tolerance for 1000 hr of exposure to air at 2200 °F.

---

[1] Figures in brackets indicate the literature references on page 271.
[2] Registered Trademark of Engelhard Industries, Inc. Patent U.S. 3,066,177, November 27, 1962.

On the basis of these promising results it was decided to establish reference tables for this thermocouple so that it can be used more widely and conveniently. It was further decided to fit empirical equations to the calibration data, if possible, in order to avoid the necessity of storing the complete table when making computer calculations.

A description of reference tables for thermocouples and instructions for their use in conjunction with deviation curves are given by Shenker et al. [6]: "The temperature-electromotive-force relationship for a thermocouple in general cannot be expressed by a simple equation. It is convenient, therefore, to have empirical tables giving the temperature-electromotive-force relationship for the various types of commercially available thermocouples. For any thermocouple type, a table is based on calibrations of representative thermocouples at sufficient points to yield a temperature-electromotive-force plot characteristic of the material. These tables, therefore, do not represent the temperature-electromotive-force relationship for a particular thermocouple but rather a mean of a number of thermocouples of that type. The reference tables so derived provide a basis for drawing deviation curves for comparing individual thermocouples with others of their type or with instruments calibrated to read temperature directly. By using the reference tables in conjunction with a deviation curve, greater precision may be obtained by using a given number of calibration points than from the use of the calibration data alone. The deviation curve is constructed by plotting the differences between the calibration data of an individual instrument and the reference table. The points so plotted may then be connected by a continuous curve which may be used for interpolating between calibration points. For example, it is desired to determine the temperature of a furnace from the measured electromotive force of a calibrated thermocouple. The electromotive force developed by the thermocouple, however, does not correspond to that of any of the calibration points. By plotting a difference curve from the calibration data, one may interpolate between the calibration points to find the correction to be added algebraically to the measured electromotive force to yield the reference table value. The reference table may now be referred to and the furnace temperature corresponding to the corrected thermocouple electromotive force determined."

2. Thermocouples

In order for the calibrations obtained in this work to be representative of Platinel II, three lots of each of the positive and negative elements from separate melts were purchased from Englehard Industries, Inc., the proprietors of this thermocouple. The three lots A, B, and C were selected from wires drawn from bars designated by numbers assigned by the maker as follows:

Lot	Bar numbers	
	Alloy 1503	Alloy 1813
A	43250	43249
B	48946	49085
C	50125	31369

Wires of each of the bars were drawn to 20-, 30-, and 40-mil diameters. Three thermocouples of each wire size and lot were made; thus, 27 thermocouples were available for calibration. They were identified by numbers such as 2–B–30, where the first number refers to the number of the thermocouple, the letter to lot, and the last number to wire diameter in mils.

All elements were 48 in. long and prior to calibration were annealed at a temperature of 2400 °F for a period of 90 min. This was accomplished through electric heating with alternating current in clean draft-free air. The reasons for this lengthy anneal at high temperature are discussed in a later section.

3. Apparatus and Experimental Procedure

All thermocouples with the exception of 3–A–40 were calibrated as described above. Thermocouple 3–A–40 was reserved for calibration at temperatures below 32 °F and comparison with other selected samples at these low temperatures. It was calibrated at six temperatures from −148 °F to 77 °F. These measurements were made in a stirred bath of a cryogenic liquid by members of the Temperature Physics Section. The uncertainty of the measurements below 32 °F was reported to be ±0.2 °F. Using thermocouple 3–A–40 as a standard, six other selected thermocouples were compared with it over the same temperature range and with approximately the same uncertainty. Thus, over the range of temperatures from −148 °F to 77 °F the reference tables are the results of the measurements on the seven following thermocouples: 3–A–40, 1–B–30, 2–B–30, 3–B–30, 1–C–20, 1–C–30, and 1–C–40. From 100 °F to 2500 °F the reference tables are determined from the results of calibrations of 26 thermocouples.

The calibrations from 100 °F to 2500 °F were conducted in a Pereny horizontal tube furnace. The tubular heating element was of silicon carbide, 36 in. long with an inside diameter of 3.5 in. Temperature regulation and control were accomplished with a 36 tap transformer, a saturable core reactor, and a Wheelco controller.

To prevent contamination of the thermocouples from the silicon carbide heating element, a high temperature porcelain, closed end, protection tube (36 in. long with an inside diameter of 3 in.) was inserted into the heating element.

Further protection was provided by another closed end tube of Degussit Al 23, a high-purity impervious alumina. It was supported only near the relatively cool open end and its axis coincided with that of the heating element. This tube had an inside diameter of 12 mm and a length of 24 in. Thermal gradients along the axis of this protection tube were found to be quite small near the center of the furnace (i.e. 18 in. from the open end of the furnace tube). A typical temperature traverse along the axis from the end to the center of the tube is shown in figure 1 for a furnace temperature of about 2400 °F where there is a drop in temperature of only 10 °F from the center of the tube to a distance 4 in. from the center.

Three Platinel II thermocouples along with a calibrated 20-mil platinum versus platinum 10 percent rhodium thermocouple used as the standard of comparison were threaded through two pieces of 24-in.-long Degussit Al 23, four-hole tubing. All eight wires were pressed into intimate electrical and thermal contact by flattening a short piece of small platinum tubing over them. This common junction was placed about 1 in. beyond the center of the furnace tube thereby locating the junction and 2 in. of the thermocouples in virtually a gradient free zone as shown in figure 1.

Measurements of the thermal emf of the standard and test thermocouples were made by simultaneous reading of two Leeds & Northrup Type K–3 potentiometers. Measurements of the thermal emf of all test thermocouple elements versus platinum were also made.

Observations were made in increments of about 50 °F from 100 °F to 2300 °F. This was followed by another series of observations made in descending order of 50 °F increments down to 100 °F. Measurements were then made from 2300 °F to 2500 °F and back down to 2300 °F, again at 50 °F intervals. These measurements were made last because of the decreased stability of the thermocouples at these higher temperatures. The maximum deviation from integral multiples of 50 °F was 5 °F while the vast majority did not exceed 2 °F.

The platinum versus platinum 10 percent rhodium thermocouples used as standards of comparison were calibrated before and after the calibration of each group of three Platinel II thermocouples. These calibrations were made with a platinum versus platinum 10 percent rhodium thermocouple which had a primary calibration and was used exclusively for this work. The thermal emfs of the individual elements of Platinel II versus platinum were determined between 0 and 1450 °C at intervals of about 100 °C. Thus, these can be referred to Pt 27, the platinum reference standard, which is maintained at the National Bureau of Standards. The uncertainties of interpolated values are ±0.5 °C up to 1100 °C and ±2 °C at 1450 °C [7]. On the Fahrenheit scale of temperature these correspond to about ±0.8 °F up to 2000 °F and ±3.0 °F at 2500 °F. The maximum change in calibration of any of the standard thermocouples was only about 0.6 °F and occurred at about 900 °F. Most of this change developed during its first use. The inaccuracies of the two potentiometers contribute slightly to the uncertainty in the values of the temperature of the test thermocouples. The maximum error in the measurement of the emf of the platinum versus platinum 10 percent rhodium thermocouple is ±0.2 to ±1.8 μV. The corresponding errors in the measurements of the Platinel II thermocouple are ±0.2 to ±7.5 μV. These errors combine to increase the uncertainty about ±1.1 °F at 2500 °F. Thus, the maximum uncertainty is about ±4 °F at 2500 °F.

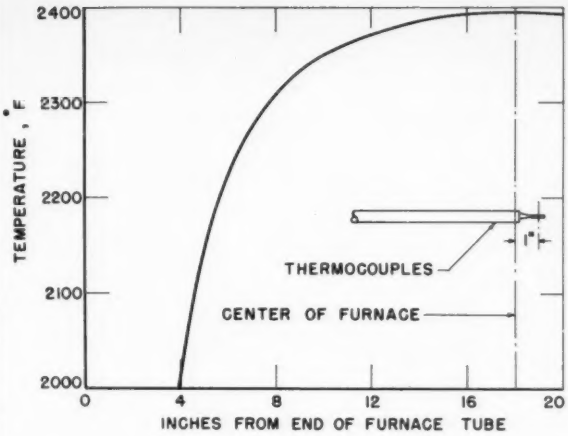

FIGURE 1. *Typical temperature gradient in furnace tube.*

4. Computations

In the temperature range from −148 °F to 77 °F the reference tables are based on the results of seven previously designated thermocouples. One observation on each thermocouple was made at each of six different temperatures within this range of temperatures. The averages of the observations (temperature and emf) on all seven thermocouples at each of these six temperatures were then calculated. From 100 °F to 2500 °F, at 50 °F intervals, the observations on 26 thermocouples in both ascending and descending order of temperature were averaged. Thus, for this range of temperatures, each averaged observation is the result of 52 separate measurements. These data consisting of 55 temperatures and their corresponding emfs are shown in table 1. In the absence of a known functional form for the relation of temperature and emf, a set of three polynomial arcs were used as an approximation to the function. There is some arbitrariness in the selection of the number of intervals and also the width of these intervals. After several trials it was found that equations for three ranges of temperature gave a good fit to the data.

TABLE 1. *Fifty-five averages of observations on Platinel II thermocouples*

Electromotive force in absolute millivolts. Temperature in degrees F*. Reference junctions at 32 °F.

Temperature	Millivolts	Temperature	Millivolts
°F		°F	
−148.0	−2.587	1198.4	26.815
−103.0	−2.008	1248.6	28.053
−58.0	−1.384	1298.4	29.274
−13.0	−0.718	1349.1	30.507
32.0	0.000	1398.1	31.688
77.0	0.768	1448.5	32.887
101.7	1.209	1497.6	34.048
149.0	2.076	1547.8	35.217
200.0	3.054	1599.2	36.396
248.8	4.038	1649.8	37.547
299.1	5.089	1698.4	38.630
349.1	6.169	1747.0	39.712
400.2	7.304	1797.5	40.816
449.9	8.432	1848.5	41.916
498.4	9.547	1898.6	42.986
549.3	10.742	1949.3	44.053
599.5	11.939	1998.2	45.070
649.6	13.154	2049.3	46.113
698.5	14.352	2099.1	47.116
749.1	15.600	2148.7	48.098
799.4	16.840	2199.2	49.082
849.5	18.091	2249.6	50.043
900.2	19.360	2300.0	50.984
948.9	20.580	2350.3	51.906
999.0	21.832	2399.1	52.791
1048.6	23.075	2450.2	53.701
1098.5	24.326	2499.7	54.568
1150.0	25.614		

*Based on the International Practical Temperature Scale of 1948.

An equation of the fourth degree with coefficients computed to give a least square fit to the data from −148 °F to 948.9 °F was found to be

$$\text{Millivolts} = 1.6522713\times10^{-2}t + 1.1041292\times10^{-5}t^2 - 6.0798812\times10^{-9}t^3 + 1.1800871\times10^{-12}t^4$$

where t = (temperature in degrees Fahrenheit) − 32°. This equation is used from −150 °F to 873 °F and shows a maximum deviation from the data of 9 μV. From 873 °F to 1178 °F the reference tables are computed from a linear equation derived from the data ranging from 900.2 °F to 1150.0 °F.

$$\text{Millivolts} = -2.3779626 + 2.5037757\times10^{-2}t.$$

In this range the maximum deviation of the data from the reference table is 2 μV. From 1178 °F to 2500 °F the reference table is developed by another equation of the fourth degree with coefficients computed from the data from 1048.6 °F to 2499.7 °F. The maximum deviation is again 9 μV.

$$\text{Millivolts} = -3.5875425 + 2.6136249\times10^{-2}t + 1.1471194\times10^{-6}t^2 - 1.1611900\times10^{-9}t^3 + 1.1112684\times10^{-13}t^4$$

The maximum deviation of 9 μV was considered satisfactorily small; hence, using the three equations the computer was used to calculate emfs for each degree Celsius from −100 to 1371, and for each degree Fahrenheit from −150 to 2500. These values are shown in tables 2A and 4A in the appendix. Tables 1A and 3A, which are emf versus degrees C and emf versus degrees F, were obtained from interpolation at 0.1 mV intervals and the temperatures are reported to the nearest tenth of a degree.

5. Results and Discussion

The principal results of this work are the reference tables, 1A, 2A, 3A, and 4A, which show excellent agreement with the earlier work of Zysk [3]. The maximum difference between these tables and his preliminary tables is only 80 μV. Other information arising from the experiments is of considerable interest and is also presented.

The maximum deviation of the reference tables from the averaged experimental values in table 1 as computed from the equations is 9 μV. A plot of all such deviations is presented in figure 2. While the

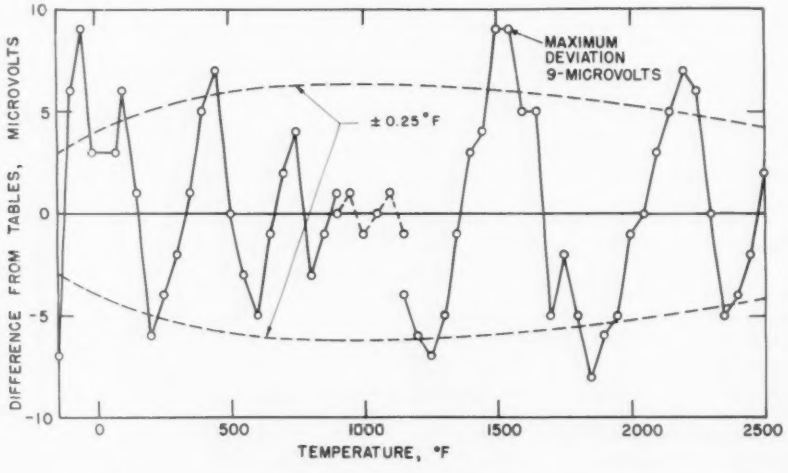

FIGURE 2. *Differences between averaged experimental and reference table values of thermal emf.*

deviations show a definite cyclic pattern, the same pattern was also present in deviations from fifth- and sixth-degree polynomials fit to the same sets of data. The situation is analogous to the mathematical problem of approximating a segment of, say, the exponential or sine curve by a polynomial. It cannot fit the function exactly, but achieves its best fit by undulating about the curve as closely as possible [11]. The reductions in the maximum deviations, going from fourth- to fifth- or sixth-degree polynomials, were small, and the deviations are small as compared to the deviation of individual thermocouples from the reference tables and to the change in emf through exposure to elevated temperatures. In view of these facts, the fourth-degree equations in conjunction with the linear equation were considered to give an adequate representation of the function for the purpose at hand. The deviations are in fact so small they can be ignored and the values in the reference tables as calculated from the three equations need not be adjusted. Thus, a temperature-emf relation with no discontinuities is provided. Such a relation is considered desirable by Benedict and Ashby [8] for computer application. They have "improved" existing tables for base-metal thermocouples with selected values at 50-deg intervals and a second-degree Lagrange interpolation for all values between selected values. If computer programming would be simplified by such interpolation, these data should be amenable to such treatment. However, it seems likely that the three equations will be more convenient in computer programming.

Figure 3 is presented to show the deviations of individual measurements from the values in the reference tables. They are derived from the measurements of all 26 thermocouples in both ascending and descending order. Thus, at each of the six selected temperatures shown, there are 52 individual deviations. The maximum deviation is 116 μV at 2500 °F, which corresponds to about 6.7 °F or 0.26 percent. At 500 °F the maximum deviation is 50 μV, which corresponds to 2.2 °F or 0.43 percent. These values are well within the usual tolerance of ¾ percent allowed for base-metal thermocouples. As a matter of fact, nearly all of the thermocouples are within the ⅜ percent tolerance for selected wires. On the basis of these experiments with 26 thermocouples from three different lots of wire it seems safe to say that the temperature of any Platinel II thermocouple, as determined from the reference tables, will

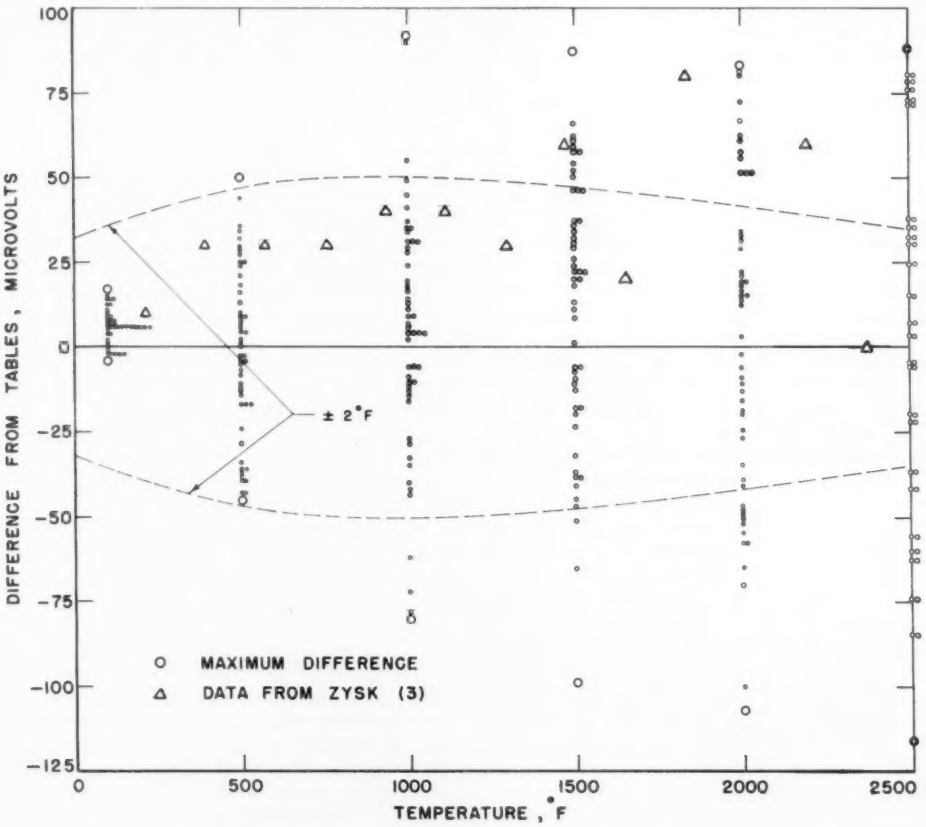

FIGURE 3. *Differences between individual experimental and reference table values of thermal emf.*

be within 0.5 percent of the true temperature. Thus, for most work, a calibration of the thermocouple will not be necessary. It is interesting to note that Zysk's calibration also falls within these limits. The triangular symbols shown on figure 3 are the data from [3].

It was not convenient to indicate individual thermocouples on figure 3 because the large number of thermocouples and observations make such indication extremely difficult; therefore, figure 4 is presented to show the deviation of the output of individual thermocouples from the values in the reference table. These plotted data are for four thermocouples selected at random. They are taken from the average of the observations obtained during both the ascending and decreasing temperature series. From the shapes of these deviation curves it is obvious that for precision thermometry these thermocouples will have to be calibrated at many different temperatures. Not one of the test thermocuples exhibits a linear deviation curve which makes corrections possible with only two calibration points. This is not too surprising since few thermocouples exhibit this desirable characteristic. In this case the lack of linearity is probably due to a shift in calibration during the calibration experiments. In some cases there was considerable change in output between two measurements, one of which was obtained from the increasing and the other from the decreasing temperature series. This change in calibration is shown clearly in figure 5 in which each plotted point is the difference in output between observations obtained at a particular temperature during the increasing and decreasing temperature series. Although this plot is for all of the thermocouples made from the wire of Lot B only it is quite similar to those for Lots A and C. There are two major points of similarity: (1), thermocouples from all three lots experienced the greatest change in output at about 1000 °F; (2) there was a change in sign in the calibration shift of many of the thermocouples in the range of temperatures between 500 and 1000 °F. Upon examination of figure 4 it will be noted that the change in slope of most of the deviation curves also occurs in this same temperature range. It is possible that the change in calibration shown in figure 5 and the change in slope of the deviation curves in figure 4 are the result of some change in one or both of the Platinel alloys. According to a survey by Vines [9] the palladium gold system appears to consist of a continuous series of solid solutions free from transformation in the solid state. However, a peculiar change in the slope of the electrical resistivity and temperature coefficient of electrical resistivity curves in the neighborhood of 70 percent gold has not been explained. This is very close to the composition of the negative element which consists of 65 percent gold and 35 percent palladium.

In some earlier work [5] in which the emf of the individual elements against platinum were measured, the negative element (1503) underwent the greatest change when aged at 2300 °F for 1500 hr. The situation was reversed in the case of the elements aged at 1900 and 2200 °F for 1500 hr. At these aging temperatures the changes in emf of the positive elements (1813) were considerably greater than those of the negative. In this more recent work the emf of the alloy 1813 versus platinum showed the smaller change in emf. In this case the maximum temperature to which the elements were exposed was 2300 °F and for at most only about ½ hr.

There are also a few significant differences in the results of the later tests. The 40-mil thermocouples from Lots B and C suffered the greatest change in emf. From Lot A the 20-mil thermocouples experienced the greatest change while the 40-mil showed very little change. The maximum changes for any thermocouple from Lots A, B, and C were 61, 74, and 92 μV. With changes of this magnitude occurring during calibration the nonlinearity of the deviation curves as shown in figure 4 assumes lesser importance, particularly in the temperature range from 500 to 1000 °F. In this region the maximum change in emf is about the same magnitude as the maximum deviation of the thermocouple emfs from the reference tables; therefore, corrections would be rather difficult to apply.

The long period and high-temperature anneal described in the section entitled Thermocouples was an effort to minimize such changes in the emf during calibration. This procedure was determined from much experience with several thermocouples and a comprehensive set of experiments with one 20-mil thermocouple. Following a determination of its emf at 2300 °F it was heated electrically for ½ hr at 2400 °F. Its emf was again determined at 2300 °F. Emf determinations were repeated following additional heating periods of ½, 1, 1, 3, and 3 hr. The change in microvolts from the original emf is plotted versus the accumulated heating times in figure 6. A large decrease in output after ½ hr of heating is followed by a partial recovery during the next half-hour of heating. Additional heating results in further recovery. Although it is not shown for this thermocouple, prolonged heating will ultimately result in an output greater than the original. It is recognized that 90 min of heating is an inconvenient annealing time; however, this annealing period is considered necessary to eliminate the large emf changes that occur in these thermocouples during the first hour of heating.

The thermal emfs of the two Platinel elements versus the platinum leg of the standard thermocouple were developed from the averages of the observations obtained during the calibrations. Tables 2 and 3, thermal emfs of the elements versus Pt 27, were obtained by adjusting these values to compensate for the difference between Pt 27 and the thermocouple platinum. The thermal emf developed between 1813 and Pt 27 is very low; thus, the emf developed between 1503 and Pt 27 is very nearly equal to that of Platinel II. 1813 is thermoelectrically positive to Pt 27 up to about 1675 °F where it becomes negative. The negative element 1503 is negative to Pt 27 from 32 to 2500 °F. These data in conjunction with a calibration of copper

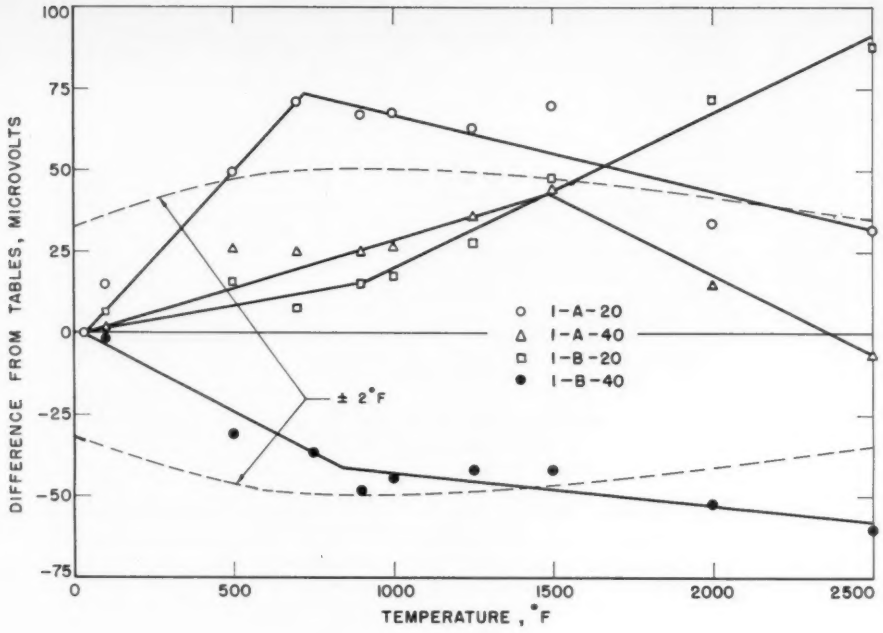

FIGURE 4. *Differences between experimental and reference table values of thermal emf for four thermocouples.*

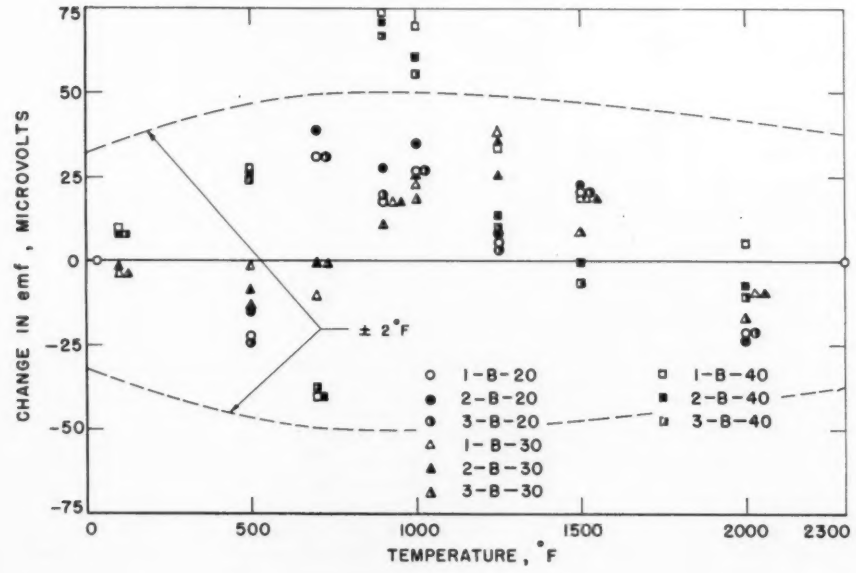

FIGURE 5. *Change in thermal emf between determinations from increasing and decreasing temperature series.*

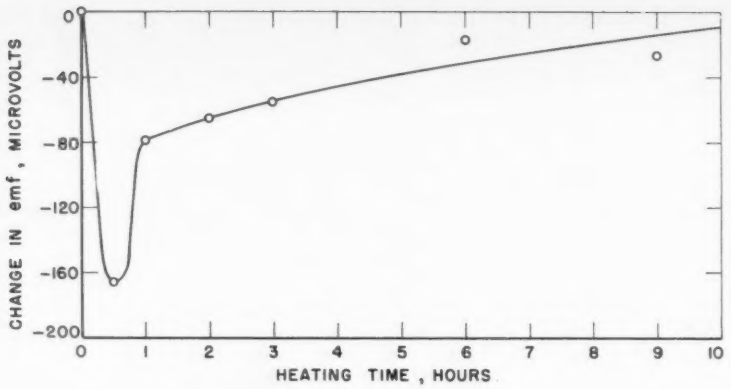

FIGURE 6. *Change in thermal emf at 2300 °F as a function of heating time at 2400 °F.*

TABLE 2. *Thermal emf of 1503 versus Pt 27*

Reference junctions at 32 °F.

Temperature	Millivolts	Temperature	Millivolts
°F		°F	
32	0.000	1400	−31.285
50	−0.300	1450	−32.534
100	−1.163	1500	−33.777
150	−2.064	1550	−35.016
200	−3.001	1600	−36.249
250	−3.971	1650	−37.476
300	−4.974	1700	−38.697
350	−6.005	1750	−39.909
400	−7.063	1800	−41.114
450	−8.147	1850	−42.309
500	−9.253	1900	−43.496
550	−10.380	1950	−44.673
600	−11.526	2000	−45.840
650	−12.689	2050	−46.997
700	−13.869	2100	−48.145
750	−15.063	2150	−49.282
800	−16.269	2200	−50.407
850	−17.488	2250	−51.521
900	−18.718	2300	−52.624
950	−19.956	2350	−53.715
1000	−21.201	2400	−54.794
1050	−22.453	2450	−55.861
1100	−23.711	2500	−56.916
1150	−24.977		
1200	−26.246		
1250	−27.510		
1300	−28.772		
1350	−30.031		

TABLE 3. *Thermal emf of 1813 versus Pt 27*

Reference junctions at 32 °F.

Temperature	Millivolts	Temperature	Millivolts
°F		°F	
32	0.000	1400	.445
50	0.001	1450	.385
100	.010	1500	.318
150	.030	1550	.243
200	.059	1600	.161
250	.095	1650	.071
300	.136	1700	−.026
350	.182	1750	−.129
400	.231	1800	−.238
450	.281	1850	−.353
500	.331	1900	−.474
550	.381	1950	−.600
600	.430	2000	−.732
650	.476	2050	−.870
700	.518	2100	−1.014
750	.556	2150	−1.163
800	.589	2200	−1.317
850	.616	2250	−1.476
900	.637	2300	−1.640
950	.651	2350	−1.809
1000	.658	2400	−1.983
1050	.658	2450	−2.162
1100	.651	2500	−2.345
1150	.637		
1200	.651		
1250	.585		
1300	.546		
1350	.499		

versus Pt 27 furnished the data for the construction of table 5A, which presents the thermal emf of copper versus 1503 and 1813 from 32 to 500° F. These values are often necessary when thermocouple cold junctions are at temperatures other than 32 °F. The values for 1503, 1813, and copper versus Pt 27 are given in 25 °F intervals in table 5A. The copper versus Pt 27 values are in excellent agreement with those of Roeser and Dahl [10] which were reported to the nearest 10 μV. It will be noted that copper is thermoelectrically positive to Pt 27 and to both elements of Platinel II.

One of the aims in the design of Platinel II was to develop a thermocouple having essentially the same thermal-emf relation as Chromel-Alumel.[3] Table 4 shows a comparison of the thermal emf of Platinel II and Chromel-Alumel from NBS Circular 561 over the entire range of calibration in increments of 50 °F. The third column is the difference in degrees F indicated by the two thermocouples if the Chromel-Alumel reference table is used for both. The thermocouples develop identical thermal emfs at 32, 1300, and 2225°F. Between 1000 and 2500 °F the maximum difference between the two thermocouples is only 18 °F.

[3] Registered Trademark of Hoskins Manufacturing Co.

TABLE 4. *Comparison of Platinel II with Chromel-Alumel thermocouple*

Reference junctions at 32 °F.

Temperature	Platinel II	Chromel-Alumel	Difference*
°F	mV	mV	°F
−150	−2.603	−3.52	+53
−100	−1.974	−2.65	+36
−50	−1.277	−1.70	+21
0	−0.517	−0.68	+8
32	0.000	0.00	0
50	0.301	0.40	−4
100	1.173	1.52	−15
150	2.094	2.66	−25
200	3.060	3.82	−33
250	4.066	4.97	−39
300	5.110	6.09	−44
350	6.187	7.20	−46
400	7.294	8.31	−46
450	8.428	9.43	−45
500	9.584	10.57	−44
550	10.761	11.71	−41
600	11.956	12.86	−39
650	13.165	14.02	−37
700	14.387	15.18	−34
750	15.619	16.35	−31
800	16.858	17.53	−28
850	18.104	18.70	−26
900	19.355	19.89	−22
950	20.607	21.07	−20
1000	21.859	22.26	−17
1050	23.110	23.44	−14
1100	24.362	24.63	−11
1150	25.614	25.81	−8
1200	26.861	26.98	−5
1250	28.095	28.15	−2
1300	29.318	29.32	0
1350	30.529	30.49	+2
1400	31.730	31.65	+3
1450	32.919	32.80	+5
1500	34.095	33.93	+7
1550	35.259	35.07	+8
1600	36.410	36.19	+9
1650	37.547	37.31	+10
1700	38.671	38.43	+11
1750	39.780	39.53	+12
1800	40.876	40.62	+12
1850	41.956	41.70	+12
1900	43.022	42.78	+11
1950	44.072	43.85	+10
2000	45.108	44.91	+10
2050	46.127	45.96	+8
2100	47.131	47.00	+6
2150	48.119	48.03	+4
2200	49.090	49.05	+2
2250	50.045	50.06	−1
2300	50.984	51.05	−4
2350	51.906	52.03	−7
2400	52.811	53.01	−10
2450	53.699	53.97	−14
2500	54.571	54.92	−18

*Temperature difference based on Chromel-Alumel table in NBS Circular 561.

6. Conclusions

It should be remembered that the reference tables cited herein were determined from the average values of 27 thermocouples of three wire diameters from three lots each of positive and negative alloys. Although the tables when plotted represent the shape of the temperature-emf curve for Platinel II very well, they cannot be depended upon to provide a calibration curve or temperature-emf relationship for a particular thermocouple. Usually these tables, when used in conjunction with any typical undamaged Platinel II thermocouple, will provide temperatures which are not in error by more than 3, 5, and 10 °F at 500, 1000, and 2500 °F respectively. These errors can be reduced somewhat with deviation curves determined by calibration at several points such as 500, 1000, 1500, and 2500 °F. The maximum error in this case is probably about 6 °F. This can be further reduced if the maximum temperature to which the thermocouple is exposed is reduced below 2300 °F. As shown in [5], thermoelectric stability is greatly improved by a reduction in maximum temperature.

The authors thank Miss J. A. Speckman of the Statistical Engineering Section of the Applied Mathematics Division for her assistance in the determination of the three equations from which these reference tables are developed. They are also indebted to Mrs. M. R. Massie and Mrs. C. S. Watkins, of the Temperature Physics Section, who made all measurements below 25 °C (77 °F).

7. References

[1] D. J. Accinno and J. F. Schneider, Platinel—A noble metal thermocouple to replace Chromel-Alumel, Engelhard Industries, Inc. Tech. Bull. **1,** No. 2, 53 (Sept. 1960).

[2] D. J. Accinno and J. F. Schneider, Platinel: A noble metal thermocouple, Temperature—Its Measurement and Control in Science and Industry **3** (ed., C. M. Herzfeld), Part 2 (ed. A. I. Dahl), p. 195, Reinhold Publ. Corp., New York (1962).

[3] E. D. Zysk, A review of recent work with the Platinel thermocouple, Engelhard Industries, Inc. Tech. Bull. **4,** No. 1, 5 (June 1963).

[4] H. J. Greenberg and E. D. Zysk, Applied research fabrication and testing of 2300 °F thermocouple for air-breathing propulsion systems, WADC Tech. Doc. Rept. ASD-TDR-62-891 (Jan. 1963).

[5] P. D. Freeze and L. O. Olsen, Thermoelectric and mechanical stability of Platinel II thermocouples in oxidizing atmospheres, WADC Tech. Doc. Rept. ASD-TDR-62-835 (Nov. 1962).

[6] H. Shenker, J. I. Lauritzen, R. J. Corruccini, and S. T. Lonberger, Reference tables for thermocouples, NBS Circ. 561, 1 (1955).

[7] W. F. Roeser and S. T. Lonberger, Methods of testing thermocouples and thermocouple materials, NBS Circ. 590 (1958); NBS Handb. 77, **2,** 88 (1961).

[8] R. P. Benedict and H. F. Ashby, Improved reference tables for thermocouples, Temperature—Its Measurement and Control in Science and Industry **3** (ed., C. M. Herzfeld), Part 2 (ed. A. I. Dahl), p. 51, Reinhold Publ. Corp., New York (1962).

[9] R. F. Vines, The platinum metals and their alloys, ed. E. M. Wise, The International Nickel Company, Inc., New York, N.Y. (1941).

[10] W. F. Roeser and A. I. Dahl, Reference tables for iron-constantan and copper-constantan thermocouples, J. Res. NBS **20,** 337 (1938) RP1080.

[11] J. M. Cameron and J. Hilsenrath, Use of general purpose coding systems for statistical calculations, Proc. IBM Scientific Computing Symp. on Statistics held October 21–23, 1963 (In press).

Appendix

Table 1A. Platinel II, millivolts versus degrees Celsius (centigrade)

Electromotive force in absolute millivolts. Temperature in degrees C (Int. 1948). Reference junctions at 0°C.

Millivolts	.000	.100	.200	.300	.400	.500	.600	.700	.800	.900	1.000	Millivolts
	Degrees C											
-2.000	-74.4	-78.6	-82.9	-87.3	-91.8	-96.3	-100.9	--	--	--	--	-2.000
-1.000	-35.2	-38.9	-42.6	-46.4	-50.3	-54.2	-58.1	-62.1	-66.1	-70.2	-74.4	-1.000
-0.000	0.0	-3.4	-6.8	-10.2	-13.7	-17.2	-20.7	-24.3	-27.9	-31.5	-35.2	-0.000
+0.000	0.0	3.4	6.7	10.0	13.2	16.5	19.7	22.9	26.1	29.3	32.4	+0.000
1.000	32.4	35.5	38.6	41.7	44.8	47.8	50.8	53.9	56.9	59.8	62.8	1.000
2.000	62.8	65.7	68.7	71.6	74.5	77.4	80.3	83.1	86.0	88.8	91.7	2.000
3.000	91.7	94.5	97.3	100.1	102.8	105.6	108.4	111.1	113.9	116.6	119.3	3.000
4.000	119.4	122.0	124.7	127.4	130.1	132.8	135.4	138.1	140.7	143.4	146.0	4.000
5.000	146.0	148.6	151.2	153.8	156.4	159.0	161.6	164.2	166.8	169.3	171.9	5.000
6.000	171.9	174.4	177.0	179.5	182.1	184.6	187.1	189.6	192.1	194.6	197.1	6.000
7.000	197.1	199.6	202.1	204.6	207.1	209.5	212.0	214.5	216.9	219.4	221.9	7.000
8.000	221.9	224.3	226.7	229.1	231.6	234.0	236.4	238.8	241.2	243.6	246.0	8.000
9.000	246.0	248.4	250.8	253.2	255.6	258.0	260.4	262.8	265.1	267.5	269.9	9.000
10.000	269.9	272.2	274.6	276.9	279.3	281.6	284.0	286.3	288.7	291.0	293.4	10.000
11.000	293.4	295.7	298.0	300.4	302.7	305.0	307.3	309.6	312.0	314.3	316.6	11.000
12.000	316.6	318.9	321.2	323.5	325.8	328.1	330.4	332.7	335.0	337.3	339.6	12.000
13.000	339.6	341.8	344.1	346.4	348.7	351.0	353.3	355.5	357.8	360.1	362.3	13.000
14.000	362.3	364.6	366.9	369.1	371.4	373.7	375.9	378.2	380.5	382.7	385.0	14.000
15.000	385.0	387.2	389.5	391.7	394.0	396.2	398.5	400.7	403.0	405.2	407.5	15.000
16.000	407.5	409.7	411.9	414.2	416.4	418.7	420.9	423.1	425.4	427.6	429.8	16.000
17.000	429.8	432.1	434.3	436.5	438.8	441.0	443.2	445.4	447.7	449.9	452.1	17.000
18.000	452.1	454.4	456.6	458.8	461.0	463.2	465.5	468.7	469.9	472.1	474.3	18.000
19.000	474.3	476.6	478.8	481.0	483.2	485.4	487.7	489.9	492.1	494.3	496.5	19.000
20.000	496.5	498.8	501.0	503.2	505.4	507.6	509.9	512.1	514.3	516.5	518.7	20.000
21.000	518.7	520.9	523.2	525.4	527.6	529.8	532.0	534.3	536.5	538.7	540.9	21.000
22.000	540.9	543.1	545.4	547.6	549.8	552.0	554.2	556.4	558.7	560.9	563.1	22.000
23.000	563.1	565.3	567.5	569.8	572.0	574.2	576.4	578.6	580.9	583.1	585.3	23.000
24.000	585.3	587.5	589.7	591.9	594.2	596.4	598.6	600.8	603.0	605.3	607.5	24.000
25.000	607.5	609.7	611.9	614.1	616.4	618.6	620.8	623.0	625.2	627.5	629.7	25.000
26.000	629.7	631.9	634.1	636.3	638.6	640.8	643.0	645.3	647.5	649.8	652.0	26.000
27.000	652.0	654.3	656.5	658.7	661.0	663.2	665.5	667.8	670.0	672.3	674.5	27.000
28.000	674.5	676.8	679.1	681.3	683.6	685.8	688.1	690.4	692.7	694.9	697.2	28.000
29.000	697.2	699.5	701.8	704.0	706.3	708.6	710.9	713.2	715.5	717.8	720.1	29.000
30.000	720.1	722.3	724.6	726.9	729.2	731.5	733.8	736.2	738.5	740.8	743.1	30.000
31.000	743.1	745.4	747.7	750.0	752.3	754.7	757.0	759.3	761.6	764.0	766.3	31.000
32.000	766.3	768.6	770.9	773.3	775.6	778.0	780.3	782.6	785.0	787.3	789.7	32.000
33.000	789.7	792.0	794.4	796.7	799.1	801.5	803.8	806.2	808.6	810.9	813.3	33.000
34.000	813.3	815.7	818.0	820.4	822.8	825.2	827.6	830.0	832.3	834.7	837.1	34.000
35.000	837.1	839.5	841.9	844.3	846.7	849.1	851.5	853.9	856.4	858.8	861.2	35.000
36.000	861.2	863.6	866.0	868.5	870.9	873.3	875.7	878.2	880.6	883.0	885.5	36.000
37.000	885.5	887.9	890.4	892.8	895.3	897.7	900.2	902.7	905.1	907.6	910.0	37.000
38.000	910.0	912.5	915.0	917.5	919.9	922.4	924.9	927.4	929.9	932.4	934.9	38.000
39.000	934.9	937.4	939.9	942.4	944.9	947.4	949.9	952.4	954.9	957.5	960.0	39.000
40.000	960.0	962.5	965.0	967.6	970.1	972.7	975.2	977.7	980.3	982.8	985.4	40.000
41.000	985.4	988.0	990.5	993.1	995.7	998.2	1000.8	1003.4	1006.0	1008.5	1011.1	41.000
42.000	1011.1	1013.7	1016.3	1018.9	1021.5	1024.1	1026.7	1029.3	1032.0	1034.6	1037.2	42.000
43.000	1037.2	1039.8	1042.5	1045.1	1047.7	1050.4	1053.0	1055.7	1058.3	1061.0	1063.6	43.000
44.000	1063.6	1066.3	1069.0	1071.6	1074.3	1077.0	1079.7	1082.3	1085.0	1087.7	1090.4	44.000
45.000	1090.4	1093.1	1095.8	1098.5	1101.3	1104.0	1106.7	1109.4	1112.1	1114.9	1117.6	45.000
46.000	1117.6	1120.4	1123.1	1125.9	1128.6	1131.4	1134.1	1136.9	1139.7	1142.5	1145.2	46.000
47.000	1145.2	1148.0	1150.8	1153.6	1156.4	1159.2	1162.0	1164.8	1167.7	1170.5	1173.3	47.000
48.000	1173.3	1176.1	1179.0	1181.8	1184.7	1187.5	1190.4	1193.2	1196.1	1199.0	1201.9	48.000
49.000	1201.9	1204.7	1207.6	1210.5	1213.4	1216.3	1219.2	1222.1	1225.0	1228.0	1230.9	49.000
50.000	1230.9	1233.8	1236.8	1239.7	1242.7	1245.6	1248.6	1251.6	1254.5	1257.5	1260.5	50.000
51.000	1260.5	1263.5	1266.5	1269.5	1272.5	1275.5	1278.5	1281.5	1284.6	1287.6	1290.6	51.000
52.000	1290.6	1293.7	1296.8	1299.8	1302.9	1306.0	1309.0	1312.1	1315.2	1318.3	1321.4	52.000
53.000	1321.4	1324.5	1327.7	1330.8	1333.9	1337.1	1340.2	1343.4	1346.5	1349.7	1352.9	53.000
54.000	1352.9	1356.0	1359.2	1362.4	1365.6	1368.8	1372.0	--	--	--	--	54.000
Millivolts	.000	.100	.200	.300	.400	.500	.600	.700	.800	.900	1.000	Millivolts

Table 2A. Platinel II, degrees Celsius versus millivolts

Electromotive force in absolute millivolts. Temperature in degrees C (Int. 1948). Reference junctions at 0°C.

°C	0	1	2	3	4	5	6	7	8	9	10	°C
	Millivolts											
-90	-2.360	-2.383	-2.405	-2.427	-2.449	-2.471	-2.493	-2.515	-2.537	-2.558	-2.580	-90
-80	-2.132	-2.155	-2.178	-2.201	-2.224	-2.247	-2.270	-2.293	-2.315	-2.338	-2.360	-80
-70	-1.894	-1.918	-1.942	-1.966	-1.990	-2.014	-2.038	-2.061	-2.085	-2.108	-2.132	-70
-60	-1.648	-1.673	-1.698	-1.723	-1.747	-1.772	-1.797	-1.821	-1.846	-1.870	-1.894	-60
-50	-1.393	-1.419	-1.445	-1.470	-1.496	-1.522	-1.547	-1.572	-1.598	-1.623	-1.648	-50
-40	-1.130	-1.157	-1.183	-1.210	-1.236	-1.263	-1.289	-1.315	-1.341	-1.367	-1.393	-40
-30	-0.859	-0.887	-0.914	-0.941	-0.968	-0.996	-1.023	-1.050	-1.077	-1.103	-1.130	-30
-20	-0.580	-0.608	-0.637	-0.665	-0.693	-0.721	-0.748	-0.776	-0.804	-0.832	-0.859	-20
-10	-0.294	-0.323	-0.352	-0.381	-0.409	-0.438	-0.467	-0.495	-0.524	-0.552	-0.580	-10
-0	-0.000	-0.030	-0.059	-0.089	-0.118	-0.148	-0.177	-0.206	-0.236	-0.265	-0.294	-0
+0	0.000	0.030	0.060	0.090	0.120	0.150	0.180	0.210	0.240	0.271	0.301	+0
10	0.301	0.331	0.362	0.393	0.423	0.454	0.485	0.516	0.547	0.578	0.609	10
20	0.609	0.640	0.671	0.703	0.734	0.765	0.797	0.828	0.860	0.892	0.923	20
30	0.923	0.955	0.987	1.019	1.051	1.083	1.115	1.148	1.180	1.212	1.245	30
40	1.245	1.277	1.310	1.342	1.375	1.408	1.440	1.473	1.506	1.539	1.572	40
50	1.572	1.605	1.638	1.672	1.705	1.738	1.772	1.805	1.839	1.872	1.906	50
60	1.906	1.939	1.973	2.007	2.041	2.075	2.109	2.143	2.177	2.211	2.245	60
70	2.245	2.280	2.314	2.348	2.383	2.417	2.452	2.486	2.521	2.556	2.591	70
80	2.591	2.625	2.660	2.695	2.730	2.765	2.800	2.836	2.871	2.906	2.941	80
90	2.941	2.977	3.012	3.048	3.083	3.119	3.154	3.190	3.226	3.262	3.298	90
100	3.298	3.334	3.369	3.405	3.442	3.478	3.514	3.550	3.586	3.623	3.659	100
110	3.659	3.695	3.732	3.768	3.805	3.842	3.878	3.915	3.952	3.988	4.025	110
120	4.025	4.062	4.099	4.136	4.173	4.210	4.247	4.285	4.322	4.359	4.397	120
130	4.397	4.434	4.471	4.509	4.546	4.584	4.621	4.659	4.697	4.735	4.772	130
140	4.772	4.810	4.848	4.886	4.924	4.962	5.000	5.038	5.076	5.114	5.153	140
150	5.153	5.191	5.229	5.268	5.306	5.344	5.383	5.421	5.460	5.499	5.537	150
160	5.537	5.576	5.615	5.653	5.692	5.731	5.770	5.809	5.848	5.887	5.926	160
170	5.926	5.965	6.004	6.043	6.083	6.122	6.161	6.200	6.240	6.279	6.319	170
180	6.319	6.358	6.398	6.437	6.477	6.516	6.556	6.596	6.636	6.675	6.715	180
190	6.715	6.755	6.795	6.835	6.875	6.915	6.955	6.995	7.035	7.075	7.115	190
200	7.115	7.155	7.196	7.236	7.276	7.317	7.357	7.397	7.438	7.478	7.519	200
210	7.519	7.559	7.600	7.641	7.681	7.722	7.763	7.803	7.844	7.885	7.926	210
220	7.926	7.967	8.008	8.049	8.090	8.131	8.172	8.213	8.254	8.295	8.336	220
230	8.336	8.377	8.418	8.460	8.501	8.542	8.584	8.625	8.666	8.708	8.749	230
240	8.749	8.791	8.832	8.874	8.915	8.957	8.999	9.040	9.082	9.124	9.165	240
250	9.165	9.207	9.249	9.291	9.333	9.375	9.416	9.458	9.500	9.542	9.584	250
260	9.584	9.626	9.668	9.711	9.753	9.795	9.837	9.879	9.921	9.964	10.006	260
270	10.006	10.048	10.090	10.133	10.175	10.218	10.260	10.302	10.345	10.387	10.430	270
280	10.430	10.472	10.515	10.558	10.600	10.643	10.685	10.728	10.771	10.814	10.856	280
290	10.856	10.899	10.942	10.985	11.027	11.070	11.113	11.156	11.199	11.242	11.285	290
300	11.285	11.328	11.371	11.414	11.457	11.500	11.543	11.586	11.629	11.672	11.716	300
310	11.716	11.759	11.802	11.845	11.888	11.932	11.975	12.018	12.062	12.105	12.148	310
320	12.148	12.192	12.235	12.279	12.322	12.365	12.409	12.452	12.496	12.539	12.583	320
330	12.583	12.626	12.670	12.714	12.757	12.801	12.845	12.888	12.932	12.976	13.019	330
340	13.019	13.063	13.107	13.150	13.194	13.238	13.282	13.326	13.370	13.413	13.457	340
350	13.457	13.501	13.545	13.589	13.633	13.677	13.721	13.765	13.809	13.853	13.897	350
360	13.897	13.941	13.985	14.029	14.073	14.117	14.161	14.205	14.249	14.294	14.338	360
370	14.338	14.382	14.426	14.470	14.514	14.559	14.603	14.647	14.691	14.736	14.780	370
380	14.780	14.824	14.869	14.913	14.957	15.002	15.046	15.090	15.135	15.179	15.223	380
390	15.223	15.268	15.312	15.357	15.401	15.446	15.490	15.535	15.579	15.623	15.668	390
400	15.668	15.713	15.757	15.802	15.846	15.891	15.935	15.980	16.024	16.069	16.114	400
410	16.114	16.158	16.203	16.247	16.292	16.337	16.381	16.426	16.471	16.515	16.560	410
420	16.560	16.605	16.650	16.694	16.739	16.784	16.828	16.873	16.918	16.963	17.008	420
430	17.008	17.052	17.097	17.142	17.187	17.232	17.276	17.321	17.366	17.411	17.456	430
440	17.456	17.501	17.545	17.590	17.635	17.680	17.725	17.770	17.815	17.860	17.904	440
450	17.904	17.949	17.994	18.039	18.084	18.129	18.174	18.219	18.264	18.309	18.354	450
460	18.354	18.399	18.444	18.489	18.534	18.579	18.624	18.669	18.714	18.759	18.804	460
470	18.804	18.849	18.894	18.939	18.984	19.029	19.074	19.119	19.165	19.210	19.255	470
480	19.255	19.300	19.345	19.390	19.435	19.480	19.525	19.570	19.615	19.660	19.705	480
490	19.705	19.750	19.795	19.841	19.886	19.931	19.976	20.021	20.066	20.111	20.156	490
500	20.156	20.201	20.246	20.291	20.336	20.381	20.426	20.471	20.517	20.562	20.607	500
°C	0	1	2	3	4	5	6	7	8	9	10	°C

Table 2A. Platinel II, degrees Celsius versus millivolts - Continued

Electromotive force in absolute millivolts. Temperature in degrees C (Int. 1948). Reference junctions at 0°C.

°C	0	1	2	3	4	5	6	7	8	9	10	°C
	Millivolts											
500	20.156	20.201	20.246	20.291	20.336	20.381	20.426	20.471	20.517	20.562	20.607	500
510	20.607	20.652	20.697	20.742	20.787	20.832	20.877	20.922	20.967	21.012	21.057	510
520	21.057	21.102	21.148	21.193	21.238	21.283	21.328	21.373	21.418	21.463	21.508	520
530	21.508	21.553	21.598	21.643	21.688	21.733	21.778	21.824	21.869	21.914	21.959	530
540	21.959	22.004	22.049	22.094	22.139	22.184	22.229	22.274	22.319	22.364	22.409	540
550	22.409	22.454	22.500	22.545	22.590	22.635	22.680	22.725	22.770	22.815	22.860	550
560	22.860	22.905	22.950	22.995	23.040	23.085	23.131	23.176	23.221	23.266	23.311	560
570	23.311	23.356	23.401	23.446	23.491	23.536	23.581	23.626	23.671	23.716	23.761	570
580	23.761	23.807	23.852	23.897	23.942	23.987	24.032	24.077	24.122	24.167	24.212	580
590	24.212	24.257	24.302	24.347	24.392	24.437	24.483	24.528	24.573	24.618	24.663	590
600	24.663	24.708	24.753	24.798	24.843	24.888	24.933	24.978	25.023	25.068	25.113	600
610	25.113	25.159	25.204	25.249	25.294	25.339	25.384	25.429	25.474	25.519	25.564	610
620	25.564	25.609	25.654	25.699	25.744	25.790	25.835	25.880	25.925	25.970	26.015	620
630	26.015	26.060	26.105	26.150	26.195	26.240	26.285	26.330	26.375	26.420	26.464	630
640	26.464	26.509	26.554	26.598	26.643	26.688	26.732	26.777	26.821	26.866	26.911	640
650	26.911	26.955	27.000	27.044	27.089	27.133	27.178	27.222	27.267	27.311	27.356	650
660	27.356	27.400	27.445	27.489	27.533	27.578	27.622	27.666	27.711	27.755	27.799	660
670	27.799	27.844	27.888	27.932	27.977	28.021	28.065	28.109	28.154	28.198	28.242	670
680	28.242	28.286	28.330	28.374	28.418	28.463	28.507	28.551	28.595	28.639	28.683	680
690	28.683	28.727	28.771	28.815	28.859	28.903	28.947	28.991	29.035	29.079	29.123	690
700	29.123	29.166	29.210	29.254	29.298	29.342	29.386	29.429	29.473	29.517	29.561	700
710	29.561	29.605	29.648	29.692	29.736	29.779	29.823	29.867	29.910	29.954	29.998	710
720	29.998	30.041	30.085	30.128	30.172	30.215	30.259	30.302	30.346	30.389	30.433	720
730	30.433	30.476	30.520	30.563	30.607	30.650	30.693	30.737	30.780	30.823	30.867	730
740	30.867	30.910	30.953	30.997	31.040	31.083	31.126	31.170	31.213	31.256	31.299	740
750	31.299	31.342	31.385	31.429	31.472	31.515	31.558	31.601	31.644	31.687	31.730	750
760	31.730	31.773	31.816	31.859	31.902	31.945	31.988	32.031	32.074	32.116	32.159	760
770	32.159	32.202	32.245	32.288	32.331	32.373	32.416	32.459	32.502	32.544	32.587	770
780	32.587	32.630	32.672	32.715	32.758	32.800	32.843	32.886	32.928	32.971	33.013	780
790	33.013	33.056	33.098	33.141	33.183	33.226	33.268	33.311	33.353	33.395	33.438	790
800	33.438	33.480	33.523	33.565	33.607	33.650	33.692	33.734	33.776	33.819	33.861	800
810	33.861	33.903	33.945	33.987	34.030	34.072	34.114	34.156	34.198	34.240	34.282	810
820	34.282	34.324	34.366	34.408	34.450	34.492	34.534	34.576	34.618	34.660	34.702	820
830	34.702	34.744	34.786	34.827	34.869	34.911	34.953	34.995	35.036	35.078	35.120	830
840	35.120	35.162	35.203	35.245	35.287	35.328	35.370	35.412	35.453	35.495	35.536	840
850	35.536	35.578	35.619	35.661	35.702	35.744	35.785	35.827	35.868	35.910	35.951	850
860	35.951	35.992	36.034	36.075	36.116	36.158	36.199	36.240	36.281	36.323	36.364	860
870	36.364	36.405	36.446	36.487	36.529	36.570	36.611	36.652	36.693	36.734	36.775	870
880	36.775	36.816	36.857	36.898	36.939	36.980	37.021	37.062	37.103	37.144	37.185	880
890	37.185	37.225	37.266	37.307	37.348	37.389	37.429	37.470	37.511	35.552	37.592	890
900	37.592	37.633	37.674	37.714	37.755	37.795	37.836	37.877	37.917	37.958	37.998	900
910	37.998	38.039	38.079	38.120	38.160	38.200	38.241	38.281	38.322	38.362	38.402	910
920	38.402	38.443	38.483	38.523	38.563	38.604	38.644	38.684	38.724	38.764	38.805	920
930	38.805	38.845	38.885	38.925	38.965	39.005	39.045	39.085	39.125	39.165	39.205	930
940	39.205	39.245	39.285	39.325	39.365	39.405	39.444	39.484	39.524	39.564	39.604	940
950	39.604	39.643	39.683	39.723	39.763	39.802	39.842	39.882	39.921	39.961	40.001	950
960	40.001	40.040	40.080	40.119	40.159	40.198	40.238	40.277	40.317	40.356	40.395	960
970	40.395	40.435	40.474	40.514	40.553	40.592	40.631	40.671	40.710	40.749	40.788	970
980	40.788	40.828	40.867	40.906	40.945	40.984	41.023	41.062	41.102	41.141	41.180	980
990	41.180	41.219	41.258	41.297	41.336	41.374	41.413	41.452	41.491	41.530	41.569	990
1000	41.569	41.608	41.646	41.685	41.724	41.763	41.802	41.840	41.879	41.918	41.956	1000
1010	41.956	41.995	42.033	42.072	42.111	42.149	42.188	42.226	42.265	42.303	42.342	1010
1020	42.342	42.380	42.418	42.457	42.495	42.534	42.572	42.610	42.649	42.687	42.725	1020
1030	42.725	42.763	42.801	42.840	42.878	42.916	42.954	42.992	43.030	43.068	43.107	1030
1040	43.107	43.145	43.183	43.221	43.259	43.297	43.334	43.372	43.410	43.448	43.486	1040
1050	43.486	43.524	43.562	43.600	43.637	43.675	43.713	43.751	43.788	43.826	43.864	1050
1060	43.864	43.901	43.939	43.976	44.014	44.052	44.089	44.127	44.164	44.202	44.239	1060
1070	44.239	44.277	44.314	44.351	44.389	44.426	44.464	44.501	44.538	44.575	44.613	1070
1080	44.613	44.650	44.687	44.724	44.762	44.799	44.836	44.873	44.910	44.947	44.984	1080
1090	44.984	45.021	45.058	45.095	45.132	45.169	45.206	45.243	45.280	45.317	45.354	1090
1100	45.354	45.391	45.427	45.464	45.501	45.538	45.574	45.611	45.648	45.685	45.721	1100
°C	0	1	2	3	4	5	6	7	8	9	10	°C

Table 2A. Platinel II, degrees Celsius versus millivolts - Continued

Electromotive force in absolute millivolts. Temperature in degrees C (Int. 1948). Reference junctions at 0°C.

°C	0	1	2	3	4	5	6	7	8	9	10	°C
	Millivolts											
1100	45.354	45.391	45.427	45.464	45.501	45.538	45.574	45.611	45.648	45.685	45.721	1100
1110	45.721	45.758	45.794	45.831	45.868	45.904	45.941	45.977	46.014	46.050	46.087	1110
1120	46.087	46.123	46.160	46.196	46.232	46.269	46.305	46.341	46.378	46.414	46.450	1120
1130	46.450	46.486	46.523	46.559	46.595	46.631	46.667	46.703	46.739	46.775	46.811	1130
1140	46.811	46.847	46.883	46.919	46.955	46.991	47.027	47.063	47.099	47.135	47.171	1140
1150	47.171	47.206	47.242	47.278	47.314	47.350	47.385	47.421	47.457	47.492	47.528	1150
1160	47.528	47.563	47.599	47.635	47.670	47.706	47.741	47.777	47.812	47.848	47.883	1160
1170	47.883	47.918	47.954	47.989	48.024	48.060	48.095	48.130	48.166	48.201	48.236	1170
1180	48.236	48.271	48.306	48.341	48.377	48.412	48.447	48.482	48.517	48.552	48.587	1180
1190	48.587	48.622	48.657	48.692	48.727	48.761	48.796	48.831	48.866	48.901	48.936	1190
1200	48.936	48.970	49.005	49.040	49.075	49.109	49.144	49.179	49.213	49.248	49.282	1200
1210	49.282	49.317	49.351	39.386	49.420	49.455	49.489	49.524	49.558	49.592	49.627	1210
1220	49.627	49.661	49.696	49.730	49.764	49.798	49.833	49.867	49.901	49.935	49.969	1220
1230	49.969	50.003	50.037	50.072	50.106	50.140	50.174	50.208	50.242	50.276	50.310	1230
1240	50.310	50.343	50.377	50.411	50.445	50.479	50.513	50.546	50.580	50.614	50.648	1240
1250	50.648	50.681	50.715	50.749	50.782	50.816	50.850	50.883	50.917	50.950	50.984	1250
1260	50.984	51.017	51.051	51.084	51.117	51.151	51.184	51.218	51.251	51.284	51.318	1260
1270	51.318	51.351	51.384	51.417	51.450	51.484	51.517	51.550	51.583	51.616	51.649	1270
1280	51.649	51.682	51.715	51.748	51.781	51.814	51.847	51.880	51.913	51.946	51.979	1280
1290	51.979	52.012	52.044	52.077	52.110	52.143	52.175	52.208	52.241	52.273	52.306	1290
1300	52.306	52.339	52.371	52.404	52.436	52.469	52.501	52.534	52.566	52.599	52.631	1300
1310	52.631	52.664	52.696	52.728	52.761	52.793	52.825	52.858	52.890	52.922	52.954	1310
1320	52.954	52.986	53.019	53.051	53.083	53.115	53.147	53.179	53.211	53.243	53.275	1320
1330	53.275	53.307	53.339	53.371	53.403	53.435	53.466	53.498	53.530	53.562	53.594	1330
1340	53.594	53.625	53.657	53.689	53.721	53.752	53.784	53.815	53.847	53.879	53.910	1340
1350	53.910	53.942	53.973	54.005	54.036	54.068	54.099	54.130	54.162	54.193	54.224	1350
1360	54.224	54.256	54.287	54.318	54.349	54.381	54.412	54.443	54.474	54.505	54.536	1360
1370	54.536	54.568	--	--	--	--	--	--	--	--	--	1370
°C	0	1	2	3	4	5	6	7	8	9	10	°C

Table 3A. Platinel II, millivolts versus degrees Fahrenheit

Electromotive force in absolute millivolts. Temperature in degrees F.* Reference junctions at 32°F.

Millivolts	.000	.100	.200	.300	.400	.500	.600	.700	.800	.900	1.000	Millivolts
	Degrees F											
-2.000	-101.9	-109.6	-117.3	-125.2	-133.2	-141.4	-149.7	--	--	--	--	-2.000
-1.000	-31.3	-38.0	-44.7	-51.6	-58.5	-65.5	-72.6	-79.8	-87.0	-94.4	-101.9	-1.000
-0.000	32.0	25.9	19.8	13.6	7.4	1.0	-5.3	-11.7	-18.1	-24.7	-31.3	-0.000
+0.000	32.0	38.0	44.0	49.9	55.8	61.7	67.5	73.3	79.0	84.7	90.3	+0.000
1.000	90.3	95.9	101.5	107.1	112.6	118.1	123.5	128.9	134.3	139.7	145.0	1.000
2.000	145.0	150.3	155.6	160.9	166.1	171.3	176.5	181.7	186.8	191.9	197.0	2.000
3.000	197.0	202.1	207.1	212.1	217.1	222.1	227.1	232.1	237.0	241.9	246.8	3.000
4.000	246.8	251.7	256.6	261.4	266.2	271.0	275.8	280.6	285.3	290.1	294.8	4.000
5.000	294.8	299.5	304.2	308.9	313.6	318.3	322.9	327.6	332.2	336.8	341.4	5.000
6.000	341.4	346.0	350.6	355.2	359.8	364.3	368.8	373.3	377.8	382.3	386.8	6.000
7.000	386.8	391.3	395.8	400.3	404.8	409.2	413.6	418.0	422.4	426.8	431.3	7.000
8.000	431.3	435.7	440.0	444.4	448.8	453.2	457.5	461.9	466.2	470.5	474.9	8.000
9.000	474.9	479.2	483.5	487.8	492.1	496.4	500.7	505.0	509.2	513.5	517.8	9.000
10.000	517.8	522.0	526.3	530.5	534.7	539.0	543.2	547.4	551.6	555.8	560.0	10.000
11.000	560.0	564.2	568.4	572.6	576.8	581.0	585.2	589.4	593.5	597.7	601.8	11.000
12.000	601.8	606.0	610.2	614.3	618.4	622.6	626.7	630.8	635.0	639.1	643.2	12.000
13.000	643.2	647.3	651.4	655.6	659.7	663.8	667.9	672.0	676.0	680.1	684.2	13.000
14.000	684.2	688.3	692.4	696.5	700.5	704.6	708.7	712.8	716.8	720.9	724.9	14.000
15.000	724.9	729.0	733.1	737.1	741.2	745.2	749.3	753.3	757.3	761.4	765.4	15.000
16.000	765.4	769.5	773.5	777.5	781.6	785.6	789.6	793.6	797.7	801.7	805.7	16.000
17.000	805.7	809.7	813.7	817.8	821.8	825.8	829.8	833.8	837.8	841.8	845.8	17.000
18.000	845.8	849.8	853.8	857.8	861.8	865.8	869.8	873.8	877.8	881.8	885.8	18.000
19.000	885.8	889.8	893.8	897.8	901.8	905.8	909.8	913.8	917.8	921.8	925.8	19.000
20.000	925.8	929.8	933.8	937.8	941.7	945.7	949.7	953.7	957.7	961.7	965.7	20.000
21.000	965.7	969.7	973.7	977.7	981.7	985.7	989.7	993.7	997.7	1001.7	1005.6	21.000
22.000	1005.6	1009.6	1013.6	1017.6	1021.6	1025.6	1029.6	1033.6	1037.6	1041.6	1045.6	22.000
23.000	1045.6	1049.6	1053.6	1057.6	1061.6	1065.6	1069.6	1073.5	1077.5	1081.5	1085.5	23.000
24.000	1085.5	1089.5	1093.5	1097.5	1101.5	1105.5	1109.5	1113.5	1117.5	1121.5	1125.5	24.000
25.000	1125.5	1129.5	1133.5	1137.4	1141.4	1145.4	1149.4	1153.4	1157.4	1161.4	1165.4	25.000
26.000	1165.4	1169.4	1173.4	1177.4	1181.4	1185.4	1189.5	1193.5	1197.5	1201.6	1205.6	26.000
27.000	1205.6	1209.7	1213.7	1217.7	1221.8	1225.8	1229.9	1233.9	1238.0	1242.1	1246.2	27.000
28.000	1246.2	1250.2	1254.3	1258.4	1262.4	1266.5	1270.6	1274.7	1278.8	1282.9	1287.0	28.000
29.000	1287.0	1291.1	1295.2	1299.3	1303.4	1307.4	1311.6	1315.7	1319.9	1324.0	1328.1	29.000
30.000	1328.1	1332.4	1336.4	1340.5	1344.6	1348.8	1352.9	1357.1	1361.2	1365.4	1369.5	30.000
31.000	1369.5	1373.7	1377.9	1382.0	1386.2	1390.4	1394.6	1398.7	1402.9	1407.1	1411.3	31.000
32.000	1411.3	1415.5	1419.7	1423.9	1428.1	1432.3	1436.5	1440.8	1445.0	1449.2	1453.4	32.000
33.000	1453.4	1457.7	1461.9	1466.1	1470.4	1474.6	1478.9	1483.1	1487.4	1491.7	1495.9	33.000
34.000	1495.9	1500.2	1504.5	1508.8	1513.0	1517.3	1521.6	1525.9	1530.2	1534.5	1538.8	34.000
35.000	1538.8	1543.1	1547.5	1551.8	1556.1	1560.4	1564.8	1569.1	1573.4	1577.8	1582.1	35.000
36.000	1582.1	1586.5	1590.8	1595.2	1599.6	1604.0	1608.3	1612.7	1617.1	1621.5	1625.9	36.000
37.000	1625.9	1630.3	1634.7	1639.1	1643.5	1647.9	1652.3	1656.8	1661.2	1665.6	1670.1	37.000
38.000	1670.1	1674.5	1679.0	1683.4	1687.9	1692.4	1696.8	1701.3	1705.8	1710.3	1714.8	38.000
39.000	1714.8	1719.3	1723.8	1728.3	1732.8	1737.3	1741.8	1746.4	1750.9	1755.4	1760.0	39.000
40.000	1760.0	1764.5	1769.1	1773.6	1778.2	1782.8	1787.4	1791.9	1796.5	1801.1	1805.7	40.000
41.000	1805.7	1810.3	1814.9	1819.6	1824.2	1828.8	1833.4	1838.1	1842.7	1847.4	1852.0	41.000
42.000	1852.0	1856.7	1861.4	1866.1	1870.7	1875.4	1880.1	1884.8	1889.5	1894.2	1899.0	42.000
43.000	1899.0	1903.7	1908.4	1913.2	1917.9	1922.7	1927.4	1932.2	1937.0	1941.7	1946.5	43.000
44.000	1946.5	1951.3	1956.1	1960.9	1965.7	1970.6	1975.4	1980.2	1985.1	1989.9	1994.8	44.000
45.000	1994.8	1999.6	2004.5	2009.4	2014.3	2019.2	2024.1	2029.0	2033.9	2038.8	2043.7	45.000
46.000	2043.7	2048.7	2053.6	2058.6	2063.5	2068.5	2073.5	2078.4	2083.4	2088.4	2093.4	46.000
47.000	2093.4	2098.5	2103.5	2108.5	2113.5	2118.6	2123.6	2128.7	2133.8	2138.9	2144.0	47.000
48.000	2144.0	2149.1	2154.2	2159.3	2164.4	2169.5	2174.7	2179.8	2185.0	2190.2	2195.3	48.000
49.000	2195.3	2200.5	2205.7	2210.9	2216.1	2221.4	2226.6	2231.8	2237.1	2242.3	2247.6	49.000
50.000	2247.6	2252.9	2258.2	2263.5	2268.8	2274.1	2279.5	2284.8	2290.1	2295.5	2300.9	50.000
51.000	2300.9	2306.2	2311.6	2317.1	2322.5	2327.9	2333.3	2338.8	2344.2	2349.7	2355.2	51.000
52.000	2355.2	2360.7	2366.2	2371.7	2377.2	2382.7	2388.3	2393.8	2399.4	2405.0	2410.6	52.000
53.000	2410.6	2416.2	2421.8	2427.4	2433.0	2438.7	2444.4	2450.0	2455.7	2461.4	2467.1	53.000
54.000	2467.1	2472.9	2478.6	2484.4	2490.1	2495.9	2501.6	--	--	--	--	54.000
Millivolts	.000	.100	.200	.300	.400	.500	.600	.700	.800	.900	1.000	Millivolts

*Based on the International Practical Temperature Scale of 1948.

Table 4A. Platinel II, degrees Fahrenheit versus millivolts

Electromotive force in absolute millivolts. Temperature in degrees F.* Reference junctions at 32°F.

°F	0	1	2	3	4	5	6	7	8	9	10	°F
	Millivolts											
-140	-2.483	-2.495	-2.508	-2.520	-2.532	-2.544	-2.556	-2.568	-2.580	-2.592	-2.603	-140
-130	-2.360	-2.373	-2.385	-2.397	-2.410	-2.422	-2.434	-2.447	-2.459	-2.471	-2.483	-130
-120	-2.234	-2.247	-2.260	-2.272	-2.285	-2.298	-2.310	-2.323	-2.335	-2.348	-2.360	-120
-110	-2.106	-2.119	-2.132	-2.145	-2.158	-2.170	-2.183	-2.196	-2.209	-2.222	-2.234	-110
-100	-1.974	-1.988	-2.001	-2.014	-2.027	-2.040	-2.053	-2.067	-2.080	-2.093	-2.106	-100
-90	-1.840	-1.854	-1.867	-1.881	-1.894	-1.908	-1.921	-1.934	-1.948	-1.961	-1.974	-90
-80	-1.703	-1.717	-1.731	-1.745	-1.758	-1.772	-1.786	-1.799	-1.813	-1.827	-1.840	-80
-70	-1.564	-1.578	-1.592	-1.606	-1.620	-1.634	-1.648	-1.662	-1.676	-1.689	-1.703	-70
-60	-1.422	-1.436	-1.450	-1.465	-1.479	-1.493	-1.507	-1.522	-1.536	-1.550	-1.564	-60
-50	-1.277	-1.292	-1.306	-1.321	-1.335	-1.350	-1.364	-1.379	-1.393	-1.407	-1.422	-50
-40	-1.130	-1.145	-1.160	-1.174	-1.189	-1.204	-1.219	-1.233	-1.248	-1.263	-1.277	-40
-30	-0.980	-0.996	-1.011	-1.026	-1.041	-1.056	-1.071	-1.085	-1.100	-1.115	-1.130	-30
-20	-0.828	-0.844	-0.859	-0.874	-0.890	-0.905	-0.920	-0.935	-0.950	-0.965	-0.980	-20
-10	-0.674	-0.690	-0.705	-0.721	-0.736	-0.752	-0.767	-0.782	-0.798	-0.813	-0.828	-10
-0	-0.517	-0.533	-0.549	-0.565	-0.580	-0.596	-0.612	-0.627	-0.643	-0.658	-0.674	-0
+0	-0.517	-0.501	-0.486	-0.470	-0.454	-0.438	-0.422	-0.406	-0.390	-0.374	-0.358	+0
10	-0.358	-0.342	-0.326	-0.310	-0.294	-0.278	-0.262	-0.245	-0.229	-0.213	-0.197	10
20	-0.197	-0.180	-0.164	-0.148	-0.131	-0.115	-0.099	-0.082	-0.066	-0.049	-0.033	20
30	-0.033	-0.017	0.000	0.017	0.033	0.050	0.066	0.083	0.100	0.116	0.133	30
40	0.133	0.150	0.166	0.183	0.200	0.217	0.233	0.250	0.267	0.284	0.301	40
50	0.301	0.318	0.335	0.352	0.369	0.386	0.403	0.420	0.437	0.454	0.471	50
60	0.471	0.488	0.505	0.523	0.540	0.557	0.574	0.592	0.609	0.626	0.643	60
70	0.643	0.661	0.678	0.696	0.713	0.730	0.748	0.765	0.783	0.800	0.818	70
80	0.818	0.835	0.853	0.871	0.888	0.906	0.923	0.941	0.959	0.977	0.994	80
90	0.994	1.012	1.030	1.048	1.065	1.083	1.101	1.119	1.137	1.155	1.173	90
100	1.173	1.191	1.209	1.227	1.245	1.263	1.281	1.299	1.317	1.335	1.353	100
110	1.353	1.371	1.389	1.408	1.426	1.444	1.462	1.481	1.499	1.517	1.535	110
120	1.535	1.554	1.572	1.590	1.609	1.627	1.646	1.664	1.683	1.701	1.720	120
130	1.720	1.738	1.757	1.775	1.794	1.812	1.831	1.850	1.868	1.887	1.906	130
140	1.906	1.924	1.943	1.962	1.981	1.999	2.018	2.037	2.056	2.075	2.094	140
150	2.094	2.113	2.131	2.150	2.169	2.188	2.207	2.226	2.245	2.264	2.283	150
160	2.283	2.302	2.322	2.341	2.360	2.379	2.398	2.417	2.436	2.456	2.475	160
170	2.475	2.494	2.513	2.533	2.552	2.571	2.591	2.610	2.629	2.649	2.668	170
180	2.668	2.687	2.707	2.726	2.746	2.765	2.785	2.804	2.824	2.843	2.863	180
190	2.863	2.883	2.902	2.922	2.941	2.961	2.981	3.000	3.020	3.040	3.060	190
200	3.060	3.079	3.099	3.119	3.139	3.158	3.178	3.198	3.218	3.238	3.258	200
210	3.258	3.278	3.298	3.318	3.338	3.357	3.377	3.397	3.417	3.438	3.458	210
220	3.458	3.478	3.498	3.518	3.538	3.558	3.578	3.598	3.619	3.639	3.659	220
230	3.659	3.679	3.699	3.720	3.740	3.760	3.781	3.801	3.821	3.842	3.862	230
240	3.862	3.882	3.903	3.923	3.944	3.964	3.984	4.005	4.025	4.046	4.066	240
250	4.066	4.087	4.107	4.128	4.149	4.169	4.190	4.210	4.231	4.252	4.272	250
260	4.272	4.293	4.314	4.334	4.355	4.376	4.397	4.417	4.438	4.459	4.480	260
270	4.480	4.500	4.521	4.542	4.563	4.584	4.605	4.626	4.647	4.668	4.688	270
280	4.688	4.709	4.730	4.751	4.772	4.793	4.814	4.835	4.856	4.878	4.899	280
290	4.899	4.920	4.941	4.962	4.983	5.004	5.025	5.047	5.068	5.089	5.110	290
300	5.110	5.131	5.153	5.174	5.195	5.216	5.238	5.259	5.280	5.302	5.323	300
310	5.323	5.344	5.366	5.387	5.409	5.430	5.451	5.473	5.494	5.516	5.537	310
320	5.537	5.559	5.580	5.602	5.623	5.645	5.666	5.688	5.709	5.731	5.753	320
330	5.753	5.774	5.796	5.818	5.839	5.861	5.883	5.904	5.926	5.948	5.969	330
340	5.969	5.991	6.013	6.035	6.056	6.078	6.100	6.122	6.144	6.165	6.187	340
350	6.187	6.209	6.231	6.253	6.275	6.297	6.319	6.341	6.363	6.384	6.406	350
360	6.406	6.428	6.450	6.472	6.494	6.516	6.538	6.561	6.583	6.605	6.627	360
370	6.627	6.649	6.671	6.693	6.715	6.737	6.759	6.782	6.804	6.826	6.848	370
380	6.848	6.870	6.893	6.915	6.937	6.959	6.982	7.004	7.026	7.048	7.071	380
390	7.071	7.093	7.115	7.138	7.160	7.182	7.205	7.227	7.249	7.272	7.294	390
400	7.294	7.317	7.339	7.362	7.384	7.406	7.429	7.451	7.474	7.496	7.519	400
°F	0	1	2	3	4	5	6	7	8	9	10	°F

*Based on the International Practical Temperature Scale of 1948.

Table 4A. Platinel II, degrees Fahrenheit versus millivolts - Continued

Electromotive force in absolute millivolts. Temperature in degrees F.* Reference junctions at 32°F.

°F	0	1	2	3	4	5	6	7	8	9	10	°F
	Millivolts											
400	7.294	7.317	7.339	7.362	7.384	7.406	7.429	7.451	7.474	7.496	7.519	400
410	7.519	7.541	7.564	7.587	7.609	7.632	7.654	7.677	7.699	7.722	7.745	410
420	7.745	7.767	7.790	7.813	7.835	7.858	7.881	7.903	7.926	7.949	7.971	420
430	7.971	7.994	8.017	8.040	8.062	8.085	8.108	8.131	8.153	8.176	8.199	430
440	8.199	8.222	8.245	8.268	8.290	8.313	8.336	8.359	8.382	8.405	8.428	440
450	8.428	8.451	8.473	8.496	8.519	8.542	8.565	8.588	8.611	8.634	8.657	450
460	8.657	8.680	8.703	8.726	8.749	8.772	8.795	8.818	8.842	8.865	8.888	460
470	8.888	8.911	8.934	8.957	8.980	9.003	9.026	9.050	9.073	9.096	9.119	470
480	9.119	9.142	9.165	9.189	9.212	9.235	9.258	9.282	9.305	9.328	9.351	480
490	9.351	9.375	9.398	9.421	9.444	9.468	9.491	9.514	9.538	9.561	9.584	490
500	9.584	9.608	9.631	9.654	9.678	9.701	9.725	9.748	9.771	9.795	9.818	500
510	9.818	9.842	9.865	9.889	9.912	9.935	9.959	9.982	10.006	10.029	10.053	510
520	10.053	10.076	10.100	10.123	10.147	10.170	10.194	10.218	10.241	10.265	10.288	520
530	10.288	10.312	10.335	10.359	10.383	10.406	10.430	10.454	10.477	10.501	10.524	530
540	10.524	10.548	10.572	10.595	10.619	10.643	10.666	10.690	10.714	10.738	10.761	540
550	10.761	10.785	10.809	10.833	10.856	10.880	10.904	10.928	10.951	10.975	10.999	550
560	10.999	11.023	11.046	11.070	11.094	11.118	11.142	11.166	11.189	11.213	11.237	560
570	11.237	11.261	11.285	11.309	11.333	11.357	11.380	11.404	11.428	11.452	11.476	570
580	11.476	11.500	11.524	11.548	11.572	11.596	11.620	11.644	11.668	11.692	11.716	580
590	11.716	11.740	11.764	11.788	11.812	11.836	11.860	11.884	11.908	11.932	11.956	590
600	11.956	11.980	12.004	12.028	12.052	12.076	12.100	12.124	12.148	12.172	12.197	600
610	12.197	12.221	12.245	12.269	12.293	12.317	12.341	12.365	12.390	12.414	12.438	610
620	12.438	12.462	12.486	12.510	12.535	12.559	12.583	12.607	12.631	12.656	12.680	620
630	12.680	12.704	12.728	12.752	12.777	12.801	12.825	12.849	12.874	12.898	12.922	630
640	12.922	12.946	12.971	12.995	13.019	13.044	13.068	13.092	13.116	13.141	13.165	640
650	13.165	13.189	13.214	13.238	13.262	13.287	13.311	13.335	13.360	13.384	13.408	650
660	13.408	13.433	13.457	13.482	13.506	13.530	13.555	13.579	13.604	13.628	13.652	660
670	13.652	13.677	13.701	13.726	13.750	13.775	13.799	13.823	13.848	13.872	13.897	670
680	13.897	13.921	13.946	13.970	13.995	14.019	14.044	14.068	14.093	14.117	14.142	680
690	14.142	14.166	14.191	14.215	14.240	14.264	14.289	14.313	14.338	14.362	14.387	690
700	14.387	14.411	14.436	14.460	14.485	14.510	14.534	14.559	14.583	14.608	14.632	700
710	14.632	14.657	14.682	14.706	14.731	14.755	14.780	14.805	14.829	14.854	14.878	710
720	14.878	14.903	14.928	14.952	14.977	15.002	15.026	15.051	15.075	15.100	15.125	720
730	15.125	15.149	15.174	15.199	15.223	15.248	15.273	15.297	15.322	15.347	15.371	730
740	15.371	15.396	15.421	15.446	15.470	15.495	15.520	15.544	15.569	15.594	15.619	740
750	15.619	15.643	15.668	15.693	15.717	15.742	15.767	15.792	15.816	15.841	15.866	750
760	15.866	15.891	15.915	15.940	15.965	15.990	16.014	16.039	16.064	16.089	16.114	760
770	16.114	16.138	16.163	16.188	16.213	16.238	16.262	16.287	16.312	16.337	16.362	770
780	16.362	16.386	16.411	16.436	16.461	16.486	16.510	16.535	16.560	16.585	16.610	780
790	16.610	16.635	16.659	16.684	16.709	16.734	16.759	16.784	16.809	16.833	16.858	790
800	16.858	16.883	16.908	16.933	16.958	16.983	17.008	17.032	17.057	17.082	17.107	800
810	17.107	17.132	17.157	17.182	17.207	17.232	17.256	17.281	17.306	17.331	17.356	810
820	17.356	17.381	17.406	17.431	17.456	17.481	17.506	17.530	17.555	17.580	17.605	820
830	17.605	17.630	17.655	17.680	17.705	17.730	17.755	17.780	17.805	17.830	17.855	830
840	17.855	17.880	17.904	17.929	17.954	17.979	18.004	18.029	18.054	18.079	18.104	840
850	18.104	18.129	18.154	18.179	18.204	18.229	18.254	18.279	18.304	18.329	18.354	850
860	18.354	18.379	18.404	18.429	18.454	18.479	18.504	18.529	18.554	18.579	18.604	860
870	18.604	18.629	18.654	18.679	18.704	18.729	18.754	18.779	18.804	18.829	18.854	870
880	18.854	18.879	18.904	18.929	18.954	18.979	19.004	19.029	19.054	19.079	19.104	880
890	19.104	19.129	19.155	19.180	19.205	19.230	19.255	19.280	19.305	19.330	19.355	890
900	19.355	19.380	19.405	19.430	19.455	19.480	19.505	19.530	19.555	19.580	19.605	900
910	19.605	19.630	19.655	19.680	19.705	19.730	19.755	19.780	19.805	19.831	19.856	910
920	19.856	19.881	19.906	19.931	19.956	19.981	20.006	20.031	20.056	20.081	20.106	920
930	20.106	20.131	20.156	20.181	20.206	20.231	20.256	20.281	20.306	20.331	20.356	930
940	20.356	20.381	20.406	20.431	20.456	20.482	20.507	20.532	20.557	20.582	20.607	940
950	20.607	20.632	20.657	20.682	20.707	20.732	20.757	20.782	20.807	20.832	20.857	950
960	20.857	20.882	20.907	20.932	20.957	20.982	21.007	21.032	21.057	21.082	21.107	960
970	21.107	21.132	21.158	21.183	21.208	21.233	21.258	21.283	21.308	21.333	21.358	970
980	21.358	21.383	21.408	21.433	21.458	21.483	21.508	21.533	21.558	21.583	21.608	980
990	21.608	21.633	21.658	21.683	21.708	21.733	21.758	21.783	21.809	21.834	21.859	990
1000	21.859	21.884	21.909	21.934	21.959	21.984	22.009	22.034	22.059	22.084	22.109	1000
°F	0	1	2	3	4	5	6	7	8	9	10	°F

*Based on the International Practical Temperature Scale of 1948.

Table 4A. Platinel II, degrees Fahrenheit versus millivolts - Continued

Electromotive force in absolute millivolts. Temperature in degrees F.* Reference junctions at 32°F.

°F	0	1	2	3	4	5	6	7	8	9	10	°F
	Millivolts											
1000	21.859	21.884	21.909	21.934	21.959	21.984	22.009	22.034	22.059	22.084	22.109	1000
1010	22.109	22.134	22.159	22.184	22.209	22.234	22.259	22.284	22.309	22.334	22.359	1010
1020	22.359	22.384	22.409	22.434	22.459	22.485	22.510	22.535	22.560	22.585	22.610	1020
1030	22.610	22.635	22.660	22.685	22.710	22.735	22.760	22.785	22.810	22.835	22.860	1030
1040	22.860	22.885	22.910	22.935	22.960	22.985	23.010	23.035	23.060	23.085	23.110	1040
1050	23.110	23.136	23.161	23.186	23.211	23.236	23.261	23.286	23.311	23.336	23.361	1050
1060	23.361	23.386	23.411	23.436	23.461	23.486	23.511	23.536	23.561	23.586	23.611	1060
1070	23.611	23.636	23.661	23.686	23.711	23.736	23.761	23.786	23.812	23.837	23.862	1070
1080	23.862	23.887	23.912	23.937	23.962	23.987	24.012	24.037	24.062	24.087	24.112	1080
1090	24.112	24.137	24.162	24.187	24.212	24.237	24.262	24.287	24.312	24.337	24.362	1090
1100	24.362	24.387	24.412	24.437	24.463	24.488	24.513	24.538	24.563	24.588	24.613	1100
1110	24.613	24.638	24.663	24.688	24.713	24.738	24.763	24.788	24.813	24.838	24.863	1110
1120	24.863	24.888	24.913	24.938	24.963	24.988	25.013	25.038	25.063	25.088	25.113	1120
1130	25.113	25.139	25.164	25.189	25.214	25.239	25.264	25.289	25.314	25.339	25.364	1130
1140	25.364	25.389	25.414	25.439	25.464	25.489	25.514	25.539	25.564	25.589	25.614	1140
1150	25.614	25.639	25.664	25.689	25.714	25.739	25.764	25.790	25.815	25.840	25.865	1150
1160	25.865	25.890	25.915	25.940	25.965	25.990	26.015	26.040	26.065	26.090	26.115	1160
1170	26.115	26.140	26.165	26.190	26.215	26.240	26.265	26.290	26.315	26.340	26.365	1170
1180	26.365	26.390	26.415	26.439	26.464	26.489	26.514	26.539	26.564	26.588	26.613	1180
1190	26.613	26.638	26.663	26.688	26.712	26.737	26.762	26.787	26.812	26.836	26.861	1190
1200	26.861	26.886	26.911	26.935	26.960	26.985	27.010	27.034	27.059	27.084	27.109	1200
1210	27.109	27.133	27.158	27.183	27.207	27.232	27.257	27.282	27.306	27.331	27.356	1210
1220	27.356	27.380	27.405	27.430	27.454	27.479	27.504	27.528	27.553	27.578	27.602	1220
1230	27.602	27.627	27.652	27.676	27.701	27.726	27.750	27.775	27.799	27.824	27.849	1230
1240	27.849	27.873	27.898	27.923	27.947	27.972	27.996	28.021	28.045	28.070	28.095	1240
1250	28.095	28.119	28.144	28.168	28.193	28.217	28.242	28.266	28.291	28.315	28.340	1250
1260	28.340	28.365	28.389	28.414	28.438	28.463	28.487	28.512	28.536	28.561	28.585	1260
1270	28.585	28.610	28.634	28.658	28.683	28.707	28.732	28.756	28.781	28.805	28.830	1270
1280	28.830	28.854	28.878	28.903	28.927	28.952	28.976	29.001	29.025	29.049	29.074	1280
1290	29.074	29.098	29.123	29.147	29.171	29.196	29.220	29.244	29.269	29.293	29.318	1290
1300	29.318	29.342	29.366	29.391	29.415	29.439	29.464	29.488	29.512	29.536	29.561	1300
1310	29.561	29.585	29.609	29.634	29.658	29.682	29.707	29.731	29.755	29.779	29.804	1310
1320	29.804	29.828	29.852	29.876	29.901	29.925	29.949	29.973	29.998	30.022	30.046	1320
1330	30.046	30.070	30.094	30.119	30.143	30.167	30.191	30.215	30.240	30.264	30.288	1330
1340	30.288	30.312	30.336	30.360	30.385	30.409	30.433	30.457	30.481	30.505	30.529	1340
1350	30.529	30.554	30.578	30.602	30.626	30.650	30.674	30.698	30.722	30.746	30.771	1350
1360	30.771	30.795	30.819	30.843	30.867	30.891	30.915	30.939	30.963	30.987	31.011	1360
1370	31.011	31.035	31.059	31.083	31.107	31.131	31.155	31.179	31.203	31.227	31.251	1370
1380	31.251	31.275	31.299	31.323	31.347	31.371	31.395	31.419	31.443	31.467	31.491	1380
1390	31.491	31.515	31.539	31.563	31.587	31.610	31.634	31.658	31.682	31.706	31.730	1390
1400	31.730	31.754	31.778	31.802	31.826	31.849	31.873	31.897	31.921	31.945	31.969	1400
1410	31.969	31.993	32.016	32.040	32.064	32.088	32.112	32.136	32.159	32.183	32.207	1410
1420	32.207	32.231	32.255	32.278	32.302	32.326	32.350	32.373	32.397	32.421	32.445	1420
1430	32.445	32.468	32.492	32.516	32.540	32.563	32.587	32.611	32.635	32.658	32.682	1430
1440	32.682	32.706	32.729	32.753	32.777	32.800	32.824	32.848	32.871	32.895	32.919	1440
1450	32.919	32.942	32.966	32.990	33.013	33.037	33.061	33.084	33.108	33.131	33.155	1450
1460	33.155	33.179	33.202	33.226	33.249	33.273	33.297	33.320	33.344	33.367	33.391	1460
1470	33.391	33.414	33.438	33.461	33.485	33.508	33.532	33.556	33.579	33.603	33.626	1470
1480	33.626	33.650	33.673	33.697	33.720	33.743	33.767	33.790	33.814	33.837	33.861	1480
1490	33.861	33.884	33.908	33.931	33.955	33.978	34.001	34.025	34.048	34.072	34.095	1490
1500	34.095	34.119	34.142	34.165	34.189	34.212	34.235	34.259	34.282	34.306	34.329	1500
1510	34.329	34.352	34.376	34.399	34.422	34.446	34.469	34.492	34.516	34.539	34.562	1510
1520	34.562	34.585	34.609	34.632	34.655	34.679	34.702	34.725	34.748	34.772	34.795	1520
1530	34.795	34.818	34.841	34.865	34.888	34.911	34.934	34.958	34.981	35.004	35.027	1530
1540	35.027	35.050	35.074	35.097	35.120	35.143	35.166	35.189	35.213	35.236	35.259	1540
1550	35.259	35.282	35.305	35.328	35.351	35.375	35.398	35.421	35.444	35.467	35.490	1550
1560	35.490	35.513	35.536	35.559	35.582	35.606	35.629	35.652	35.675	35.698	35.721	1560
1570	35.721	35.744	35.767	35.790	35.813	35.836	35.859	35.882	35.905	35.928	35.951	1570
1580	35.951	35.974	35.997	36.020	36.043	36.066	36.089	36.112	36.135	36.158	36.181	1580
1590	36.181	36.203	36.226	36.249	36.272	36.295	36.318	36.341	36.364	36.387	36.410	1590
1600	36.410	36.433	36.455	36.478	36.501	36.524	36.547	36.570	36.593	36.615	36.638	1600
°F	0	1	2	3	4	5	6	7	8	9	10	°F

*Based on the International Practical Temperature Scale of 1948.

Table 4A. Platinel II, degrees Fahrenheit versus millivolts - Continued

Electromotive force in absolute millivolts. Temperature in degrees F.* Reference junctions at 32°F.

°F	0	1	2	3	4	5	6	7	8	9	10	°F
	Millivolts											
1600	36.410	36.433	36.455	36.478	36.501	36.524	36.547	36.570	36.593	36.615	36.638	1600
1610	36.638	36.661	36.684	36.707	36.729	36.752	36.775	36.798	36.821	36.843	36.866	1610
1620	36.866	36.889	36.912	36.935	36.957	36.980	37.003	37.026	37.048	37.071	37.094	1620
1630	37.094	37.116	37.139	37.162	37.185	37.207	37.230	37.253	37.275	37.298	37.321	1630
1640	37.321	37.343	37.366	37.389	37.411	37.434	37.457	37.479	37.502	37.524	37.547	1640
1650	37.547	37.570	37.592	37.615	37.637	37.660	37.683	37.705	37.728	37.750	37.773	1650
1660	37.773	37.795	37.818	37.841	37.863	37.886	37.908	37.931	37.953	37.976	37.998	1660
1670	37.998	38.021	38.043	38.066	38.088	38.111	38.133	38.156	38.178	38.200	38.223	1670
1680	38.223	38.245	38.268	38.290	38.313	38.335	38.357	38.380	38.402	38.425	38.447	1680
1690	38.447	38.469	38.492	38.514	38.537	38.559	38.581	38.604	38.626	38.648	38.671	1690
1700	38.671	38.693	38.715	38.738	38.760	38.782	38.805	38.827	38.849	38.871	38.894	1700
1710	38.894	38.916	38.938	38.961	38.983	39.005	39.027	39.050	39.072	39.094	39.116	1710
1720	39.116	39.138	39.161	39.183	39.205	39.227	39.249	39.272	39.294	39.316	39.338	1720
1730	39.338	39.360	39.382	39.405	39.427	39.449	39.471	39.493	39.515	39.537	39.560	1730
1740	39.560	39.582	39.604	39.626	39.648	39.670	39.692	39.714	39.736	39.758	39.780	1740
1750	39.780	39.802	39.824	39.846	39.868	39.890	39.912	39.935	39.957	39.979	40.001	1750
1760	40.001	40.022	40.044	40.066	40.088	40.110	40.132	40.154	40.176	40.198	40.220	1760
1770	40.220	40.242	40.264	40.286	40.308	40.330	40.352	40.374	40.395	40.417	40.439	1770
1780	40.439	40.461	40.483	40.505	40.527	40.549	40.570	40.592	40.614	40.636	40.658	1780
1790	40.658	40.679	40.701	40.723	40.745	40.767	40.788	40.810	40.832	40.854	40.876	1790
1800	40.876	40.897	40.919	40.941	40.963	40.984	41.006	41.028	41.049	41.071	41.093	1800
1810	41.093	41.115	41.136	41.158	41.180	41.201	41.223	41.245	41.266	41.288	41.310	1810
1820	41.310	41.331	41.353	41.374	41.396	41.418	41.439	41.461	41.483	41.504	41.526	1820
1830	41.526	41.547	41.569	41.590	41.612	41.634	41.655	41.677	41.698	41.720	41.741	1830
1840	41.741	41.763	41.784	41.806	41.827	41.849	41.870	41.892	41.913	41.935	41.956	1840
1850	41.956	41.978	41.999	42.021	42.042	42.063	42.085	42.106	42.128	42.149	42.171	1850
1860	42.171	42.192	42.213	42.235	42.256	42.277	42.299	42.320	42.342	42.363	42.384	1860
1870	42.384	42.406	42.427	42.448	42.470	42.491	42.512	42.534	42.555	42.576	42.597	1870
1880	42.597	42.619	42.640	42.661	42.683	42.704	42.725	42.746	42.768	42.789	42.810	1880
1890	42.810	42.831	42.852	42.874	42.895	42.916	42.937	42.958	42.980	43.001	43.022	1890
1900	43.022	43.043	43.064	43.085	43.107	43.128	43.149	43.170	43.191	43.212	43.233	1900
1910	43.233	43.254	43.275	43.297	43.318	43.339	43.360	43.381	43.402	43.423	43.444	1910
1920	43.444	43.465	43.486	43.507	43.528	43.549	43.570	43.591	43.612	43.633	43.654	1920
1930	43.654	43.675	43.696	43.717	43.738	43.759	43.780	43.801	43.822	43.843	43.864	1930
1940	43.864	43.885	43.905	43.926	43.947	43.968	43.989	44.010	44.031	44.052	44.072	1940
1950	44.072	44.093	44.114	44.135	44.156	44.177	44.198	44.218	44.239	44.260	44.281	1950
1960	44.281	44.302	44.322	44.343	44.364	44.385	44.405	44.426	44.447	44.468	44.488	1960
1970	44.488	44.509	44.530	44.551	44.571	44.592	44.613	44.633	44.654	44.675	44.695	1970
1980	44.695	44.716	44.737	44.757	44.778	44.799	44.819	44.840	44.861	44.881	44.902	1980
1990	44.902	44.922	44.943	44.964	44.984	45.005	45.025	45.046	45.067	45.087	45.108	1990
2000	45.108	45.128	45.149	45.169	45.190	45.210	45.231	45.251	45.272	45.292	45.313	2000
2010	45.313	45.333	45.354	45.374	45.395	45.415	45.436	45.456	45.476	45.497	45.517	2010
2020	45.517	45.538	45.558	45.579	45.599	45.619	45.640	45.660	45.681	45.701	45.721	2020
2030	45.721	45.742	45.762	45.782	45.803	45.823	45.843	45.864	45.884	45.904	45.925	2030
2040	45.925	45.945	45.965	45.985	46.006	46.026	46.046	46.066	46.087	46.107	46.127	2040
2050	46.127	46.147	46.168	46.188	46.208	46.228	46.248	46.269	46.289	46.309	46.329	2050
2060	46.329	46.349	46.369	46.390	46.410	46.430	46.450	46.470	46.490	46.510	46.531	2060
2070	46.531	46.551	46.571	46.591	46.611	46.631	46.651	46.671	46.691	46.711	46.731	2070
2080	46.731	46.751	46.771	46.791	46.811	46.831	46.851	46.871	46.891	46.911	46.931	2080
2090	46.931	46.951	46.971	46.991	47.011	47.031	47.051	47.071	47.091	47.111	47.131	2090
2100	47.131	47.151	47.171	47.191	47.210	47.230	47.250	47.270	47.290	47.310	47.330	2100
2110	47.330	47.350	47.369	47.389	47.409	47.429	47.449	47.468	47.488	47.508	47.528	2110
2120	47.528	47.548	47.567	47.587	47.607	47.627	47.646	47.666	47.686	47.706	47.725	2120
2130	47.725	47.745	47.765	47.785	47.804	47.824	47.844	47.863	47.883	47.903	47.922	2130
2140	47.922	47.942	47.962	47.981	48.001	48.020	48.040	48.060	48.079	48.099	48.119	2140
2150	48.119	48.138	48.158	48.177	48.197	48.216	48.236	48.255	48.275	48.295	48.314	2150
2160	48.314	48.334	48.353	48.373	48.392	48.412	48.431	48.451	48.470	48.490	48.509	2160
2170	48.509	48.529	48.548	48.567	48.587	48.606	48.626	48.645	48.665	48.684	48.703	2170
2180	48.703	38.723	48.742	48.761	48.781	48.800	48.820	48.839	48.858	48.878	48.897	2180
2190	48.897	48.916	48.936	48.955	48.974	48.994	49.013	49.032	49.051	49.071	49.090	2190
2200	49.090	49.109	49.128	49.148	49.167	49.186	49.205	49.225	49.244	49.263	49.282	2200
°F	0	1	2	3	4	5	6	7	8	9	10	°F

*Based on the International Practical Temperature Scale of 1948.

Table 4A. Platinel II, degrees Fahrenheit versus millivolts - Continued

Electromotive force in absolute millivolts. Temperature in degrees F.* Reference junctions at 32°F.

°F	0	1	2	3	4	5	6	7	8	9	10	°F
	Millivolts											
2200	49.090	49.109	49.128	49.148	49.167	49.186	49.205	49.225	49.244	49.263	49.282	2200
2210	49.282	49.301	49.321	49.340	49.359	49.378	49.397	49.417	49.436	49.455	49.474	2210
2220	49.474	49.493	49.512	49.531	49.550	49.570	49.589	49.608	49.627	49.646	49.665	2220
2230	49.665	49.684	49.703	49.722	49.741	49.760	49.779	49.798	49.817	49.836	49.855	2230
2240	49.855	49.874	49.893	49.912	49.931	49.950	49.969	49.988	50.007	50.026	50.045	2240
2250	50.045	50.064	50.083	50.102	50.121	50.140	50.159	50.177	50.196	50.215	50.234	2250
2260	50.234	50.253	50.272	50.291	50.310	50.328	50.347	50.366	50.385	50.404	50.423	2260
2270	50.423	50.441	50.460	50.479	50.498	50.516	50.535	50.554	50.573	50.591	50.610	2270
2280	50.610	50.629	50.648	50.666	50.685	50.704	50.723	50.741	50.760	50.779	50.797	2280
2290	50.797	50.816	50.835	50.853	50.872	50.891	50.909	50.928	50.946	50.965	50.984	2290
2300	50.984	51.002	51.021	51.039	51.058	51.077	51.095	51.114	51.132	51.151	51.169	2300
2310	51.169	51.188	51.206	51.225	51.244	51.262	51.281	51.299	51.318	51.336	51.354	2310
2320	51.354	51.373	51.391	51.410	51.428	51.447	51.465	51.484	51.502	51.520	51.539	2320
2330	51.539	51.557	51.576	51.594	51.612	51.631	51.649	51.668	51.686	51.704	51.723	2330
2340	51.723	51.741	51.759	51.778	51.796	51.814	51.833	51.851	51.869	51.887	51.906	2340
2350	51.906	51.924	51.942	51.960	51.979	51.997	52.015	52.033	52.052	52.070	52.088	2350
2360	52.088	52.106	52.124	52.143	52.161	52.179	52.197	52.215	52.234	52.252	52.270	2360
2370	52.270	52.288	52.306	52.324	52.342	52.360	52.379	52.397	52.415	52.433	52.451	2370
2380	52.451	52.469	52.487	52.505	52.523	52.541	52.559	52.577	52.595	52.613	52.631	2380
2390	52.631	52.649	52.667	52.685	52.703	52.721	52.739	52.757	52.775	52.793	52.811	2390
2400	52.811	52.829	52.847	52.865	52.883	52.901	52.918	52.936	52.954	52.972	52.990	2400
2410	52.990	53.008	53.026	53.044	53.061	53.079	53.097	53.115	53.133	53.151	53.168	2410
2420	53.168	53.186	53.204	53.222	53.240	53.257	53.275	53.293	53.311	53.328	53.346	2420
2430	53.346	53.364	53.381	53.399	53.417	53.435	53.452	53.470	53.488	53.505	53.523	2430
2440	53.523	53.541	53.558	53.576	53.594	53.611	53.629	53.647	53.664	53.682	53.699	2440
2450	53.699	53.717	53.735	53.752	53.770	53.787	53.805	53.822	53.840	53.858	53.875	2450
2460	53.875	53.893	53.910	53.928	53.945	53.963	53.980	53.998	54.015	54.033	54.050	2460
2470	54.050	54.068	54.085	54.102	54.120	54.137	54.155	54.172	54.190	54.207	54.224	2470
2480	54.224	54.242	54.259	54.277	54.294	54.311	54.329	54.346	54.363	54.381	54.398	2480
2490	54.398	54.415	54.433	54.450	54.467	54.485	54.502	54.519	54.536	54.554	54.571	2490
2500	54.571	--	--	--	--	--	--	--	--	--	--	2500
°F	0	1	2	3	4	5	6	7	8	9	10	°F

*Based on the International Practical Temperature Scale of 1948.

Table 5A. Thermal emf relations between 1813, 1503, Pt 27, and copper

Temperature °F	Platinel II	1813 vs Pt 27	1503 vs Pt 27	Copper vs Pt 27	Copper vs 1813	Copper vs 1503
	Millivolts					
32	0.000	0.000	0.000	0.000	0.000	0.000
50	.301	.001	- .300	.062	.061	.362
75	.730	.004	- .726	.153	.149	.879
100	1.173	.010	-1.163	.250	.240	1.413
125	1.627	.019	-1.608	.354	.335	1.962
150	2.094	.030	-2.064	.464	.434	2.528
175	2.571	.044	-2.527	.580	.536	3.107
200	3.060	.059	-3.001	.703	.644	3.704
225	3.558	.076	-3.482	.831	.755	4.313
250	4.066	.095	-3.971	.966	.871	4.937
275	4.584	.115	-4.469	1.107	.992	5.576
300	5.110	.136	-4.974	1.254	1.118	6.228
325	5.645	.159	-5.486	1.404	1.245	6.890
350	6.187	.182	-6.005	1.560	1.378	7.565
375	6.737	.206	-6.531	1.720	1.514	8.251
400	7.294	.231	-7.063	1.886	1.655	8.949
425	7.858	.256	-7.602	2.055	1.799	9.657
450	8.428	.281	-8.147	2.229	1.948	10.376
475	9.003	.306	-8.697	2.408	2.102	11.105
500	9.584	.331	-9.253	2.591	2.260	11.844

JOURNAL OF RESEARCH of the National Bureau of Standards—C. Engineering and Instrumentation
Vol. 68C, No. 4, October–December 1964

Effects of Cathodic Currents on the Corrosion of an Aluminum Alloy

William J. Schwerdtfeger

(May 28, 1964)

A laboratory investigation was made using 6063–T5 aluminum alloy. In order to determine the most anodic potentials of the alloy under varying conditions of *p*H specimens were exposed for 6 months to 21 water-saturated soils (air free) ranging in *p*H from 3.4 to 10.0. The data obtained should be useful in selecting protective potentials where cathodic protection is desirable and feasible.

The effects of continuously applied cathodic currents were studied by exposing the alloy for 6 months to still city water to which was added 3 percent by weight of sodium chloride. In addition, the effect of *p*H was observed by using similar salt water solutions, adjusted to *p*H 4 and *p*H 10. In each environment, cathodic and anodic polarization data were obtained periodically on freely corroding specimens. The cathodic data were used to choose protective potentials and together with the anodic data to calculate instantaneous rates of corrosion. The data indicate that cathodic protection is feasible, especially in the low-*p*H range. Cathodic corrosion occurred at *p*H 10 and can occur even at a lower *p*H.

1. Introduction

Aluminum and its alloys have an enviable reputation for resistance to atmospheric corrosion. Their ability to resist corrosion is attributed to the rapid formation of protective oxide films. However, the behavior of aluminum to underground and aqueous exposures is somewhat controversial. A breakdown of the oxide film will result in varying degrees of corrosion depending on such factors as differential aeration, *p*H, and conductivity of the electrolyte.

Aluminum alloys are subject to corrosion in some aqueous and underground environments hence it seems logical to think in terms of protection such as applied to ferrous structures. Iron and steel are protected by coatings, cathodic protection, or a combination of both. However, upon searching the literature one soon learns that the application of cathodic protection to aluminum is fraught with many uncertainties. There is the possibility of cathodic corrosion, a factor which is no cause for concern in the cathodic protection of iron and steel. Also, even a break in or loosening of a coating on aluminum exposed to a very corrosive environment can result in accelerated attack because of a breakdown of the oxide film.

Mears and Brown [1][1] have suggested that aluminum can be cathodically protected provided that the current density is below a critical value. Caldwell and Albano [2] found that in a neutral salt solution, when aluminum is cathodic, the increase in hydroxyl-ion concentration will corrode the metal if the current density is excessive. These investigators also said that in a strongly alkaline solution (NaOH 0.1 *N* to 0.25 *N*) the increase in hydroxyl-ion at the cathode is negligible compared with the concentration of alkali in the body of the electrolyte, hence cathodic protection will have no effect. In a discussion of this paper, Mears and Brown [3] again stated that cathodic protection is possible in neutral chlorides or near neutral solutions provided current densities are not too high. Still later, Mears [4] pointed out that cathodic corrosion is caused by excessive current and that to his knowledge there was no case on record where aluminum has been cathodically corroded when zinc was the sacrificial anode, but corrosion has been known to occur where magnesium or external current was used. He also mentioned that while zinc is anodic to aluminum in acid solutions it is also severely attacked and is therefore undesirable. Because of the amphoteric nature of aluminum, Mears mentioned that the use of cathodic protection may not be feasible in alkaline solutions because of the increased concentration of alkali on the cathode caused by the current.

Wanderer and Sprowls [5] concluded that cathodic protection was unnecessary in referring to aluminum pipe alloys 6063–T5 and 6061–T6 exposed to saline water.

[1] Figures in brackets indicate the literature references at the end of this paper.

Dalrymple [6] reported virtually no corrosion, after 5 years of exposure on 8¾ in. o.d. aluminum alloy (6063) pipeline buried unprotected in 10,000 ohm-cm soil. Nevertheless, he suggested coating aluminum lines and supplementing this with cathodic protection to eliminate the hazards of corrosion in soils.

Deltombe and Pourbaix [7] reported that cathodic protection of aluminum is practically impossible because of the low value of the protective potential (−1.78 V, H_2 scale).

Sprowls and Carlisle [8] concluded that it is difficult to predict the performance of aluminum underground from characteristics of the soil and that some soils cause severe corrosion on aluminum and aluminum alloys. They subscribe to the feasibility of cathodic protection, as demonstrated in some environments, indicating that eventually cathodic protection may permit bare aluminum alloys to be buried in the most corrosive soils. In cathodically protecting aluminum pipe (6063–T5) for 8 years in 3500 ohm-cm soil (*p*H 6.1) they found the deepest pit to be only 22 mils as compared with 80 mils on unprotected pipe. The potentials of the protected pipe varied between −0.9 and −1.1 V referred to the copper-copper sulfate electrode. Sprowls and Carlisle tentatively suggested a protective potential between −0.9 and −1.2 V referred to copper-copper sulfate and warn that excessive current densities can cause cathodic corrosion.

Whiting and Wright [9] tell of deep pitting on an unprotected aluminum (AA3003) pipeline 11 months after installation in areas where the soil resistivity was less than 1500 ohm-cm. Magnesium anodes were then installed which resulted in an average current density of 0.225 mA/ft [2] and a pipe potential of −1.0 V or more to a copper-copper sulfate electrode. After an additional 9 months, the line was reexcavated for inspection and an examination revealed that corrosion had been arrested.

In cathodic protection tests made with aluminum alloy specimens buried in 400 to 1000 ohm-cm soil, Hewes [10] found no severe cathodic corrosion on specimens maintained at potentials as high as −1.5 V with reference to the copper-copper electrode and therefore believes that the potential of −1.2 V as an upper limit is too conservative.

In view of the foregoing, it appears that additional research is warranted in order to learn more about the effects of cathodic current on aluminum. The alloy 6063–T5 [2] was chosen for this investigation. An experiment was designed to measure the maximum anodic potential of the alloy specimens in various soils ranging in *p*H from 3.4 to 10.0 and to select a value as the protective potential. All of the other experiments involving applied current were carried out with a 3 percent sodium chloride solution and also with a similar solution made both acidic and alkaline by the addition of acetic acid and sodium carbonate, respectively.

[2] Nominal composition, in percent: 0.7 Mg, 0.4 Si, Al and normal impurities constitute the remainder.

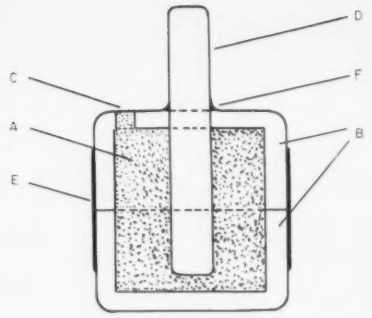

FIGURE 1. *Cell for measuring the potential of an aluminum alloy in a soil.*

A, soil; B, rubber caps; C, hole for contact between soil and reference electrode; D, alloy; E, tape; F, sealer.

2. Experimental Procedure

2.1. Preparation and Exposure of Specimens for Potential Measurements in Soils

Specimens were cut to a length of 3¼ in. from ½ in. diam aluminum alloy rods. Two were prepared for each of 21 soils. The soils varied in *p*H from 3.4 to 10.0, the majority of them being classified as poorly aerated with resistivities less than 500 ohm-cm. Chemical and physical properties of the soils, with the exception of 3 soils (126, 127, 128) from new test sites, have been published [11]. Soils at sites 126, 127, and 128 have resistivities under 500 ohm-cm. Numbers 126 and 127 are poorly aerated and No. 128 is well aerated. A cross-sectional sketch of the cell used for measuring potentials is shown in figure 1. Finely ground soil, A, saturated with distilled water and puddled was carefully packed into two rubber caps, B. Before packing, two holes were drilled in the upper cap, one ¼ in. diam, C, for permitting contact between the soil and the reference electrode and the other ½ in. diam to accommodate the alloy specimen, D. The cell shown in figure 1 is drawn to scale, each cap being 1 in. deep and 1⅞ in. i.d. The alloy was cleaned in varsol, the edges rounded off, the entire surface rubbed vigorously with fine grit abrasive cloth, scrubbed under hot running water with soap and rinsed. After packing soil around the specimen positioned in the upper cap and then packing the other cap, the cell was assembled as shown, care being taken to leave no voids in the soil. The caps were then joined and sealed with polyvinyl-chloride pressure-sensitive tape, E. A mixture of paraffin and beeswax, F, was used for sealing between the specimen and the cap. To prevent the soil in the cells from drying out, the hole C was covered with a patch of polyvinyl tape and then the cells were stored in a water-saturated enclosure. The cells were removed from this environment for about 25 min per week in order to make potential measure-

ments. One cell of each pair was disassembled after 6 months. The remaining 21 cells were left assembled for an additional 18 weeks for reasons to be discussed later.

2.2. Preparation and Exposure of Specimens With Applied Cathodic Currents

Eight pairs of specimens were prepared, each pair from a single ½ in. diam aluminum alloy rod and each specimen cut to a length of 18 in. They were cleaned for exposure as previously described for the soil specimens and weighed to the nearest 2 mg. Finally, except for 9 in. on one end (approximately 0.1 ft^2) for exposure to the electrolyte and 1 in. on the other end for an electrical connection, each specimen was spirally wrapped with polyvinyl-chloride pressure-sensitive tape.

Three pairs of specimens, each pair consisting of a freely corroding specimen (control) and a cathode, were exposed for approximately 6 months to Washington, D.C., city water to which had been added 3 percent by weight of sodium chloride. The salt water was contained in a wooden vat about 66 in. i.d. and maintained at a depth of 18 in.; the volume of water being about 265 gal. The water temperature was not controlled but was measured regularly during the exposure period. A photograph of some of the specimens, just prior to removal, during exposure to the salt water is shown in figure 2. Three zinc rods, one for each cathode, were used as auxiliary electrodes. The specimens were left undisturbed throughout the entire exposure period, wires from the specimens being connected to a terminal block mounted on the side of the vat.

The remaining 5 pairs of specimens were set up in 5 Pyrex jars (approximately 12 in. in diameter by 12 in. high) containing about 4.5 gal of city water with 3 percent by weight of sodium chloride added. The salt water in 2 of these jars was made alkaline by the addition of sodium carbonate while the water in 2 other jars was make acidic by the addition of acetic acid. The *p*H of the alkaline solutions was maintained between 9.7 and 10.0 and that of the acid solutions was kept between 4.0 and 4.3. One of the jars was left with the salt water only shown in the foreground of the photograph, figure 3. Each jar contained 2 specimens, one corroding freely and the other made cathodic. It will be seen in the photograph that the specimens in the front jar are fitted with cylindrical objects about centrally located on the rods. These are rubber caps (open end up), similar to those used for the soil cells previously described, filled with clay soil in order to concentrate the corrosion in that area. With the exception of the two jars in the background containing acidic salt solutions, zinc strips were used as auxiliary anodes located diametrically opposite each other; the center specimen was the cathode. An aluminum alloy was used as the auxiliary anode in the acidic salt solutions as zinc corroded very rapidly. The temperatures of the electrolytes were measured periodically although no attempt was made to regulate them. The specimens in the jars were also exposed for about 6 months.

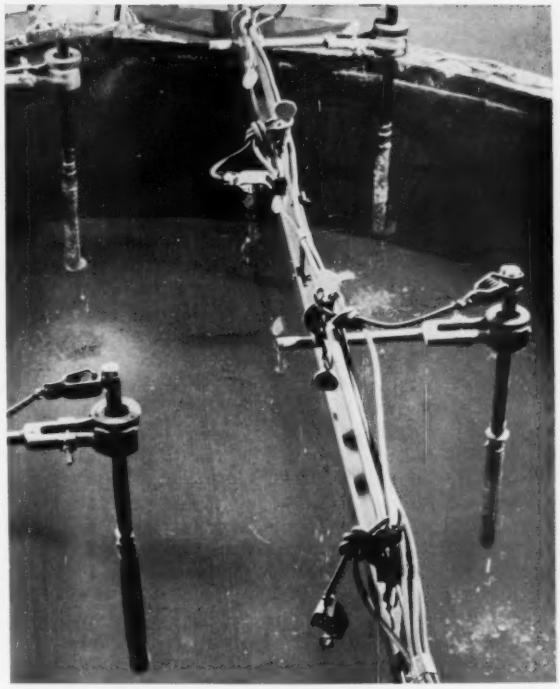

FIGURE 2. *Aluminum alloy specimens exposed to salt solution in wooden vat.*

Specimens 9 and 10, foreground, right and left, respectively.
Specimens 7 and 8, background, right and left, respectively.
Note absence of corrosion products on floor of vat under cathode 10 (protected).

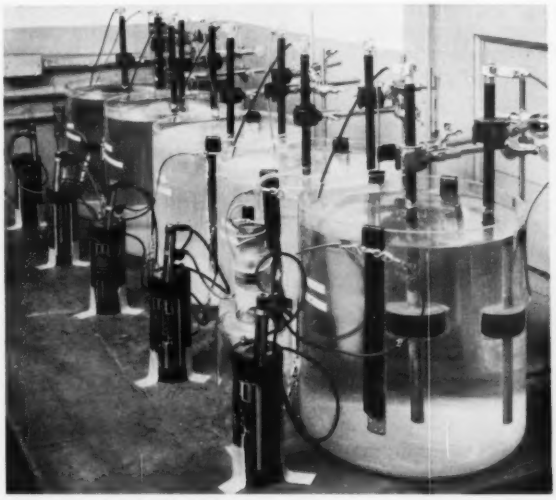

FIGURE 3. *Aluminum alloy specimens exposed to solutions in the jars.*

a. Electrical Measurements

Potentials of the alloy in the 21 soils were measured about weekly with a potentiometer and a saturated calomel half-cell.[3] When making potential measurements, direct contact between the soil and the calomel half-cell was avoided by using an intermediate electrolyte of puddled soil. This procedure prevented contamination of the soil in the cell by salt from the agar-salt bridge. At the end of 6 months, when one cell of each soil was taken apart, the *p*H of the 21 soils adjacent to the specimens was measured. For most soils, the *p*H was not significantly different from the value measured before the cells were assembled. The temperature of the room where the cells were stored varied between 70 and 90 °F. This variation in temperature would account for less than a 10 mV change in the potential of the saturated calomel half-cell [12].

For the cathodes in the salt solutions, except for one in the wooden vat which was connected directly to a zinc anode, a 500 ohm voltage-divider connected across a 1.5 V No. 6 dry cell was used to control potential and furnish applied current. This arrangement made it possible to hold the potential of a cathode within ±15 mV, usually closer.

Potentials and applied currents were measured about twice weekly. The potentials, referred to the saturated calomel electrode, were measured with a potentiometer and then the currents with a milliammeter. The currents were checked occasionally with a zero-resistance milliammeter. The potentials of some of the cathodes were adjusted on the basis of data obtained from cathodic polarization curves on the controls. IR drops associated with potential measurements were negligible. Polarization data were obtained weekly or biweekly. Anodic polarization data were also obtained, usually the day after making the cathodic measurements. A two-pen strip-chart recorder was used for these measurements. The polarizing current resulted from linear increments in applied voltage obtained with a synchronously driven 10-turn potentiometer connected across a battery which delivered current through two zinc lectrodes exposed to the solutions only while olarization measurements were being made.

b. Removal of Corrosion Products

All specimens were removed from the solutions after about 6 months of exposure. Loose corrosion products were removed with a nonmetallic bristle brush while the specimens were held under running hot water. Following this, they were immersed for 10 min in an aqueous solution consisting of 5 percent phosphoric acid and 2 percent chromic acid at 90 °C contained in an ultrasonic cleaning tank. After rinsing with running hot water and drying by blowing compressed air over the surface, the specimens were weighed. The cycle was repeated until there was no significant weight change, but usually the first cleaning was found to be sufficient.

[3] All potentials specified hereafter are with respect to the saturated calomel half-cell.

3. Results and Discussion

3.1. Potentials of the Aluminum Alloy in Air-Free Soils

A logical step in experimentally determining a protective potential generally applicable to a particular aluminum alloy in soils, assuming that cathodic protection is possible, would be that of measuring the most anodic potentials of the alloy peculiar to a variety of soils covering the *p*H range. These potentials would presumably exist under oxygen-deficient conditions or during exposure in so-called air-free soils. Cells were assembled as previously described with this idea in mind.

Potentials based on two specimens for each of the 21 soils (fig. 4) are plotted versus the *p*H of the soil, the *p*H measured being the value upon disassembly. The potentials were measured between the 2d and 6th months of exposure when day-by-day variations in potential were less than during the first 2 months. Maximum, minimum and average potentials are shown. Where the range of potentials for a given soil during the 4 month period is not over 100 mV, the potentials of a pair of specimens were always within 20 mV. Where the difference between maximum and minimum is over 100 mV, the greater part of the potential difference can be attributed to aeration differences between cells of a pair.

There appears to be no consistent relationship between *p*H and potential. The specimen in the most alkaline soil, 116, does have the most anodic potential. The specimen in soil 13 (*p*H 8.9) has the most cathodic potential (−0.68 V) but during early exposure was −1.28 V.

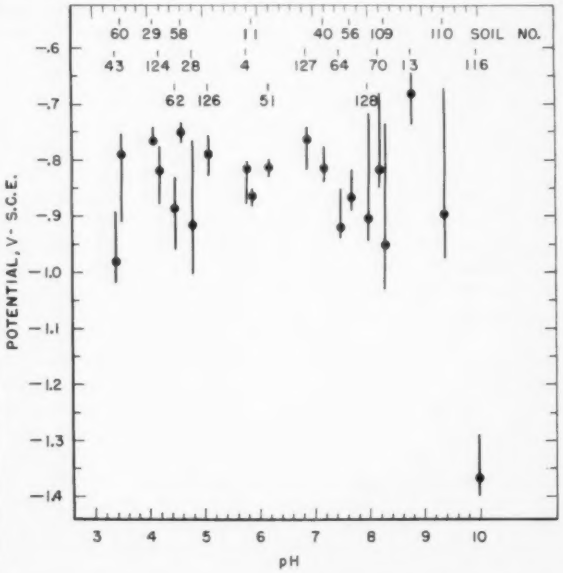

FIGURE 4. *Relation between the potential of aluminum alloy (6063–T5) in air-free soil and the* pH *of the soil.*

Range of potentials and average potential of 2 specimens in 21 soils from 2nd through 6th month of exposure.

Limited, yet significant, data were also obtained on the 21 soil cells which were kept in operation for an additional 18 weeks. The cells were left stored in the water-saturated environment as during the previous 6 months except that 1 in. of tape was cut from that which held the two rubber caps of the cell together so as to permit access of air to the soil. The effect, without exception, was to make the potentials more cathodic, that is more typical of the normal corrosion potentials. Except for soil 116 (pH 10) in which the potential was −1.06 V at the end of 18 weeks, the range of potentials varied between −0.64 V (soils 58, 124) and −0.895 V (soil 64). This proves the effect of the exclusion of air in producing the more anodic potentials observed in the sealed cells.

There was a significant difference in corrosion rates of the specimens removed from the air-free soils from the rates in the same soils after permitting access of air for an additional 18 weeks. During the 6 months under air-free exposure the corrosion in all the soils was only superficial in nature being apparently the worst in soil 116. Strangely enough the specimen in soil 116 appeared about the same after 18 weeks more of aerated exposure but the specimens in soils 60, 109, and 127 had pits of 50, 70, and 110 mils deep, respectively. Pitting increased on the alloy in all the other soils (pits 20 to 40 mils on some) with the exception of soils 4 and 11 having resistivities of 6670 and 11,000 ohm-cm, respectively.

On the basis of the data (fig. 4) it appears that, with the exception of the extremely alkaline soil 116, −1.0 V (S.C.E.) might be a reasonable protective potential. However, experience at the site of one of the most corrosive soils (No. 127) shows otherwise. The site is a tidal marsh (pH7) with a soil resistivity of about 300 ohm-cm. Two aluminum alloy (3003) pipe specimens were buried there and connected directly to individual zinc anodes for an uninterrupted period of 30 months. The potentials of the couples just prior to removing them from the soil were about −0.98 V. Immediately after open-circuiting the couples, the potentials of the specimens were −0.90 V and −0.98 V and the current densities just before opening the circuits were 12 mA/ft² and 17 mA/ft², respectively. Severe cathodic corrosion took place on both specimens being worst on the one which had the higher current density. The potentials of the specimens remained almost unchanged for several minutes after the initial open-circuit readings; this aspect will be discussed later on experiments in the salt solutions. Another aluminum alloy (1188) specimen was buried at the same site and for about the same length of time. There is no reason to believe that there is any marked difference in the corrosion characteristics of the alloys mentioned in this paper. Cathodic polarization curves, such as those to be discussed later in connection with specimens in salt solutions, were obtained on the 1188 specimen after 8 and 30 months of uninterrupted burial. Based on the curves, the current presumably required for protection both times was between 5 and 6 mA/ft² and the corrosion potential was −0.65 V. These data suggest that the current densities on the 3003 specimens previously discussed were unnecessarily high and not self-regulating as probably would have been the case with steel cathodes. The curves on the aluminum cathodes indicated that complete protection was possible at about −0.73 V. The laboratory data for the 6063 alloy in the same soil suggest a value of −0.765 V (fig. 4).

The wide range of potentials (fig. 4) and the field experience at site 127 leads the writer to conclude that a protective potential value, generally applicable to aluminum alloys in all soils, cannot be specified, even excluding strongly alkaline soils such as 116. It is believed that changing the potential about 100 mV by cathodic polarization is a safer approach in cathodically protecting aluminum alloys underground.

3.2. Aluminum Alloy in Salt Solution

Pertinent data pertaining to the effects of cathodic currents on the aluminum alloy exposed to salt water are given in table 1. Specimens Nos. 7 through 12 were exposed to the salt water in the wooden vat. Specimens 7, 9, and 11 were permitted to corrode freely for 182 days, except at those times when polarization data were obtained which required a gradually increasing current for about 20 min per run. Specimens 8, 10, and 12 had cathodic currents applied continuously for 180 days after corroding freely for 2 days. High-purity zinc rods (⅜ in. diam) were used as anodes, one for each of the cathodes. Some of the polarization data from the recorder charts replotted on semilogarithmic coordinates for control 9 are shown in figure 5. Curves such as these were used to determine the potential criterion E_a (corresponding to the various values of I_p) and to calculate rates of corrosion [13].

Potentials and applied currents plotted versus time are shown in figure 6 for cathodes 8, 10, and 12. Also shown are the corrosion potentials for control 7 (potentials for controls 9 and 11 corresponded within a few millivolts and are therefore omitted) and the currents, I_p, required for cathodic protection based on the controls. It will be noted for cathode 10 that the applied current corresponds reasonably well with the values of I_p.

A comparison of the cathodic effects based on three potential criteria, namely, E_a (curves), −1.0 V and −1.5 V is given by the weight loss and remarks columns (table 1). The −1.5 V (cathode 8) caused cathodic corrosion presumably because of the excessive current required to maintain the potential. Cathodes 10 and 12 were both protected to a reasonable degree but not as well as was hoped for. The potential on cathode 12 (connected directly to zinc anode) seemed to be more effective in reducing pitting (under the edge of the tape) than was potential E_a applied to cathode 10. This suggests, perhaps, that the potential corresponding to the beginning of the hydrogen over-voltage curve (at arrows, fig. 5) is more reasonable and also that −1.0 V is not unreasonable.

TABLE 1. *Effect of cathodic currents on aluminum alloy (6063–T5) exposed for 6 months to salt solution (pH 8)*

Specimen [a]	Cathodic polarization curve—controls				Potential criterion, cathodes	Applied current			Potential		Weight loss [c]	Remarks—Nature of corrosion and pitting [d]
	Current at break, I_p		Potential at break, E_a									
	Range—6 mo.		Range—6 mo.			Range—6 mo.			Range—6 mo.			
	Min	Max	Min	Max		Min	Max	Mean [b]	Min	Max		
	mA-ft²	*mA-ft²*	*V*	*V*	*V*	*mA-ft²*	*mA-ft²*	*mA-ft²*	*V*	*V*	*mg*	
7, control	1.2	6.2	−0.76	−0.83				0.0	−0.730	−0.755	531	Numerous pits (10-20 mils) over entire exposed surface. Corrosion under tape at water line. No reduction in rod diameter.
8, cathode					−1.5	4.2	110	10.8	−1.480	−1.580	1924	Several pits (15 mils). Most metal loss on bottom end of rod (completely corroded away). No reduction in rod diameter.
9, control	1.3	5.6	−0.78	−0.84				0.0	−0.725	−0.763	605	Same as control No. 7.
10, cathode					[e] E_a	2.1	8.4	3.3	−.794	−.842	172	A few pits up to 5 mils deep. Most corrosion under the tape at the waterline. No reduction in rod diameter.
11, control	1.3	6.5	−0.77	−0.81				0.0	−.730	−.750	543	Same as control No. 7.
12, cathode					−1.0–1.1	2.5	10.2	3.8	−1.000	−1.010	182	Several pits up to 3 mils deep. No corrosion under the tape. No reduction in rod diameter.
13, control	0.5	1.4	−0.83	−0.96				0.0	−0.745	−0.885	49	Corrosion confined to a ring of metal loss (2 mils deep) where rubber cap was in contact with the metal.
14, cathode					−1.1	0.4	3.5	0.84	−1.090	−1.120	34	Several pits (2–4 mils) where soil was in contact with the metal. No corrosion under the rubber.

[a] Specimens 7–12 were exposed to 250 gal of water in open vat (fig. 2). Specimens 13 and 14 were exposed to 4.5 gal of water in open glass jar (fig. 3).
[b] Based on area under current-time curve (fig. 6).
[c] Exposed area 0.1 ft².
[d] Diameter measurements made with micrometer caliper.
[e] E_a, potential corresponding to I_p, cathodic polarization curves of controls, Nos. 7, 9, 11.

Based on the evidence in table 1 and that which is to follow for the salt solutions made alkaline and acidic, potential-decay curves obtained on the cathodes upon removing the applied currents appear to offer a clue as to whether cathodic protection had taken place or whether the currents caused cathodic corrosion. The curves (fig. 7) were recorded on cathodes 8, 10, and 12 after 180 days of exposure during which currents were applied continuously. Cathodic protection which took place on cathodes 10 and 12 is indicated by relatively rapid depolarization to the corrosion potentials of the controls while cathodic corrosion on cathode 8 seems to be indicated by little depolarization, with the potential remaining quite anodic to the corrosion potential of the control for a much longer period of time. Where cathodic protection has resulted, the better degree of protection appears to be associated with the greater depolarization. Depolarization to potentials which are cathodic to the corrosion potentials, as with cathodes 10 and 12, might be explained by the increased cathodic area resulting from previous cathodic protection, the effect being only temporary while the applied current is off. The slow depolarization apparently associated with cathodic corrosion was also observed on the aluminum alloy 3003 exposed underground as previously described.

The pair of specimens 13 and 14 were exposed to salt water in the Pyrex jar. Data for this pair are shown in table 1 and in figures 8 and 9. The corrosion rates on these specimens were less than 10 percent of those on the specimens exposed to the salt water in the large open vat. This is attributed in part to the lesser availability of oxygen in the jar. The clay soil contained in the rubber cap centrally positioned on each of the specimens was intended to localize the corrosion in that area. This turned out to be so, but the comparative weight losses of control 13 and cathode 14 do not indicate much benefit as a result of cathodic protection. However, visual examination of cathode 14 revealed the absence of a ring of corroded metal adjacent to the rubber so very evident on control 13. The cathodic polarization data (fig. 8) indicated potentials (corresponding to the currents I_p) of between −0.8 and −0.95 V. Because it was anticipated that the metal in the soil area would be the most anodic, it was decided to hold the potential of cathode 14 at −1.1 V. Figure 9 indicates that, except for the first 25 days, this potential resulted in applied current density on cathode 14 which agreed quite well with what was required based on I_p. It may be of interest to mention that the *p*H of the soil adjacent to specimen 14, after 180 days, was 9.1 while the *p*H of the salt water was never over 8. On the basis of figure 4 and figure 8, it now appears as if a protective potential of about −0.95 V would have been adequate and possibly given better protection. The potential-decay curve (not shown) of cathode 14 revealed that after 15 min without applied current the potential was still about 0.1 V anodic to the potential of control 13. On the basis of what has been previously said about potential-decay curves, this suggests that there may have been some cathodic corrosion in the soil area where pitting took place.

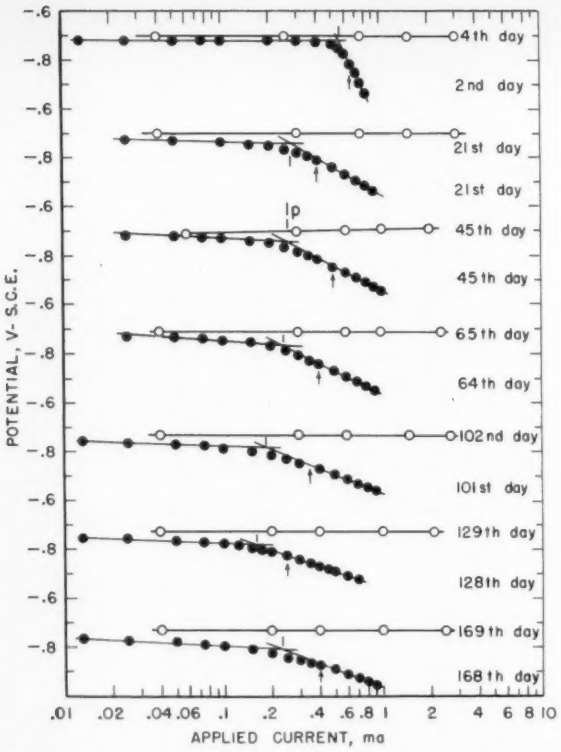

FIGURE 5. *Some polarization curves of alloy control 9 during 6 months of exposure to salt solution in wooden vat.*

0—anodic, ●—cathodic; Arrow shows probable beginning of hydrogen-overvoltage curve.

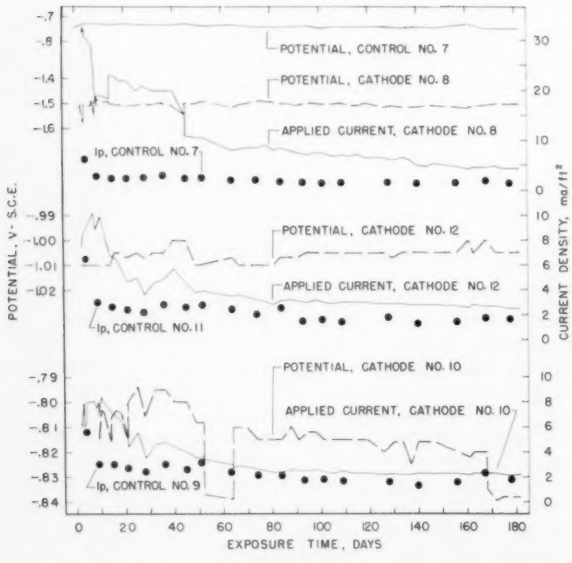
POTENTIAL, CONTROL NO. 7
POTENTIAL, CATHODE NO. 8
APPLIED CURRENT, CATHODE NO. 8
Ip, CONTROL NO. 7
POTENTIAL, CATHODE NO. 12
APPLIED CURRENT, CATHODE NO. 12
Ip, CONTROL NO. 11
POTENTIAL, CATHODE NO. 10
APPLIED CURRENT, CATHODE NO. 10
Ip, CONTROL NO. 9
POTENTIAL, V- S.C.E.
CURRENT DENSITY, ma/ft²
EXPOSURE TIME, DAYS
0 20 40 60 80 100 120 140 160 180

FIGURE 6. *Relation between applied currents (to cathodes) and currents (I_p) indicated by cathodic polarization curves (of controls) for aluminum alloy in salt solution (wooden vat)*

Cathodes are controlled by three potential criteria, as shown.

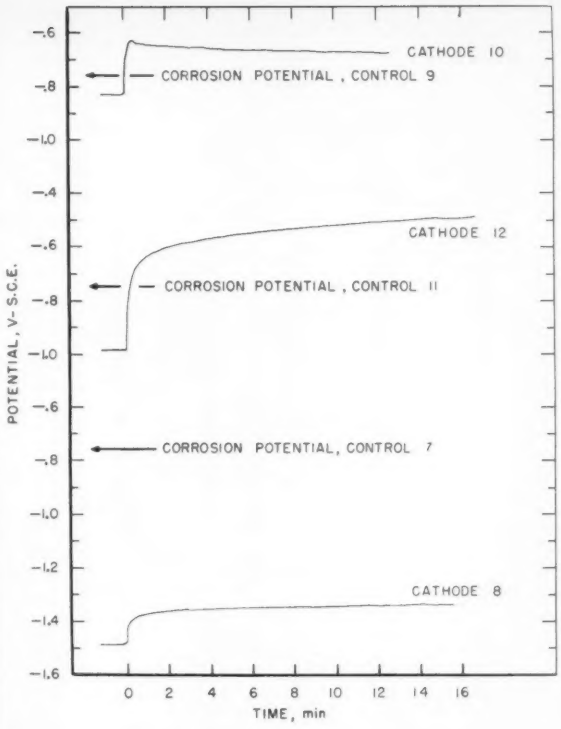

FIGURE 7. *Potential-decay curves of cathodes exposed to salt solution of pH 8 following removal of currents applied for 6 months.*

Some preliminary results obtained with the same type and size of specimens are believed to be worthy of mentioning. A control, cathode and anode were exposed for 5 months to a salt solution in a setup similar to that just described, except that soil rings were omitted. During exposure, the control gradually become more anodic, changing in potential from −0.73 V to −1.107 V. Based on cathodic polarization curves, obtained on the control periodically during exposure and indicating cathodic control, it was decided to hold the potential of the cathode about 0.1 V anodic to the potential of the control at all times. The *p*H of the salt solution gradually increased from 7.9 to 8.2 and the current density on the cathode decreased from 3.4 mA/ft² at the beginning to 0.05 mA/ft² at the end of exposure. The metal loss on the control due to corrosion was 147 mg, being mostly under the tape at the waterline and in pits over the exposed surface. The cathode lost 38 mg yet there was little visual evidence of corrosion.

All of the polarization data obtained on the controls exposed to city water with 3 percent NaCl added are given in table 2. These data are used to calculate corrosion rates for comparison with actual rates as revealed by the weight losses. It will be noted that the corrosion reactions of the specimens exposed to salt water in the wooden vat were under

TABLE 2. *Corrosion rates of alloy controls as calculated from polarization curves*

Exposure for 6 months to salt solution (*p*H 8)

Exposure time	Current at break in curve [a]		Corrosion current i_o [b]	Weight loss [c]	
	Cathodic I_p	Anodic I_q		Calculated cumulative	Actual
Days	*mA*	*mA*	*mA*	*mg*	*mg*
Specimen No. 7					
4	0.62	$>>I_p$	0.62	20	
9	.30	$>>I_p$	.30	38	
15	.26	$>>I_p$	.26	52	
21	.24	$>>I_p$	.24	64	
28	.25	$>>I_p$	.25	78	
36	.30	$>>I_p$	.30	96	
45	.25	$>>I_p$	.25	116	
52	.26	$>>I_p$	.26	131	
64	.21	$>>I_p$	.21	154	
74	.20	$>>I_p$	.20	170	
84	.17	$>>I_p$	.17	185	
93	.15	$>>I_p$	.15	197	
101	.13	$>>I_p$	.13	206	
109	.13	$>>I_p$	.13	214	
128	.14	$>>I_p$	.14	234	
140	.12	$>>I_p$	.12	247	
156	.14	$>>I_p$	.14	264	
168	.17	$>>I_p$	.17	278	
178	.14	$>>I_p$	.14	291	
182				[d] 296	531
Specimen No. 9					
4	0.56	$>>I_p$	0.56	18	
9	.30	$>>I_p$	.30	35	
15	.30	$>>I_p$	.30	49	
21	.27	$>>I_p$	.27	63	
28	.24	$>>I_p$	.24	78	
36	.30	$>>I_p$	.30	95	
45	.26	$>>I_p$	.26	115	
52	.31	$>>I_p$	.31	131	
64	.24	$>>I_p$	.24	157	
74	.21	$>>I_p$	.21	176	
84	.21	$>>I_p$	.21	193	
93	.17	$>>I_p$	.17	207	
101	.18	$>>I_p$	.18	218	
109	.16	$>>I_p$	.16	229	
128	.16	$>>I_p$	.16	253	
140	.13	$>>I_p$	.13	268	
156	.15	$>>I_p$	.15	286	
168	.23	$>>I_p$	.23	304	
178	.18	$>>I_p$	.18	321	
182				[d] 327	605
Specimen No. 11					
4	0.65	$>>I_p$	0.65	21	
9	.30	$>>I_p$	.30	40	
15	.26	$>>I_p$	.26	53	
21	.24	$>>I_p$	.24	65	
28	.22	$>>I_p$	.22	78	
36	.28	$>>I_p$	.28	94	
45	.26	$>>I_p$	.26	114	
52	.28	$>>I_p$	.28	129	
64	.24	$>>I_p$	.24	154	
74	.21	$>>I_p$	.21	172	
84	.25	$>>I_p$	.25	190	
93	.15	$>>I_p$	.15	204	
101	.16	$>>I_p$	.16	214	
109	.14	$>>I_p$	.14	224	
128	.16	$>>I_p$	.16	247	
140	.13	$>>I_p$	.13	261	
156	.14	$>>I_p$	.14	278	
168	.17	$>>I_p$	.17	293	
178	.16	$>>I_p$	.16	307	
182				[d] 312	543
Specimen No. 13					
2	0.080	[e] $>>I_p$	0.080	1.3	
8	.050	$>>I_p$	.050	4.4	
27	.042	0.075	.027	10.2	
33	.14	[e] .075	.049	12.0	
43	.075	[e] .075	.038	15.5	
53	.10	.075	.043	18.8	
63	.090	.050	.032	21.8	
75	.090				
81	[e] .090	.035	.025	25.9	
91	.075	.040	.026	27.9	
102	.075	.050	.031	30.4	
118	.055	.075	.032	34.5	
130	.060	.15	.043	38.1	
147	.050	[e] .15	.037	43.6	
151		.15			
158	.050	[e] .090	.032	46.7	
174	.055	.090	.034	50.9	
180				52.5	49.0

[a] See polarization curves—figures 5 and 8 for controls 9 and 13, respectively.

[b] $i_o = I_p I_q / (I_p + I_q)$. $i_o = I_p$ approximately, when $I_q >> I_p$.

[c] Calculated weight loss (g) $= kti$, where $K = 0.9316 \times 10^{-4}$ g/C, $i = i_o$ = average current (amperes) for the period (t in seconds) between successive readings. The value of i_o at the instant of exposure and at the end of exposure is taken as the initial and final values, respectively, as calculated. Weight loss in mg = $8.05\, t\, i_o$, approximately; where t = days, i_o = mA.

[d] By taking for I_p the value of current at the assumed beginning of the hydrogen—over voltage curve (straight line through points, see fig. 5), the calculated values for specimens 7, 9, and 11 become, respectively, 499 mg, 545 mg, and 517 mg. See the text.

[e] Assumed (no curve) on the basis of measurements made before or after.

cathodic control while the corrosion reactions of the pair of specimens with soil rings exposed to salt water in the glass jar were of mixed control. For controls 7, 9, and 11, the use of the current indicated by the arrow on the cathodic polarization curves (fig. 5) in place of the current I_p in the equation for corrosion rate (footnote b, table 2) results in better agreement between calculated and actual weight losses (footnote d, table 2). This observation is also suggested in some unpublished data on aluminum previously obtained by the author and also on published data on aluminum exposed underground [14]. The theoretical aspects of the current indicated by the arrow as a value required for complete cathodic protection (for iron) have been previously discussed by the author and by others [15, 16, 17].

3.3. Aluminum Alloy in Salt Solution of *p*H 10

Data on the aluminum alloy in salt water made alkaline (*p*H 10) by the addition of sodium carbonate are shown in tables 3 and 4 and in figures 10 and 11. The sodium carbonate has caused the corrosion to be under anodic control (fig. 10 and table 4) and apparently made cathodic protection impossible and undesirable because the cathodic currents produced cathodic corrosion (table 3) and greatly accelerated corrosion over that on the controls. Also, noteworthy is how an increase in polarization potential of the cathodes (from −1.3 to −1.5 V) stepped up the corrosion rate tremendously.

The potential-decay curves (fig. 12) obtained on cathodes 16 and 18 at the end of exposure are indicative of cathodic corrosion. The greater corrosion on

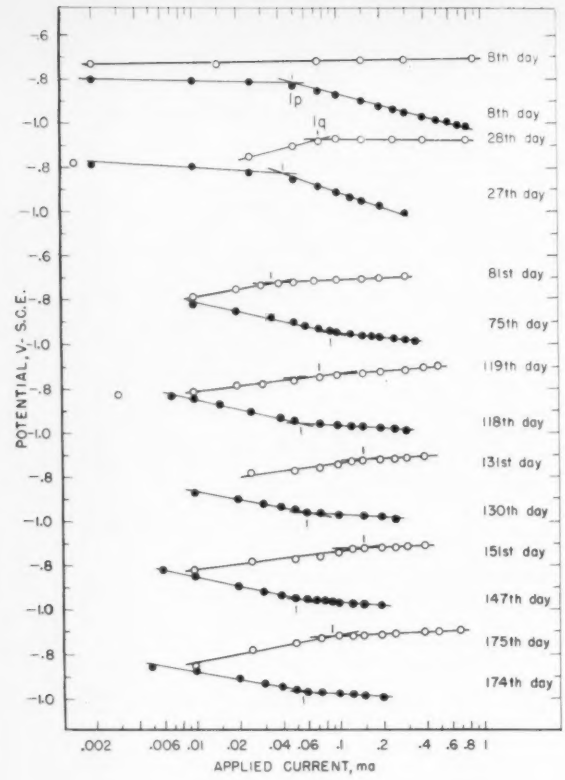

FIGURE 8. *Some polarization curves of control 13 during 6 months of exposure to salt solution and soil in jar.*
0—anodic; ●—cathodic.

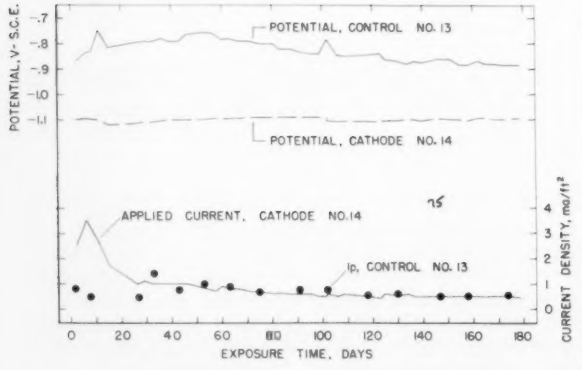

FIGURE 9. *Relation between applied current (to cathode) and currents (I_p) indicated by cathodic polarization curves (of control) for aluminum alloy exposed to saltwater and soil in jar.*
Cathode held at about −1.1 volt as shown

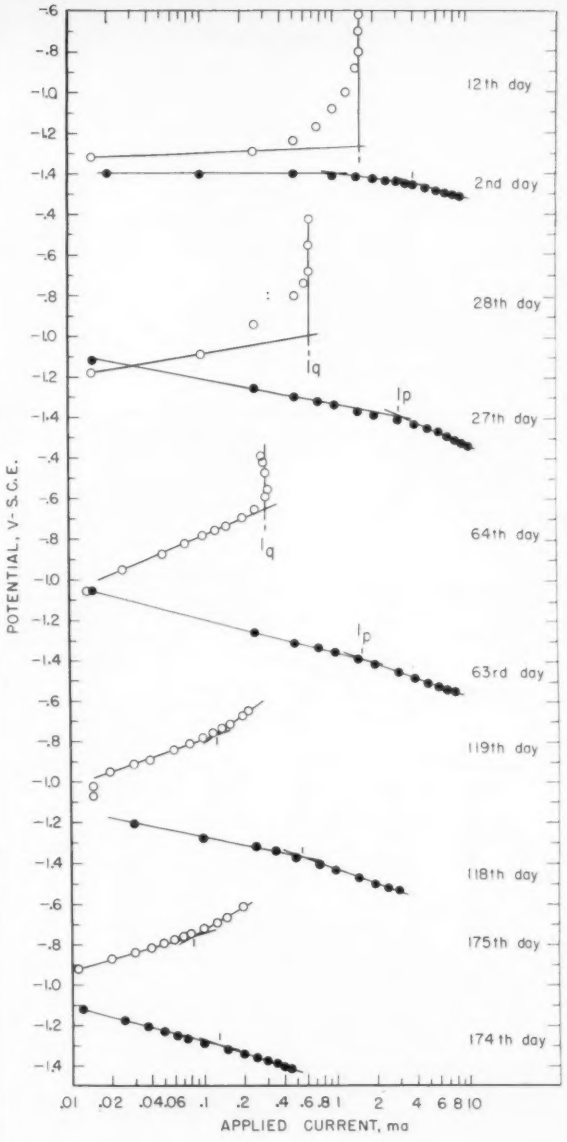

FIGURE 10. *Some polarization curves of alloy control 15 during 6 months of exposure to salt solution of pH 10.*
0—anodic; ●—cathodic

cathode 18 is predictable from the curves. That the applied cathodic currents were not unnecessarily high is indicated by the fair agreement of the polarization currents, I_p, on the controls with the applied currents to the cathodes (fig. 11). An additional reason for believing that lower values of applied currents would not have resulted in cathodic protection lies in the fact that calculated corrosion rates (table 4) using the currents I_p are in reasonable agreement with the actual corrosion rates. However, it should be noted that the corrosion current (table 4)

741-635—64——7

TABLE 3. *Effect of cathodic currents on aluminum alloy (6063–T5) exposed for 6 months to salt solution (pH 10)*

Specimen [a]	Cathodic polarization curve—controls				Potential criterion, cathodes	Applied current			Potential		Weight loss [c]	Remarks—Nature of corrosion and pitting [d]
	Current at break, I_p		Potential at break, E_a			Range—6 mo.			Range—6 mo.			
	Range—6 mo.		Range—6 mo.									
	Min	Max	Min	Max		Min	Max	Mean [b]	Min	Max		
	mA-ft²	*mA-ft²*	*V*	*V*	*V*	*mA-ft²*	*mA-ft²*	*mA-ft²*	*V*	*V*	*mg*	
15, control	1.0	50.0	−1.30	−1.46				0.0	−1.055	−1.420	523	Uniform corrosion—about 0.001 in. reduction in rod diameter. Little or no measurable pitting.
16, cathode					[e] E_a	2.4	32.0	11.5	−1.365	−1.490	1231	Numerous pits up to 4 mils. About 0.0029 in. reduction in rod diameter.
17, control	1.6	60.0	−1.30	−1.45				0.0	−1.050	−1.420	495	Uniform corrosion—about 0.00084 in. reduction in rod diameter. Little or no measurable pitting.
18, cathode					−1.5	4.0	58.0	14.6	−1.455	−1.550	3091	Considerable pitting with several pits 60 to 100 mils. Reduction in rod diameter was about 0.0068 in.

[a] Specimens 15 and 16 were exposed to 4.5 gal of solution contained in one glass jar and specimens 17 and 18 to the same kind of solution in a second jar.
[b] Based on area under current-time curve (fig. 11).
[c] Exposed area 0.1 ft².
[d] Rod diameter change based on average change of 25 measurements made with micrometer caliper on both exposed and unexposed parts of the specimen.
[e] E_a, Potential corresponding to I_p, cathodic polarization curve of control No. 15.

TABLE 4. *Corrosion rates of alloy controls as calculated from polarization curves*

Specimen No. 15						Specimen No. 17					
Exposure time	Current at break in curve [a]		Corrosion current i_o [b]	Weight loss [c]		Exposure time	Current at break in curve [a]		Corrosion current i_o [b]	Weight loss [c]	
	Cathodic I_a	Anodic I_q		Calculated cumulative	Actual		Cathodic I_a	Anodic I_q		Calculated cumulative	Actual
Days	*mA*	*mA*	*mA*	*mg*	*mg*	*Days*	*mA*	*mA*	*mA*	*mg*	*mg*
2	4.0	[d] 1.6	1.1	18		8	5.0	[d] 1.4	1.1	71	
12		1.6				11		1.4			
15	5.0	[d] 1.6	1.2	143		15	6.0	[d] 1.4	1.1	133	
26	3.1	[d] 0.65	0.54	220		28	2.9	0.65	0.53	218	
32	2.5	.65	.52	246		43	[d] 1.6	.35	.29	268	
63	1.6	.30	.25	341		53	1.6	.060	.058	282	
88	1.3	.10	.093	375		75	1.3	[d] .060	.057	292	
118	0.55	.13	.11	399		102	1.0	.060	.057	304	
130	.70	.060	.055	407		118	1.0	[d] .060	.057	311	
148	.50	.10	.083	417		130	0.90	.040	.038	316	
158	.10	[d] .10	.050	423		131		.040			
174	.13	.080	.050	429		147	0.50				
180				431	523	148	[d] 0.50	.080	.069	324	
						158	0.15	[d] .080	.052	329	
						174	0.10	[d] .060	.037	335	
						175	[d] 0.10	.060	.037		
						180				337	495

[a] See polarization curves—figure 10.
[b] $i_o = I_p I_q / (I_p + I_q)$.
[c] Calculated weight loss (g) $= kti$, where $K = 0.9316 \times 10^{-4}$ g/C, $i = i_o$ = average current (amperes) for the period (t in seconds) between successive readings. The value of i_o at the instant of exposure and at the end of exposure is taken as the initial and final values, respectively, as calculated. Weight loss in mg = 8.05 t i_o, approximately; where t = days, i_o = mA.
[d] Assumed (no curve) on basis of measurements made before or after.

diminished greatly with time and that the corrosion reaction was becoming less under the influence of anodic control. This suggests the possibility that eventually, given additional time of exposure, cathodic protection might have been possible, for example on cathode 16.

3.4. Aluminum Alloy in Salt Solution of *p*H 4

Data on the aluminum alloy in salt water made acid (*p*H 4) by the addition of acetic acid are shown in tables 5 and 6 and in figures 13 and 14.

The data indicate that cathodic protection is necessary and possible in such an environment. Of the two potential criteria used, polarization to about −1.0 V seems to be the more desirable. The potentials and the corrosion rates seemed to be very susceptible to changes in solution temperature and therefore the temperature (typical of all solutions in jars) of the acid solution is shown in figure 14. The corrosion rate (corrosion current, table 6) is more stable over the long run than the rates for any of the other exposures and is under strict cathodic control (fig. 13). Thus, the current required for cathodic

TABLE 5. *Effect of cathodic currents on aluminum alloy (6063–T5) exposed for 6 months to salt solution (pH 4)*

Specimen [a]	Cathodic polarization curve—controls				Potential criterion, cathodes	Applied current			Potential		Weight loss [c]	Remarks—Nature of corrosion and pitting [d]
	Current at break, I_p		Potential at break, E_a			Range—6 mo			Range—6 mo			
	Range—6 mo		Range—6 mo									
	Min	Max	Min	Max		Min	Max	Mean [b]	Min	Max		
	mA-ft²	*mA-ft²*	*V*	*V*	*V*	*mA-ft²*	*mA-ft²*	*mA-ft²*	*V*	*V*	*mg*	
19, control	4.2	22.0	−0.76	−0.93				0.6	−0.720	−0.865	1533	Many pits 10–12 mils—max. 20 mils. Ring of corrosion at edge of tape. Reduction of about 0.0032 in. in rod diameter.
20, cathode					[e] E_a	4.8	19.0	10.3	−.775	−.935	484	A few pits to 5 mils deep. Most corrosion at edge of tape. Reduction of about 0.0014 in. in rod diameter.
21, control	3.9	16.0	−.76	−0.90				0.0	−.720	−0.845	1556	Many pits, six or more 20 mils deep. Ring of corrosion at edge of tape. Reduction of about 0.0027 in. in rod diameter.
22, cathode					−1.0 to 1.05	5.2	22.0	10.6	−1.010	−1.055	303	Most pitting (1–2 mils at edge of tape. Two pits (5 mils). Reduction of about 0.00046 in. in rod diameter.

[a] Specimens 19 and 20 were exposed to 4.5 gal of solution contained in one glass jar and specimens 21 and 22 to the same solution in a second jar.
[b] Based on area under the current-time curve (fig. 14).
[c] Exposed area 0.1 ft².
[d] Rod diameter change based on average change of 25 measurements made with micrometer caliper on both exposed and unexposed parts of the specimen.
[e] E_a, potential corresponding to I_p, cathodic polarization curve of control No. 19.

TABLE 6. *Corrosion rates of alloy controls as calculated from polarization curves*

Exposure for 6 months to salt solution (pH 4).

Specimen No. 19						Specimen No. 21					
Exposure time	Current at break in curve [a]		Corrosion current i_0 [b]	Weight loss [c]		Exposure time	Current at break in curve [a]		Corrosion current i_0 [b]	Weight loss [c]	
	Cathodic I_p	Anodic I_q		Calculated cumulative	Actual		Cathodic I_p	Anodic I_q		Calculated cumulative	Actual
Days	*mA*	*mA*	*mA*	*mg*	*mg*	*Days*	*mA*	*mA*	*mA*	*mg*	*mg*
2	1.6	$>>I_p$	1.6	26		8	1.5	$>>I_p$	1.5	97	
15	1.6	$>>I_p$	1.6	193		54	1.0	$>>I_p$	1.0	578	
27	2.2	$>>I_p$	2.2	376		81	0.85	$>>I_p$	0.85	778	
33	1.3	$>>I_p$	1.3	464		102	.75	$>>I_p$	.75	913	
43	0.75	$>>I_p$	0.75	544		119	1.6	$>>I_p$	1.6	1077	
63	.64	$>>I_p$	.64	657		130	0.85	$>>I_p$	0.85	1183	
71	.54	$>>I_p$	.54	695		147	1.1	$>>I_p$	1.1	1316	
75	.56	$>>I_p$	.56	713		158	0.39	$>>I_p$	0.39	1382	
90	.75	$>>I_p$	.75	791		173	.75	$>>I_p$	.75	1451	
119	1.4	$>>I_p$	1.4	1047		180				1493	1556
130	0.60	$>>I_p$	0.60	1135							
147	1.4	$>>I_p$	1.4	1272							
158	0.42	$>>I_p$	0.42	1352							
173	1.0	$>>I_p$	1.0	1438							
180				1494	1533						

[a] See polarization curves—figure 13.
[b] $i_0 = I_p I_q / (I_p + I_q)$. $i_0 = I_p$ approximately, when $I_q >> I_p$.
[c] Calculated weight loss (g) $= kti$, where $K = 0.9316 \times 10^{-4}$ g/C, $i = i_0$ = average current (amperes) for the period (t in seconds) between successive readings. The value of i_0 at the instant of exposure and at the end of exposure is taken as the initial and final values, respectively, as calculated. Weight loss in mg $= 8.05\ t\ i_0$, approximately; where t = days, i_0 = mA.

protection is equal to the corrosion current as verified by the good agreement between calculated and actual weight losses (table 6).

Observations of decay potentials (fig. 15) when applied currents were removed from the cathodes after 6 months of exposure are again of interest and as previously reasoned are indicative of cathodic protection. Greater depolarization took place on cathode 22 which had the better degree of protection. The relation between the cathode potential after depolarization and the control corrosion potential is probably not too significant here because the control potentials were subject to considerable change in relatively short periods of time.

4. Summary

Pairs of aluminum alloy (6063–T5) specimens were exposed to 21 saturated soils under substantially air-free conditions for 6 months in the laboratory. The soils ranged in *p*H from 3.4 to 10.0 and their resistivities with two exceptions were between 60 and

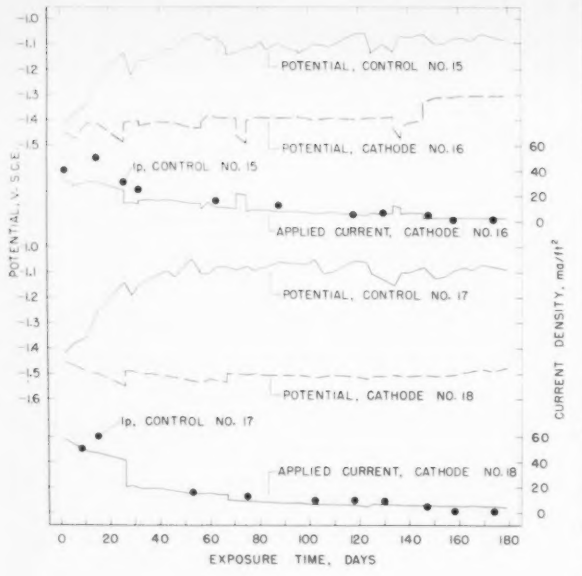

FIGURE 11. *Relation between applied currents (to cathodes) and currents (I_p) indicated by cathodic polarization curves (of controls) for aluminum alloy exposed to salt solution of pH 10.*

Cathodes are controlled by two potential criteria, as shown.

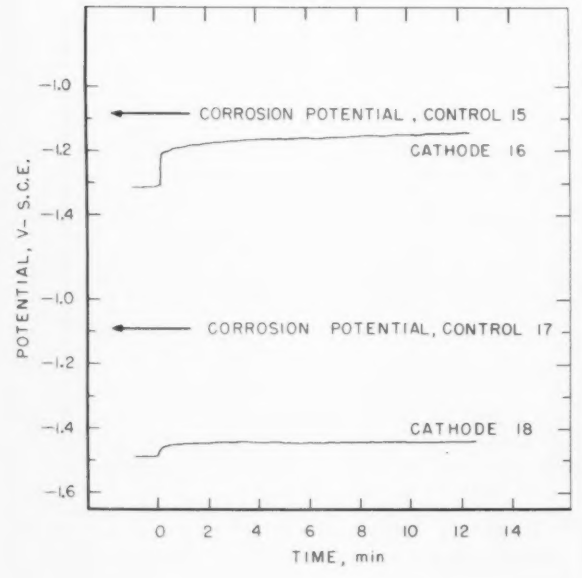

FIGURE 12. *Potential-decay curves of cathodes exposed to salt solution of pH 10 following removal of currents applied for 6 months.*

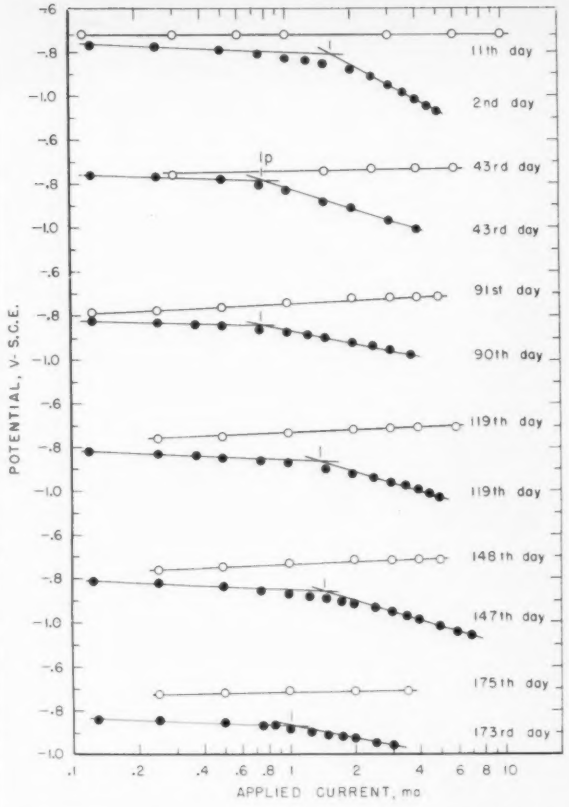

FIGURE 13. *Some polarization curves of alloy control 19 during 6 months of exposure to salt solution of pH 4.*

0—anodic; ●—cathodic.

1500 ohm-cm. After stabilization, the potentials of the specimens in 20 of the 21 soils were between −0.68 and −0.98 V (S.C.E.) and the potential in the remaining soil (*p*H 10) was −1.36 V. Except for the latter soil, there seemed to be no particular relation between potential and *p*H. The corrosion which occurred during the 6 months was only superficial in nature. In order to observe the effect of aeration of the soils on the potentials of the alloy and on the corrosion rates, that is, under more normal conditions of exposure,one specimen of each pair was observed for an additional 18 weeks by making air accessible. The result was that all potentials became more cathodic and, except for 2 soils with fairly high resistivities, the corrosion rates increased tremendously with pits up to 110 mils deep. The selection of a protective potential generally applicable to aluminum alloys underground is considered undesirable because of the danger of cathodic corrosion.

Aluminum alloy (6063–T5) specimens were exposed to still city water with 3 percent sodium chloride added contained in a large open wooden vat (265 gal) and also to water similarly treated contained by 4.5 gal Pyrex jars. Of five jars, the *p*H (8) of the water in one jar was left unchanged while the water

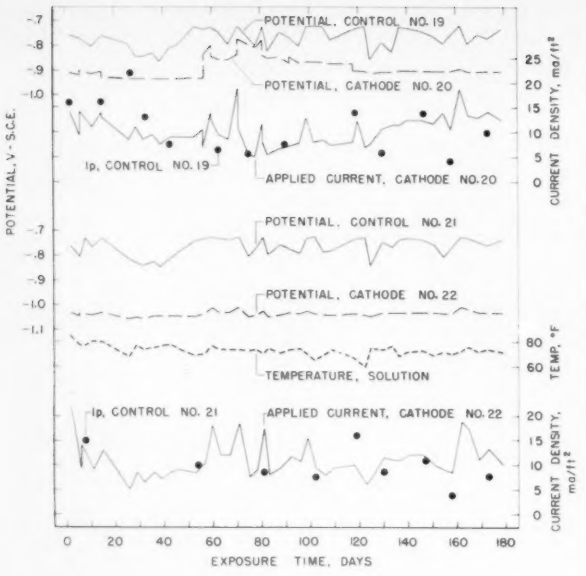

FIGURE 14. *Relation between applied currents (to cathodes) and currents (I_p) indicated by cathodic polarization curves (of controls) for aluminum alloy exposed to salt solution of pH 4.*

Cathodes are controlled by two potential criteria, as shown.

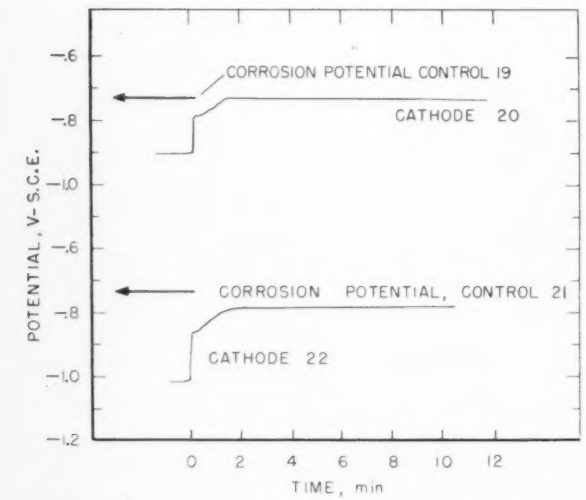

FIGURE 15. *Potential-decay curves of cathodes exposed to salt solution of pH 4 following removal of currents applied for 6 months.*

in two jars was adjusted to *p*H 4 by the addition of acetic acid and the water in the other two jars was adjusted to *p*H 10 by the addition of sodium carbonate. All specimens were exposed for 6 months.

Six specimens were exposed to the salt solution in the wooden vat, 3 being left to corrode freely and the other 3 with cathodic currents applied after corroding freely for 2 days. The currents were dependent on controlled potentials, namely, a value from the cathodic polarization curve, potential of a high purity zinc anode (about −1 V), and the potential of −1.5 V (S.C.E). The −1.5 V potential caused severe cathodic corrosion while the other two potentials provided about equal degrees of cathodic protection, the more anodic potential of the zinc being somewhat better in reducing pitting under the tape at the waterline.

Measurements were made on a pair of specimens in the jar of salt water, a control and a cathode, each fitted with a rubber cap containing clay soil in contact with about 12 percent of the area exposed. A ring of corrosion which had occurred adjacent to the rubber on the control was hardly perceptible on the cathode which was held at about −1.1 V, yet corrosion was not arrested.

A pair of specimens consisting of a control and a cathode were exposed in each of the 2 jars containing the acidic-salt water. In one of the jars the cathode was controlled by the potentials (−0.775 to −0.935 V) periodically obtained from the cathodic polarization curves of the control while the cathode in the other jar was held between −1.01 and −1.05 V. Cathodic protection was achieved on both and was better on the cathode held in the more anodic range of potentials. The current density necessary for protection was well indicated by the current at the breaks in the cathodic polarization curves of the controls.

Cathodic corrosion took place on the two cathodes which were exposed to the salt solution of *p*H 10.

Potential-decay curves obtained on all cathodes when applied currents were removed after 6 months of continuous exposure gave a clue as to whether the accumulative cathodic effects were protective or corrosive in nature.

Thanks are due Ray I. Lindberg, Metallurgical Research Laboratories, Reynolds Metals Company, who furnished the aluminum anodes used in some of the experiments. The cooperation of Melvin Romanoff, Corrosion Section, National Bureau of Standards, in permitting the use of one of his test sites and some of his unpublished data is appreciated.

5. References

[1] R. B. Mears and R. H. Brown, Industrial Engineering Chemistry **29,** 1087 (1937).

[2] B. P. Caldwell and V. J. Albano, Rate of solution of zinc and aluminum white cathodic, Trans. E.C.S. **76,** 271 (1939).

[3] R. B. Mears and R. H. Brown, ibid, p. 283.
[4] R. B. Mears, Trans. A.I.C.E. **37,** No. 6 (Dec. 25, 1941.)
[5] Edward T. Wanderer and Donald O. Sprowls, Aluminum alloys for offshore pipelines, Corrosion **8,** 227 (July 1952).
[6] R. S. Dalrymple, Underground aluminum gas line, Corrosion **12,** 602t (Dec. 1956).
[7] E. Deltombe and M. Pourbaix, The electrochemical behavior of aluminum; potential-pH diagram of the System Al·H_2O at 25 °C, Corrosion **14,** 496t (Nov. 1958).
[8] D. O. Sprowls and M. E. Carlisle, Jr., Resistance of aluminum alloys to underground corrosion, Corrosion **17,** 125 (Mar. 1961).
[9] J. F. Whiting and T. E. Wright, Cathodic protection for an uncoated aluminum pipeline, Corrosion **17,** 9 (Aug. 1961).
[10] F. W. Hewes, Investigation of maximum and minimum criteria for the cathodic protection of aluminum in soil, paper presented at the 18th Annual Conference, National Association of Corrosion Engineers, Kansas City, Missouri, March 1962.
[11] Melvin Romanoff, Underground corrosion, NBS Circ. 579.
[12] David J. G. Ives and George J. Janz, Reference Electrodes, (Academic Press, New York and London, 1961).
[13] W. J. Schwerdtfeger and O. N. McDorman, Measurement of the corrosion rate of a metal from its polarizing characteristics, J. Electrochem. Soc. **99,** 407 (1952).
[14] W. J. Schwerdtfeger A study by polarization techniques of the corrosion rates of aluminum and steel underground for sixteen months, J. Res. NBS **65C** (Engr. and Instr.) No. 4, 271 (Oct.–Dec. 1961).
[15] W. J. Schwerdtfeger and O. N. McDorman, Potential and current requirements for the cathodic protection of steel in soils, J. Res. NBS **47,** 104 (1951) RP2233; Corrosion **8,** 391 (1952).
[16] Scott Ewing, Proc. Am. Gas Assoc. 613 (1940).
[17] E. W. Haycock, Current requirements for cathodic protection of oil well casings, Corrosion **13,** 767t (Nov. 1957).

(Paper 68C4–175)

JOURNAL OF RESEARCH of the National Bureau of Standards—C. Engineering and Instrumentation
Vol. 68C, No. 4, October–December 1964

Photooxidation of Asphalts in the Presence of Ozone

James R. Wright and Paul G. Campbell

(May 8, 1964)

The effects of ozone on the photooxidation of coating-grade asphalts were compared to those of air and of oxygen under a variety of radiant energy conditions. Oxidative changes were measured by infrared spectroscopy and by the time to film failure as denoted by cracking.

Surfaces of noncatalyzed asphalts were oxidized when treated with ozone in total darkness, room light, solar radiation, and the radiant energies of the carbon and xenon arcs. No oxidation was detected when the asphalts were exposed to room light in oxygen alone. A $FeCl_3$-catalyzed asphalt was not oxidized by ozone in total darkness. Photooxidation rates of all asphalts increased as exposures were made to carbon-arc radiation in air, in oxygen, and in ozone-enriched oxygen. Each asphalt exhibited a different oxidative response to solar, xenon-arc, and carbon-arc radiant energy sources.

1. Introduction

In recent years, the high interest in the problem of atmospheric smog has led to extensive research on atmospheric oxidants other than oxygen and their reactions with organic materials in the presence of sunlight [1].[1] While this problem appears pertinent to air-blown asphalts, which are organic materials and are exposed to the same atmospheric conditions during weathering, it has received little attention in asphalt weathering research. Pfeiffer [2] described the effects of various oxidants (aromatic nitro compounds) on asphalt. Nellensteyn and Steffelaar [3] passed nitrogen dioxide through solutions of asphalt in carbon tetrachloride and observed the formation of a precipitate which contained 25 percent oxygen and 5 percent nitrogen. In a very general way, Brown [4] discussed the effects of ozone on asphalt but presented no experimental data.

As part of a program for studying the environmental conditions which influence asphalt degradation, the effects of an ozone-oxygen atmosphere on the photooxidation of asphalt films (25μ thick) were examined. Using infrared spectroscopy it was possible to follow oxidative changes in asphalt films due to ozonation in the dark, in room light, in sunlight, and in the radiant energies of the carbon arc and the xenon arc, and to compare the changes so produced with those found in oxygen and in air.

2. Experimental Procedure

2.1. Materials

Three commercial coating-grade roofing asphalts (Nos. 6, 16, and 3) and one experimental asphalt (No. 3X) were used in this study. Asphalt No. 6 was of Southeastern U.S.A. origin, asphalt No. 16 was of Midcontinent U.S.A. origin, and asphalt No. 3 was a California Coastal asphalt which had been catalyzed with ferric chloride. The experimental asphalt No. 3X was blown in the laboratory from the same asphalt flux as the commercial asphalt 3, but did not contain the $FeCl_3$ catalyst. The physical properties of these asphalts and other pertinent data are given in table 1.

TABLE 1. *Physical properties of asphalts*

No.	Source	Softening point [1]	Penetration at 25 °C	Flash point (COC)[3]	Specific gravity at 25 °C	Durability [2]
		°C	1/10 mm	°C		days
3	California Coastal (catalyzed)	105	18	252	1.032	44
3X	California Coastal (noncatalyzed)	104	18			
6	Talco	110	17	288	1.040	41
16	Illinois-Kansas-Oklahoma	117	15	343	1.008	93

[1] Ring and ball method.
[2] ASTM D 529-59T, "Tentative recommended practice for accelerated weathering of bituminous materials" (51-9C cycle).
[3] Cleveland open cup method.

2.2. Ozone Preparation and Analysis

A quartz mercury-arc ultraviolet generator, Ozone Research and Equipment Corporation (Model O_3Q), was used as the ozone source. This instrument produces ozone concentrations from 0 to 20,000 pphm vol^{-1} (0 to 200 ppm vol^{-1}). Dry oxygen was used in the preparation of the ozone. Ozone concentrations were determined by the iodometric method, i.e., the quantitative release of iodine from an aqueous solution of potassium iodide and titration of the released iodine with sodium thiosulfate (standardized immediately before use). The ozone concentration in the present experiments was 5200 pphm vol^{-1}.[2]

2.3. Photooxidation

The method used to measure photooxidation rates was based on changes in the infrared spectra of 25-μ

[1] Figures in brackets indicate the literature references at the end of this paper.

[2] Separate experiments showed that the amount of ozone generated by the enclosed carbon- and xenon-arc weatherometers was negligible. The open carbon arc (Atlas Weather-Ometer, Model XW) generated ozone as high as 43 pphm vol^{-1}.

thick films at 1700 cm^{-1} (5.88 μ) due to exposure to carbon-arc radiant energy. Detailed procedures for the preparation, irradiation, and infrared analysis of these films in air have been reported previously [5, 6, 7]. The irradiation of asphalt films in an ozone-oxygen or oxygen atmosphere required modified aluminum holders and glass apparatus designed to permit replacement of air with the selected atmosphere and subsequent irradiation in that environment.

The use of aluminum panels has proved very useful in conjunction with the infrared analysis of asphalt thin films [6]. However, new modified aluminum holders have been designed for use where space is limited. The holder is depicted in figure 1. The holder dimensions are 3/8 in. $\times$ 1/4 in. $\times$ 2 in., with an opening 5/16 in. $\times$ 13/16 in., which is larger than the slit opening of the infrared spectrophotometer. The film holder may then be fitted tightly into a modified spectrophotometer sample holder. The experimental procedure was the same as that used with the regular aluminum panels. Separate experiments established that ΔA values (changes in absorbance at 1700 cm^{-1}) obtained from asphalt films mounted on either the usual aluminum panels or on the newer film holders were identical. However, time to film failure was altered, due to the different dimensions of the unsupported asphalt film. In general, asphalt films mounted on the smaller holders did not crack as soon as those mounted on the larger panels.

The irradiation of thin films of asphalt in an atmosphere other than air necessitated the construction of exposure tubes which would transmit appreciable amounts of radiant energy and which could be conveniently sealed. For this purpose, flat culture tubes (Corning 9200, 23 mm $\times$ 11.5 mm $\times$ 152 mm) were modified with ball joints and with stopcocks. The tubes used had a range in transmission of 81.5 to 82.05 percent at 350 mμ as measured by a Beckman DU Spectrophotometer. The assembled apparatus is shown in figure 2.

Most of the asphalt exposures were made in an Atlas Weather-Ometer, Model SMC–R, equipped with an automatic line voltage regulator which controlled arc voltage at 210 V $\pm$1 percent. This machine controlled temperature within $\pm$1 °C of a selected value. The radiant energy source was a single, enclosed carbon arc. Exposures were made at a black panel temperature of 49 °C for selected durations. For those exposures in an ozone-oxygen atmosphere or in oxygen, duplicate specimens were placed in the glass apparatus, flushed for 1 hr (in light and at room temperature), and then irradiated. For comparative purposes, exposures in air were also made in the glass apparatus. The exposures of asphalt in ozone-oxygen to solar radiant energy were made on a clear, sunny day in February in Washington, D.C. The xenon-arc exposures were made at 49 °C with Atlas Weather-Ometer, Model 60–WR, equipped with a constant wattage transformer.

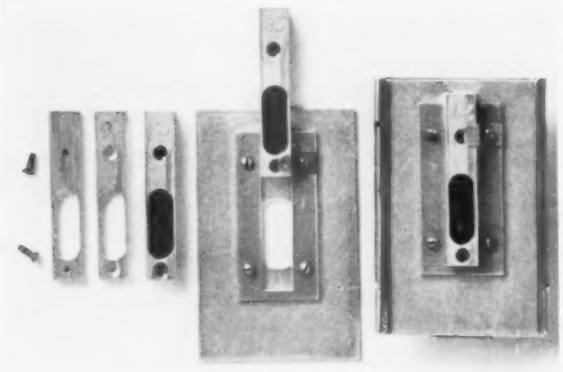

FIGURE 1. *Asphalt-film exposure holder.*

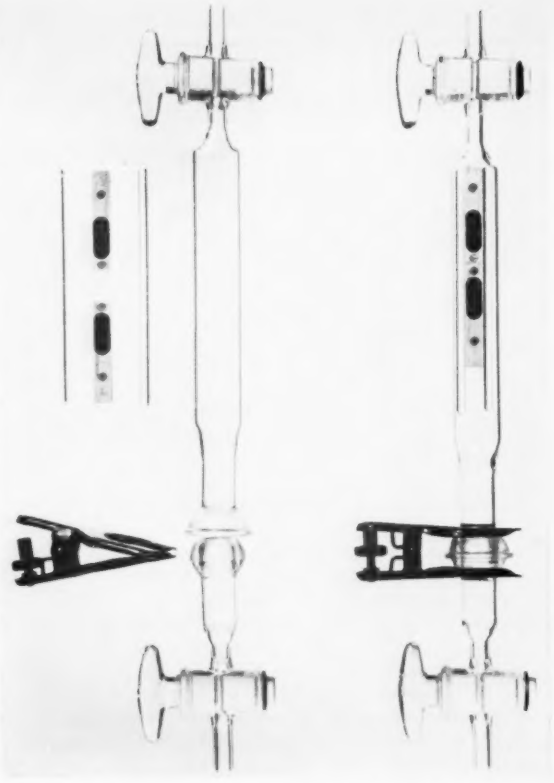

FIGURE 2. *Glass irradiation apparatus for asphalt films.*

3. Results and Discussion

3.1. Southeastern U.S.A. Asphalt

Films of commercial asphalt 6 were found to undergo oxidation and/or photooxidation under all experimental conditions in which the asphalt surface was brought into contact with ozone. The resultant oxidative changes are shown by the infrared spectra in figure 3a. The spectrum of the original asphalt,

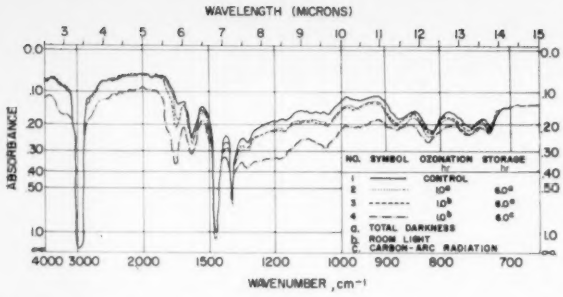

FIGURE 3a. *Infrared spectra of asphalt No. 6 showing the effects of ozone under various radiant energy conditions (see text).*

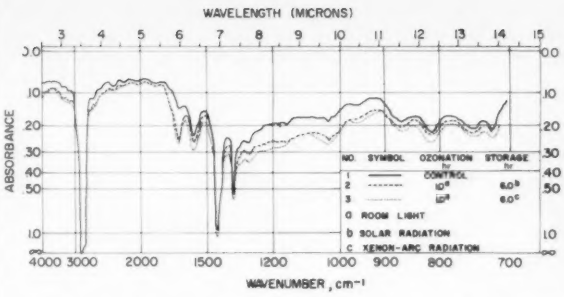

FIGURE 3b. *Infrared spectra of asphalt No. 6 showing the effects of ozone in the presence of solar and xenon-arc radiation.*

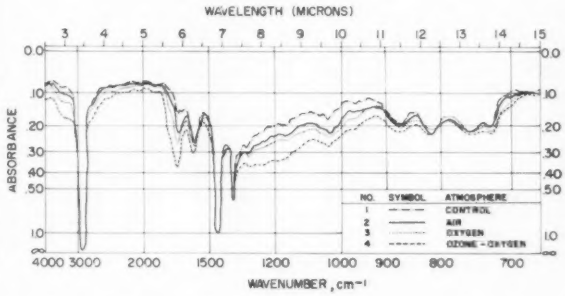

FIGURE 4. *Infrared spectra of asphalt No. 6 showing the effects of exposure to the carbon arc (49 °C, 6 hr) in various environments.*

which had been exposed to room light and air, is shown in curve 1. The second spectrum (curve 2) is that of asphalt 6 after it had been flushed with ozone for 1.0 hr and stored for 6.0 hr, all in total darkness. Increased absorbance was observed in all of the identifiable oxygen-containing functional groups, the greatest change being in the carbonyl band at 1700 cm^{-1}. The ΔA value at this wave number was 0.025 absorbance units.

The effect of room light on the oxidation of asphalt 6 in the presence of ozone is shown in curve 3. The asphalt was flushed for 1.0 hr in room light followed by 6.0 hr storage in the dark. Changes in absorbance as compared to curve 2 were primarily in the carbonyl band where a ΔA value of 0.066 was obtained. The same experiment using oxygen, produced no detectable oxidation.

Far greater effects were found, however, when films of asphalt 6 were flushed with ozone-enriched oxygen for 1.0 hr in room light and exposed to the radiant energy of the carbon arc for 6.0 hr at a black panel temperature of 49 °C (curve 4). Pronounced changes were observed in the infrared spectrum from 4000 to 850 cm^{-1}. The ΔA value at 1700 cm^{-1} was 0.172.

Films of asphalt 6 in ozone-oxygen were exposed to two other radiant energy sources, i.e., solar radiant energy and to the xenon arc. Both sources promoted extensive photooxidation over a 6-hr period. Infrared spectra of the exposed asphalt films are shown in figure 3b. The changes in absorbances of the oxygen-containing functional groups were, in general, the same as those produced in the carbon arc. Since the asphalt specimens received different incident radiant energy dosages from each source, absorbances cannot be compared directly. However, the change in the absorbance of any given asphalt exposed to ozone in total darkness may be compared directly with the changes occurring when the same asphalt is exposed to radiant energy sources. In all cases, much more oxidation occurred in the presence of radiant energy.

In a series of experiments designed to observe photooxidation of asphalt in the presence of air, oxygen, and ozone-enriched oxygen under the same conditions of carbon-arc exposure time, intensity, and temperature, the presence of ozone greatly accelerated the photooxidation reaction(s). Oxidative changes were measured by infrared analysis as in the previous experiments. The spectra of the exposed asphalts are shown in figure 4. The respective ΔA values at 1700 cm^{-1} obtained with air, oxygen, and ozone-enriched oxygen after 6 hr exposure were 0.074, 0.098, and 0.182. Also, in the presence of ozone, large increases in absorbance were observed in other bands of oxygen-containing functional groups, namely, the 3500 cm^{-1} region (alcohols, free OH absorbances), the 2700 cm^{-1} region (acids, bonded OH stretching frequencies), and at 1600 cm^{-1} (aromatic and conjugated alkene and OH bonding). Much less absorbance was observed in these same areas when exposures were made in air or in oxygen.

In photooxidation-rate experiments with commercial asphalt 6 in air, in oxygen, and in ozone-enriched oxygen, respectively, the length of the induction period, the slope of the straight-line portion of the curve, and the time to film failure were affected by the atmosphere used (fig. 5). (Film failure, as denoted by cracking, occurred during the time interval following the last infrared scan and before the next sampling period.) The induction period in oxygen was less than that in air. In the presence of ozone, however, the induction period was completely eliminated. (Although the curve begins at the origin, it should be realized that some oxidation occurred

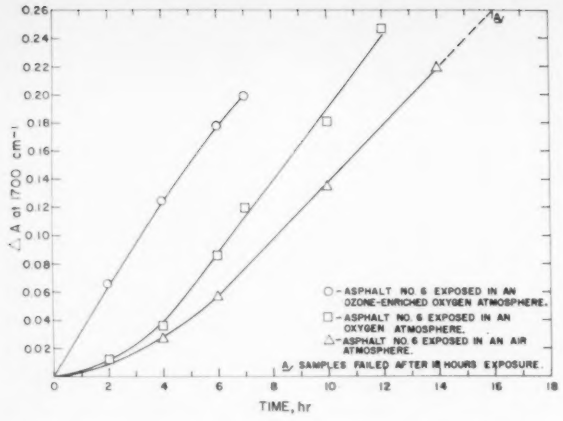
ΔA at 1700 cm⁻¹
TIME, hr
○ - ASPHALT NO. 6 EXPOSED IN AN OZONE-ENRICHED OXYGEN ATMOSPHERE.
□ - ASPHALT NO. 6 EXPOSED IN AN OXYGEN ATMOSPHERE.
△ - ASPHALT NO. 6 EXPOSED IN AN AIR ATMOSPHERE.
△ SAMPLES FAILED AFTER 18 HOURS EXPOSURE.

FIGURE 5. *Effects of various environments on asphalt No. 6 as measured by changes in infrared absorbance at 1700 cm⁻¹ with time of carbon-arc exposure (49 °C).*

during the ozone-flushing period.) The slopes of the curves are 0.0203 ΔA/hr for air, 0.0258 ΔA/hr for oxygen, and 0.0308 ΔA/hr for ozone-enriched oxygen.[3] When the slope for air is considered as unity, the ratio of the slopes for air, oxygen, and ozone-enriched oxygen becomes 1.0: 1.27: 1.52. Overall photodegradation rates as measured by film failure time for air were approximately 18 hr, for oxygen 12 hr, and for ozone-enriched oxygen 7 hr. Treatment of asphalt with ozone caused an approximate three-fold increase in photooxidation.

3.2. Midcontinent U.S.A. Asphalt

Experiments comparable to those described in section 3.1 were made with asphalt No. 16, a Midcontinent U.S.A. asphalt which had a durability (carbon-arc, 51–9C cycle) of 93 days (table 1). Ozonation of this asphalt in total darkness as well as to various radiant energy sources (carbon arc, xenon arc, and sunshine) produced results similar to those with asphalt 6. Changes as detected by infrared spectroscopy are shown in figures 6a and 6b. The greater stability of asphalt 16 to photodegradation is manifested by the smaller absorbance changes for any given radiant energy source. However, even in total darkness oxidation occurred to some extent, particularly in the carbonyl absorbance at 1700 cm^{-1}.

The effect of ozone, for a given radiant energy source (carbon arc), is clearly demonstrated in figure 7 where typical infrared spectra are given for 10-hr exposures in air, oxygen, and ozone-oxygen, respectively. Ozone greatly increased the amount of photooxidation that took place. The average ΔA (1700 cm^{-1}) values for air, oxygen, and ozone-oxygen were 0.062, 0.160, and 0.175, respectively.

[3] A straight-line slope was calculated for this system even though the curve deviates slightly from linearity for the last two exposure points.

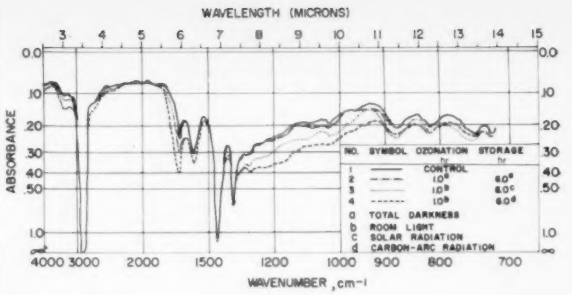

FIGURE 6a. *Infrared spectra of asphalt No. 16 showing the effects of ozone under various radiant energy conditions.*

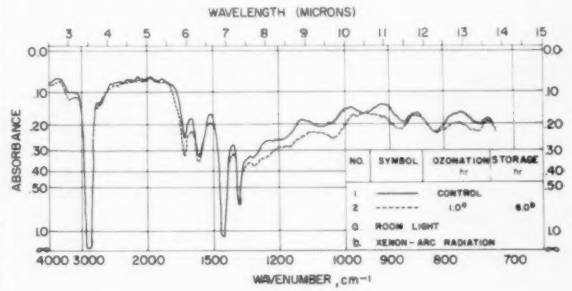

FIGURE 6b. *Infrared spectra of asphalt No. 16 showing the effects of ozone in the presence of xenon-arc radiation.*

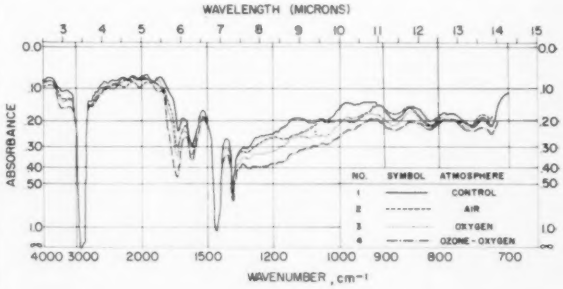

FIGURE 7. *Infrared spectra of asphalt No. 16 showing the effects of exposure to the carbon arc (49 °C, 10 hr) in various environments.*

The accelerating effect of ozone on the photooxidation of asphalt was demonstrated further by photooxidation rate experiments in the three respective gaseous environments. The rates may be compared in figure 8. For direct comparison the exposures in air were made in the glass apparatus as described in section 2.3.

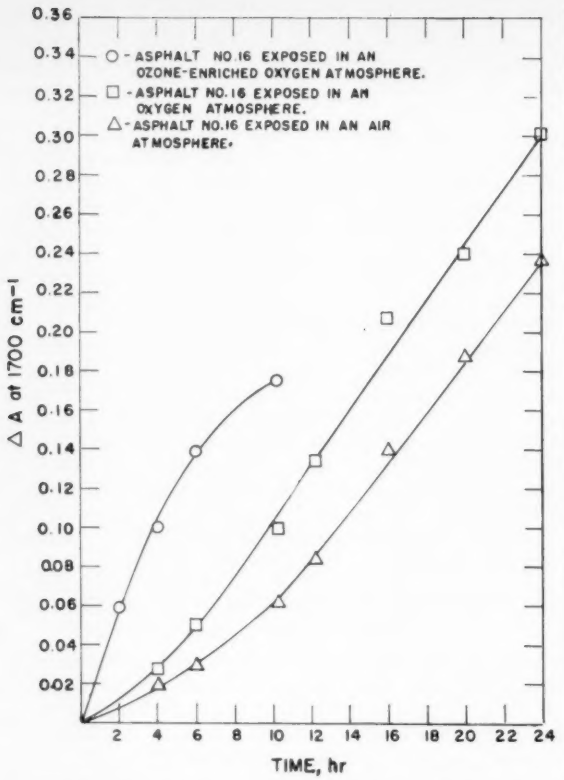
○ - ASPHALT NO.16 EXPOSED IN AN OZONE-ENRICHED OXYGEN ATMOSPHERE.
□ - ASPHALT NO.16 EXPOSED IN AN OXYGEN ATMOSPHERE.
△ - ASPHALT NO.16 EXPOSED IN AN AIR ATMOSPHERE.
Δ A at 1700 cm⁻¹
TIME, hr

FIGURE 8. *Effects of various environments on asphalt No. 16 as measured by changes in infrared absorbance at 1700 cm^{-1} with time of carbon arc exposure (49 °C).*

The results with asphalt 16 were similar to those of asphalt 6 in that the environments in the order of increasing oxidation rates were air, oxygen, and ozone-oxygen. With both asphalts, ozone reduced the film failure time to approximately one-half that in air. The values of ΔA (1700 cm^{-1}) per hour for the straight-line portions of the curves for asphalt 16 were 0.0126 in air, 0.0145 in oxygen, and 0.0200 in ozone-enriched oxygen. These results again manifest the greater photooxidation stability of asphalt 16 (93 days, 51–9C cycle) over that of asphalt 6 (41 days, 51–9C cycle).

3.3. California Coastal Asphalt

In addition to being from a different geographical source, the California Coastal asphalt (No. 3) differed from asphalts 6 and 16 in that it contained ferric chloride, an air-blowing (asphalt hardening) catalyst. Since this catalyst produced some unusual effects in the asphalt hardening process (necessary to make a coating-grade asphalt) [8], it was included in the present work to elucidate any effects on the photooxidation process with ozone. In order to separate the effects of catalyst and source, some experiments were made with asphalt No. 3X which had been air-blown in the laboratory from the same asphalt flux as that used for asphalt 3, but without the $FeCl_3$ catalyst.

Upon exposure to ozone in total darkness, asphalt 3 showed no detectable oxidation as determined by infrared techniques. Similar treatment of asphalt 3X produced measurable changes in the carbonyl absorbance at 1700 cm^{-1} as had asphalts 6 and 16. Thus, $FeCl_3$ appeared to inhibit the oxidation reaction caused by ozone in the darkness. (No oxidation could be induced with oxygen alone with any of the asphalts in total darkness.)

In the presence of radiant energy (solar, carbon arc, and xenon arc), however, photooxidation of asphalt 3 took place readily. Changes, as measured by infrared techniques, are shown in figure 9 for 6.0 hr exposures of asphalt 3 in ozone-oxygen to these three radiant energy sources. As with the previous asphalts, absorbance intensities are not directly comparable due to different incident radiant energy dosage for each source.

In general, absorbance changes indicate the formation of the same types of oxygen-containig groups in the three environments. A marked similarity of the spectra in the 4000 to 3000 cm^{-1} region (free hydroxyl) may be observed for the solar and xenon-arc exposures. The greater absorbance change caused by carbon-arc exposure may well be in part an effect of the difference in the spectral distribution of the radiant energy from this source.

Campbell and Wright have reported previously [8] that $FeCl_3$ appeared to act as a photosensitizer when $FeCl_3$-catalyzed asphalt was irradiated (carbon arc) in air. A direct comparison was made in the present work between asphalts 3 and 3X in ozone-oxygen to 6.0 hr solar irradiation. The carbonyl absorbance change, ΔA at 1700 cm^{-1}, was 0.101 for asphalt 3X and 0.133 for asphalt 3. These results confirm those for photooxidation in air and indicate that $FeCl_3$ may well accelerate the photooxidation of asphalt, but inhibits oxidation in total darkness.

The response of asphalt 3 to the conditions of photooxidation with air, oxygen, and ozone-enriched oxygen are shown in figure 10. The radiant energy source was the carbon arc and an exposure duration

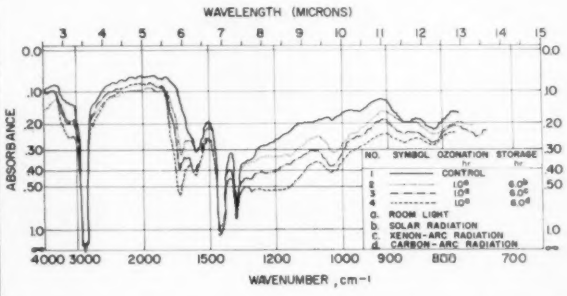

FIGURE 9. *Infrared spectra of asphalt No. 3 showing the effects of ozone under various radiant energy conditions.*

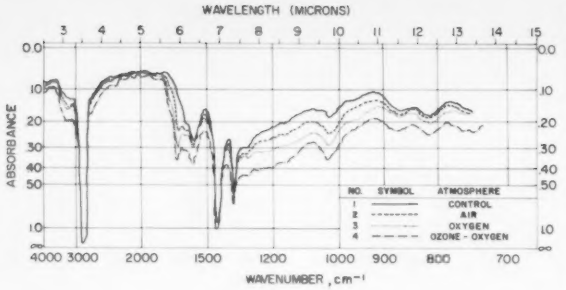

FIGURE 10. *Infrared spectra of asphalt No. 3 showing the effects of exposure to the carbon arc (49 °C, 3 hr) in various environments.*

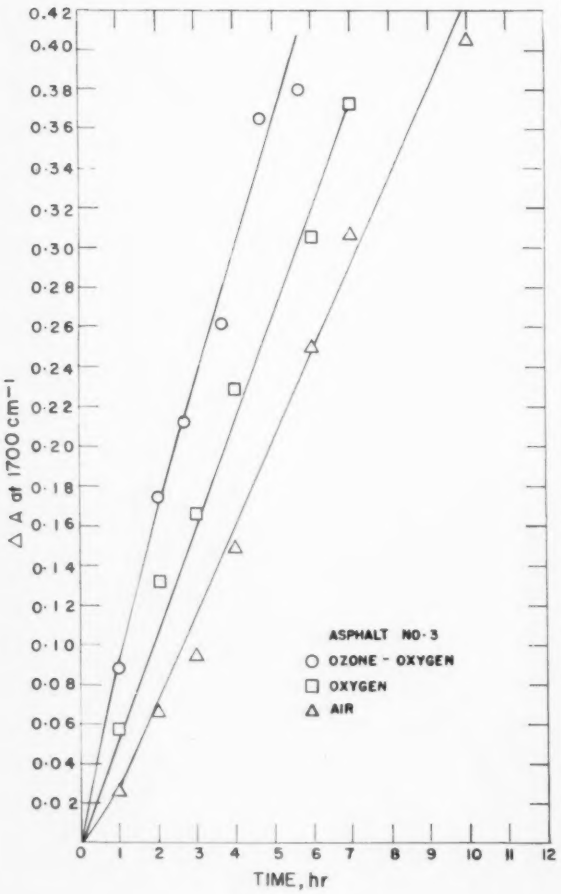

FIGURE 11. *Effects of various environments on asphalt No. 3 as measured by changes in infrared absorbance at 1700 cm⁻¹ with time of carbon-arc exposure (49 °C).*

of 3 hr was used. The general effect was the same as for asphalts 6 and 16, namely, that the amount of photooxidation increased as the environment was changed from air to oxygen to ozone-enriched oxygen, respectively.

This same effect, i.e., the acceleration of photooxidation with ozone, was confirmed by a series of photooxidation-rate experiments in air, oxygen, and ozone-enriched oxygen as shown in figure 11. The values of ΔA (1700 cm^{-1}) per hour for the straight-line part of the curves produced slopes of 0.0463 in air, 0.0538 in oxygen, and 0.0660 in ozone-oxygen. It may be noted that in both oxygen and ozone-oxygen no induction period was observed.

Asphalts 6, 16, and 3 had more than a twofold range in durability (carbon arc, 51–9C cycle), yet, when photooxidized in ozone, the time to film failure due to cracking was reduced by one-half for each asphalt. As mentioned previously, infrared spectra indicated that the same photooxidation products were formed in air, oxygen, or in ozone. Therefore, ozone could well be used as a realistic means of accelerating the photodegradation of asphalt in laboratory weathering.

3.4. Interrelation of Asphalt, Radiance Sources, and Gaseous Environments

Figures 12a, 12b, and 12c provide a direct comparison of the photooxidation rates for asphalts 6, 16, and 3, in air, oxygen, and ozone-enriched oxygen, respectively. With all three gaseous systems the asphalts in order of decreasing photooxidation stability are California Coastal, Southeastern U.S.A., and Mid continent U.S.A. For air (fig. 12a), the shapes of the curves were similar for each asphalt. With oxygen (fig. 12b), this similarity remained with the exception that the California asphalt had no measurable induction period. The curves for ozone-enriched oxygen (fig. 12c), were different than for oxygen or air in that no induction periods were observed with any of the asphalts. Also, for the two asphalts which failed after 6 hours, a definite decrease in rate occurred. It is possible that such an effect could be caused by total utilization of the ozone after 6-hours exposure time and that ozone, as well as some component of the asphalt, is necessary throughout the photooxidation process. Dardin and Albright [9] have shown that ozone serves to initiate the free radical, thermal, decomposition of propane and is not required throughout the reaction period. While in the present work degradation was promoted by photolysis, the reactions are believed to be the free-radical type [1] and, thus, similar to that described in [9]. However, if the photooxidation rate decreased due to exhaustion of ozone, it should thereafter remain about the same as that found for exposures in oxygen alone. Since this is not the case (figs. 5 and 8), it suggested that a "skinning" effect may be taking place on the asphalt surface and thereby reducing the oxidation rate. Dickinson et al. [10] have reported such an effect in oxygen and in air, but for longer exposure periods.

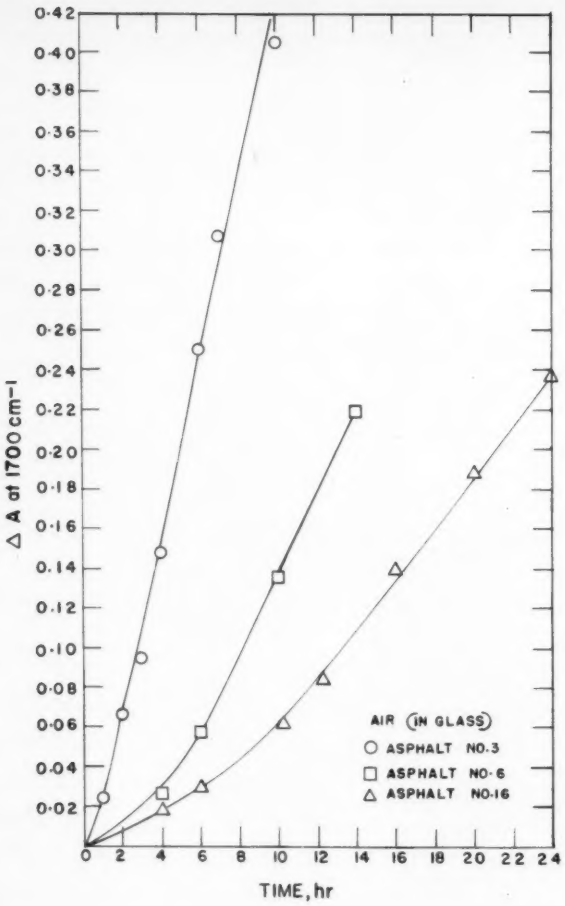

FIGURE 12a. *Effects of air on asphalts No. 3, 6, and 16 as measured by changes in infrared absorbance at 1700 cm⁻¹ with time of carbon-arc exposure (49 °C).*

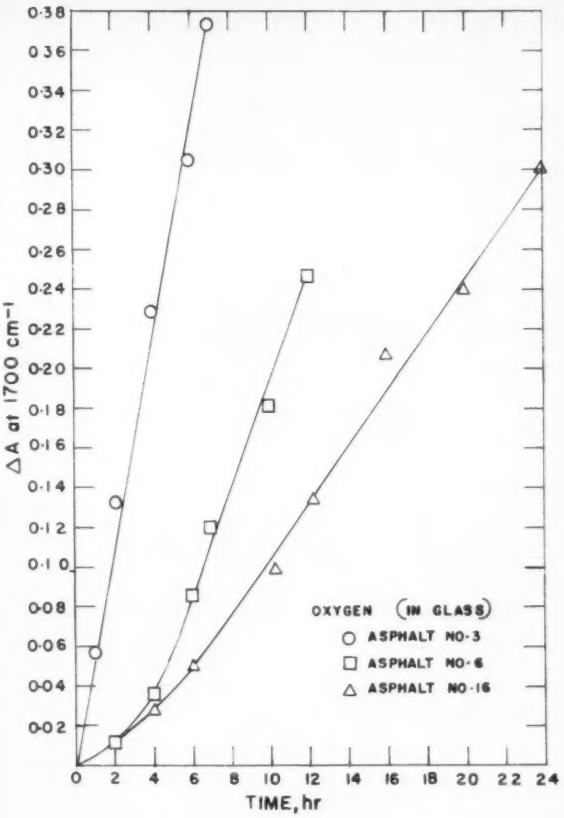

FIGURE 12b. *Effects of oxygen on asphalts No. 3, 6, and 16 as measured by changes in infrared absorbance at 1700 cm⁻¹ with time of carbon-arc exposure (49 °C).*

The effects of gaseous environments on the photooxidation rates of asphalts 3, 6, and 16 are compared further in table 2. The slopes of the curves for each asphalt in air, oxygen, and ozone are presented (ΔA/hr) and then compared on a common basis, namely, the ratios of the rates in oxygen and in ozone to those in air as unity. For all three asphalts, a slight but noticeable increase was noted in the oxidation rate in oxygen compared to that in air. This increase would be expected on the basis of the higher oxygen concentration alone. However, the rates in ozone-oxygen show a pronounced increase over those both in air and in oxygen, indicating considerable more reactivity under photooxidation conditions. Furthermore, the asphalt most durable by the ASTM test, No. 16, had the highest relative rate in ozone, while the least durable, No. 3, had the lowest. Thus, it may be inferred that the Mid-continent U.S.A. asphalt, No. 16, had more reactive sites for ozone attack than did the California Coastal asphalt, No. 3.

TABLE 2. *Effect of gaseous environment on photooxidation rates [1] of various asphalts*

Asphalt	Photooxidation rates in:			Relative ratio of photooxidation rates [2]		
	Air	Oxygen	Oxygen+ ozone [3]	Air	Oxygen	Oxygen+ ozone [3]
3	0.0463	0.0538	0.0660	1.0	1.16	1.42
6	.0203	.0258	.0308	1.0	1.27	1.52
16	.0126	.0145	.0200	1.0	1.15	1.59

[1] Expressed as ΔA/hr. Absorbances measured at 1700 cm⁻¹.
[2] Rate for air considered as unity.
[3] Ozone concentration 5200 pphm vol⁻¹ in oxygen.

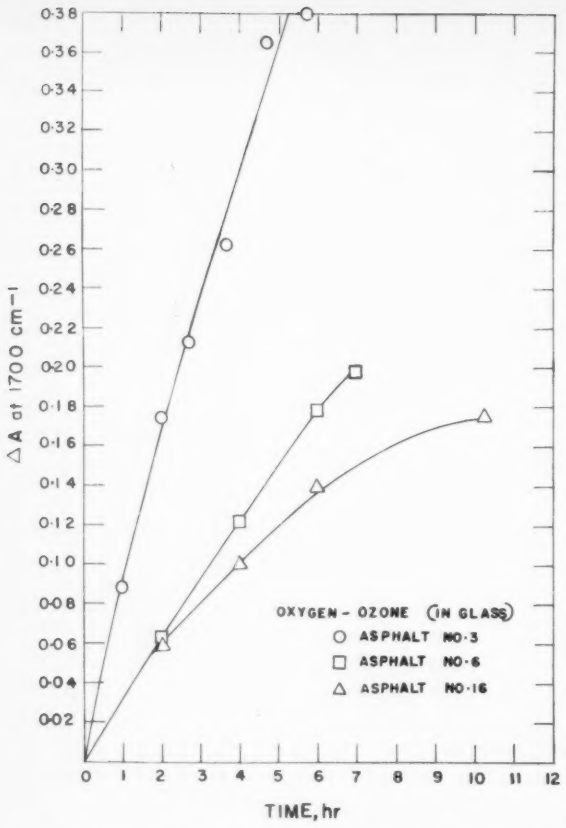

FIGURE 12c. *Effects of ozone-enriched oxygen on asphalts No. 3, 6, and 16 as measured by changes in infrared absorbance at 1700 cm⁻¹ with time of carbon-arc exposure (49 °C).*

In table 3, the response of four asphalts (3, 3X, 6, 16) to solar, xenon-arc, and carbon-arc radiant energy are compared. An exposure period of 6 hr was used for each source and asphalt response was measured by ΔA values at 1700 cm^{-1}. For direct comparison, the ratios of ΔA values are shown for xenon-arc, carbon-arc, and solar exposures with the latter considered as unity. These ratios show that: (a) each asphalt responded differently to each radiant energy source, and (b) as would be expected from the spectral distribution of radiant energy, the response to the xenon source was much more like that to solar exposure than was the response to the carbon arc. These preliminary results are indicative of the selectivity of individual asphalts toward radiant energy sources.

TABLE 3. *Ozone-oxygen exposures of four asphalts to various radiance sources* [1]

Asphalt	Source of radiance			Relative response [2]		
	Solar	Xenon arc	Carbon arc	Solar	Xenon arc	Carbon arc
	ΔA values (1700 cm^{-1})					
3	0.135	0.184	0.408	1	1.36	3.02
3X	.111	.142	----	1	1.28	----
6	.091	.093	.178	1	1.02	1.96
16	.040	.066	.139	1	1.65	3.47

[1] Exposed for 6 hr. Ozone concentration in oxygen = 5200 pphm vol^{-1}.
[2] ΔA for solar radiation considered as unity.

4. References

[1] Leighton, P. A., Photochemistry of Air Pollution, Academic Press (New York, 1961).
[2] Pfeiffer, J. Ph., The Properties of Asphaltic Bitumen, p. 115, Elsevier Publ. Co. (New York, 1950).
[3] Nellensteyn, F. J., and G. M. A. Steffelaar, Chem. Weekblad **41,** 5 (1945).
[4] Brown, A. B., Am. Soc. Testing Materials Spec. Tech. Publ. **280,** 75 (1959).
[5] Wright, J. R., and P. G. Campbell, J. Appl. Chem. (London) **12,** 256 (1962).
[6] Greenfeld, S. H., and J. R. Wright, Mater. Res. Std. **2,** 738 (1962).
[7] Campbell, P. G., J. R. Wright, and P. B. Bowman, Mater. Res. Std. **2,** 998 (1962).
[8] Campbell, P. G., and J. R. Wright, Ind. Eng. Chem. Prod. Res. Develop. **3,** 186 (1964).
[9] Dardin, V. J., Jr., and L. F. Albright, Am. Chem. Soc. Abstracts, p. 10M (Sept. 1963).
[10] Dickinson, E. J., J. H. Nicholas, and S. Boas-Traube, J. Appl. Chem. (London) **8,** 673 (1958).

(Paper 68C4–176)

JOURNAL OF RESEARCH of the National Bureau of Standards—C. Engineering and Instrumentation
Vol. 68C, No. 4, October–December 1964

Designs for Temperature and Temperature Gradient Compensated Capacitors Smaller Than Ten Picofarads

Robert D. Cutkosky

(July 22, 1964)

A theoretical study is made of the dependence of capacitance upon electrode temperature in an air dielectric capacitor. The possibility of constructing a three-terminal standard whose capacitance depends only upon the temperature of one electrode is pointed out, and some practical capacitors utilizing the principle are described. The temperature sensitive electrodes of these capacitors are constructed of fused silica, which results in temperature coefficients of capacitance near 0.5 ppm/°C. The temperature independent electrodes of these capacitors may be constructed of any stable metal, facilitating adjustment to nominal value.

1. Introduction

One of the problems encountered in the construction of standard air dielectric capacitors is that of reducing the dependence of capacitance upon temperature. The best technique seems to be to construct the capacitor entirely of materials which have very small mechanical temperature coefficients. Then provided that the electrode distortions and displacements caused by temperature dependences of the elastic coefficients of the electrodes and electrode supports are not significant, the capacitance temperature coefficient will also be small. Materials of small mechanical temperature coefficient which have been used for the construction of capacitors are fused silica and Invar. Fused silica is difficult to form and mount, and must be metalized to provide electrodes. Its exclusive use in a capacitor with air dielectric results in temperature coefficients of capacitance around 0.5 ppm/°C. Invar is somewhat unstable and must be carefully heat treated. When treated for optimum stability, temperature coefficients around +2 ppm/°C are typical.

The disadvantages of fused silica and Invar are often avoided by the use of two or more materials of different but relatively high temperature coefficients in an arrangement that provides temperature compensation. Temperature compensated capacitors using two metals have been built in many ways and with varying degrees of success. One simple but somewhat unsatisfactory design makes use of coaxial cylinders in which the outer cylinder has a higher temperature coefficient than the inner. The dimensions of the capacitor are chosen so that the capacitance between the cylinders is independent of temperature, provided that no temperature differential exists between the two cylinders.

Since the temperatures of the various elements in a capacitor are not generally equal but vary with the room or bath temperature with possibly different time lags, quite large temperature differentials and capacitance changes can result. The cylindrical design is particularly objectionable from this standpoint, since the outer cylinder is often in more intimate contact with the surroundings than the inner cylinder, and hence responds to temperature changes more rapidly.

A temperature compensation technique often used for capacitors larger than 100 pF involves stacking plates between spacers having a higher temperature coefficient than the plates. A second similar stack of plates is interleaved with, but insulated from, the first set of plates. Since the dissimilar metals are in intimate thermal contact, temperature differentials between plates and spacers remain relatively small, and the capacitance between the two stacks is not strongly affected by temperature fluctuations.

A more elaborate system of temperature compensation may be developed by considering the effect on the direct capacitance caused by independent variations in the temperatures of the separate electrodes. This procedure is found to be most useful for capacitors smaller than a few picofarads in which the temperature of the ground electrode may also be important.

2. Partial Capacitance-Temperature Coefficients

Consider a three terminal capacitor whose direct capacitance is given by $C=C(t_1, t_2, t_3)$ where the t's are the temperatures of the three electrodes. Then for small departures from the reference temperature,

$$C=C_0+\frac{\partial C}{\partial t_1}\Delta t_1+\frac{\partial C}{\partial t_2}\Delta t_2+\frac{\partial C}{\partial t_3}\Delta t_3,$$

or

$$C=C_0\left(1+\frac{1}{C_0}\frac{\partial C}{\partial t_1}\Delta t_1+\frac{1}{C_0}\frac{\partial C}{\partial t_2}\Delta t_2+\frac{1}{C_0}\frac{\partial C}{\partial t_3}\Delta t_3\right)$$

$$=C_0(1+\alpha_1\Delta t_1+\alpha_2\Delta t_2+\alpha_3\Delta t_3). \quad (1)$$

The terms $\frac{1}{C_0}\frac{\partial C}{\partial t_1}=\alpha_1$ etc., are the partial capacitance-temperature coefficients of the three electrodes.

If we let l_1 be a characteristic length of electrode 1, we may write

$\alpha_1=\frac{l_1}{C_0}\left(\frac{\partial C}{\partial l_1}\right)\cdot\frac{1}{l_1}\left(\frac{\partial l_1}{\partial t_1}\right)$. We recognize $\frac{1}{l_1}\left(\frac{\partial l_1}{\partial t_1}\right)=\beta$ as the thermal expansion coefficient of electrode 1, and write

$$\alpha_1=P_1\beta_1 \text{ where } P_1=\frac{l_1}{C_0}\frac{\partial C}{\partial l_1}, \text{ etc., and obtain}$$

$$\frac{C}{C_0}=1+P_1\beta_1\Delta t_1+P_2\beta_2\Delta t_2+P_3\beta_3\Delta t_3. \tag{2}$$

If $\beta_1=\beta_2=\beta_3$ and $\Delta t_1=\Delta t_2=\Delta t_3$, we know from geometrical considerations that $\frac{C}{C_0}=1+\beta\Delta t$, and hence $P_1+P_2+P_3=1$, but no other restrictions on the P's exist.

Equation (2) suggests the possibility of designing capacitors with $P_2=P_3=0$ so that $P_1=1$. Then if β_1 is small, C will be relatively independent of Δt_1, Δt_2, and Δt_3. This can be done by constructing electrode 1 of fused silica and choosing a suitable geometry. Such a capacitor may be adjusted by machining operations on electrodes 2 and 3, which may be of any stable metal, and the principle objection to the use of fused silica is eliminated.

The above analysis is correct if no temperature gradients exist in any electrode, and if the capacitance changes caused by motions of the electrodes with respect to each other are not appreciable. The first criterion can be partially satisfied by avoiding the use of long, thin electrodes. The second criterion can be satisfied by locating the electrodes at saddle points in the capacitance-displacement function.

Experimentally it is often convenient to set one of the P's, say $P_2=0$, by a geometrical consideration, and then either to adjust $P_3=0$ or $P_1=1$ by observing the capacitance changes brought about by changing the dimensions of electrode 1 or electrode 3. The easiest approach will be determined by the capacitor configuration.

3. Guard-Cylinder Capacitor

Consider a guarded cylindrical capacitor whose inner electrode has a radius a_1 and whose outer electrode and guards have a radius a_2. If the length of the outer electrode is l and if ϵ is the permittivity of the dielectric, the direct capacitance of this system is given by

$$C=\frac{2\pi\epsilon l}{\ln\left(\frac{a_2}{a_1}\right)}. \tag{3}$$

Differentiation yields

$$\frac{C}{C_0}=1+\frac{1}{\ln\left(\frac{a_2}{a_1}\right)}\frac{\Delta a_1}{a_1}-\frac{1}{\ln\left(\frac{a_2}{a_1}\right)}\frac{\Delta a_2}{a_2}+\frac{\Delta l}{l}. \tag{4}$$

For a uniform expansion of the outer cylinder, $\frac{\Delta a_2}{a_2}=\frac{\Delta l}{l}$, and C is independent of the temperature of the outer cylinder if $\ln\frac{a_2}{a_1}=1$, or $\frac{a_2}{a_1}=e$. This relationship results in temperature compensation for the outer cylinder, but only if the guard expands at the same rate as the guarded electrode; and results in a capacitor whose temperature coefficient of capacitance is equal to the thermal expansion coefficient of the inner cylinder.

Although independent compensation for guard and guarded electrode temperature changes cannot be achieved with the simple guard cylinder capacitor, some insight into the behavior of more complicated cylindrical systems is derived from the results obtained. The critical ratio of radii, which is e for the simple guard cylinder capacitor, is found to be quite close to this value for a large variety of completely compensated cylindrical designs.

4. Practical Compensated Capacitors

After some model studies, an experimental 5 pF capacitor was constructed as shown in figure 1. The inner electrode was a metallized fused silica cylinder. The guard electrodes were set back as illustrated to reduce the influence of their temperatures upon the direct capacitance of interest. It was found experimentally that small changes in the length of electrode 2 did not appreciably affect the compensation, so that adjustment to nominal value is simple.

Tests of the completed capacitor showed an overall temperature coefficient less than 1 ppm/°C and no appreciable overshoot when subjected to a rapid temperature change.

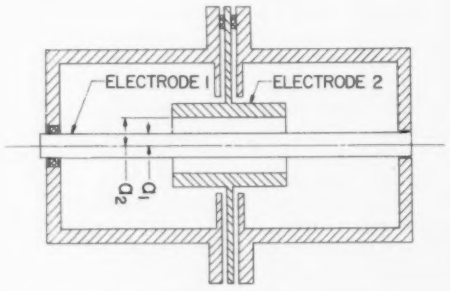

FIGURE 1. *An experimental 5 pF completely temperature compensated capacitor drawn roughly to scale for correct compensation,* $a_2/a_1\approx 2.5$.

It is found that the design of figure 1 is not easily modified to yield either much larger or much smaller capacitance. Other designs have been investigated, however, which may be useful for the construction of arbitrarily small completely compensated capacitors. One such design is sketched in figure 2. It makes use of a cylindrical shield between the two capacitor electrodes. The inner electrode is once again constructed of metalized fused silica. Holes in the cylindrical shield may be varied in sizes to provide a range of capacitances between the inner and outer electrodes. The outer electrode is automatically temperature compensated by virtue of its shape. Any increase in its temperature will increase the spacing between it and the cylindrical shield, but will not change the position of the critical conical surfaces. The outer ends of the cones must of course be truncated, but it is found that this can be done without greatly upsetting the compensation. Experimentally it is found that the critical ratio of cylindrical shield radius to inner electrode radius is somewhat dependent upon the size and shape of the holes in the shield, but remains remarkably close to e.

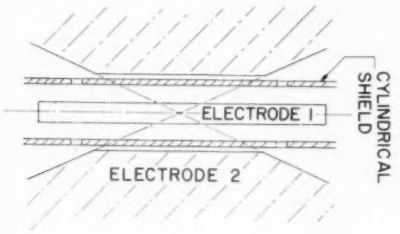

FIGURE 2. *A completely temperature compensated capacitor for values smaller than 0.1 pF.*

5. Conclusions

Most practical capacitors are found to be not greatly dependent upon temperature differentials. However, complete disregard for the principles of partial temperature compensation can result in capacitors which are unduly sensitive to rapid temperature changes. It is possible at least in principle to design capacitors which depend only upon the temperature of one element; and if this element has a small thermal expansion coefficient, very close temperature control is not necessary. The technique seems most practical for capacitors smaller than 10 pF.

(Paper 68D4–177)

JOURNAL OF RESEARCH of the National Bureau of Standards—C. Engineering and Instrumentation
Vol. 68C, No. 4, October-December 1964

Publications of the National Bureau of Standards*

Selected Abstracts

Viscosity of a standard soda-lime-silica glass, A. Napolitano and E. G. Hawkins., *J. Res. NBS* **68A** (*Phys. and Chem.*), *No. 5, 439–448 (Sept.–Oct. 1964), 70 cents.*

The viscosity of a soda-lime-silica glass has been measured at the National Bureau of Standards and seven other laboratories. Determinations were made in the range of 10^2 to 10^{15} P. The rotating cylinder was used at the higher temperatures (800 to 1450 °C) and the fiber elongation method at the lower temperatures (520 to 658 °C). The results have been critically evaluated and the glass has been issued as Standard Sample No. 710. This glass is available from the National Bureau of Standards.

Some changes in double-bond structure during the vulcanization of natural rubber, F. J. Linnig, E. J. Parks, and J. E. Stewart, *J. Res. NBS* **68A** (*Phys. and chem.*), *No. 5, 499–512 (Sept.-Oct. 1964)., 70 cents.*

Near infrared studies indicate the absence or near absence of isolated *cis* and terminal double bonds in rubber vulcanized either with or without accelerators as well as in the squalene sulfur reaction product. The use of purified natural rubber indicates a new absorption near 6.1 μ on reaction with sulfur either with or without accelerators in the rubber system. This new absorption may be due either to a double bond with an attached sulfur atom or to conjugated double bond systems that do not react readily with maleic anhydride. Ultraviolet spectra of chromatographic fractions show that squalene reacted with 15 percent sulfur contains conjugated trienes, tetraenes and possibly dienes, hexaenes, and heptaenes. The conjugated dienes, trienes, and tetraenes probably are present in sufficient quantities to account for a large portion of the band at 10.4 μ. There is some evidence that the trienes and tetraenes at least may be largely all *trans* in configuration. Other contributors to the band at 10.4 μ are possibly isolated *trans* double bonds and heterocyclic sulfur structures along the chain.

Dislocations in polymer crystals, H. D. Keith and E. Passaglia, *J. Res. NBS* **68A** (*Phys. and Chem.*). *No. 5, 513–518 (Sept.-Oct. 1964), 70 cents.*

The role that dislocations are likely to play in chain-folded polymer crystals is examined, particularly with regard to their influence on plastic deformation. It is assumed that primary bonds cannot be broken in back-bone molecular chains; and this restriction, together with further restrictions brought about by chain folding, limits substantially the number of permissible dislocations and glide processes. It is shown that deformations of appreciable magnitude in chain-folded polymer crystals almost certainly cannot be attributed solely to dislocation mechanisms. Crystals of the *n*-alkanes and "extended chain" polymer crystals are also discussed briefly.

Precision density measurement of silicon, I. Henins, *J. Res. NBS* **68A** (*Phys. and Chem.*), *No. 5, 529–533 (Sept.-Oct. 1964), 70 cents.*

The densities of 22 large highly perfect silicon single crystals have been measured by hydrostatic weighing in water, yielding and average value of

$$d_{Si}(25\ °C) = 2.329002 \pm (7 \times 10^{-6})\ g/cm^3.$$

An experimental precision has been achieved which exceeds the accuracy with which the absolute density of water is known. The effect of variations of the water surface tension force on the suspension wire has been minimized by using a 0.001 in. suspension wire coated with platinum black, and by doing a large number of repeated weighings of each crystal.

Dependence of mechanical relaxation on morphology in isotactic polypropylene, E. Passaglia and G. M. Martin, *J. Res. NBS* **68A** (*Phys. and Chem.*), *No. 5, 519–527 (Sept.–Oct. 1964), 70 cents.*

The shear modulus and logarithmic decrement at approximately 1 c/s have been measured from −180 °C to about 150 °C for a series of samples of isotactic polypropylene prepared by various thermal treatments. The samples had varying densities (degrees of crystallinity) and morphologies as characterized by spherulite size. All of the samples exhibited the three relaxations characteristic of polypropylene. The maxima in the three measures of relaxation, (logarithmic decrement, G'', and J'') occur at about −60 °C, 0 to 10 °C, and 50 to 100 °C for the three processes. However, the relation between crystallinity and the magnitude of the peak value of the particular measure of loss depends upon the relaxation and the function used to measure the loss. The loss is almost independent of density and morphology for all three relaxations when G'' is used to characterize the loss, whereas the loss increases monotonically as the density decreases when using J'' to characterize the loss behavior. The logarithmic decrement behaves in a more complicated manner. The implications of this behavior are discussed, and it is shown that the primary effect of changing density is to change the equilibrium modulus rather than the relaxation processes.

Thermodynamics of perfect elastic fluids, B. Bernstein, E. A. Kearsley, and L. J. Zapas, *J. Res. NBS* **68B** (*Math. and Math. Phys.*), *No. 3, 103–113 (July–Sept. 1964), 75 cents.*

A simple nonequilibrium thermodynamics is developed and a particular example is studied. The theory is formulated to describe a viscoelastic fluid, capable of finite deformation, which need not be locally in or near a state of thermodynamic equilibrium. This fluid may support shear stresses only when away from local thermodynamic equilibrium. A notion of time-temperature superposition is contained in the formulation of the constitutive equations. Conservation of energy is obeyed and the second law of thermodynamics is satisfied as a consequence of simple requirements on the constitutive relations. In an adiabatic isochoric motion the temperature increases when work is done on the material and decreases when the material does work. For given volume and temperature, entropy decreases when the material is deformed from equilibrium. It is shown in what general way viscosity depends upon temperature. For infinitesimal strain, the special form of the stress-strain relations are derived in order to determine how temperature and time-temperature superposition enter in this case.

Measurement of the complex time-frequency channel correlation function, P. A. Bello, *Radio Sci. J. Res. NBS/USNC-URSI,* **68D,** *No. 10, 1161–1165 (Oct. 1964),* $1.00.

The time and frequency selective fading properties of radio channels may be characterized by evaluating the cross-correlation function between two received carriers as a function of their frequency separation. In practice such correlation functions have been measured using only the envelopes of the received carriers. Recent studies of the effect of time and frequency selective fading on digital data transmission have shown that envelope correlation information is insufficient for an accurate evaluation of system performance and that the complex envelope correlation function is needed. This paper presents an experimental technique for the measurement of the complex time-frequency correlation function of radio channels that uses independent frequency standards

at transmitter and receiver. An analytical study is made of the theory of operation of this system and of the effects of instabilities of the frequency standards.

Propagation in nonuniform waveguides with impedance walls, R. L. Gallawa, *Radio Sci. J. Res. NBS/USNC-URSI,* **68D,** *No. 11, 1201–1213 (Nov. 1964),* $1.00.
Under certain conditions it is useful to exchange Maxwell's equations for an infinite set of coupled total differential equations; the set takes the form of generalized telegraphist's equations. This is done for a parallel-plate waveguide with impedance walls and varying plate separation. The characteristic modes of the waveguide are used in order that coupling between equations depends only on geometric perturbations of the guide walls. The utility of the technique is demonstrated by evaluating the mode conversion in an overmoded waveguide containing a geometric perturbation. A comparison with experimental work is presented for the perfectly conducting case.

A VLF timing experiment, A. H. Morgan and O. J. Baltzer, *Radio Sci. J. Res. NBS/USNC-URSI,* **68D,** *No. 11, 1219–1222 (Nov. 1964),* $1.00.
The purpose of the experiment given in this paper was to measure the differential phase stability of two VLF carriers (19.9 kc/s and 20.0 kc/s) as received at Austin, Texas, as a function of the observing time, using the former low power standard frequency broadcasts of WWVL, Sunset, Colo.
These measurements indicate that, at the distance involved (1400 km) and with an averaging time of a few hours, the envelope or group delay variations will cause a "jitter" in the received envelope zeros at the receiver of less than one cycle at 20.0 kc/s. Therefore, a particular cycle of the 20.0 kc/s carrier as transmitted may be identified at the receiver, thus providing "microsecond" timing.

Phase and time variations in VLF propagation over long distances, D. D. Crombie, *Radio Sci, J. Res. NBS/USNC-URSI,* **68D,** *No. 11, 1223–1224 (Nov. 1964),* $1.00.
It is argued that the custom of referring to changes in the phase of VLF signals as changes in transmission time is incorrect, is likely to lead to confusion and should be abandoned.

Errors induced by the atmosphere in microwave range measurements, H. B. Janes and M. C. Thompson, *Radio Sci. J. Res. NBS/USNC-URSI,* **68D,** *No. 11, 1229–1235 (Nov. 1964),* $1.00.
This paper describes experimental measurements designed to study atmosphere-induced errors in microwave baseline tracking systems. The ground-to-air configuration was simulated by 300–400 m baselines on level ground east of Boulder, Colo., and a fixed target antenna on a mountain top at a range of about 15 km and a path elevation angle of 44 milliradians. A radio frequency of 9.4 Gc/s was used. Continuous recordings were made of variations in apparent range, range difference, and refractive index. The data are analyzed in terms of power spectra. The correlation between range and surface refractivity variations and the correlation of range variations on adjacent paths are discussed.

The NBS standard hygrometer, A. Wexler and R. W. Hyland, *NBS Mono. 73 (May 1, 1964), 30 cents.*
A gravimetric hygrometer is described that serves as the NBS standard instrument for the measurement of the moisture content of gases on an absolute basis in terms of mixing ratio (mass water vapor/unit mass of dry gas). The National Bureau of Standards and other laboratory reference and working instruments are compared and calibrated with this instrument. The measuring operation involves the absorption of the water vapor from a water vapor-gas mixture by a solid desiccant and the determination of the mass of this water vapor by precision weighing; it also involves the determination of the volume of the associated gas of known density by counting the fillings of two calibrated stainless steel cylinders. An automatic system permits the sampling of the test gas at any desired flow rate up to 2 liters per minute (STP) and for any desired number of fillings. The instrument provides a value of the mixing ratio averaged over the time interval of a test.
The construction and operation of the instrument is described. Discussions of the tests and calibrations of component parts, and of the sources of errors also are included. An analysis of the random and systematic errors effecting the overall accuracy in the determination of mixing ratio shows that if 0.60 g of water vapor is collected from moist air, then the estimated maximum uncertainty expected for mixing ratios between 27 mg/g and 0.19 mg/g is 12.7 parts in 10^4.

Creep and drying shrinkage and lightweight and normal-weight concretes, T. W. Reichard, *NBS Mono. 74 (Mar. 4, 1964), 30 cents.*
A description is given of a series of tests and test results from an investigation of the mechanical properties of structural-grade lightweight and normal-weight concretes. The major part of the work was planned to obtain comparative values of compressive creep, drying shrinkage, strengths, and moduli of elasticity for concretes made with 24 lightweight and 5 natural, normal-weight aggregates and having the same nominal strength at the time the specimens were placed under load.
Data are presented from a total of 76 different concretes which show that there is a wide range in values of the mechanical properties of concretes of the same nominal compressive strength. It is shown that relatively high values of creep and drying shrinkage are not always associated with lightweight concretes and that, in fact, some lightweight concretes have practically the same mechanical properties as some normal-weight concretes.
In addition to environmental conditions, the two major factors affecting the creep of concrete appear to be the ratio of the applied stress to the strength at the time of loading, and the aggregate used. Curing conditions, type of cement, mix proportions, and several other variables appear to affect the creep chiefly insofar as they affect the stress-strength ratio.
It was observed that the creep at the age of two years can be estimated from the 90-day results with reasonable accuracy.

Handbook of mathematical functions with formulas, graphs, and mathematical tables, Ed. M. Abramowitz and I. Stegun, *NBS Applied Math. Series 55 (June 1964), $6.50.* A, This publication not only combines the material found in all former reference volumes on the subject; it additionally expands the work of past authors by increasing the number of functions covered, presenting more extensive numerical tables, and giving larger collections of mathematical properties of the tabulated functions. It also provides comparatively simple methods of obtaining values of functions outside the tabulated range.
As a result of scientific advances and, especially, the increasing use of automatic computers, a greater variety of functions and a higher accuracy of tabulation are now in demand by users of mathematical functions. The *Handbook* includes rational approximation formulas for all the functions, tailored to the modern computer and tables useful for a preprogramming survey of the access to a computer; for the researcher who does not, and who must do his own computations, they are, of course, indispensable. Subjects covered are included by the following chapter headings: Mathematical Constants; Physical Constants and Conversion Factors; Elementary Analytical Methods; Elementary Transcendental Functions-Logarithmic, Exponential, Circular, and Hyperbolic Functions; Exponential Integral and Related Functions; Gamma Function and Fresnel Integrals; Legendre Functions; Bessel Functions of Integer Order; Bessel Functions of Fractional Order; Integrals of Bessel Functions; Struve Functions and Related Functions; Confluent Hypergeometric Functions; Coulomb Wave Functions; Hypergeometic Functions; Jacobian Elliptic Functions and Theta Functions; Elliptic Integrals; Weierstrass Elliptic and Related Functions; Parabolic Cylinder Functions; Mathieu Functions; Spheroidal Wave Functions; Orthogonal Polynomials; Bernoulli and Euler Polynomials, Riemann Zeta Functions; Combinatorial Anal-

ysis; Numerical Interpolation, Differentiation, and Integration; Probability Functions; Miscellaneous Functions; Scales of Notation, and Laplace Transforms.

Vinyl-coated glass fiber insect screening and louver cloth, *NBS CS248–64 (Feb. 17, 1964), 10 cents.*
This Standard gives the nomenclature, definitions, and general requirements for commercial standard glass fiber insect screening designed and woven primarily for installation in or on any dwelling, patio, screen enclosure, building or structure, for the purpose of preventing the ingress of flies, mosquitoes, or other insects. This Standard specifies the requirements for weatherability, flame resistance, color stability, bond and bursting strength, stiffness, and other chemical and physical characteristics of the product. Test procedures for determining these properties are described.

Structural insulating board (wood or cane fiber), *NBS R–179–63, (Dec. 23, 1963), 10 cents, (supersedes R179–56).*
Structural insulating board is a preformed, rigid, fibrous insulating material made principally from wood or cane fibers, such that its use contributes substantially to the strength and to the thermal and/or sound insulation of a structure. The insulating properties are due chiefly to the minute air cells that are produced in great numbers between the fibers during the manufacturing process. The surface of most boards is factory finished to any type of surface treatment ordinarily desired.

Correction factor tables for four-point resistivity measurements on thin, circular semiconductor samples, L. J. Swartzendruber, *NBS Tech. Note 199 (Apr. 15, 1964), 30 cents.*
Extensive tables of the geometrical correction factors for four-point probe resistivity measurements on thin, circular semiconductor samples with all surfaces insulating are given, (1) for an in-line probe array displaced radially with points along a diameter, (2) for an in-line probe array displaced radially with the line of points perpendicular to a diameter, and (3) for a displaced square probe array.

The normal phase variations of the 18 kc/s signals from NBA observed at Maui, Hawaii, A. H. Brady, A. C. Murphy, and D. D. Crombie, *NBS Tech. Note 206–2 (Mar. 19, 1964), 25 cents.*
Observations of the normal phase variations of the 18 kc/s signals radiated from the Canal Zone and received in Maui, Hawaii are given in the form of monthly averages and standard deviations at five minute intervals. The relations between the diurnal phase variations and the diurnal variation in the length of sunlit path are shown. The calculated mean diurnal change in effective height of reflection is 13.7 km. Values of the short term phase differences are also given.

The normal phase variations of the 18 kc/s signals from NBA observed at Boulder, Colorado, U.S.A., A. H. Brady, A. C. Murphy and D. D. Crombie, *NBS Tech. Note 206–3 (Apr. 10, 1964), 25 cents.*
Observations of the normal phase variations of the 18 kc/s signals radiated from the Canal Zone and received in Boulder, Colorado, U.S.A., are given in the form of monthly averages and standard deviations at five minute intervals. The relations between the diurnal phase variations and the diurnal variation in the length of sunlit path are shown. The calculated mean diurnal change in effective height of reflection is 18 km. Values of the short term phase differences are also given.

A portable rubidium-vapor frequency standard, R. J. Carpenter, *NBS Tech. Note 235 (Apr. 6, 1964), 25 cents.*
Three portable optically-pumped rubidium-vapor frequency standards have been constructed. Output frequencies of 5 MHz and 100 kHz with a stability of better than $1:10^{10}$ have been realized. The weight without power supply is 18 kg and the power required, exclusive of temperature control, is about 11 watts. The power supply, which also contains batteries for up to 15 hours operation, weighs 26 kg. Sufficient detail is presented to allow the construction of similar units.

Research on crystal growth and characterization at the National Bureau of Standards, July to December 1963, *ed. H. S. Peiser, NBS Tech. Note 236 (Apr. 6, 1964), 40 cents.*
The National Bureau of Standards with partial support from the Advanced Research Projects Agency is continuing diverse research projects on the growth and characterization of crystals. This note summarizes the individual NBS activities in this and closely related fields during July to December 1963. Lists of NBS publications appertaining to that period and of participating NBS scientists are appended.

Disclosures on various subjects: A frequency meter, A phase shifter, A double-tuned transformer, and A ram-controlled system, *NBS Tech. Note 237 (Apr. 10, 1964), 15 cents.*
This Note presents four devices embodying interesting and unusual solutions to problems prevalent in their respective arts. These devices, developed at the National Bureau of Standards and the U.S. Weather Bureau, comprise a pulse frequency meter; a variable phase shifter; a variable bandwidth, double-tuned transformer, and a control system for any hydraulic ram-operated press.

Miscellaneous studies in probability and statistics: distribution theory, small-sample problems, and occasional tables, *The Statistical Engineering Laboratory, NBS Tech. Note 238 (Apr. 24, 1964), 20 cents.*
This publication makes available some notes and tables prepared at various times by the staff of the Statistical Engineering Laboratory.
Contents: (1) Distribution of the ratio of two F variates having $n-1$ and n degrees of freedom, by J. M. Cameron and Cyrus Derman. (2) Some notes on the Cauchy distribution, by Cyrus Derman. Includes variance of the sample mean for truncated Cauchy distribution; the Cauchy distribution whose cumulative distribution function deviates least from the standard normal c.d.f. (3) The better one out of two, by E. P. King. Variance of the observation closest to the population mean. (4) Variance of medians and pseudomedians, by Mary G. Natrella. For sample sizes m up to 10, gives the variances ($5D$) of the median (m odd), pseudomedian (m even), and average of two values on either side of the median (m odd), for the normal and rectangular distributions and ($m \leq 6$) for the extreme-value distribution. (5) Probability points of order statistics in random samples of size n from a uniform distribution over (0, 1), by Churchill Eisenhart and Lola S. Deming. Gives probability points ($4S$) of each order statistic for probabilities $\alpha = .001, .005, .01, .025, .05, .10, .20, .25, .50$ and $n = 2(1)10$.

Average power dissipated in a diode swept along its reverse characteristic, H. A. Schafft, *NBS Tech. Note 240 (Apr. 30, 1964), 20 cents.*
The commonly used method of sweeping to a fixed power in order to compare the reverse characteristics of a group of similar diodes is found lacking under conditions for which an average temperature is meaningful. It is shown how a determination may be made of the average power dissipation in a diode (or in any device with a similarly shaped characteristic) when it is swept along its reverse characteristic by a full-wave rectified sinusoidally varying voltage in series with a resistive load. The uncertainty in the determination due to the variability of the characteristic is for most cases less than $\pm 5\%$ if the ratio of the maximum voltage drop across the current limiting resistor to the maximum voltage across the device is larger than or equal to two. Errors introduced by small uncertainties in the pertinent parameters are also presented. Finally it is shown how the reverse characteristics of similar diodes can be examined under relatively equivalent heating conditions.

A Fortran program for analysis of ellipsometer measurements and calculation of reflection coefficients from thin films, F. L. McCrackin and J. P. Colson, *NBS Tech. Note 242 (May 27, 1964), 30 cents.*
A Fortran computer program to calculate the reflection coefficients for both single and multiple thin films and to analyze optical measurements of such films by an ellipsometer is presented. Both the films and the substrate may be

absorbing and have complex indexes of refraction. The reflection coefficients of inhomogeneous films (films of varying refractive index) may be computed by determining the reflection coefficients of an equivalent series of homogeneous films.
The ellipsometer measurements for a given film may be calculated or the index of refraction and thickness of a film may be calculated from ellipsometer readings. The ellipsometer measurements may be corrected for the retardation of the compensator or for multiple reflections of the light.

Bolometric microwave power calibration techniques at the National Bureau of Standards, R. F. Desch and R. E. Larson, *IEEE Trans. Instr. Meas.* **IM-12,** *No. 1, 29–33 (June 1963).*
A bolometric method of calibrating low-level microwave power measuring devices is currently employed at the National Bureau of Standards in Boulder, Colo. The technique is one of direct comparison between the standard and the unknown, and utilizes NBS working standard bolometer units and self-balancing dc bridges. In general, the unknown is calibrated to an accuracy of one percent. The following quantities are defined and the associated errors are discussed: 1) Calibration factor of a bolometer unit in combination with a directional coupler, 2) Calibration factor of a bolometer unit, and 3) Effective efficiency of a bolometer unit.

Gage blocks of superior stability. II. Fully hardened steels, M. R. Meyerson and W. A. Pennington, *Am. Soc. Metals Trans. Quart.* **57,** *No. 1, 3–25 (Mar. 1964).*
The possibility of obtaining temporal dimensional stability of 1 to 2 x 10^{-7} in./in./yr in through-hardened steels with high hardness levels was studied. This goal could not be attained at hardness levels of R_c 65, but at slightly lower levels this degree of stability could be obtained under limited conditions.
The effect of various fabricating technique and stress-relieving temperatures on the surface residual stresses were established and the results correlated with observed trends in the stability patterns. The presence of surface compressive residual stresses were effective in reducing the rate of contraction in 52100 steel on a submicroinch level.
The possible influence on dimensional stability of surface films, lattice defects, unstable carbides, and extended tempering was considered. Surface films were found to be an insignificant factor, a quantitative relationship between dislocation content and length changes was established, and a tentative finding of instability of carbides was noted. It was found that the hardened structure of 52100, or of similar conventionally hardened steels without secondary hardening peaks, cannot be fully stabilized at a hardness level of R_c 65 even with extended tempering.

The U.S. basis of electromagnetic measurements, J. M. Richardson and J. F. Brockman, *IEEE Spectrum* **1,** *No. 1, 129–138 (Jan. 1964).*
The Radio Standards Laboratory of the National Bureau of Standards is responsible for providing the central basis of the scientific system of electromagnetic measurement in the United States and for assuring international coordination of such measurement. This article describes the effect of the rapid growth of electronics upon electromagnetic measurement, the problems faced by industry when a standard of measurement does not exist, the development of a national standard, the dimensions of electromagnetic measurement, the research areas of the Radio Standards Laboratory, and the impact of modern technology and physics upon the science of electromagnetic measurement.

An "air-core" primary radio frequency permeameter for reversible permeability measurements, C. A. Hoer and R. D. Harrington, *Proc. IEEE* **51,** *No. 12, 3–25 (Dec. 1963).*
A radio frequency permeameter with an air core primary for measuring the complex permeability of magnetic materials subjected to a dc magnetic field transverse to the rf field in the material is described.

Comparative rate measurements with a single-pulse shock tube, W. Tsang, *J. Chem. Phys.* **40,** *No. 4, 1171–1172 (Feb. 15, 1964).*
The use of the single-pulse shock tube to obtain accurate kinetic data is hampered by uncertainties in the measurement of reaction temperature and reaction time. Rate constants so determined may be off by as much as a factor of two or three. In this note comparative rate measurements with a single-pulse shock tube are described. Data of improved reliability and accuracy may be obtained by this means. The method involves measurement of relative rates of decomposition of two compounds in the same reflected shock. In the present work, rates of decomposition of tert-butyl chloride and tert-butyl bromide were (separately) compared with that of isopropyl bromide as a "standard". Taking the rate of thermal decomposition of isopropyl bromide as given by $k(C_3H_7Br) = 10^{13.62}e^{-47,800/RT}$ (sec^{-1}), these experiments give

$$\log_{10} k(C_4H_9Cl) = (0.935 \pm .003)\ \log_{10} k(C_3H_7Br) + 1.006 \pm .003$$

$$\log_{10} k(C_4H_9Br) = (0.868 \pm .005)\ \log_{10} k(C_3H_7Br) + 2.047 \pm .005$$

The precision and accuracy obtainable in relative rate measurements represents a great improvement over results usually obtained by conventional shock tube techniques. Errors in reaction temperature are no longer significant since temperature is not employed in the treatment of experimental data. Thus shock velocity measurements are no longer necessary. At the same time, the unique advantages of the shock wave technique; short dwell time, homogeneity of reaction, etc., are preserved.

Fabry-Perot dilatometer, V. E. Bottom, *Rev. Sci. Instr.* **35,** *No. 3, 374–376 (Mar. 1964).*
A dilatometer based upon the principle of the Fabry-Perot interferometer is described. The device is capable of measuring displacements as small as 10^{-7} cm or less. The measurements are made directly in terms of the wavelength of a spectral line such as the green line of Hg^{198}. No calibration of the apparatus is required and it is not necessary to know the distance between the mirrors or the focal length of the lens which forms the fringes. Neither is it necessary to know the calibration of the micrometer eyepiece so long as it may be assumed that the screw is regular. The instrument should be useful for measuring magnetostriction, piezoelectric, electrostriction and thermal expansion coefficients, especially when small samples must be used.

Observations on dislocation loops in deformed copper, A. W. Ruff, Jr. and L. M. Kushner, *Proc. Conf. Relation Between the Structure and Mechanical Properties of Metals, National Physical Lab., Teddington, Middlesex, England 1, 146–156 (1963).*
Single crystals of copper were deformed by rolling, then thinned and examined by transmission electron microscopy. A cellular distribution of dislocations was found, in addition to a high density of small prismatic dislocation loops. Measurements were made of the line dislocation density and the loop density as a function of the deformation. The loops were found to have a (111) habit plane with a (110) Burgers vector. It is believed that these loops were produced from a supersaturation of point defects resulting from the deformation. For samples deformed 36 percent, the corresponding point defect concentration was 2 x 10^{18} cm^{-3}.

Gage blocks of superior stability. III. The attainment of ultrastability, M. R. Meyerson and M. S. Sola, *Am. Soc. Metals Trans. Quart.* **57,** *No. 1, 164–185 (Mar. 1964).*
Metals and techniques of processing them to produce a degree of temporal dimensional stability of 0.1 to 0.2 μ in./in./yr and a surface hardness of R_c 65 minimum are described. Effects of surface hardening and other factors on dimensional stability are reported. Three categories of materials and processes are included in the study; steels with annealed cores and hardened surfaces, steel with partially hardened cores and hardened surfaces, and cermets and ceramics.
Two materials exceeded the goal of the investigation with a degree of stability better than 0.1 μ in./in./yr. Twelve other combinations of materials and treatments produced ultrastable gage blocks with dimensional stability between 0.1 and 0.2 μ in./in./yr.
Included in the summary is a comparison of the stability of these materials and processes with those reported in prior

papers, including through-hardened steels. At surface hardness levels of R_c 65 or greater, the dimensional stability obtained with the best surface-hardened steels exceeded that obtained with any of the through-hardened steels. Two of the titanium carbide types were ultrastable and were the best of the cermet and ceramic group.

Magnetic tape recording and reproducing of atmospheric noise with a wide dynamic range, E. C. Bolton, *Rev. Sci. Instr.* **35,** *No. 3, 377–380 (Mar. 1964).*
To properly evaluate the performance of radio systems in the presence of atmospheric noise, it is necessary to be able to reproduce atmospheric noise of various known amplitude distributions whenever necessary. However, conventional tape-recording techniques cannot be used because of the large dynamic range of atmospheric noise. This paper describes a tape-recording and reproducing system which has been developed that can record and reproduce atmospheric noise with a dynamic range of 90 db. The frequency range is 1 kc to 25 kc with a one-half octave bandwidth and by using frequency conversion, frequencies from 25 kc to 500 kc may be recorded with a maximum bandwidth of 10 kc.

Standards and contact lenses, A. G. McNish, *Contacto* **7,** *No. 9, 4–5 (Nov.–Dec. 1963).*
Standards have been found very valuable in many industries. They are valuable both to the consumer and to the industry. They serve to assure the consumer that the product he is obtaining meets certain minimum requirements and protect him from being a prey to the unscrupulous. They protect the industry in establishing a means to shield the reputable members of the industry from competition by unscrupulous competitors whose products may not only be worthless, but even worse, will tend to discount the good work being done by the industry as a whole.

Developments in polymer evaluation procedures, G. M. Kline, *Mod. Plastics* **41,** *No. 5, 182 (Jan. 1964).*
Five research investigations on measurement problems in the NBS Polymers Division during 1962–1963 are described. These include 1) the use of point-projection X-ray microscopy for examination of the internal structure of reinforced and cellular plastics, 2) the determination of the macropore structure of natural and synthetic porous materials such as leather, cork, wood, and microporous plastics, 3) the measurement of the crystallization of rubber under pressure, 4) the determination of propylene content of ethylene-propylene copolymers by infrared spectroscopic analysis of their pyrolyzates, and 5) the characterization of polystyrenes of narrow and broad molecular weight distributions for use as standard samples in the calibration of measurements of molecular weights of polymers. References are given to 14 other projects completed during the past year. The results of this research provide the engineering data and test procedures needed in the preparation of technically adequate quality standards to assure the suitability of commercial products for specific uses.

Spherical mirror Fabry-Perot resonators, R. W. Zimmerer, *IEEE Trans. Microwave Theory Tech.* **MTT-11,** *No. 5, 371–379 (Sept. 1963).*
An experimental investigation of spherical mirror Fabry-Perot plates at millimeter wavelengths has clearly demonstrated the salient features of the theory as so far developed by various workers. The experimental data clearly shows the forbidden region which occurs when the two mirrors have different radii of curvature. It is shown that the fundamental TEM_{00q} mode is a mixed state. Attempts to fit the data quantitatively with theory have met with partial success.

Local curvature of wavefronts in an optical system, J. A. Kneisly II, *J. Opt. Soc. Am.* **54,** *No. 2, 229–235 (Feb. 1964).*
The local principal curvatures (shape) of a wavefront propagating through an optical system can be calculated from geometrical optics. Formulas are derived for the change in shape during transfer, refraction, reflection, and diffraction by a grating in a system of homogeneous isotropic media. The results not only have immediate application to design, but also provide necessary data for treating points where the geometric approximation fails.

Electrical properties of elastomers and related polymers, A. T. McPherson, *Rubber Chem. Technol.* **36,** *No. 5, 1230–1302* (Dec. 1963).
This review, prepared at the request of Rubber Chemistry and Technology, deals with the electrical properties of rubber and a number of related polymers such as polyethylene and polytetrafluoroethylene which are sufficiently flexible to be used as the insulation of wires and cables. Principal emphasis is placed on the dielectric constant, dissipation factor, conductivity, and dielectric strength, and, insofar as possible, these properties have been related to the molecular structure of the polymer.

Relationships between different kinds of network parameters, not assuming reciprocity or equality of the waveguide or transmission line characteristic impedances, R. W. Beatty and D. M. Kearns, *Proc. IEEE* **52,** *No. 1, 84 (Jan. 1964).*
A table is presented showing the relationships between different kinds of network parameters, not assuming reciprocity or equality of the waveguide or transmission line characteristic impedances.

Examples relating to the simplex method, A. J. Goldman and D. Kleinman, *Operations Res.* **12,** *No. 1, 159–161 (Jan.–Feb. 1964).*
An example is given showing that the most common variant of the simplex algorithm does not satisfy a condition conjectured by Saaty in an analysis of the maximum possible number of iterations. Situations are exhibited in which the simplex method encounters all vertices of the constraint polyhedron.

The ultraviolet realm of spectroscopy, C. E. Moore, *J. Wash. Acad. Sci.* **54,** *58–62 (1964).*
A very brief description is given of the present situation in ultraviolet atomic spectroscopy. Extra-terrestrial observations of the ultraviolet solar spectrum have provided a great impetus to research in this field. Interesting identifications of ultraviolet lines are mentioned to illustrate the progress that has been made in interpreting the spectra.
A large number of solar lines have been measured, whose chemical origin is unknown. This emphasizes the need for extensive laboratory programs on the analyses of spectra of the most abundant elements. Of special importance are studies of high-ionization spectra of light elements, and the re-observation of familiar complex spectra such as those of iron and nickel.

Rare dependence in a solarizing commercial X-ray emulsion: Sensitometric properties, number, and structure of developed grains, M. Ehrlich, Wm. L. McLaughlin, and E. Zeitler, *J. Opt. Soc. Am.* **54,** *No. 2, 176–183 (Feb. 1964).*
A comparison was made of optical density, mass of developed silver, number, projected area, and structure of the grains of a solarizing radiographic bromo-iodide emulsion exposed to Co^{60} gamma radiation at two different intensities, and developed in a surface developer. In contrast to the optical density and the mass of silver developed for a given exposure, which show only little rate dependence before solarization sets in, the rate dependence of the number of developed grains is quite marked. Another anomaly is observed in the reversal region for exposure to high-intensity radiation. There, mass of silver and optical density do not vary in the same sense.
Associated with the changes in photometric behavior are marked changes in grain structure, while the changes in the projected area of developed silver are small. Yet, not any one of the photometric properties can be uniquely correlated with grain structure over the entire exposure range.

High-resolution infrared determination of the structure of carbon suboxide, W. J. Lafferty, A. G. Maki, and E. K. Plyer, *J. Chem. Phys.* **40,** *No. 1, 224–229 (Jan. 1, 1964).*

High-resolution spectra have been obtained and the vibration-rotation absorption spectrum has been analyzed for a Σ_u–Σ_g and a Π_g–Π_u transition in C_3O_2 between 3142 and 3195 cm^{-1}. The absorption region studied contains a parallel combination band and a series of associated "hot bands." The successive "hot bands" are displaced toward high frequencies in such a manner that the Σ–Σ and Π–Π bands are relatively free of overlapping lines. The analysis shows that the molecule must have $D_{\infty h}$ symmetry with $B_0 = 0.073206$ cm^{-1}. The large number of "hot bands," the variation of intensity of these with temperature, and the large value of the *l*-doubling constant *q* all indicate that the lowest frequency bending mode must be of very low energy.

Iron, V. A. Lamb and C. T. Thomas, *Modern Electroplating, pp. 228–241 (1963).*
The history and applications of iron plating are reviewed, and procedures for preparing, maintaining, and operating various types of iron plating solutions are described. Significant recent developments as reported in the technical literature are reviewed.

Methods of testing, F. Ogburn, *Modern Electroplating, p. 661–697 (1963).*
Methods of testing electroplated coatings are reviewed. The principles of the various test methods are given along with references and comments; but without detailed procedures. Thickness, adhesion, corrosion resistances, appearance, porosity, smoothness and brightness, hardness, ductility, tensile strength, and internal stress are the qualities and properties covered by the tests discussed.

New method for constructing EPR cavities, A. R. Cook, L. M. Matarrese, and J. S. Wells, *Rev. Sci. Instr.* **35,** *114–115 (Jan. 1964).*
A new method of making thin-walled microwave reasonant cavities for EPR work is described. An aluminum mandrel is plated with silver, potted in epoxide casting resin, and then dissolved out with caustic solution. The silver adheres to the plastic and forms the cavity walls. By turning a helical groove in a plated cylindrical mandrel before potting, a TE_{101} cavity similar to a wire-wound cavity can be made. This type of construction is advantageous for EPR work, since it suppresses unwanted modes and permits passage of high-frequency magnetic field modulation.

Soft X-ray microscopy of paper, S. B. Newman and D. Fletcher, *Tappi* **47,** *No. 4, 177–180 (Apr. 1964).*
A point-projection X-ray tube was employed to produce microradiographs of a number of paper samples containing non-cellulosic additives or fillers. The radiation used was substantially monochromatic and in the 8 A wavelength region. Distribution and location of titanium dioxide at different concentrations could be readily ascertained. Added clay could also be resolved but with less contrast. The penetration and distribution of adhesive in the cellulosic matrix was uniquely revealed. The point-projection X-ray microscope should lend itself to technological control problems involving the incorporation of such additives to paper products.

The transmission of Rayleigh waves across an ocean floor with two surface layers, U. W. Hochstrasser and R. Stoneley, *Geophys. J. (Jeffreys Jubilee Number)* **4,** *197–201 (1961).*
The velocity of Rayleigh waves across an ocean floor with two surface layers is computed for various depths of the ocean and the two layers and for a set of wave length. From these values the group velocities and the period has been derived and the corresponding dispersion curves are compared with experimental data.

Accumulation of calibration errors and their optimum distribution, E. L. Crow, *Trans. 18th Midwest Quality Control Conf., Am. Soc. Quality Control, Tulsa, Okla., pp. 86–100 (Oct. 10–12, 1963).*
How can the accuracies required of instruments at the production line and in the field best be achieved? Usually instruments can be compared only indirectly with national primary standards through a hierarchy of calibration laboratories. The old question of how much accuracy each echelon in the hierachy should have is considered mathematically, and applications are made to five types of electronic measurements.

Phase variations in V. L. F. propagation, C. J. Chilton, D. D. Crombie, and A. G. Jean, *AGARDograph* **74,** *Propagation of Radio Waves at Frequencies below 300 Kilocycles, ch. 19, pp. 257–290 (Pergamon Press Inc., New York, N.Y., 1964).*
It is the purpose of this paper to review the experimental work describing the variations in phase of VLF signals received after ionospheric reflections at small and large distances.

Error rate in a multiple-frequency-shift system and the output signal/noise ratio in a frequency-modulation and a pulse-code-modulation/frequency-shift system, H. Akima, Proc. Inst. Elec. *Engrs.* **111,** *No. 3, 547–555 (Mar. 1964).*
Based on the assumption of a fading-free signal and an additive white Guassian noise, the element and symbol error rates in a multiple-frequency-shift (m.f.s.) system and the output signal/noise ratio in a frequency-modulation (f.m.) and a pulse-code-modulation/frequency-shift (p.c.m.f.s.) system are evaluated for wide ranges of system parameters. It is shown that the required intrinsic signal/noise ratio for a given symbol error rate in an m.f.s. system can be reduced by increasing the number of frequencies in the keying. The possibility of improving the threshold of an f.m. system beyond that of a conventional one, by frequency-modulating the carrier with sampled values and demodulating the modulated wave with a band-dividing demodulator, is shown. A brief discussion on the threshold effects in the frequency-lock and phase-lock f.m. demodulators suggests that the threshold of these feedback demodulators cannot be improved beyond that of a band-dividing one. It is shown that the threshold in a p.c.m.f.s. system can be reduced by increasing the base in the coding. The comparison of a p.c.m.f.s. system with a band-dividing f.m. system shows the inferiority of the former to the latter, in so far as the minimum-power criterion of system comparison is concerned.

Polymer compression: visual observations on stressed biaxially oriented nylon 66, J. Powers and A. Van Valkenberg, *J. Polymer Sci. Polymer Letters, Pt. B,* **2,** *No. 3, 553–536 (May 1964).*
Nylon 66 was stressed along its different orientation directions on a diamond anvil apparatus. Changes in morphology showed a definite correlation with sample orientation. These observations indicate that the deformation may arise partially from slippage along crystal planes.

Gloss standards and glossmeters standardization, H. K. Hammond, III, *Am. Paint J., pp. 360–364 (Apr. 1964).*
Gloss standards provide very fine adjuncts for quickly checking the accuracy of geometric adjustment of glossmeters and the correctness of their readings. An instrument that is not in accurate geometric adjustment, however, cannot be calibrated by simply noting the scale corrections required to provide the assigned values of the standards. Standardization of specular-gloss measurements necessitates specification of the angles of illumination and reception and the sizes of the source and receptor field angles or apertures. The apertures, together with permissible tolerances, are specified in each ASTM method. The user of an instrument, however, may not wish to dismantle the instrument to check aperture dimensions or to ascertain if the image of the source is centered in and focused on the receptor entrance window. A simple check of the overall accuracy of instrument adjustment is provided by setting the instrument scale to read the gloss value of a polished opaque-glass standard, and then noting the readings for several standards of lower gloss. If the readings for these latter standards do not agree closely with the assigned values, usually within a unit or two, the instrument should be readjusted according to the manufacturer's instructions or returned to him for adjustment.

Audiofrequency compliances of prestressed quartz, fused

silica, and aluminum, M. Greenspan and C. E. Tschiegg, *J. Acoust. Soc. Am.* **36,** *No. 3, 450–457 (Mar. 1964).*
The anomalies in the audiofrequency compliances reported by Fitzgerald were searched for in vain. The present technique involves a vibrating duplex reed; the biasing steady stress is of either piezoelectric or thermal origin. An extension of the common theory of the "bimetallic strip" to anisotropic materials is presented.

Changes in relation between refractive index and Young's modulus as the result of successive heat treatments, E. H. Hamilton, *J. Am. Ceram. Soc.* **47,** *No. 4, 167–170 (Apr. 1964).*
The relation between refractive index and elastic modulus is found to be a senstive indicator of the nucleation and separation of submicroscopic phases in glass. In a study of the changes in properties with heat treatments of a wide variety of glasses containing SiO_2, B_2O_3, and ZnO as major constituents, it was observed that large decreases in Young's moduli were not accompanied by decreases in refractive indices of the magnitude usually observed. The abnormal changes in properties resulted from a sequence of two heat treatments. The results indicate that during the first heat treatment an immiscible phase is nucleated which, on subsequent heat treatment at a higher temperature, develps into heterogeneous regions producing changes in the relation between the refractive index and the elastic modulus.

Calorimetry of portland cement. I. Effect of various procedures on determination of heat of solution, H. A. Berman and E. S. Newman, *ASTM Proc.* **63,** *830–851 (1963).*
Nine calculation procedures for correcting the observed temperature rise in a solution calorimeter are compared. Eight of these procedures are used in various specifications for determining the heat of hydration of hydraulic cements by the heat-of-solution method.
The best reproducibility was found with methods that use long rating periods and reading intervals rather than short ones; that use constants of stirring energy and heat leakage that are independently calculated from calibrations or other pertinent tests of the apparatus or that are obtained in part from temperatures of the initial rating period rather than from temperatures of the final rating period (provided that they are accurately obtained); and that are not restricted by definitely specified duration times for the solution and rating periods. The best accuracy was found in methods that employ solution periods longer than 20 min and in those that employ the most rigorous possible approach to the heat-leakage integration calculation consistent with the data available.

Pointwise bounds in the first biharmonic value problem, J. H. Bramble and L. E. Payne, *J. Math. Phys.* **42,** *No. 4, 278–286 (Dec. 1963).*
Error bounds are derived in the approximation of the solution to the first biharmonic boundary value problem. These bounds are obtained by combining mean value inequalities and a priori mean square inequalities for biharmonic functions. Bounds are given for the function and for derivatives up to order three at interior points. Since the error is quadratic the Rayleigh-Ritz technique may be used for improving the bounds.

Calorimetry of portland cement. II. Application of various heat-of-solution procedures to determination of heat of hydration, E. S. Newman and H. A. Berman, *ASTM Proc.* **63,** *852–860 (1963).*
The heats of hydration of two cement samples were determined using three types of heat-of-solution calorimeter: the ASTM standard air-bath Dewar, a submerged Dewar with a metal cover, and a submerged metal precision calorimeter using a resistance thermometer. The data were taken in sufficient detail to permit the computation of the corrected temperature rise by eight different methods, all based on Newton's law of cooling, recommended by various authorities in the United States and abroad. The determinations were made in two different rounds of duplicates, and the accuracy and precision of the calorimeters and of the methods are discussed on the basis of the results obtained. Differences among the calorimeters and methods found in heat-of-solution determinations largely disappeared in computing the heats of hydration. By the most rigorous method, standard deviations of 1.45, 1.38, and 0.70 cal per g were found for the heat of hydration as determined by the air-bath Dewar, the submerged Dewar, and the precision calorimeter, respectively.

Four-terminal-pair networks as precision admittance and impedance standards, R. D. Cutkosky, *IEEE Trans. Commun. Elec.* **CE–70,** *19–22 (Jan. 1964).*
Practical accuracy limitations of four terminal impedance and three terminal admittance measurements are discussed. It is shown that there exists a middle impedance range in which neither technique results in good measurement precision. A theoretical analysis of measurement systems using the two techniques simultaneously is made.

A differential microwave phase shifter, R. W. Beatty, *IEEE Trans. Microwave Theory Tech.* **MTT–12,** *250–251 (Mar. 1964).*
A differential microwave phase shifter is described in which two phase shifters of a certain type are connected in series. These are of the type consisting of a section of waveguide containing a sliding short-circuit and a tuned, single directional coupler reflectometer. By connecting these back-to-back and ganging the short-circuits in the two waveguide sections, one causes the phase shift of the output to be the difference between the individual phase shifts. If the waveguides are identical this, differential phase shift is zero, but if they are not identical, the resulting phase shift varies as slowly as desired with movement of the short-circuits. This device has possible applications at millimeter and submillimeter wavelengths as a standard phase shifter, and as an indicator of differential displacement. It may also be used in evaluating the uniformity of waveguides and sliding short-circuits.

Fluctuations in a Laser beam over 9- and 90-mile paths, W. R. Hinchman and A. L. Buck, *Proc. IEEE* **52,** *305–306 (Mar. 1964).*
Some preliminary results of a study of long distance laser transmission are given. Measured quantities include beam-width, angular scintillation, and fade-rate spectrum.

Tapered inlets for pipe culverts, J. L. French, *J. Hydraulics Div., ASCE* **90,** *No. HY2, 255–299 (Mar. 1964).*
Laboratory data relating to the performance of pipe culverts with tapered inlets and steep barrel slopes are reported. The effects of vortex action over the inlet are examined and it is concluded that subatmospheric pressures in the inlet region are subject to ventilation effects caused by air-carrying vortices and hence that flow regimes in the culvert dependent upon such pressures cannot be assumed. In general, the minimum performance of the culvert structure under adverse conditions is shown to approximate entrance control flow. The significance of various aspects of the inlet geometry with respect to the performance of the culvert, as well as to the location of the applicable inlet control section is explored.

Field trial of the 1959 supplementary standard observer proposal, I. Nimeroff, *J. Opt. Soc. Am.* **54,** *No. 5, 696–704 (May 1964).*
The field trials of the 10°-field supplementary standard observer proposal performed by Stiles and Wyszecki on the National Research Council, three-primary, Donaldson colorimeter have been repeated on the National Bureau of Standards Donaldson colorimeter. Only the least selective eleven of the eighteen NRC filters were used in the NBS repetition, which employed eleven observers each making two sets of matches. The NBS Donaldson colorimeter with a 10°-field of view was calibrated both in terms of the 1931 CIE standard observer system and in terms of the 1959 supplementary proposal. As expected, visual matches with a 10° field compared quite unsatisfactorily with predictions made by the 1931 standard observer. The results are in general agreement with the Stiles-Wyszecki field-trial data. The agreement with the predictions by the 1959 proposal is improved when the results of the two field trials are combined, because the resulting arrays of individual-observer data encompass the predicted chromaticites of all of the filters

but the red one. It is concluded that, although the proposal is not completely satisfactory, it does yield a significant improvement over the agreements achieved between predictions by the 1931 observer and observations.

An experimental 350-kv, 1-picofarad air capacitor, A. E. Peterson, *IEEE Trans. Commun. Elec. No. 71, 129–131 (Mar. 1964).*
This paper describes a 350 kv, 1-picofarad, shielded, atmospheric air capacitor. Its constructional details, features, voltage coefficient and short-time stability are discussed.

Optical studies at high pressures, L. S. Whatley, E. R. Lippincott, A. Van Valkenburg, and C. E. Weir, *Science* **144,** *No. 3621, 968–976 (May 22, 1964).*
Application of pressures up to 150 kbars in microscopy, spectroscopy, and X-ray crystallography should yield information about the nature of atomic and molecular interaction forces in a substance and about possible pressure-induced internal distortions of the molecules. The development of a miniaturized high pressure cell which employs diamond anvils and which fits easily into the small sample areas of commercial optical equipment has greatly facilitated the application of high pressures in optical studies. The nature and optical characteristics of polymorphic changes in transparent solids and liquids have been investigated using this diamond cell. A microscope spectrophotometer has been devised so that absorption spectra of small areas of the compressed sample could be obtained. A camera attachment allows convenient recording of the visual observations. X-ray diffraction powder patterns have been made for low and high pressure forms of several substances, and new high pressure forms have been discovered in some cases.

Distillation analysis, R. T. Leslie and E. C. Kuehner, *Anal. Chem.* **36,** *56R (Apr. 1964).*
The literature relating to distillation which has appeared in domestic and foreign journals in the past two years has been summarized briefly, accompanied by a bibliography. Emphasis is on fundamental developments and information which can be of assistanse in analysis or separation of materials by distillation.

A comparison of the TA_1 and the NBS—A atomic time scales, J. Bonanomi, P. Kartaschoff, J. Newman, J. A. Barnes, and W. R. Atkinson, *Proc. IEEE* **52,** *No. 4, 439 (Apr. 1964).*
A comparison has been made between two independent atomic time scales by using the WWV time pulses as a link. The results of the comparison indicate that during the last two years unaccounted for divergences are of the order of one part in 10^{11}.

Jet thinning device for preparation of Al_2O_3 electron microscope specimens, N. J. Tighe, *Rev. Sci. Instr.* **35,** *No. 4, 520–521 (Apr. 1964).*
A jet thinning device has been developed for preparation of single crystal Al_2O_3 specimens suitable for study by transmission electron microscopy. The device is used with boiling phosphoric acid up to temperatures of 50 °C. Details are given on the design of the device and its use in a procedure for preparing specimens, of any crystallographic orientation, from bulk material.

Direct quantitative analysis of photomicrographs by a digital computer, G. A. Moore, *Photo Sci. Eng.* **8,** *No. 3, 152–161 (May–June 1964).*
A program on the National Bureau of Standards SEAC Computer directly accepts photomicrographs or other pictures as the information input. Commands in English format cause compilation of operational orders as required to carry out modifications or analyses of the pictures. The 28 operations now functional include lineal and area analyses of whole pictures, sorting out of individual coherent objects and determining 15 parameters of each. Special photographic precautions are necessary to supply only truthful information to the computer. Studies of complex niobium-tin superconductors and dispersed particle structures are shown. Probable applicability to biological problems and to photographic emulsions is considered.

Microwave standards and measurements, a progress review 1960–1963, R. W. Beatty, *IEEE Trans. Instr. Meas.* **IM–12,** *No. 3, 134–138 (Dec. 1963).*
Rather than a comprehensive survey of the field, highlights of the progress in microwave standards and measurement methods are given. Power, attenuation, impedance or reflection coefficient, noise, phase shift, and field strength are covered. Microwave frequencies are assumed to start at 1 Gc/s and extend upwards, including coherent electromagnetic energy in the spectrum of visible light, approximstely 400–800 Tc/s.
A discussion of the intercomparisons of power standards of different nations is followed by a report on newly developed power measuring devices and techniques. Some methods of measuring the power of lasers are given.
The present status of attenuation measurements and standards is indicated, giving ranges and accuracies of calibrations at the U.S.A. National Bureau of Standards (NBS). New types of standards for millimeters and submillimeter waves and for attenuation of laser beams are mentioned.
Impedance standards and measuring techniques are discussed, as well as 2-port measurements and the development of greatly improved coaxial connectors.
The recent development of phase shift standards and measurement techniques in the U.S.A. is summarized.
The essential lack of microwave field strength standards is noted and small progress is reported.

Colorimetry in parafoveal fields I. Color-matching functions, I. Nimeroff, *J. Opt. Soc. Am.* **54,** *No. 6, 824–832 (June 1964).*
Minor defects in the 1931 CIE Standard Observer System, derived from 2° foveal viewing conditions, have increased interest in large parafoveal viewing fields. As the parafoveal region of the retina gives rod as well as cone responses, the CIE is considering a new observer system in which contributions of the rods to overall vision have been removed so that the system reflects only the cone response. The author, a normal trichromat in 2° foveal vision, has measured his 10°-field color-matching functions on the Wright visual tristimulus colorimeter. These color-matching functions, reported here, are compared with other such data and with data taken for foveal, parafoveal, and extrafoveal fields. The author's 10°-field data confirm that, with the retinal illuminance of that achieved in the Wright visual tristimulus colorimeter, rod responses are an important part of the total visual response. It is concluded that rod responses should not be neglected in color-matching with retinal illumination less than 1000 trolands.

Colorimetry in parafoveal fields II. Additivity failure, I. Nimeroff, *J. Opt. Soc. Am.* **54,** *No. 6, 833–838 (June 1964).*
Field trials of the proposed 10°-field observer system, derived by removing rod response from the color-matching data, indicate that many subsequent visual color matches made on existing additive colorimeters require correction for rod response. Although these corrections are made additivity failure still may persist. There is speculation that the additivity failures result from rod-cone interactions, either inhibitive or facilitative. Additivity checks made by the author are in general agreement with results obtained in the extrafoveal investigations of Wright, of Moreland, and of Clarke and with the results of the 10° parafoveal field trials of Wright and Wyszecki and of Stiles and Wyszecki.

Other NBS Publications

Journal of Research 68A (Phys. and Chem.), No. 5, (Sept.–Oct. 1964), 70 cents.

Relaxation modes of trapped crystal point defects: the three-neighbor shells model in NaCl. A. D. Franklin, A. Shorb, and J. B. Wachtman, Jr.

Viscosity of a standard soda-lime-silica glass. A. Napolitano and E. G. Hawkins. (See above abstracts.)

Hydrothermal preparation of a gehlenite hydrate. E. T. Carlson.

Action of water on calcium aluminoferrites. E. T. Carlson.

Infrared spectra of the crystalline inorganic borates. C. E. Weir and R. A. Schroeder.

Effect of pressure and temperature upon the optical dispersion of benzene, carbon tetrachloride, and water. R. M., Waxler, C. E. Weir, and H. W. Schamp, Jr.
Some changes in double-bond structure during the vulcanization of natural rubber. F. J. Linnig, E. J. Parks, and J. E. Stewart. (See above abstracts.)
Dislocations in polymer crystals. H. D. Keith and E. Passaglia. (See above abstracts.)
Dependence of mechanical relaxation on morphology in isotactic polypropylene. E. Passaglia and G. M. Martin. (See above abstracts.)
Precision density measurement of silicon. I. Henins. (See above abstracts.)
Franck-Condon factors to high vibrational quantum numbers IV: NO band systems. R. W. Nicholls.

Journal of Research 68B (Math. and Math. Phys.), No. 3, (July–Sept. 1964), 75 cents.

Generation and composition of functions. A. J. Goldman.
Thermodynamics of perfect elastic fluids. B. Bernstein, E. A. Kearsley, and L. J. Zapas. (See above abstracts.)
Zeros of polynomials in several variables and fractional order differences of their coefficients. B. Mond and O. Shisha.
Theory of radiation from sources immersed in anisotropic media. J. R. Wait.

Radio Sci. J. Res. NBS/USNC-URSI, 68D, No. 9 (Sept. 1964), $1.00.

Symposium on Signal Statistics, Seattle, Washington, U.S.A., December 6–7, 1963:
Signal statistics, yesterday and today. F. L. H. M. Stumpers.
Rayleigh distribution and its generalizations. P. Bechmann.
Some nonlinear problems arising in the study of random processes. M. Rosenblatt.
An approach to empirical time series analysis. E. Parzen. (See above abstracts.)
Effect of linear and nonlinear signal processing on signal statistics. A. V. Balakrishnan. (See above abstracts.)
Random volume scattering. H. Bremmer.
Phase fluctuation statistics. J. B. Smyth.
Current topics in the stochastic theory of radiation. F. J. Zucker.
On the intensity distribution

$$\frac{2R}{\sqrt{\alpha\beta}} \exp\left[-\frac{R^2}{2}\left(\frac{1}{\alpha}+\frac{1}{\beta}\right)\right] I_0\left(\frac{R^2}{2}\left[\frac{1}{\beta}-\frac{1}{\alpha}\right]\right)$$

and its application to signal statistics. M. Nakagami.
Statistical inference for Rayleigh distributions. M. M. Siddiqui.
A probabilistic approach to the problem of large antenna arrays. Y. T. Lo.
Influence of data processing on the design and communication of experiments. S. W. Golomb. (See above abstracts.)
Spectral measurement techniques in planetary radar. G. Pettengill. (See above abstracts.)
Quantum statistics and lasers. J. P. Gordon. (See above abstracts.)
Statistics of random surfaces. I. Kay and P. Swerling.
Modified gaussian distributions for slightly nonlinear variables. M. S. Longuet-Higgins.

Radio Sci. J. Res. NBS/USNC-URSI, 68D, No. 10 (Oct. 1964), $1.00.

Theoretical heights and durations of echoes from large meteors. L. A. Manning.
Experimental determination of meteoric line densities and attachment rates. L. A. Manning.
Broadband radio-star scintillations, II. Interpretation. D. G. Singleton.
Electron collision frequency in the ionospheric *D* region. R. F. Benson.
A discussion of the theory of ionospheric cross modulation. R. F. Benson.
Theory of a slotted-sphere antenna immersed in a compressible plasma. Part I. J. R. Wait.
Theory of a slotted-sphere antenna immersed in a compressible plasma. Part II. J. R. Wait.
Electromagnetic scattering coefficients for concentric spheres and the problem o, interference free enclosures. R. A. Eldred, H. A. Lasitter, and J. Roberts.
Ionospheric sounding using coded pulse signals. D. C. Coll and J. R. Storey.
Measurement of the complex time-frequency channel correlation function. P. A. Bello. (See above abstracts.)

Radio Sci. J. Res. NBS/USNC–URSI, 68D, No. 11 (Nov. 1964), $1.00.

Interaction of an antenna with a hot plasma and the theory of resonance probes. J. A. Fejer.
Observations of earth-ionosphere cavity resonances and their interpretation in terms of a two-layer ionosphere model. F. W. Chapman and D. Llanwyn Jones.
On the theory of reflection of electromagnetic waves from the interface between a compressible magnetoplasma and a dielectric. J. R. Wait.
Propagation over plane earth through an exponential atmosphere. I. H. Gerks and R. M. Anderson.
Propagation in nonuniform waveguides with impedance walls. R. L. Gallawa. (See above abstracts.)
Some approximate formulas concerning the reflection of electromagnetic waves from a stratified semi-infinite medium. R. Burman.
A VLF timing experiment. A. H. Morgan and O. J. Baltzer. (See above abstracts.)
Phase and time variations in VLF propagation over long distances. D. D. Crombie. (See above abstracts.)
Geometrical optics convergence coefficient for whistler propagation. G. McK. Allcock.
Errors induced by the atmosphere in microwave range measurements. H. B. Janes and M. C. Thompson. (See above abstracts.)
Some features of *Es*—ionization of the equatorial ionosphere. P. Bandyopadhyay and H. Montes.
A note on the insulated loops antenna immersed in a conducting medium. J. R. Wait and K. P. Spies.
Observation and analysis of transequatorial propagation. J. A. Thomas and B. A. McInnes.

Bound volume of the Journal of Research, Section A. Physics and Chemistry **67A,** Nos. 1 to 6, January to December 1963, $6.00.
Bound volume of the Journal of Research, Section B. Mathematics and Mathematical Physics **67B,** Nos. 1 to 4, January to December 1963, $3.25.
Bound volume of the Journal of Research, Section C. Engineering and Instrumentation, **67C,** Nos. 1 to 4, January to December 1963, $3.75.
Bound volume of the Journal of Research, Section D. Radio Propagation **67D,** Nos. 1 to 6, January to December 1963 $7.00.
Tables of chemical kinetics homogeneous reactions (Supplementary Tables) NBS Mono. 34, Vol. 2 (July 1, 1964) $2.75.
Physical aspects of irradiation, Recommendations of the International Commission on Radiological Units and Measurements, NBS Handb. 85 (Mar. 31, 1964), 70 cents. (Supersedes parts of H78. Handbooks 84 through 89 extend and largely replace H78.)
Microstructure of ceramic materials. Proceedings of an American Ceramic Society Symposium, Pittsburgh, Pa., April 27–28, 1963, NBS Misc. Publ. 257 (Apr. 6, 1964), $1.75.
Quarterly radio noise data December, 1962; January, February, 1963, W. Q. Crichlow, R. T. Disney, and M. A. Jenkins, NBS Tech. Note 18–17 (May 21, 1964), 50 cents.
Quantum field theoretic techniques and the electromagnetic properties of a uniformly magnetized electron gas, L. A. Steinert, NBS Tech. Note 207 (Apr. 6, 1964), $1.50.
Conference on non-linear processes in the ionosphere, December 16–17, 1963, Ed. D. H. Menzel and E. K. Smith, Jr., NBS Tech. Note 211, Vol. 2 (Apr. 17, 1964); Vol. 3 (Apr. 19, 1964); Vol. 4 (Apr. 22, 1964); Vol. 5 (Apr. 24 1964); and Vol. 6 (Apr. 24, 1964), 45 cents each.
Percentage points of the beta distribution, L. E. Vogler. NBS Tech. Note 215 (May 30, 1964), 25 cents.
Computation of Hankel functions, L. A. Berry, NBS Tech. Note 216 (June 12, 1964), 20 cents.

A bibliography of thermophysical properties of argon from 0 to 300°K, L. A. Hall, J. G. Hurst, and A. L. Gosman, NBS Tech. Note 217 (June 12, 1964), 55 cents.

Potential distribution method in equilibrium statistical mechanics, J. L. Jackson and L. S. Klein, Phys. Fluids **7,** No. 2, 228–231 (Feb. 1964). Radio propagation by reflection from meteor trails, G. R. Sugar, Proc. IEEE **52,** No. 2, 116–136 (Feb. 1964).

Data processing system for the automatic transformation of observed plasma intensities into their radial distribution, D. R. Paquette and W. L. Wiese, Appl. Opt. **3,** No. 2, 291–295 (Feb. 1964).

Estimation of weighting factors in linear regression and analysis of variance, J. Mandel, Technometrics **6,** No. 1, 1–25 (Feb. 1964).

Mechanism of the photolysis of ethane at 1470 A, R. F. Hampson, Jr., J. R. McNesby, H. Akimoto, and I. Tanaka, J. Chem. Phys. **40,** No. 4, 1099–1105 (Feb. 15, 1964).

Precession equation of a spinning particle in nonuniform fields, U. Fano, Phys. Rev. **133,** No. 3B, B828–B830 (Feb. 10, 1964).

Classical model for the study of isotope effects in energy exchange and particle exchange reactions, R. J. Rubin, J. Chem. Phys. **40,** No. 4, 1069–1077 (Feb. 15, 1964).

Condensation model producing crystalline or amorphous tetrahedral networks, F. Ordway, Science **143,** No. 3608, 800–801 (Feb. 21, 1964).

Continuum theory of a plasma, J. L. Jackson and L. S. Klein, Phys. Fluids **7,** No. 2, 232–241 (Feb. 1964).

On the anomalous NMR linewidth in lithium and sodium, D. Zamir, R. C. Wayne, and R. M. Cotts, Phys. Rev. Letters **12,** No. 12, 327 (Mar. 23, 1964).

Linewidths in the 2–0 band of carbon monoxide broadened by nitrogen and hydrogen, T. C. James and E. K. Plyler, J. Chem. Phys. **40,** No. 1, 221–223 (Jan. 1, 1964).

Intensity of the quadrupole fundamental of molecular hydrogen. Rotation-vibration interaction correction, T. C. James and W. Klemperer, J. Chem. Phys. **40,** No. 3, 914–915 (Feb. 1, 1964).

Observatory reports, C. E. Moore and L. M. Branscomb Astron. J. **68,** No. 9, 657–659 (Nov. 1963).

Absorption spectrum of the "pink" afterglow of nitrogen in the vacuum ultraviolet, A. M. Bass, J. Chem. Phys. **40,** No. 3, 695–700 (Feb. 1, 1964).

Pressure broadening of DCl by HCl and of HCl by DCl. A comparison of experimental results with Anderson's theory, T. C. James and R. J. Thibault, J. Chem. Phys. **40,** No. 2, 534–540 (Jan. 15, 1964).

Excitation by local electric fields in the aurora and airglow, L. R. Megill and N. P. Carleton, J. Geophys. Res. **69,** No. 1, 101–122 (Jan. 1, 1964).

Energy losses and elastic resonances in electron scattering from H_2, C. E. Kuyatt, S. R. Mielczarek, and J. A. Simpson, Phys. Rev. Letters **12,** 293 (1964).

The γ-absorption cross section of holmium in the dynamic collective theory, M. Danos and W. Greiner, Phys. Letters **8,** No. 2, 113–115 Jan. 15, 1964).

Determination of error rates for narrow-band communication of binary-coded messages in atmospheric radio noise, A. D. Spaulding, Proc. IEEE **52,** No. 2, 220–221 (Feb. 1964).

Intensity of the forbidden $X^2\Pi_{3/2} - X^2\Pi_{1/2}$ satellite bands in the infrared spectrum of nitric oxide, T. C. James, J. Chem. Phys. **40,** No. 3, 762–771 (Feb. 1, 1964).

Energy spectra and angular distribution of electrons transmitted through sapphire (Al_2O_3) foils, M. J. Berger and S. M. Seltzer, Natl. Aero. Space Admin. Spec. Publ. SP3008, pp. 1–107 (1964).

The 1963 Symposium on Humidity and Moisture, 20–23 May 1963, Washington, D.C., A. Wexler, Intern. J. Heat Mass Transfer **7,** 275–277 (1964).

Hydride and proton transfer reactions involving sec-propyl ions, R. P. Borkowski and P. Ausloos, J. Chem. Phys. **40,** No. 4, 1128–1132 (Feb. 15, 1964).

Effects of anharmonicity on vibrational energy transfer, F. H. Mies, J. Chem. Phys. **40,** No. 2, 523–531 (Jan. 15, 1964).

Cation-exchange between molten salts and a special porcelain of high sodium content, R. J. Labrie, J. Electrochem Soc. **111,** No. 4, 473–476 (Apr. 1964).

On the height distribution of the ratio of negative ion and electron densities in the lowest ionosphere, G. C. Reid, D. K. Bailey, and H. Leinbach, J. Atmospheric and Terrest. Phys. **26,** 145–147 (1964).

The following are chapters in the book, Modern Electroplating (1963):

Electroless plating, A. Brenner, pp. 698–713.
Iron, V.A. Lamb and C. T. Thomas, pp. 228–241.
Methods of testing, F. Ogburn, pp. 661–697.

Electron density profile analysis of topside sounder ionograms, A. K. Paul and J. W. Wright, J. Geophys. Res. **69,** 1431–1435 (Apr. 1964).

On phase changes in very-low-frequency propagation induced by an ionospheric depression of finite extent, J. R. Wait. J. Geophys. Res. **69,** No. 3, 441–445 (Feb. 1964).

Electronic transport in strontium titanate, H. P. R. Frederikse, W. R. Thurber, and W. R. Hosler, Phys. Rev. **134,** No. 2A, A442–A445 (Apr. 20, 1964).

Hydrogen reaction with carbon and nickel evaporated films, V. R. Deitz and E. F. McFarlane, Carbon **1,** 117–125 (1964).

Discussion of spin-spin relaxation formulae and experiments, R. L. Peterson, Phys. Letters **8,** No. 3, 158–159 (Feb. 1, 1964).

Thermal decomposition of some tert-butyl compounds at elevated temperatures, W. Tsang, J. Chem. Phys. **40,** No. 6, 1498–1505 (Mar. 15, 1964).

Vacuum ultraviolet absorption spectra of oxygen in liquid and crystalline argon and nitrogen, A. M. Bass and H. P. Broida, J. Mol. Spectry. **12,** No. 3, 221–230 (Mar. 1964).

The electron paramagnetic resonance spectrum of some tris-complexes of copper (II), H. C. Allen, Jr., G. F. Kokoszka, and R. G. Inskeep, J. Am. Chem. Soc. **86,** 1023–1025 (1964).

The structure and physics of the upper atmosphere, T. E. Van Zandt and R. W. Knecht, Book, Space Physics, pp. 166–225 (John Wiley & Sons, Inc., New York, N.Y., 1964).

An implication for lasers of an aspect of interference at high field strengths, J. A. White, Nature **201,** No. 4922, 911–912 (Feb. 29, 1964).

Weierstrass points of $\Gamma_0(n)$, J. Lehner and M. Newman, Ann. Math. **79,** No. 2, 360–368 (Mar. 1964).

The infrared spectra, structures and thermodynamics of gaseous LiO, Li_2O, and Li_2O_2, D. White, K. S. Seshadri, D. F. Dever, D. E. Mann, and M. J. Linevsky, J. Chem. Phys. **39,** No. 10, 2463–2473 (Nov. 15, 1963).

A two-parameter family of hyper-Poisson distributions, G. E. Bardwell and E. L. Crow, J. Am. Stat. Assoc. **59,** 133–141 (Mar. 1964).

On the geomagnetic effect of the Starfish high-altitude nuclear explosion, H. Maeda, A. J. Shirgaokar, M. Yasuhara, and S. Matsushita, J. Geophys. Res. **69,** 917–945 (Mar. 1964).

Note on "interferometric measurement of vibration amplitudes", K. D. Mielenz, Appl. Opt. **3,** 542 (Apr. 1964).

Weights and measures and aerosols, M. W. Jensen, Scale J. **50,** No. 6, 2 (Mar. 1964).

Radiative tail in elastic electron scattering, L. C. Maximon and D. B. Isabelle, Phys. Rev. **133,** No. 5B, B1344–B1350 (Mar. 9, 1964).

Exact conditions for the preservation of a canonical distribution in Markovian relaxation processes, H. C. Andersen, I. Oppenheim, K. E. Shuler, and G. H. Weiss, J. Math. Phys. **5,** No. 4, 522–536 (Apr. 1964).

Further observations of synchrotron radiation decay, G. R. Ochs, J. Geophys. Res. **69,** No. 3, 399–405 (Feb. 1964).

A note on the attenuation function for propagation over a flat layered ground, L. E. Vogler, IEEE Trans. Ant. Prop. **AP-12,** 240–242 (Mar. 1964).

Solubility of helium in liquid hydrogen, R. J. Corruccini, J. Chem. Phys. **40,** 2039–2040 (Apr. 1964).

All trophy in some rare-earth metals at high pressures, G. J. Piermarini and C. E. Weir, Science **144,** No. 3614, 69–71 (Apr. 3, 1964).

Relative oscillation strengths of some O II and O III lines from measurements on shock-heated plasmas, H. F. Berg K. L. Eckerle, R. W. Burris, and W. L. Wies, Astrophys J. **139,** No. 2, 751–757 (Feb. 15, 1964).

The crystallography of some M^{2+} borates, S. Block, A. Perloff, and C. E. Weir, Acta Cryst. **17,** Pt. 3, 314–315 (Mar. 1964).

Theory of the electronic susceptibilities of stoichiometric rutile (TiO_2), A. R. Ruffa, Phys. Rev. **133,** No. 5A, 1418–1426 (Mar. 2, 1964).

An explanation for the apparent polarization of some geomagnetic micropulsations (pearls), J. H. Pope, IEEE Spectrum **1,** 129–138 (Jan. 1964).

The electrolysis of formamides, acetamides and propionamides, D. E. Couch, Electrochem. Acta **9,** No. 4, 327–336 (Apr. 1964).

Solvent participation in the anionic polymerization of styrene, L. J. Fetters, Polymer Letter **2,** 425–428 (1964).

Conductance of potassium chloride in highly purified *n*- methylpropionamide from 20 to 40°, T. B. Hoover, Phys. Chem. **68,** 876–879 (1964).

A review of photodetachment and related negative ion processes relevant to aeronomy, L. M. Branscomb, Ann. Geophys. **20,** 88–102 (Jan.–Mar. 1964).

The relation between VLF propagation and D-layer characteristics, J. R. Wait, IEEE Trans. Ant. Prop. **AP–12,** 239–240 (Mar. 1964).

Analog simulation of zone melting, H. L. Mason, Instr. Control Systems **37,** No. 1, 121–123 (Jan. 1964).

Microwave studies of butadiene, derivatives. II. Isoprene, D. R. Lide, Jr., and M. Jen, J. Chem. Phys. **40,** No. 1, 252–253 (Jan. 1, 1964).

Correlation between observed wavelength shifts produced in electrodeless discharge tubes and predicted Stark-effect shifts in the spectrum of neutral germanium (Ge I), L. Minnhagen, J. Opt. Soc. Am. **54,** No. 3, 320–322 (Mar. 1964).

Determination of *p*H, Theory and Practice, R. G. Bates, Book, 450 pages (John Wiley & Sons, Inc., New York, N.Y., Feb. 1964).

Disproportionation—combination reactions of alkyl radicals and hydrogen atoms at low temperatures, R. Klein, M. D. Scheer, and R. Kelley, J. Phys. Chem. **68,** 598 (1964).

Effects of tensile stress on the domain structure in grain-oriented 3.25% silicon, J. J. Gniewek, J. Appl. Phys. **34,** No. 12, 3618–3622 (Dec. 1963).

Correlation of the phase of microwave signals on the same line-of-sight path at different frequencies, H. B. Janes, IEEE Trans. Ant. Prop. **AP–11,** 716–717 (Nov. 1963).

The theory of an antenna over an inhomogeneous ground plane, J. R. Wait, Book, Electromagnetic Theory and Antennas, Ed. E. C. Jordan, Pt. 2, pp. 1079–1098 (Pergamon Press, Oxford, England, 1963).

Mass-spectrometric investigation of the nickel-bromine surface reaction, J. D. McKinley, J. Chem. Phys. **40,** No. 2, 576–581 (Jan. 15, 1964).

Some observations of short-duration cosmic noise absorption events in nearly conjugate regions at high magnetic latitude, K. W. Eriksen, C. S. Gillmor, and J. K. Hargreaves, J. Atmospheric Terrest. Phys. **26,** 77–90 (1964).

The effect of Coulomb collisions on incoherent scattering of radio waves by a plasma, D. T. Farley, Jr., J. Geophys. Res. **69,** 197–200 (Jan. 1964).

Mass-spectrometric investigation of the high-temperature reaction between nickel and chlorine, J. D. McKinley J. Chem. Phys. **40,** No. 1, 120–125 (Jan. 1, 1964).

Ferromagnetic resonance relaxation, wide spin-wave coverage by ellipsoids, A. S. Risley and H. E. Bussey, J. Appl. Phys. **35,** No. 3, 896–897 (Mar. 1964).

The effect of coulomb collisions on incoherent scattering of radio waves by a plasma, D. T. Farley, Jr., J. Geophys. Res. **69,** No. 1, 197–200 (Jan. 1, 1964).

On the connection between the theories of collisions and of atomic spectra, U. Fano and F. Prats, Proc. Nat. Acad. Sci., India, **XXXIII,** Part IV, 553–562 (1963).

Electromagnetic scattering from a radially inhomogeneous sphere, J. R. Wait, J. Appl. Phys. Sec. B, **10,** 441–450 (Jan. 7, 1963).

An approach to the classification of electromagnetic surface waves, J. R. Wait, Book, Radio Waves and Circuits by S. Silver, Pt. 1, pp. 86–95 (Elsevier Publ. Co., Princeton, N.J., 1963).

Mass spectrometry, R. M. Reese and F. N. Harldee, Anal. Chem. **36,** No. 5, 278R–295R (April 1964).

The association of plane-wave electron density irregularities with the equatorial electro jet, K. L. Bowles, J. Geophys. Res. **68,** No. 9, 2503–2525 (May 1, 1963).

Infrared spectra of NF, NCl, and NBr, D. E. Milligan and M. E. Jacox, J. Chem. Phys. **40,** No. 9, 2461–2466 (May 1, 1964).

Some results of the energy-dependent Milne problem for thermal neutrons and light gases, C. Eisenhauer, Nucl. Sci. Eng. **19,** 95–101 (1964).

Nitrogen NMR chemical shifts in the azide ion, R. A. Forman, J. Chem. Phys. **39,** No. 9, 2393 (Nov. 1, 1963).

Exact Faxén solution for centrifugation when sedimentation depends linearly on concentration, I. H. Billick and G. H. Weiss, Nature **201,** No. 4922 912–913 (Feb. 29, 1964).

$4f^3$ and $4f^2$ $5d$ configurations of doubly ionized praseodymium (Pr III), R. E. Trees, J. Opt. Soc. Am. **54,** No. 5, 651–657 (May 1964).

Refractive properties of barium fluoride, I. H. Malitson, J. Opt. Soc. Am. **54,** No. 5, 628–632 (May 1964).

The second industrial revolution (Spanish translation), A. T. McPherson, Rev. Centro Estud. Ing., **132,** No. 669, 348–354 (1963).

Nuclear magnetic resonance in lead alloys, R. J. Snodgrass and L. H. Bennett, Phys. Rev. **134,** No. 5A, A1294 (June 1, 1964).

Radar echoes from Venus at 50 Mc/sec, W. K. Klemperer, G. R. Ochs, and K. L. Bowles, Astron. J. **69,** No. 1 (1316), 22–28 (Feb. 1964).

On the theory of Schumann resonances in the earth-ionosphere cavity, J. R. Wait, Can. J. Phys. **42,** 575–582 (Apr. 1964).

Statistical model for the beta zirconium hydrides, T. B. Douglas, J. Chem. Phys. **40,** No. 8, 2248–2257 (Apr. 15, 1964).

Optical constants of thin films from the characteristic electron energy losses, R. E. LaVilla and H. Mendlowitz, J. Phys. **25,** 114–118 (Jan.–Feb. 1964).

Thermodynamics of solutions of deuterium chloride in heavy water from 5 to 50°, R. Gary, R. G. Bates, and R. A. Robinson, J. Phys. Chem. **68,** 1186–1190 (1964).

Absorption spectra of diatomic molecules in liquid and crystalline rare gases, G. L. Pollack and A. A. Pollack (Proc. 14th Annual Mid-America Spectroscopy Symp., Chicago, Ill., May 20–23, 1963), Book, Developments in Applied Spectroscopy **3,** 376–382, Ed. J. E. Foreette and E. Lanterman (Plenum Press, New York, N.Y., 1964).

A note on some quadrature formulas for the interval $(-\infty, \infty)$, S. Haber, Math., Computation **18,** No. 86, 313–314 (Apr. 1964).

Comments by J. R. Wait on the paper "Obstacle gain and shadow loss," by G. H. Crenier, to the Editor of Microwave J. **6,** No. 7, 83 (July 1963).

Absence of pronounced quadrupole effects in the nuclear resonance of In^{115} in a non-cubic environment, L. H. Bennett and R. J. Snodgrass, Phys. Rev. **134,** No. 5A, A1290 (June 1, 1964).

Kinetics and mechanism of the low-cubic to hexagonal phase transformation of silver iodide, J. Phys. Chem. **68,** No. 5, 1111–1113 (1964).

Superconductivity in semiconducting $SrTiO_3$, J. F. Schooley, W. R. Hosler, and M. L. Cohen, Phys. Rev. Letters **12,** 474 (1964).

On the concentrations of vibrationally excited O_2 formed in the flash photolysis of NO_2, A. M. Bass and D. Garvin, J. Chem. Phys. **40,** No. 6, 1772–3 (Mar. 15, 1964).

Energy, temperature, and organisms, D. M. Gates, Sci. Teacher **31,** No. 4 (May 1964).

Some aspects of the coordination chemistry of boron, T. D. Coyle and F. G. A. Stone, Progr. Boron Chem. **1,** 83–166 (1964).

The relation between VLF propagation and *D*-layer characteristics, J. R. Wait, IEEE Trans. Ant. Prop. **AP-12,** No. 2 (Mar. 1964).

**Publications for which a price is indicated are available by purchase from the Superintendent of Documents, U.S. Government Printing Office, Washington, D.C., 20402 (foreign postage, one-fourth additional). Reprints from outside journals and the NBS Journal of Research may often be obtained directly from the authors.*

UNITED STATES DEPARTMENT OF COMMERCE · John T. Connor, *Secretary*
NATIONAL BUREAU OF STANDARDS · A. V. Astin, *Director*

Engineering and Instrumentation

Section C

JOURNAL OF RESEARCH

of the

NATIONAL BUREAU OF STANDARDS

Volume 68C—January to December 1964

Papers 68C1–147 to 68C4–177

For sale by the Superintendent of Documents, U.S. Government Printing Office
Washington, D.C. 20402

Corrections to be noted in Volume 68 of the JOURNAL OF RESEARCH of the National Bureau of Standards—C. Engineering and Instrumentation

Page	Column	Line	Now reads in part	Should read
2	1	21	changing current	charging current
25	2	22	along the other	along the other when the laser is excited without the diaphragm.
27	1	Fig. 4, legend	in figure 5	in figure 2.
41	1	16	furance	furnace
44	1	Table 3	The values of the column attributed to Sine are for the iridium 40 percent-rhodium 60 percent versus iridium thermocouple and should not be included in table 3 nor in the discussion on page 43.	
93	1	Fig. 1b, legend	Full size	3/4×
94	2	Figs. 3 and 4	These two figures should be transposed.	
95	1	Fig. 5, legend	environmental tests	environment tests
116	1	2	pounds	pounds
		3	changes	changes
266	2	4	$\times 10^{-2}t^3$	$\times 10^{-2}t$.

CONTENTS OF VOLUME 68C

Volume 68C—No. 1—January–March 1964

Page

A Fabry-Perot spectrometer for high-resolution spectroscopy and laser work. Klaus D. Mielenz, Robert B. Stephens, and Karl F. Nefflen 1
A variable impedance power meter, and adjustable reflection coefficient standard. Glenn F. Engen 7
A laser with a multihole diaphragm. Tadashi Morokuma 25
Principles of cryometric impurity determination as applied to samples of small sizes. Charles P. Saylor and Gaylon S. Ross 35
Reference tables for thermocouples of iridium-rhodium alloys versus iridium. G. F. Blackburn and F. R. Caldwell 41

Volume 68C—No. 2—April–June 1964

Fringe pattern of an oscillating Fabry-Perot interferometer. K. D. Mielenz 73
Interferometer for testing extended surfaces such as surface plates and precision ways. J. B. Saunders and John V. McDermott 83
Ferrimagnetic resonance in polycrystalline ferrite and garnet disks at L-band frequencies. W. E. Case, R. D. Harrington, and L. B. Schmidt 85
Changes in the influence of atmospheric humidity during fatigue of an aluminum alloy. John A. Bennett 91
The theory of a stable high-speed externally pressurized gas-lubricated bearing. H. Sixsmith and W. A. Wilson 101
Infrared spectra of asphalts: some aspects of the changes caused by photo-oxidation. Paul G. Campbell and James R. Wright 115

Volume 68C—No. 3—July–September 1964

Response of highly precise balances to thermal gradients. L. B. Macurdy . 135
A direct-reading two-knife 50-pound balance of high precision suitable for State weights and measures laboratories. H. E. Almer, H. A. Bowman, M. W. Jensen, L. B. Macurdy, H. S. Peiser, and B. Wasko 141
Wave front shearing prism interferometer. J. B. Saunders 155
A new high resolution small-angle x-ray camera. H. Brumberger and R. Deslattes 173
Experimental determination of air drag on a textile yarn struck transversely by a high-velocity projectile. Jack C. Smith, Carl A. Fenstermaker, and Paul J. Shouse 177

Volume 68C—No. 4—October–December 1964

Page

Theory of mirror spectrographs I. Astigmatic illumination of plane gratings and prisms. Klaus D. Mielenz 195
Theory of mirror spectrographs II. General theory of focal surfaces and slit curvatures. Klaus D. Mielenz 201
Theory of mirror spectrographs III. Focal surfaces and slit curvature of Ebert and Ebert-Fastie spectrographs. Klaus D. Mielenz 205
Heat flow in a right circular cylinder with arbitrary temperature boundary conditions—applications to the determination of thermal conductivity. D. R. Flynn 215
Digitized phasemeter. William S. Epstein 223
Active and passive direct-reading ratio sets for the comparison of audio-frequency admittances. Robert D. Cutkosky 227
Review of methods for the excitation of atomic and ionic spectra by means of high-frequency discharges and sliding sparks. Lennart Minnhagen 237
Standards for the calibration of Q-meters 50 kHz to 45 MHz. R. N. Jones. 243
X-ray measurement of residual strains in individual grains of polycrystalline aluminum. Clarence J. Newton 249
Ferrimagnetic resonance measurements using IF substitution techniques. W. E. Case, R. D. Harrington, and L. B. Schmidt 255
A Pienkowsky-type calibration scheme for 5211Σ1 weight series using two knife-edge direct-reading balances. H. S. Peiser 261
Reference tables for the Platinel II thermocouple. L. O. Olsen and P. D. Freeze 263
Effects of cathodic currents on the corrosion of an aluminum alloy. William J. Schwerdtfeger 283
Photooxidation of asphalts in the presence of ozone. James R. Wright and Paul G. Campbell 297
Designs for temperature and temperature gradient compensated capacitors smaller than ten picofarads. Robert D. Cutkosky 305

U.S. GOVERNMENT PRINTING OFFICE:1965

JOURNAL OF RESEARCH of the National Bureau of Standards—C. Engineering and Instrumentation
Vol. 68C, No. 4, October–December 1964

INDEX TO VOLUME 68C

January to December 1964

A

Page
Air drag on a textile yarn struck transversely by a high-velocity projectile, experimental determination ... 177
Almer, H. E., H. A. Bowman, M. W. Jensen, L. B. Macurdy, H. S. Peiser, B. Wasko, A direct-reading two-knife 50-pound balance of high precision for state weights and measures laboratories ... 141
Alloy, aluminum, cathodic protection ... 283
Alloy, aluminum, effects of cathodic currents on the corrosion ... 283
Aluminum alloy, changes in influence of atmospheric humidity during fatigue ... 91
Aluminum alloy, effects on cathodic currents on corrosion ... 283
Asphalts, infrared spectra of some aspects of the changes caused by photo-oxidation ... 115
Asphalts, photooxidation in the presence of ozone ... 297
Atmospheric humidity, changes in influence during fatigue of aluminum alloy ... 91
Audio-frequency admittances, comparison of, active and passive direct-reading ratio sets ... 227

B

Balance, a direct-reading two-knife 50-pound, of high precision suitable for state weights and measures laboratories ... 141
Balances, response to thermal gradients ... 135
Bearing, theory of a stable high-speed externally pressurized gas-lubricated ... 101
Bennett, J. A., Changes in the influence of atmospheric humidity during fatigue of an aluminum alloy ... 91
Blackburn, G. F., F. R. Caldwell, Reference tables for thermocouples of iridium-rhodium alloys versus iridium ... 41
Bowman, H. A., H. E. Almer, M. W. Jensen, L. B. Macurdy, H. S. Peiser, B. Wasko, A direct-reading two-knife 50-pound balance of high precision suitable for state weights and measures laboratories ... 141
Brumberger, H., R. Deslattes, A new high resolution small-angle x-ray camera ... 173

C

Caldwell, F. R., G. F. Blackburn, Reference tables for thermocouples of iridium-rhodium alloys versus iridium ... 41
Calibration of weight series using two knife-edge direct-reading balances ... 261
Campbell, P. G., J. R. Wright, Infrared spectra of asphalts: some aspects of the changes caused by photooxidation ... 115
—, —, Photooxidation of asphalts in the presence of ozone ... 297
Case, W. E., R. D. Harrington, L. B. Schmidt, Ferrimagnetic resonance in polycrystalline ferrite and garnet disks at L-band frequencies ... 85
—, —, —, Ferrimagnetic resonance measurements using IF substitution techniques ... 255
Cathodic currents, effects of, on the corrosion of an aluminum alloy ... 283
Changes in the influence of atmospheric humidity during fatigue of an aluminum alloy ... 91
Cryometric impurity determination, principles of, as applied to samples of small sizes ... 35
Cutkosky, R. D., Active and passive direct-reading ratio sets for the comparison of audio-frequency admittances ... 227
—, Designs for temperature and temperature gradient compensated capacitors smaller than ten picofarads ... 305
Cylinder, right circular, heat flow in, with arbitrary temperature boundary conditions—applications to the determination of thermal conductivity ... 215

D

Designs for temperature and temperature gradient compensated capacitors smaller than ten picofarads ... 305
Deslattes, R. H. Brumberger, A new high resolution small-angle x-ray camera ... 173
Digitized phasemeter ... 223
Direct-reading ratio sets, active and passive, for the comparison of audio-frequency admittances ... 227
Direct-reading two-knife 50-pound balance of high precision suitable for state weights and measures laboratories ... 141

E

Ebert and Ebert-Fastie spectographs, focal surfaces and slit curvatures of, theory of mirror spectographs ... 205
Effects of cathodic currents on the corrosion of an aluminum alloy ... 283
Engen, G. F., Variable impedance power meter, and adjustable reflection coefficient standard ... 223
Epstein, W. S., Digitized phasemeter ... 223
Excitation of atomic and ionic spectra by means of high-frequency discharges and sliding sparks ... 237
Experimental determination of air drag on a textile yarn struck transversely by a high-velocity projectile ... 177

F

Page
Fabry-Perot interferometer, oscillating, fringe pattern ... 73
Fabry-Perot spectrometer for high-resolution spectroscopy and laser work ... 1
Fatique of aluminum alloy, changes in influence of atmospheric humidity ... 91
Fenstermaker, C. A., J. S. Smith, P. J. Shouse, Experimental determination of air drag on a textile yarn struck transversely by a high-velocity projectile ... 177
Ferrimagnetic resonance in polycrystalline ferrite and garnet disks at L-band frequencies ... 85
Ferrimagnetic resonance measurements using IF substitution techniques ... 255
Flynn, D. R., Heat flow in a right circular cylinder with arbitrary temperature boundary conditions—applications to the determination of thermal conductivity ... 215
Freeze, P. D., L. O. Olsen, Reference tables for the Platinel II thermocouple ... 263
Fringe pattern of an oscillating Fabry-Perot interferometer ... 73

H

Harrington, R. D., W. E. Case, L. B. Schmidt, Ferrimagnetic resonance in polycrystalline ferrite and garnet disks at L-band frequencies ... 85
—, —, —, Ferrimagnetic resonance measurements using IF substitution techniques ... 255
Heat flow in a right circular cylinder with arbitrary temperature conditions—applications to the determination of thermal conductivity ... 215
High-frequency discharges and sliding sparks, excitation of atomic and ionic spectra ... 237

I

Infrared spectra of asphalts: some aspects of the changes caused by photo-oxidation ... 115
Interferometer for testing extended surfaces such as plates and precision ways ... 83
Interferometer, oscillating Fabry-Perot fringe pattern ... 73
Interferometer, wave front shearing prism ... 155
Iridium-rhodium alloys versus iridium, reference tables for thermocouples ... 41

J

Jensen, M. W., H. E. Almer, H. A. Bowman, L. B. Macurdy, H. S. Peiser, B. Wasko, A direct-reading two-knife 50-pound balance of high precision suitable for state weights and measures laboratories ... 141
Jonee, R. N., Standards for the calibration of *Q*-meters 50 kHz to 45 MHz ... 243

L

Laser with a multihole diaphragm ... 25
Laser work, a Fabry-Perot spectrometer for high-resolution spectroscopy ... 1
Lens testing ... 155

M

Macurdy, L. B., Response of highly precise balances to thermal gradients ... 135
—, *H. E. Almer, H. A. Bowman, M. W. Jensen, H. S. Peiser, B. Wasko,* A direct-reading two-knife 50-pound balance of high precision suitable for state weights and measures laboratories ... 141
McDermott, J. V., J. B. Saunders, Interferometer for testing extended surfaces such as surface plates and precision ways ... 83
Mielenz, K. D., Fringe pattern of an oscillating Fabry-Perot interferometer ... 73
—, Theory of mirror spectrographs. I. Astigmatic illumination of plane gratings and prisms ... 195
—, Theory of mirror spectrographs. II. General theory of focal surfaces and slit curvatures ... 201
—, Theory of mirror spectrographs. III. Focal surfaces and slit curvature of Ebert and Ebert-Fastie spectrographs ... 205
—, *R. B. Stephens, K. F. Nefflen,* A Fabry-Perot spectrometer for high-resolution spectroscopy and laser work ... 1
Minnhagen, L., Review of methods for the excitation of atomic and ionic spectra by means of high-frequency discharges and sliding sparks ... 237
Morokuma, T., A laser with a multihole diaphragm ... 25

N

Nefflen, K. F., K. D. Mielenz, R. B. Stephens, A Fabry-Perot spectrometer for high-resolution spectroscopy and laser work ... 1
New high resolution small-angle x-ray cameras ... 173
Newton, C. J., X-ray measurement of residual strains in individual grains of polycrystalline aluminum ... 249

O

Page

Olsen, L. O., P. D. Freeze, Reference tables for the Platinel II thermocouple 263
Ozone, photooxidation of asphalts in the presence 297

P

Peiser, H. S., A Pienkowsky-type calibration scheme for 5211Σ1 weight series using two knife-edge direct-reading balances 261
—, *H. E. Almer, H. A. Bowman, M. W. Jensen, L. B. Macurdy, B. Wasko,* A direct-reading two-knife 50-pound balance of high precision suitable for state weights and measures laboratories 141
Phasemeter, digitized 223
Photooxidation of asphalts in the presence of ozone 297
Photooxidation, the changes caused by, some aspects of, infrared spectra of asphalts 115
Pienkowsky-type calibration scheme for 5211Σ1 weight series using two knife-edge direct-reading balances 261
Platinel II ther mocouple, reference tables 263
Polycrystalline aluminum, x-ray measurement of residual strains in individual grains 249
Polycrystalline ferrite and garnet disks at L-band frequencies, ferrimagnetic resonance 85
Power meter, variable impedance, and adjustable reflection coefficient standard 7
Principles of cryometric impurity determination as applied to samples of small sizes 35
Prism interferometer, wave front shearing 155

Q

Q-meters 50 kHz to 45 MHz, standards for the calibration 243

R

Reference tables for the Platinel II thermocouple 263
Reference tables for thermocouple of iridium-rhodium alloys versus iridium 41
Residual strains in individual grains of polycrystalline aluminum, x-ray measurement 249
Response of highly precise balances to thermal gradients 135
Review of methods for the excitation of atomic and ionic spectra by means of high-frequency discharges and sliding sparks 237
Ross, G. S., C. P. Saylor, Principles of cryometric impurity determination as applied to samples of small sizes 35

S

Saunders, J. B., Wave front shearing prism interferometer 155
—, *J. V. McDermott,* Interferometer for testing extended surfaces such as plates and precision ways 83
Saylor, C. P., G. S. Ross, Principles of cryometric impurity determination as applied to samples of small sizes 35
Schmidt, L. B., W. E. Case, R. D. Harrington, Ferrimagnetic resonance in polycrystalline ferrite and garnet disks at L-band frequencies 85
—, —, —, Ferrimagnetic resonance measurements using IF substitution techniques 255
Schwerdtfeger, W. J., Effects of cathodic currents on the corrosion of an aluminum alloy 283
Shouse, P. J., J. C. Smith, C. A. Fenstermaker, Experimental determination of air drag on a textile yarn struck transversely by a high-velocity projectile 177

Page

Sizmith, H., W. A. Wilson, Theory of a stable high-speed externally pressurized gas-lubricated bearing 101
Sliding sparks and high-frequency discharges, excitation of atomic and ionic spectra 237
Smith, J. C., C. A. Fenstermaker, P. J. Shouse, Experimental determination of air drag on a textile yarn struck transversely by a high-velocity projectile 177
Spectra, infrared, of asphalts, some aspects of the changes caused by photooxidation 115
Spectrographs, mirror, astigmatic illumination of plane gratings and prisms 195
Spectrograph, mirror, focal surfaces and slit curvature of Ebert and Ebert-Fastie spectrographs 205
Spectrographs, mirror, general theory of focal surfaces and slit curvatures 201
Spectrometer, a Fabry-Perot, for high-resolution spectroscopy and laser work 1
Standards for the calibration of *Q*-meters 50 kHz to 45 MHz 243
Stephens, R. B., K. D. Mielenz, K. F. Nefften, A Fabry-Perot spectrometer for high-resolution and laser work 1
Surface plates, interferometric testing 83

T

Temperature and temperature gradient compensated capacitors smaller than ten picofarads, designs 305
Testing of lens 155
Textile yarn struck transversely by a high-velocity projectile, experimental determination of air drag 177
Theory of a stable high-speed externally pressurized gas-lubricated bearing 101
Theory of mirror spectrographs. I Astigmatic illumination of plane gratings and prisms 195
Theory of mirror spectrographs. II. General theory of focal surfaces and slit curvatures 201
Theory of mirror spectrographs. III. Focal surfaces and slit curvature of Ebert and Ebert-Fastie spectrographs 205
Thermal conductivity, applications to the determination of, heat flow in a right cylinder with arbitrary temperature boundary conditions 215
Thermal gradients, response of highly precise balances 135
Thermocouples of iridium-rhodium alloys versus iridium, reference tables 41
Thermocouple reference tables (Platinel II) 263

V

Variable impedance power meter, and adjustable reflection coefficient standard 7

W

Wasko, B., H. E. Almer, H. A. Bowman, M. W. Jensen, L. B. Macurdy, H. S. Peiser, A direct-reading two-knife 50-pound balance of high precision suitable for state weights and measures laboratories 141
Wave front shearing prism interferometer 155
Ways, precision, testing 83
Wilson, W. A., H. Sizmith, Theory of a stable high-speed externally pressurized gas-lubricated bearing 101
Wright, J. R., P. G. Campbell, Infrared spectra of asphalts: some aspects of the changes caused by photooxidation 115
—, —, Photooxidation of asphalts in the presence of ozone 297

X

X-ray camera, small-angle, a new high resolution 173
X-ray measurement of residual strains in individual grains of polycrystalline aluminum 249

U.S. GOVERNMENT PRINTING OFFICE : 1964

UNIVERSITY MICROFILMS INC
EDITORIAL DEPARTMENT
313 NORTH FIRST ST
ANN ARBOR MICH

UNITED STATES
GOVERNMENT PRINTING OFFICE
DIVISION OF PUBLIC DOCUMENTS
WASHINGTON, D.C. 20402

OFFICIAL BUSINESS

PENALTY FOR PRIVATE USE TO AVOID
PAYMENT OF POSTAGE, $300
(GPO)

JOURNAL OF RESEARCH of the National Bureau of Standards Vol. 68C, No. 4 October–December 1964
C. Engineering and Instrumentation

Contents

	Page
Theory of mirror spectrographs I. Astigmatic illumination of plane gratings and prisms. Klaus D. Mielenz.	195
Theory of mirror spectrographs II. General theory of focal surfaces and slit curvatures. Klaus D. Mielenz.	201
Theory of mirror spectrographs III. Focal surfaces and slit curvature of Ebert and Ebert-Fastie spectrographs. Klaus D. Mielenz.	205
Heat flow in a right circular cylinder with arbitrary temperature boundary conditions—applications to the determination of thermal conductivity. D. R. Flynn.	215
Digitized phasemeter. William S. Epstein.	223
Active and passive direct-reading ratio sets for the comparison of audio-frequency admittances. Robert D. Cutkosky.	227
Review of methods for the excitation of atomic and ionic spectra by means of high-frequency discharges and sliding sparks. Lennart Minnhagen.	237
Standards for the calibration of Q-meters 50 kHz to 45 MHz. R. N. Jones.	243
X-ray measurement of residual strains in individual grains of polycrystalline aluminum. Clarence J. Newton.	249
Ferrimagnetic resonance measurements using IF substitution techniques. W. E. Case, R. D. Harrington, and L. B. Schmidt.	255
A Pienkowsky-type calibration scheme for 5211Σ1 weight series using two knife-edge direct-reading balances. H. S. Peiser.	261
Reference tables for the Platinel II thermocouple. L. O. Olsen and P. D. Freeze.	263
Effects of cathodic currents on the corrosion of an aluminum alloy. William J. Schwerdtfeger.	283
Photooxidation of asphalts in the presence of ozone. James R. Wright and Paul G. Campbell.	297
Designs for temperature and temperature gradient compensated capacitors smaller than ten picofarads. Robert D. Cutkosky.	305
Publications of the National Bureau of Standards.	309
Index to volume 68C, January to December 1964.	321

Library of Congress Catalog Card Number: 62–3900

For sale by the Superintendent of Documents, U.S. Government Printing Office, Washington, D.C., 20402. Price 75 cents (single copy). Subscription price: $2.25 a year; 50 cents additional for foreign mailing.

UNITED STATES GOVERNMENT PRINTING OFFICE, WASHINGTON : 1964